SYNTHESIS AND CHARACTERIZATION OF $ACrO_2$ (A = Cu, Ag) DELAFOSSITE COMPOUNDS

Teză destinată obţinerii
titlului ştiinţific de doctor inginer
la
Universitatea "Politehnica" din Timişoara
în domeniul INGINERIA MATERIALELOR
de către

Fiz. Ing. Sanjay Kumar

Conducător ştiinţific: CS I dr. fiz. Ioan Grozescu
Referenţi ştiinţifici: Dr. Christine Martin
Dr. Sylvie Hebert
Conf. Dr. Ing. Corneliu Marius Craciunescu

Ziua susţinerii tezei: 27.09.2012

Seriile Teze de doctorat ale UPT sunt:

1. Automatică
2. Chimie
3. Energetică
4. Ingineria Chimică
5. Inginerie Civilă
6. Inginerie Electrică
7. Inginerie Electronică şi Telecomunicaţii
8. Inginerie Industrială
9. Inginerie Mecanică
10. Ştiinţa Calculatoarelor
11. Ştiinţa şi Ingineria Materialelor
12. Ingineria sistemelor
13. Inginerie energetică
14. Calculatoare şi tehnologia informaţiei

Universitatea „Politehnica” din Timişoara a iniţiat seriile de mai sus în scopul diseminării expertizei, cunoştinţelor şi rezultatelor cercetărilor întreprinse în cadrul şcolii doctorale a universităţii. Seriile conţin, potrivit H.B.Ex.S Nr. 14 / 14.07.2006, tezele de doctorat susţinute în universitate începând cu 1 octombrie 2006.

România, 300159 Timişoara, Bd. Republicii 9,
tel. 0256 403823, fax. 0256 403221
e-mail: editura@edipol.upt.ro

ACKNOWLEDGMENTS

I would like to express my deepest gratitude and heartfelt thanks to **Dr. Marinela Miclau** for her constructive guidance, encouragement, intellectual support and her inspiring words. Also, I would like to thank my co-advisor, **Dr. Christine Martin** from CRISMAT, Caen, France, for her thoughtful input and help in my research. One of the greatest lesson I learned from my advisors is to know the limits of my own knowledge and seek out the assistance of others when necessary. They have also taught me to think critically and question incessantly, and for that I am grateful to them. I would like to thank my institute director **Dr. Ion Grozescu** for his continuous support, encouragement, and genuine excitement for my work. I am gratefully acknowledge financial support for this research project from the Initial Training Network SOPRANO, supported by the EU Seventh Framework Programme.

I owe special thanks to every members of my institute for their valuable advice and support. Working with each of them has taught me to think about my research from a different perspective, which has made it more thorough and definitely more interesting. I express my heartiest gratitude to 3 respectable ladies of my institute Mrs. Atena, Mrs. Miora, Mrs. Angelika and Mrs. Mihela Lazea, the administrative professionals who, in addition to securing logistical arrangements, provided encouragement and emotional energy at both high and low times making the process more enjoyable. I acknowledge my colleagues Mr. Daniel Ursu, Dr. Paula Sfirloaga (SEM), Dr. Anamaria (FT-IR measurement), Dr. Radu Banica (UV-Vis), Mr. Liviue, Kiran, Andrei Racu, Ivan Pirrotta, Alaxendra, Srinivas Rao for their support and help during my research work. A special thank to Gurgu Radu, Patean Ioan, Topciov Gheorghe (technical team), for providing their technical support and valuable discussion. I especially thank to Miss. Cristina Mosoarca, for her support and help that have given me great self-confidence and encouragement. Without her help, I would never have ended up at my research work. Words are not enough to describe her role in completion of my thesis work.

I wish to extend special thanks to CRISMAT, Caen professional team especially Dr. A. Maignan, Dr. Sylvie Hebert, Dr. Sylvain Marinel, Magali Kerdreux (SOPRANO Project Manager) and Jerome, Fafa, Marie, Febian (technical team) for their support and help during my one year stay in Caen. I am indebted to my predecessors, especially Dr. Kiran Patyal and Dr. Tapati Sarkar, for their mentorship, friendship, and continuous discussion in and out of laboratory (CRISMAT). I would also like to thank my colleagues from CRISMAT Mr. Raghvendra Nunna, Venakatesh Gopal, Victor Duffort, Dr. Maria Poienar, Dr. Pravin Walke, Mr. Takashi, Dr. Claudy R. Serrao including all members of Indo-Caen Cricket Club and Tandoori Night Club for their love and support.

Most importantly, I would like to thank my family members for their undying love, support and care. I would like to give special thank to my mom and dad for all their love and concern. Thanks to my brothers (Manoj Kumar, Satbir Singh) and sisters (Mrs. Meena) for their constant love and encouragement. Least but not last, I would like to special thank to my friends especially Ali Sher, Ankur, Nitin Malik, Divinadain, Buddhi, S. Saini, Bhaskar & family, Avinash & family, for their encouragement and support.

Timisoara, September 2012 Sanjay Kumar

Sanjay Kumar

Synthesis and characterization of $ACrO_2$ (A = Cu, Ag) delafossite compounds

Teze de doctorat ale UPT, Seria 15, Nr. 3, Editura Politehnica, 2012, 169 pagini, 95 figuri, 25 tabele.

ISSN: 2285-1720

ISSN-L: 2285-1720

ISBN: 978-606-554-530-4

Cuvinte cheie: Multiferroics, $CuCrO_2$ delafossite, $AgCrO_2$ delafossite, Monomode microwave, Hydrothermal, Spin glass, Ag based photocatalyst.

Rezumat,

The field of multiferroics has become more important for both: a basic understanding of the interaction between magnetic and electric coupling and the potential use of such materials in technical devices. Although there are many magnetic and ferroelectric materials, there are relatively few choices for multiferroic materials, since the conditions for co-existence of several types of order are stringent. Recent discovery of multiferroicity and p-type conductivity in delafossite compounds finds a potential application in transparent semiconductor devices.

Hydrothermal synthesis of $AgCrO_2$ delafossite was difficult to prepare at low temperature (<230 $^{\circ}$C) in an aqueous solution. Cu and Ag based delafossite compounds generally require high process temperature and exhibit minor impurity phases prepared via other conventional methods. Furthermore, very few reports are available for magnetic cation substitution study in $CuCrO_2$ system.

Thus, in the search of a new multiferroics, new $ACrO_2$ (A= Cu, Ag) delafossite compounds were prepared by hydrothermal, solid state and monomode microwave (MW) method. $CuCrO_2$ prepared by MW heating proved to be the fastest method compare to conventional methods. Study of vanadium substituted $CuCr_{1-x}V_xO_2$ ($0 \leq x \leq 0.5$) compounds prepared by solid state reaction method showed spin glass state for higher vanadium substituted samples ($0.2 \leq x \leq 0.5$) and remains long range antiferromagnetic ordered system for lower vanadium substituted samples ($0 \leq x < 0.2$). Hydrothermal method was developed to obtain $AgCrO_2$ polycrystalline sample in supercritical water condition using $K_2Cr_2O_7$ as an oxidizing agent. Also, hydrothermal method was developed to obtain Ag-based photocatalysts.

Thus, after a successful growth of pure $CuCrO_2$ and $AgCrO_2$ delafossite, hydrothermal process can be used to grow the single crystal of these compounds which is a basic block of fabrication of highly efficient transparent optoelectronic devices, microelectronics, spintronics, and sensors.

TABLE OF CONTENTS

LIST OF FIGURES

LIST OF TABLES

ABBREVIATION

AFM- Atomic force microscope
BET- S. Brauner, P. H. Emett, E. Teller
DMW- Direct microwave
EM- Electromagnetic
EDAX- Energy dispersive X-ray analysis
FT-IR- Fourier Transform Infrared
FC- Field cooling
FM- Ferromagnetic
HMW- Hybrid microwave
HT1- Hydrothermal preparation of $CuCrO_2$ at temperature 210 $^{\circ}C$ and pressure 50 bars in 2.5 M of NaOH for 48 hrs of reaction time
HT2- Hydrothermal preparation of $CuCrO_2$ at temperature 220 $^{\circ}C$ and pressure 70 bars in 2.5 M of NaOH for 48 hrs of reaction time
HT3- Hydrothermal preparation of $CuCrO_2$ at temperature 250 $^{\circ}C$ and pressure 100 bars in 2.5 M of NaOH for 48 hrs of reaction time
HT4- Hydrothermal preparation of $CuCrO_2$ at temperature 300 $^{\circ}C$ and pressure 200 bars in 2.5 M of NaOH for 48 hrs of reaction time
HRT1- Hydrothermal preparation of $CuCrO_2$ at temperature 300 $^{\circ}C$ and pressure 200 bars in 2.5 M of NaOH for 24 hrs of reaction time
HRT2- Hydrothermal preparation of $CuCrO_2$ at temperature 300 $^{\circ}C$ and pressure 200 bars in 2.5 M of NaOH for 48 hrs of reaction time
HM1- Hydrothermal preparation of $CuCrO_2$ at temperature 300 $^{\circ}C$ and pressure 200 bars in 1 M of NaOH for 48 hrs of reaction time
HM2- Hydrothermal preparation of $CuCrO_2$ at temperature 300 $^{\circ}C$ and pressure 200 bars in 2.5 M of NaOH for 48 hrs of reaction time
HP1- Hydrothermal preparation of $CuCrO_2$ at temperature 300 $^{\circ}C$ and pressure 50 bars in 1 M of NaOH for 48 hrs of reaction time
HP2- Hydrothermal preparation of $CuCrO_2$ at temperature 300 $^{\circ}C$ and pressure 300 bars in 1 M of NaOH for 48 hrs of reaction time
HP3- Hydrothermal preparation of $CuCrO_2$ at temperature 300 $^{\circ}C$ and pressure 500 bars in 1 M of NaOH for 48 hrs of reaction time
HP4- Hydrothermal preparation of $CuCrO_2$ at temperature 300 $^{\circ}C$ and pressure 50 bars in 2.5 M of NaOH for 48 hrs of reaction time
HP5- Hydrothermal preparation of $CuCrO_2$ at temperature 300 $^{\circ}C$ and pressure 200 bars in 2.5 M of NaOH for 48 hrs of reaction time
HP6- Hydrothermal preparation of $CuCrO_2$ at temperature 300 $^{\circ}C$ and pressure 500 bars in 2.5 M of NaOH for 48 hrs of reaction time
LCD- Liquid crystal display
LED- Light emitting diodes
MPMS- Magnetic property measurement system
MD- Magnetodielectric
ME- Magnetoelectric
MW- Microwave
MAE- Magnetic alter effect
PEC- Photoelectrochemical
PPMS- Physical property measurement system

SG- Spin glass
SQUID- Superconducting quantum interference device
SEM- Surface electron microscope
SS- Solid state
SDS-sodium dodecyl sulphate
TRM- Thermo remnant magnetization
TEC- Thermal expansion coefficient
TOF- Time of flight
TLA- Triangular lattice antiferromagnetic
TCO- Transparent conducting oxides
UV-Vis- Ultra vilot-visible
XRD- X-ray diffraction
ZFC- Zero field cooling

ABSTRACT

Over the past few years, transition metal oxides have received enormous amount of research interest because of their remarkable properties including piezo/ferroelectricity, high temperature superconductor, colossal magnetoresistance, and nonlinear optical behavior, and these properties can be tailored for a wide variety of technological applications. Mostly, these properties originate from the interplay between spin, lattice, charge, and orbital degrees of freedom of the material. Among these transitional metal oxides, multiferroic materials have attracted increasing interest due to their potential application in multifunctional devices as well as their fascinating fundamental physics. Multiferroic materials are those which possess both ferroelectric and ferromagnetic properties. Several multiferroics demonstrating magnetoelectric coupling effects have been discovered in the past few years. The field of multiferroics has become more important for both: a basic understanding of the interaction between magnetic and electric coupling and the potential use of such materials in magnetoelectric devices. Indeed, one could imagine the switching of magnetic states using an electric field or vice versa. These applications play a vital role in magnetoelectronic devices. Although there are many magnetic and ferroelectric materials, there are relatively few choices for multiferroic materials, since the conditions for co-existence of several types of order are stringent. The material falls under these categories are $BaTiO_3$, $BiFeO_3$, $BiMnO_3$, $PbVO_3$, $TbMn_2O_5$, $YMnO_3$, respectively (type I multiferroics). Another class of multiferroics which is a high interest of research is type II multiferroics where magnetism causes multiferrocity with high value of magnetoelectric coupling compared to type I multiferroics. Due to extensive research in the field of multiferroic materials, in 2003, people discovered large ferroelectric polarization in the epitaxial grown $BiFeO_3$ thin film. These new discoveries broken the traditional thinking about multiferroics and opened a new gate for industries: if charge can be controlled by external magnetic fields and spins can be controlled by applied voltage, new devices with varieties of functions may be designed.

Recent discovery of multiferroicity in delafossite compounds (type II multiferroics) made them a special class of materials that has a potential application in transparent semiconductor devices. Delafossite compound with general formulae ABO_2 have been reported in the triangular lattice antiferromagnets at transition temperature T_N = 24 K crystallizing in the rhombohedral (R-3m) or hexagonal (2H) crystal structure. Delafossite-type oxides are ABO_2 compounds characterized by a structural arrangement made of layers of edge-sharing BO_6 octahedra linked by linear O-A-O dumbbell bonds perpendicular to the layers. Because of this particular A-cation coordination, they are encountered mainly with d^{10} metal cations (Cu^+ or Ag^+). Variations in the layer stacking can lead to two different polytypes, 3R and 2H, with rhombohedral or hexagonal unit cell, respectively. Both polytypes can be regarded as belonging to the delafossite structure, because they retain the characteristic linear O-A-O structural units. These O-A-O layers and BO_6 layers act as separate conduction paths for holes and electrons, respectively. In addition, each oxygen atom builds an OB_3A tetrahedron, forming an O-$2sp^3$ orbital, which does not form localized O2p nonbonding states. These tetrahedra are favourable for hole conduction. Furthermore, the dumbbell O-A-O bonding reduces the O-O repulsion,

resulting in short A-O bond lengths. The interaction between the A^+ and O^{2-} ions then becomes stronger, and a highly dispersed valence band structure is expected. This highly dispersed valence band leads to a small effective mass of the holes with a higher hole mobility. In contrast to the strong interactions between them, interactions between the A^+ ions are weak because they work mainly through A^+-O^{2-}-B^{3+}-O^{2-}-A^+ links, which are two-dimensional in delafossite oxides.

Mostly these compounds are synthesized by solid state reaction method, sol-gel, pulsed laser deposition method, hydrothermal synthesis methods. Hydrothermal synthesis offers many advantages over conventional and non-conventional ceramic synthetic methods. From the standpoint of ceramic powder production, there are far fewer time and energy-consuming processing steps since high temperature calcination, mixing, and milling steps are either not necessary or minimized. Another important advantage of the hydrothermal synthesis is that the purity of hydrothermally synthesized powders significantly exceeds the purity of the starting materials. The impurities are subsequently removed from the system together with the crystallizing solution, which does not take place during other synthesis routes, such as hightemperature calcination. Delafossite compounds are electrically anisotropic in nature. $ACrO_2$ (A= Cu, Ag) delafossite show semi-metallic behaviour. Among the delafossite structure oxides, the $CuCrO_2$ thin film had shown a conductivity of the order 1 $S.cm^{-1}$, and upon doping with 5% Mg the conductivity can be improved to 220 $S.cm^{-1}$ which is the largest conductivity in p-TCOs. It is well studied that substitution of Mg^{2+} ions at the Cr site, the resistivity and seebeck coefficient drastically decrease without a change of Neel temperature (T_N = 26K). Also, substitution of Mn at Cr site of $CuCrO_2$ increases the resistivity compared to parent $CuCrO_2$ compound. And the resistivity of the samples increases as the Mn concentration increases for $x \leq 0.10$. Demonstration of p-type in delafossite type transparent conducting oxides (TCO) has attracted people's attention due to their capability to fill in the vacancy of p-type TCO in transparent electronic devices.

In $CuFeO_2$, substitution of trivalent diamagnetic cations for Fe^{3+} is known to change the antiferromagnetic state and induce ferroelectricity. But partial occupation of the Fe^{3+} site by V^{3+} is responsible for disordered magnetism in $CuFe_{0.5}V_{0.5}O_2$. Therefore, in the search of a new multiferroics, the symmetry of the structure is of prime importance and the possibility offered by magnetic structures to break the inversion symmetry has been used to discover numerous spin induced ferroelectrics and strong magnetoelectric (ME) coupling.

The aim of this thesis work is to investigate new chromium based $ACrO_2$ (A= Cu, Ag) delafossite synthesized by hydrothermal, solid state reaction method and monomode microwave method. We have studied the structural, magnetic and dielectric properties of vanadium substituted samples of $CuCr_{1-x}V_xO_2$ ($0 \leq x \leq 0.5$) delafossite compounds prepared by solid state reaction method. In addition to this, we have studied the synthesis conditions, structural and optical properties of Ag-based photocatalysts synthesized by hydrothermal method useful for photocatalytic application.

In the first part of thesis, $CuCrO_2$ with delafossite structure (rhombohedral R-3*m* structure) were successfully synthesized by hydrothermal process. Structure analysis of sample prepared at 300 ^{0}C temperature in 2.5 M of NaOH in an aqueous solution for reaction time 48 hours revealed that the final product showed the

characteristics of the delafossite structure with rhombohedral (3R) phase with presence of any impurity phase. It belongs to the space group R-3*m* and rhombohedral crystal system with cell parameters *a* and *c* are 2.9718 Å and 17.105 Å. SEM images shows microspheres with diameter of about 2-4 μm. The micron size sphere appear a bunch of pure $CuCrO_2$ platelets of size ranges from 0.7 μm to 3 μm. Role of reaction temperature, reaction time, molarity and pressure is thoroughly discussed and reveal increase in reaction time, molarity and temperature increases the solubility of reactants and rate of conversion into their corresponding hydrate species. Effect of pressure study reveals that there was no evidence of phase transformation at elevated pressure. Samples prepared in the pressure regime between 200 to 300 bars leads to the formation of single phase of $CuCrO_2$. Furthermore to enhance the electrical and magnetic properties of $CuCrO_2$, a new approach, based on microwave heating, is used to synthesis $CuCrO_2$ delafossite by solid state reaction, starting from Cu_2O and Cr_2O_3. It is evidenced that microwave heating enhances solid state reaction kinetics as only 5 minutes are needed to achieve the reaction. Powder X-ray diffraction as well as magnetic and electrical measurements shows characteristics typical of the 3R delafossite. Microstructures are observed by scanning electron microscopy, the smaller size of the grains, compared to samples prepared by conventional solid state reaction method, is confirmed by the particle size analysis.

Effect of vanadium substitution at Cr site has been studied in $CuCrO_2$ compounds with delafossite crystal structure. We performed the detailed study on structural, magnetic, dielectric and polarization properties of series of sample $CuCr_{1-x}V_xO_2$ ($0 \le x \le 0.5$). Structural and phase analysis showed that series of sample $CuCr_{1-x}V_xO_2$ ($0 \le x \le 0.5$) have characteristic of the 3R delafossite. The powder diffraction patterns indicate the absence of any structural phase transition in the whole investigated range of the V^{3+} content in series of sample $CuCr_{1-x}V_xO_2$ ($0 \le x \le 0.5$). The lattice parameters changes linearly with increasing x: cell parameter *a* and *c* increases with increase in x that in turn increases the unit cell volume.

Magnetic property study of vanadium (V) substituted samples of the series $CuCr_{1-x}V_xO_2$ ($0 \le x \le 0.5$) showed the two different range of composition with different magnetic susceptibility curves. For the lower V^{3+} substituted samples ($0 \le x < 0.18$) the magnetization curves M_{ZFC} (T) and M_{FC} (T) for ZFC and FC modes follows a broad anomaly (varies with vanadium content in $CuCrO_2$) where as in higher V^{3+} substituted samples ($0.18 \le x \le 0.5$), M_{ZFC} (T) exhibits a cusp at low temperature (< 15 K) and merge with M_{FC} (T) at a slightly higher temperature. Also for the higher V^{3+} substituted samples ($0.18 \le x \le 0.5$) M_{FC} (T) remains temperature independent below magnetic transition temperature ($T_{\chi(max)}$) which is a typical characteristic of spin glass (freezing of spins). This kind of magnetic transition could be due to the strong competing interaction between Cr^{3+} and V^{3+} cations that gives rise to three types of magnetic interactions: strong antiferromagnetic interaction in Cr^{3+}-Cr^{3+}, weak antiferromagnetic interaction in V^{3+}-V^{3+}, and ferromagnetic interaction in Cr^{3+}-V^{3+}. These competing interactions are responsible for the origin of disordered magnetic behavior in $CuCr_{1-x}V_xO_2$ for $0.18 \le x \le 0.5$. $T_{\chi(max)}$ (K) decreases abruptly with increase in V^{3+} content for samples of series $CuCr_{1-x}V_xO_2$ ($0 \le x < 0.18$) and remains almost constant (~ 11 K) for higher V^{3+} substitution in $CuCr_{1-x}V_xO_2$ ($0.18 \le x \le 0.5$). The isothermal magnetization (M) versus magnetic field (H) curves at constant temperature 5 K demonstrated the linear curve in lower vanadium substituted samples of $CuCr_{1-x}V_xO_2$ ($0 \le x < 0.18$)

which is a typical characteristic of parent compound $CuCrO_2$ suggesting the presence of long range ordering. Similarly, the M-H curve of high vanadium content samples i.e. x=0.18, 0.2, 0.3, 0.5 are S shaped and different in shape from the low vanadium content samples. This proves the argument that there exists different magnetic ground state at lower and higher V compositions. Thus, the S shape exists in M (H) curve and temperature independent magnetization (M_{FC} (T)) below 15 K for the samples of the series $CuCr_{1-x}V_xO_2$ ($0.18 \leq x \leq 0.5$) arrests characteristic of a spin glass and the lack of saturation reflects the randomness of the magnetic moments. For further confirmation of spin glass (SG) like behavior in samples of $CuCr_{1-x}V_xO_2$ for $0.18 \leq x \leq 0.5$, the temperature dependent ac magnetic susceptibility measurement χ'_{ac} (T, f) were performed in zero dc magnetic field (H_{dc} = 0 Oe) at different frequencies ranging from 10 Hz up to 10 kHz. A sharp cusp was visible in the in-phase component of χ'_{ac} (T) for all samples of $CuCr_{1-x}V_xO_2$ for $0.18 \leq x \leq 0.5$. All samples for $0.18 \leq x \leq 0.5$ shows the frequency dependent peaks in the ac susceptibility measurements. The imaginary component of the ac magnetic susceptibility also showed that the maximum of χ''_{ac} (T) appears at a lower temperature than the maximum of χ'_{ac} (T) and was also frequency dependent. Furthermore, analyzing the frequency dependence of the peak in χ'_{ac} (T, f) by using the power law of the form $\ln \tau = \ln\tau_o - z\nu\ln\{(T_f - T_g)/T_g\}$ and the phenomenological parameter $p = (\Delta T_f/T_f)/(\Delta \log f)$ gives the corresponding values of p lied in the range of ~ 0.04, the spin relaxation time τ_o lied in the range of values typical of spin glass (10^{-10} s) and the $z\nu$ values lied between 4 and 11. The ac frequency dependant magnetic susceptibility data and power law fitting strongly supported the argument of true spin glass in high vanadium substituted samples ($0.18 \leq x \leq 0.5$). Also, we have demonstrated the aging and memory phenomena using aging protocol on sample $CuCr_{0.7}V_{0.3}O_2$.

We have also studied the ferroic properties of vanadium substituted samples. Dielectric property characterization on series of samples showed that sample with composition x< 0.18 showed a long range ordering with ferroelectricity induced by spin ordering (long range ordering) whereas in sample with $0.18 \leq x \leq 0.5$, there exist spin glass behaviour that precludes the existence of ferroelectricity induced by an antiferromagnetic state as observed in parent $CuCrO_2$. In addition to this, we have measured the magnetodielectric coupling effect ($MD = [\varepsilon(H) - \varepsilon(H = 0)]/\varepsilon(H = 0)$) as a function of magnetic field at frequency of 100 kHz at temperature T = 5K with varying vanadium content in $CuCrO_2$. A large quadratic coupling was observed in sample with x=0.18 (~ 0.6 %) and a smaller one at composition x = 0.5 (~ < 0.1 %).

Finally we have concluded that the magnetic and ferroelectric properties of polycrystalline sample of series $CuCr_{1-x}V_xO_2$ ($0 \leq x \leq 0.5$) proved that higher vanadium substituted samples ($0.18 \leq x \leq 0.5$) showed the existence of a spin glass state is evidenced by magnetization, ac susceptibility and dielectric property measurements. Large polarization values were observed in all high vanadium substituted samples ($0.18 \leq x \leq 0.5$) as compared to lower vanadium substituted samples. Thus there exist a critical composition range ($0 \leq x < 0.18$) where spins are ordered antiferromagnetically (long range ordering) at low temperature (below transition temperature) but in high vanadium substituted samples ($0.18 \leq x \leq 0.5$) short range ordering or random interactions of spins appears at the expense of long range ordering.

In chapter 3, we studied the problem encountered by the previous researchers for the hydrothermal synthesis of $AgCrO_2$ delafossite type compound. We modified the synthesis process that leads us for successful growth of polycrystalline sample of pure $AgCrO_2$ compound. Herein for the first time, we have obtained a fast, high yield and controlled method for a one-step synthesis of $AgCrO_2$ polycrystalline sample using $K_2Cr_2O_7$ as oxidizing agent in an aqueous solution by new hydrothermal method. X-ray diffraction and SEM analysis proves the quality of the material, crystallizing in *R-3m* with expected lattice parameters with the average particle size is in the 0.5-2 μm range. Magnetization study of $AgCrO_2$ sample showed a clear antiferromagnetic kink at temperature T_N = 21 K and Curie–Weiss law (χ = C/T-θ_{cw}) was used to calculate θ_{cw} = −202 K, $\theta_{cw}|/T_N$ = 9.6 leads to strong magnetic frustration. The UV-visible study and FT-IR measurement show double absorption band in the visible region with optical band gap of 1.69 eV and the absorptions due to vidrations of Cr^{3+}-O at 555 and 665 cm^{-1}, respectively. Dealing with the synthesis mechanism of $AgCrO_2$ pure phase it is proposed that at temperature 400 $^{\circ}$C, the $K_2Cr_2O_7$ undergoes the following reaction:

$$4\ K_2Cr_2O_7(s) \rightarrow 4\ K_2CrO_4(s) + 2\ Cr_2O_3(s) + 3\ O_2(g)$$

At this temperature, the $K_2Cr_2O_7$ as an oxidizing agent gives excess oxygen in an aqueous solution that in turn oxidizes the metallic silver into Ag^+ oxidation state which reacts with the Cr^{3+} impurity in an aqueous solution. This leads to the formation of final $AgCrO_2$ compound which is free of metallic silver or CrOOH impurity.

In search of a new and highly efficient semiconductor photocatalysts, we have studied the synthesis and structural, surface, and optical property characterization of Ag based photocatalysts. Herein, for the first time we have explored a simple, fast and easily controlled method for the synthesis of single phase of polycrystalline sample Ag_2CrO_4 and single crystal of $Ag_2Cr_2O_7$ via direct reaction between Ag_2O and CrO_3 precursors under mild hydrothermal condition. pH value of the solution played an important role during the final phase formation. It is concluded that sample prepared in acidic medium gives rise to the formation of single crystal of $Ag_2Cr_2O_7$ whereas addition of the NaOH in the solution turns the solution more basic that leads to the formation of Ag_2CrO_4 compound (polycrystalline sample). Ag_2CrO_4 sample is typical characteristic of an orthorhombic crystal structure with the space group *Pnma* whereas $Ag_2Cr_2O_7$ powder sample (piece of the crystal crushed into powder) prepared by hydrothermal synthesis is found to be characteristic of a triclinic crystal structure with the space group *P*-1. SEM analysis of Ag_2CrO_4 sample revealed that the average particle size varied from 1 to 10 μm with Ag/Cr ratio ~ 2 confirms the desired stoichiometry of Ag_2CrO_4. While in case of $Ag_2Cr_2O_7$ sample the SEM-EDX confirms the desired stoichiometry of Ag/Cr ratio ~ 1. The UV-visible and FT-IR properties of Ag_2CrO_4 sample and $Ag_2Cr_2O_7$ sample are in line with the available literature. The indirect optical band gap was calculated as 1.68 eV for $Ag_2Cr_2O_7$ sample and 1.83 eV (direct bandgap) for Ag_2CrO_4 sample. The surface area of Ag_2CrO_4 sample is 3.42 m^2/g large than the one reported for conventional method. The pore volume and average pore diameter of Ag_2CrO_4 sample was found to be 0.01 $cm^3.g^{-1}$ and 3.42 nm. Thus the large value of surface area reported in hydrothermally grown Ag_2CrO_4 sample may find enhancement in photocatalytic properties.

CHAPTER I
DELAFOSSITE COMPOUNDS: AN INTRODUCTION

1.1. Background

Over the past few years, transition metal oxides have received enormous amount of research interest because of their remarkable properties including piezo/ferroelectricity, high temperature superconductor, colossal magnetoresistance, and nonlinear optical behavior, and these properties can be tailored for a wide variety of technological applications [1]. Mostly, these properties originate from the interplay between spin, lattice, charge, and orbital degrees of freedom of the material [1,2]. These competing factors typically result in complicated phase diagrams and render their properties highly sensitive to a variety of chemical and physical perturbations [3]. Among these transitional metal oxides, multiferroic materials, which exhibit both ferroelectric (FE) and ferromagnetic (FM) properties in a single phase, have attracted increasing interest due to their potential application in multifunctional devices as well as their fascinating fundamental physics [4,5]. However, there are very few single phase multiferroics existing in nature, because the ferroelectricity and ferromagnetism require empty and partially filled transition metal orbital [6], respectively. In the past few years, there has been a large increase in interest in materials exhibiting more than one type of ferroic order *e.g.* ferromagnetism, ferroelectricity, etc. [2,7-18]. The field of multiferroics has become more important for both: a basic understanding of the interaction between magnetic and electric coupling and the potential use of such materials in technical devices. Indeed, one could imagine the switching of magnetic states using an electric field or vice versa. These applications play a vital role in magnetoelectronic devices [19]. Although there are many magnetic and ferroelectric materials, there are relatively few multiferroic materials, since the conditions for co-existence of several types of order are stringent as shown in figure 1.1 [20]. Typical materials showing such properties are perovskite transition metal compounds including for example $TbMnO_3$, $HoMn_2O_5$, bismuth compounds like $BiFeO_3$, etc. [10,11]. The term multiferroic was first used by H. Schmid in 1994 [21]. He defined multiferroics as of materials in which two or three types of ferroic order (ferroelectricity, ferromagnetism and ferroelasticity) occur simultaneously in the same phase [21]. More recently, people extended the definition of multiferroic materials that is to include other long-range orders, such as antiferromagnetic [22]. In this extended definition, we can say that this research field was born in the 60's even the 50's. From then onwards people triggered the research under the name magnetoelectric. Due to extensive research in the field of multiferroic materials, in 2003, people discovered large ferroelectric polarization in the epitaxial grown $BiFeO_3$ [11] thin film and strong magnetoelectric coupling in $TbMnO_3$ [10] and $TbMn_2O_5$ [14]. These new discoveries broke the traditional thinking about multiferroics and opened a new gate for industry: if charge can be controlled by external magnetic fields and spins can be controlled by applied voltage, new devices with varieties of functions may be designed [23].

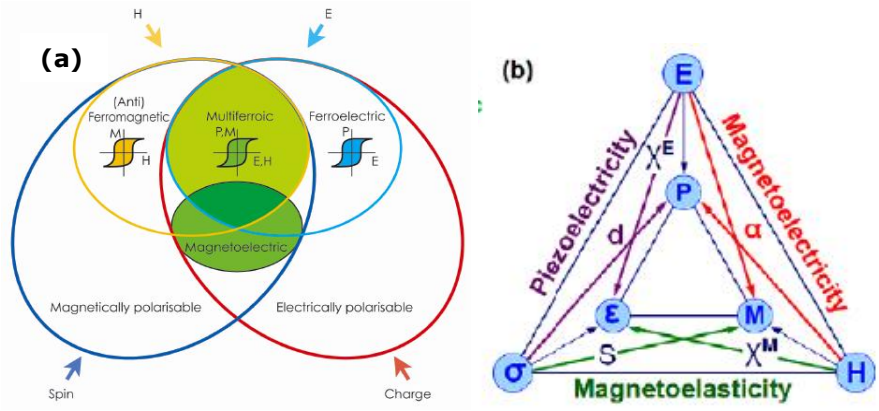

Figure 1.1. (a) Multiferroic material combines magnetic and ferroelectrical properties. (b) Schematic representation of different coupling between magnetic and ferroic properties [24].

There are four basic primary ferroic order parameters, i.e. ferromagnetism, ferroelectricity, ferroelasticity, and ferrotoroidicity. The material which show one primary order parameter and one non-primary order parameter, in a combination such as antiferromagnetism and ferromagnetism, are also considered as multiferroics [24,25]. There are two types of multiferroics; proper (or type I) and improper (or type II) multiferroics [20]. There is active research going on to understand both classes of multiferroics. In type-I multiferroics ferroelectricity (FE) and magnetism have different origins and are often due to different active 'subsystems' of a material. In such type-I multiferroics the magnetic order parameter, breaking time reversal symmetry, and the ferroelectric order parameter, breaking spatial inversion symmetry, coexist and have a certain coupling between them. In the materials that belong to the class of type- I multiferroics the ferroelectricity can have a number of possible microscopic origins [26]. In type-I multiferroics a cause of ferroelectricity can be as following:

(i) The presence of a transition metal (TM) with d^0 configuration for example $BaTiO_3$ [11];
(ii) The presence of bismuth or lead where the ferroelectricity is predominantly due to lone pairs of Bi^{3+} and Pb^{2+};
(iii) The presence of 'geometric' ferroelectricity as in $YMnO_3$, where ferroelectricity is caused by a rotation of rigid M–O polyhedra (in this case MnO_5 trigonal bi-pyramids).

In general in these type-I materials the ferroelectric ordering temperature is much higher than the magnetic one. In type-II multiferroics ferroelectricity occurs only in the magnetically ordered state: ferroelectricity sets in at the same temperature as a certain type of magnetic ordering and is driven by it. In type-II multiferroics, the magnetic ordering induces electric polarization so that the magnetization and electric polarization are coupled. Spiral magnetic ordering, for example, can give rise to type-II multiferroicity [27,28]. Further dividing the type-II multiferroics in two large families, compounds with complex non collinear

antiferromagnetic (AF) structures (AMO_2 delafossite [29-32]) and those with collinear structures (Ca_3CoMnO_6 [33], CdV_2O_4 [34]). Both structural types are well known for their geometric frustration with triangular network of M cations in the AMO_2 delafossite.

Magnetically driven multiferroics are insulating materials, mostly transition metal oxides, in which macroscopic electric polarization is induced by magnetic long-range order. The absence of inversion symmetry is a necessary (but not sufficient) condition for the appearance of spontaneous electric polarization. In these materials inversion symmetry, as well as time reversal symmetry is broken by magnetic ordering. Such a symmetry breaking often occurs in so-called frustrated magnets, where competing interactions between spins favour unconventional magnetic states. As shown in figure 1.2, three magnetic ions reside on the corners of a triangle with antiferromagnetic interactions between them—the energy is minimized when each spin is aligned opposite to its neighbors. Once the first two spins align anti-parallel, the third one is frustrated because of its two possible orientations, up and down, give the same energy. The third spin cannot simultaneously minimize its interactions with both of the other two. Thus the ground state is twofold degenerate.

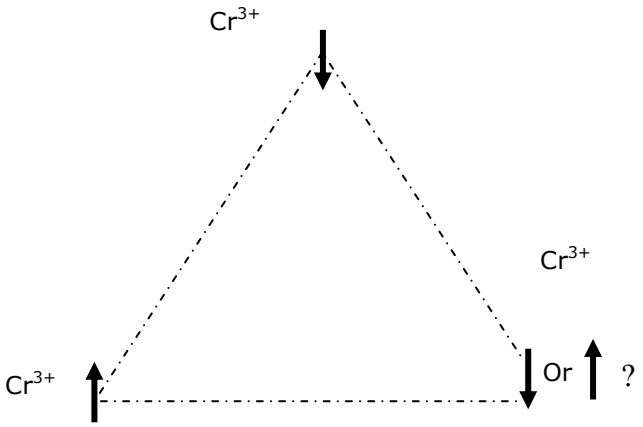

Figure 1.2. Magnetic frustration in $CuCrO_2$ (triangular antiferromagnetic) compound.

Recent discovery of multiferroicity and dielectric properties study in delafossite compounds [29-32], made them a special class of materials that has a potential application in memory devices. Several type II multiferroics have been reported in the triangular lattice antiferromagnets ABO_2 crystallizing in the delafossite structure. They are related to the delafossite itself, $CuFeO_2$, or to $CuCrO_2$ [33-43]. In case of $CuFeO_2$, the paraelectric collinear antiferromagnet ground state, can be transformed into a ferroelectric incommensurate non collinear antiferromagnetic state under application of an external magnetic field or by

chemical substitutions at the Fe site such as in $CuFe_{1-x}Al_xO_2$ ($0.014 \leq x \leq 0.030$ [30,35,36]), and $CuFe_{1-x}Rh_xO_2$ ($0.02 \leq x \leq 0.15$ [41]). The electric and magnetic ground state of $CuCrO_2$ is a ferroelectric proper-screw order [30,31]. Thus, for all these phases, ferroelectricity is induced by magnetic ordering that placed them in the class of type II multiferroics. Apart from the search of a new and improved ferroelectric property in delafossite compounds, also, research were focused on the enhancement of optical properties of delafossite compounds after the discovery of p-type conductivity in $CuAlO_2$ thin film with delafossite structure by H. Kawazoe in 1997 in sight of future transparent optical device[44].

Transparent Conducting Oxides (TCOs) constitute a class of materials which exhibit outstanding combination of optical and electrical properties: high optical transparency (>80%) in the visible range as well as high electrical conductivity ($\sim 10^4$ $S.cm^{-1}$) [45-48]. Thus, TCO materials suitable for use as thin-film transparent electrodes should have a carrier concentration of the order of 10^{20} cm^{-3} or higher and a large band gap above approximately 3 eV: i.e., degenerated n-type or p-type semiconductors. TCOs are widely used as transparent electrodes in various optoelectronic devices such as liquid crystal displays (LCD's), organic light emitting diodes (LED's) and solar cells. Despite of wide range of applications in various ranges of applications as mentioned above, very little work has been done on active device fabrication using TCOs because of the inherent nature of TCO semiconductors [49,50]. In 1990's, n-type semiconductor was known to be a good candidate for a fabrication of transparent electrodes but the lack of suitable p-type transparent electrode delays the fabrication of transparent optoelectronic devices or transparent electrodes for solar cells. But the major discovery came in 1997 when Kawazoe *et al*. from Tokyo Institute of Technology reported p-type conductivity in a highly transparent thin film of copper aluminium oxide ($CuAlO_{2+x}$) which were also well known as delafossite compounds [44]. This discovery of p-type conductivity in copper aluminium oxide with delafossite structure has opened up a new field in optoelectronics device technology, the so called "Transparent Electronics" or "Invisible Electronics" [51]. This discovery motivated various researchers around the globe to improve the physical and magnetic properties of these compounds to make them suitable p-type semiconductor material for thin film transparent devices.

Delafossite compound was discovered by Friedel, in 1873, who observed the existence of $CuFeO_2$ compound. The mineral was named delafossite compound in honor of the French mineralogist and crystallographer Gabriel Delafosse, whose work paved the way for studying the interrelationship between crystal chemistry and physical properties of these compounds. Later many researchers worked on these compounds such as Shannon, Rogers, Prewitt, Benko, Koffyberg, etc [52-54]. Delafossite compounds are materials of interest because of their remarkable optical, transport, electrical and magnetic properties [55-57]. Interest in the delafossite compounds immensely grew first with the demonstration of p-type conductivity and transparency in $CuAlO_2$ thin films by Kawazoe et al. [44]. These compounds are prominent materials for catalysts [58], batteries [59] and p-type conducting oxides [60]. Then onwards people started special interest in delafossite compound. Conductivities as high as 10 S/cm were recorded, as well as good transparency over the visible spectrum (E_g near about 3.5 eV). With this development, transparent pn-junctions could be fabricated, and from this basic building block a wide range of transparent optoelectronic devices have been developed. These compounds are the prominent materials for catalysts, luminescent, batteries, and p-type conducting

oxides. Doped p-type TCO materials have been reported which include iron doped copper gallium oxide ($CuGaO_2$:Fe), calcium doped copper indium oxide ($CuInO_2$:Ca), magnesium doped copper scandium oxide ($CuScO_2$:Mg), magnesium doped copper chromium oxide (CuCrO2:Mg), and copper calcium doped copper yttrium oxide ($CuYO_2$:Ca). Recently, $CuCr_{1-x}Mg_xO_2$ has been shown to exhibit relatively high conductivity and good optical transparency in the visible range. The majority phase is the delafossite structure as shown figure 3, although minority phases like spinel crystal structure are often observed [55, 61]. Patrick *et al.* also has shown that phase-pure delafossite material was found at relatively narrow temperature window of 650 to 700°C [61]. The electrical properties of $CuCr_{1-x}Mg_xO_2$ have been examined by Nagarajan et al [55] using RF magnetron sputtering from a single target. While undoped $CuCrO_2$ films deposited on amorphous quartz at 400-700 °C had a resistivity slightly less than about 1 Ω.cm, 5%-Mg doped films deposited under the same conditions had much lower as-deposited resistivities, ~ 4.5×10^{-2} Ω.cm, corresponding to a conductivity of 220 $S.cm^{-1}$. The transparency of such films about 250 nm thick was about 40% in the visible range.

The first all-TCO diodes were reported by Sato et al. [62]. They fabricated a semitransparent thin film of p-i-n structure consisting of p-NiO/i-NiO/i-ZnO/n-ZnO:Al. The rectifying properties of the structure confirmed the formation of the junction. Similarly, fabrication of all-TCO p-n heterojunction diode (p-$CuCrO_2$:Mg/n-ZnO) by pulsed laser deposition (PLD) was reported by Tonooka et al. [63]. The rectifying characteristics demonstrated that undoped and Mg doped $CuCrO_2$ films were suitable for the p-type semiconductor layer in diode applications. This 0.4-μm-thick junction exhibited an optical transparency of greater than 80% in the visible range.The synthesis, crystal structure, and electric transport properties of delafossite-type compounds were reported by Shannon, Rogers and Prewitt [52-54] and reviewed by Cann et al. [64].

1.2. Description of delafossite structure

1.2.1. Delafossite structure

Delafossite compounds are the family of compounds comprises the general formula ABO_2. The A cation is linearly coordinated to two neighbouring oxygen ions. The A cation is occupied by a noble metal cation which is nominally in the +1 oxidation state. The noble metal cations comes under this category are Pd, Pt, Ag, or Cu. The interatomic distance between A-A cations are in the range of 2.8 Å – 3.0 Å. The B cation is located in edge-shared $B^{3+}O_6$ octahedra with a central metal cation having a +3 charge. Cations fitting this requirement can be either p-block metal cations such as Ga, In, and Al; transition metal cations such as Fe, Co, and Y; and rare earth elements such as La, Nd, and Eu. The oxygen ion is in pseudo tetrahedral coordination with one A and three B cations, as B_3AO. As shown below in figure 1.3, the host delafossite structure consists of the alternate stacking of layers of edge sharing BO_6 octahedra and A^+ cation planes, perpendicular to the *c*-axis directions. Each A^+ ion is coordinated linearly by two oxygen ions from two successive $[BO_2]^-$ layers [64]. Depending on the stacking sequence of octahedral sites occupied by the $\boldsymbol{B^{3+}}$ cations in the subsequent layers, these compounds can present a hexagonal structure described by the $P6_3/mmc$ space group (2H

polytype), or a rhombohedral structure, described by the *R*-3*m* space group (3R polytype). By stacking the double layers with alternating **A** layers oriented 180^0 relative to each other, the hexagonal 2H type is formed. This structure has $P6_3/mmc$ space group symmetry. If the double layers are stacked with the A layers oriented the same direction relative to one another but offset from each other in a three layer sequence, the rhombohedral 3R type is formed. This structure has space group symmetry of R-3*m*.

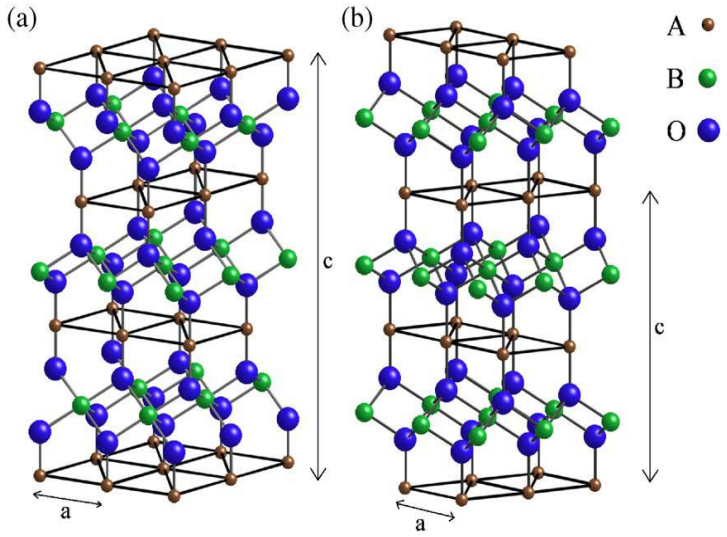

Figure 1.3. The Delafossite structure. The A layer cation is highlighted to observe the stacking sequences in the two polytypes: (a) 3R polytype, R-3*m* space group symmetry (b) 2H polytype, $6_3/mmc$ space group symmetry [64].

Discussing crystal chemistry of delafossite compounds, four individual coordination classes of ABO_2 compounds have been identified [52] summarized in table 1.1 [64]. First three coordination classes, $A^{VI}B^{VI}O_2{}^{VI}$, $A^{IV}B^{IV}O_2{}^{IV}$, and $A^{VIII}B^{IV}O_2{}^{VI}$ form structures which are explained by analyzing the radii of the A and B cations. The most prevalent coordination class of ABO_2 compounds is the type of $A^{VI}B^{VI}O_2{}^{VI}$, in which A and B cation layers are ordered along the (111) direction of the cubic NaCl type pseudocell [53]. A cations of the delafossite compounds with coordination class $A^{II}B^{VI}O_2{}^{IV}$, consists of smallest ionic radius of all the ABO_2 type oxides.

Table 1.1. Coordination classes of different compounds

Coordination Class	Compounds	Phase Symmetry
$A^{VI}\ B^{VI}O_2{}^{VI}$	NaCl α-$NaFeO_2$ α-$LiFeO_2$	Cubic Rhombohedral Tetragonal
$A^{IV}\ B^{IV}O_2{}^{IV}$	β-$NaFeO_2$	Orthorhombic
$A^{VIII}\ B^{IV}O_2{}^{VI}$	$KFeO_2$	Orthorhombic
$A^{II}\ B^{VI}O_2{}^{IV}$	$CuFeO_2$ $CuYO_2$ (Delafossite)	Rhombohedral Hexagonal

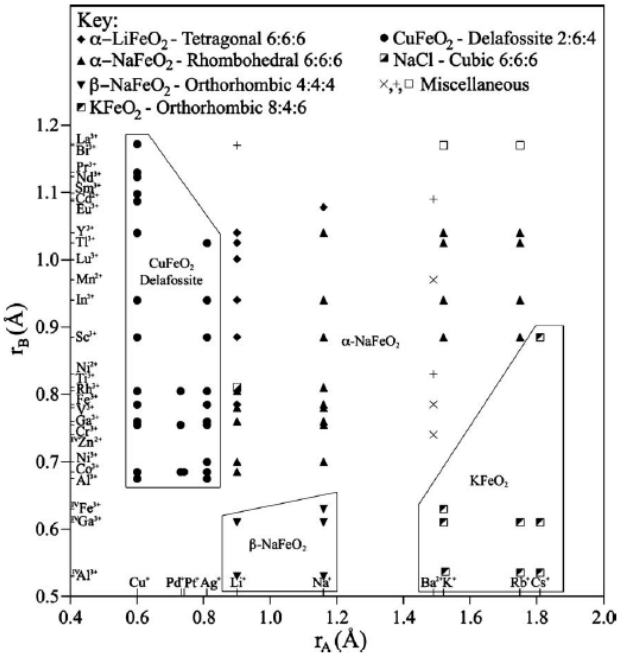

Figure 1.4. Structure field map of ABO_2 delafossite compound [52,64].

Table 1.2. Crystal structure data of all known ABO_2 delafossite compounds [52,53,64].

Composition	Space group	a(Å)	c(Å)
$AgAlO_2$	R-3*m*	2.8729	18.336
$AgCoO_2$	R-3*m*	2.890	18.27
$AgCrO_2$	R-3*m*	2.9843	18.511
$AgFeO_2$	R-3*m*	3.0391	18.59
$AgGaO_2$	R-3*m*	2.9889	18.534
$AgInO_2$	R-3*m*	3.2772	18.881
$AgNiO_2$	R-3*m*	2.936	18.35
$AgRhO_2$	R-3*m*	3.0684	18.579
$AgScO_2$	R-3*m*	3.2112	18.538
$AgTlO_2$	R-3*m*	3.568	18.818
$CuAlO_2$	R-3*m*	2.8571	16.94
$CuAlO_2$	$P6_3/mmc$	2.863	11.314
$CuCoO_2$	R-3*m*	2.8488	16.92
$CuCrO_2$	R-3*m*	2.975	17.096
$CuEuO_2$	R-3*m*	3.63	17.08
$CuFeO_2$	R-3*m*	3.0351	17.166
$CuGaO_2$	R-3*m*	2.975	17.154
$CuInO_2$	R-3*m*	3.2922	17.338
$CuLaO_2$	R-3*m*	3.83	17.10
$CuNdO_2$	R-3*m*	3.71	17.09
$CuPrO_2$	R-3*m*	3.75	17.05
$CuRhO_2$	R-3*m*	3.074	17.094
$CuScO_2$	R-3*m*	3.2204	17.099
$CuScO_2$	$P6_3/mmc$	3.223	11.413
$CuSmO_2$	R-3*m*	3.65	17.03
$CuYO_2$	R-3*m*	3.533	17.136
$CuYO_2$	$P6_3/mmc$	3.531	11.418
$PdCoO_2$	R-3*m*	2.83	17.43
$PdCrO_2$	R-3*m*	2.9239	18.087
$PdRhO_2$	R-3*m*	3.0209	18.083
$PtCoO_2$	R-3*m*	2.83	17.84

The structure field map of ABO_2 oxides shown in Figure 1.4 [52,53,64] shows that the delafossite structure is stable for only four ions on the A site, while several B cations are possible. Table 1.2 presents the structural data of known ABO_2 delafossite compounds. It can be easily seen from table 1.2 that Cu Pd, Pt, and Ag based delafossites crystallize mostly in R-3*m* whereas few selective Cu based delafossite crystallizes in $P6_3/mmc$. The lattice parameters of delafossite structures are strongly influenced the ionic radii of the A and B cations. Figure 1.5.a demonstrates that the a-axis is increases linearly with the ionic radii of B cations, while *c*-axis is fixed for each A cations.

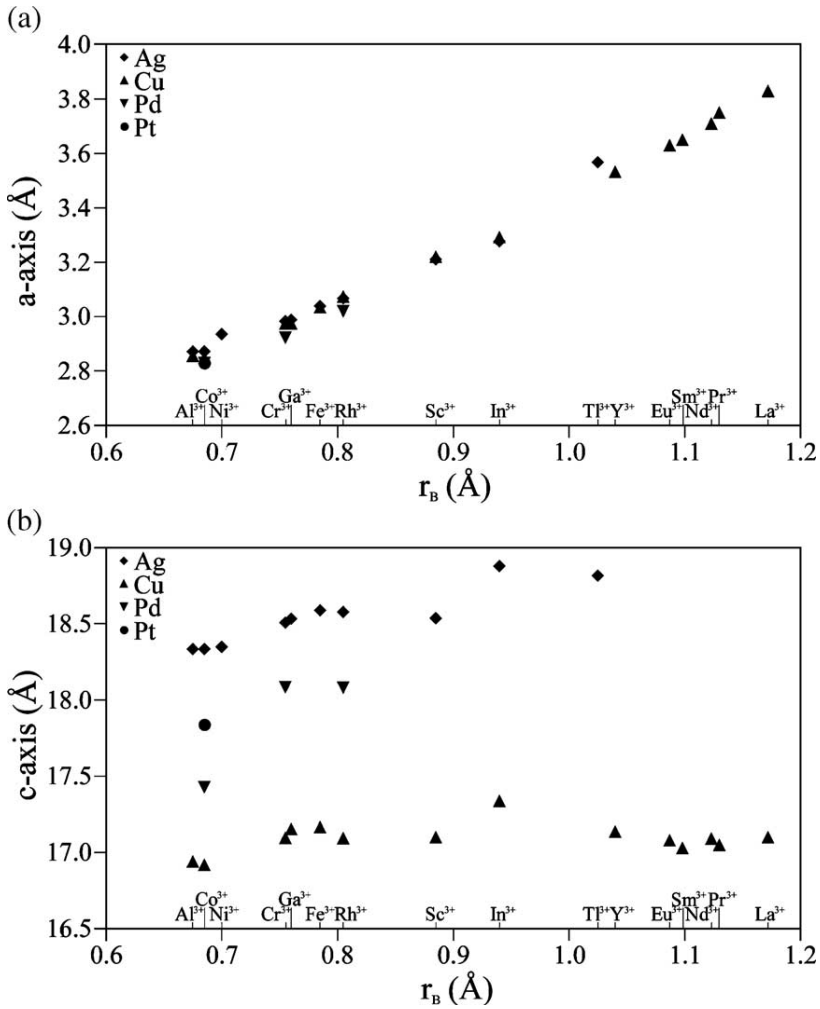

Figure 1.5. Variation of lattice parameters of delafossite compound with the radii. (a) Variation in a-axis lattice parameter (b) Variation in c-axis lattice parameter [64].

1.2.2. Characterization method of delafossite structure

The crystal structure of delafossite compound is characterized by powder X-ray diffraction method. The respective diffraction pattern is refined by using FullProf refinement software [66]. X-ray diffraction (XRD) is a powerful and common technique that reveals information about the crystallographic structure, chemical composition, and physical properties of the delafossite materials. XRD is based on observing the scattered intensity of an X-ray beam hitting a sample as a function of incident and scattered angle, polarization, and wavelength or energy. When a monochromatic X-ray beam with wavelength lambda *(λ)* is projected onto a crystalline material at an angle *theta (θ)*, diffraction occurs only when the distance

traveled by the rays reflected from successive planes differs by a complete number *n* of wavelengths (shown in figure 1.6).

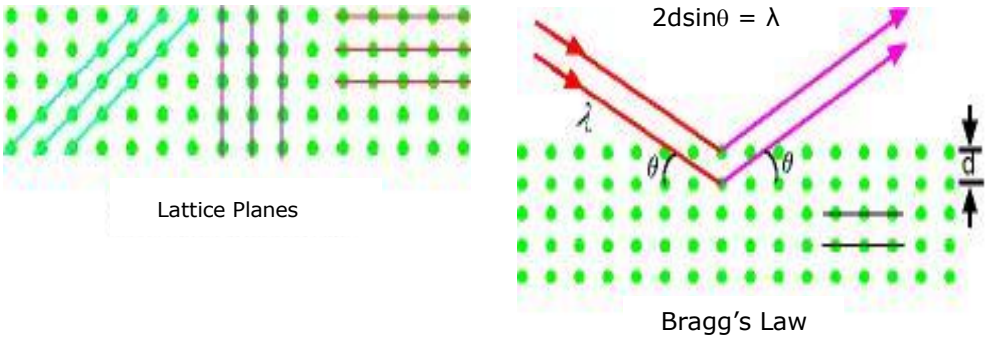

Figure 1.6. Schematic representation of X-ray beam interacting with the crystalline plannes.

As shown in figure 1.6, the interaction of the incident X-rays with the sample produces constructive interference (and a diffracted ray) when conditions satisfy Bragg's Law ($n\lambda=2d\sin\theta$). This law relates the wavelength of electromagnetic radiation to the diffraction angle and the lattice spacing in a crystalline sample. These diffracted X-rays are then detected, processed and counted. By scanning the sample through a range of 2θ angles, all possible diffraction directions of the lattice should be attained due to the random orientation of the powdered material. Conversion of the diffraction peaks to d-spacing allows identification of the mineral because each mineral has a set of unique d-spacing. Typically, this is achieved by comparison of d-spacing with standard reference patterns.

The diffraction pattern obtained from X-ray diffraction technique is refined by using FullProf program. The Rietveld method is a technique which is used to refine the user-selected parameters to minimize the difference between an experimental pattern (observed data) and calculated patterns. The observed pattern is obtained from the XRD diffractometer and the calculated pattern is a model based on the hypothesized crystal structure and instrumental parameters. This technique is given by Hugo Rietveld for use in the characterization of crystalline materials. The neutron and x-ray diffraction of powder samples results in a pattern characterized by peaks in intensity at certain positions. The height, width and position of these reflections can be used to determine many aspects of the materials structure. The sources of the systematic errors are preferred orientation, background, anisotropic reflection profile broadening, profile shapes, absorption, specimen displacement, specimen transparency, extinction, 2θ- zero error, graininess, incident beam instability, instrument electrical or mechanical instability.

The FullProf program has been mainly developed for Rietveld analysis (structure profile refinement) of neutron (constant wavelength, time of flight, nuclear and magnetic scattering) or X-ray powder diffraction data collected at constant or variable step in scattering angle 2θ. The program can be also used as a Profile Matching (or pattern decomposition using Le Bail method) tool, without the knowledge of the structure.

In this work, all X-ray diffraction measurement was performed by using a PANalytical X'pert Pro diffractometer (Cu K_α, $10^\circ \leq 2\theta \leq 110^\circ$, step size of 0.0131°). Also, in situ-high temperature XRD diffraction measurement was performed on different samples by using high temperature attachment in θ-2θ geometry. The diffraction pattern was measured on sample placed on platinum sample holder attached to the assembly.

1.3. Synthesis methods of delafossite compound

1.3.1. Conventional synthesis method

There are various methods available for the synthesis of delafossite compound. Under elevated pressure most of the delafossite compounds can be obtained via solid state reaction. The important thing in any synthesis method is to control the stoichiometry that is required to make reproducible measurements of the conductivity and mobility of these materials. The following mentioned are the some method to synthesize the delafossite compound oxides [64]. Earlier it was difficult to synthesize the highly crystalline noble metal (Pt, Pd and Ag) based delafossite oxides at low decomposition temperature. To overcome this various closed system and low temperature synthesis techniques have been employed. These include metathesis, high pressure, hydrothermal, oxidizing flux, cation exchange, and other chemical solution reactions.

Metathesis Technique: In metathetical reactions for the formation of the delafossite phase, the halide of a chosen noble metal is reacted with a B cation oxide precursor in a sealed silica ampoule and heated to a temperature approaching 900 $^\circ$C. No external pressure is required for synthesis. Example metathetical reactions for the synthesis of $PdCoO_2$ and $CuFeO_2$ are shown in Eqs. (1.1) and (1.2). The halide salt reaction product can be removed by leaching with H_2O to leave a single-phase delafossite product.

$$PdCl_2 + 2CoO \rightarrow PdCoO_2 + CoCl_2 \quad (1.1)$$
$$CuCl + LiFeO_2 \rightarrow CuFeO_2 + LiCl \quad (1.2)$$

Oxidizing Flux Synthesis Technique: Oxidizing flux synthesis techniques are a means to facilitate cation exchange reactions. In this technique, a low-melting point flux, typically a chloride or nitrate from of one of the components, is utilized as a catalyst for the cation exchange reaction. As an example, undoped or doped $AgInO_2$ delafossite can be synthesized via a two step reaction. First a precursor layer structure phase is synthesized via solid state reaction as shown:

$$Na_2CO_3 + In_2O_3 \rightarrow 2NaInO_2 + CO_2 \quad (1.3)$$

The $NaInO_2$ powder is then reacted in a flux of $AgNO_3$–KNO_3 to obtain the delafossite phase via the following reaction:

$$AgNO_3 + NaInO_2 \rightarrow AgInO_2 + NaNO_3 \quad (1.4)$$

The $NaNO_3$ product can be removed using water, leaving behind crystalline $AgInO_2$.

Chemical Synthesis Technique: Another low temperature chemical solution synthesis technique attempted for various delafossite compounds is the sol–gel method. $CuAlO_2$ has been successfully dip-coated onto a silica glass substrate using a mixture of copper acetate hydrate, ethanol, 2-methoxyethanol, and butanolic 1.0 M aluminum-trisec-butoxide solution. Additional solution synthesis methods have been attempted for $CuAlO_2$, involving mixtures of various copper and aluminum sources and a dipcoating technique.

Solid State Synthesis Technique: This technique is not a suitable technique for the synthesis of Ag, Pt, and Pd based delafossite compounds but a promising technique for the synthesis of Cu based delafossite compounds. The only exception is $CuInO_2$, for which cation exchange reactions are the only way to synthesize the delafossite phase directly. However, it is possible to synthesize the compound $Cu_2In_2O_5$ in ceramic form to serve as a target for pulsed laser deposition of $CuInO_2$ delafossite thin films. To stabilize monovalent Cu, it is necessary to quench from high temperatures (generally 1000–1200 $^{\circ}C$). For example, the phase field for $CuAlO_2$ delafossite exists at temperatures and pO_2 values at the boundary between ($Cu+Al_2O_3$) on the reducing side and between ($Cu_2O+CuAl_2O_4$) on the oxidizing side. Many compounds, such as $CuAlO_2$, can be processed to single phase delafossite with quenching in air. Using a high-temperature controlled-atmosphere furnace with quenching capability, it is possible to synthesize other delafossite compounds such $CuGaO_2$ in both powder and ceramic forms. Typical processing conditions for $CuGaO_2$ are pO_2=0.001 atm at 1100 $^{\circ}C$. Solid state synthesized powders and ceramics typically exhibit a high degree of crystallinity. Polycrystalline ceramics can be prepared via this technique with typical densities ranging between 60% and 95% of the theoretical density.

Thin Film Synthesis Technique: This synthesis technique involve deposition delafossite compound as a thin film on the substrate. There are various thin film deposition techniques have been used to deposit delafossite compounds such as pulsed laser deposition technique, RF sputtering, and chemical deposition technique.

Pulsed Laser Deposition Synthesis Technique: This process has been used for synthesis of compound like $CuAlO_2$, $CuInO_2$, $CuGaO_2$, $CuScO_2$, and $AgInO_2$. In general, this technique utilizes a high-energy laser pulse, typically from a KrF excimer laxer, to vaporize a sintered disc target to deposit a thin film on a variety of substrates. Common substrate materials are sapphire, quartz, and yttria-stabilized zirconia. This technique requires a substrate temperature ranging from 450 to 700 $^{\circ}C$ and a base pressure of 10^{-6} Pa.

Chemical Vapor Deposition Technique: Chemical vapor deposition was used to deposit $CuAlO_2$ films from metallorganic precursors. This deposition technique

requires low pressure, typically on the order of 5^{-10} Pa. For the $CuAlO_2$ deposition, a quartz substrate at a temperature of 745 $^{\circ}$C was used.

RF Sputtering Technique: RF sputtering deposition techniques have been utilized to deposit thin films of $CuAlO_2$, $CuGaO_2$, $CuGa_{1\_x}$ Fe_xO_2, $CuScO_2$, $CuCr_{1\_x}Mg_xO_2$, and $AgInO_2$. This deposition technique requires a vacuum pressure of approximately 10^{-4} Pa. Deposition temperature can range from 100 to 700 $^{\circ}$C, and the substrate material is typically SiO_2 glass.

1.3.2. Microwave Synthesis: An Introduction

In early 18th century, fire was the only source of applying heat to a chemical reaction in synthetic chemistry. Robert Bunsen invented the burner in 1855, the energy from this heat source could be applied to a reaction vessel in a focused manner. The Bunsen burner was later superseded by the isomantle, oil bath or hot plate as a source of applying heat to a chemical reaction. In the past few years, heating chemical reactions by microwave energy has been an increasingly popular theme in the scientific community. Since the first published reports on the use of microwave irradiation to carry out organic chemical transformations by the groups of Gedye and Giguere/Majetich in 1986 [67], more than 3500 articles have been published in this fast moving and exciting field, today generally referred to as microwave-assisted organic synthesis [68, 69]. In many of the published examples, microwave heating has been shown to dramatically reduce reaction times, increase product yields and enhance product purities by reducing unwanted side reactions compared to conventional heating methods. The advantages of this enabling technology have, more recently, also been exploited in the context of multistep total synthesis [70] and medicinal chemistry/drug discovery [71], and have additionally penetrated related fields such as polymer synthesis [72], material sciences [73], nanotechnology [74] and biochemical processes [75]. The use of microwave irradiation in chemistry has thus become such a popular technique in the scientific community that it might be assumed that, in a few years, most chemists will probably use microwave energy to heat chemical reactions on a laboratory scale.

The short reaction times provided by microwave synthesis make it ideal for rapid reaction scouting and optimization of reaction conditions, allowing very rapid progress. Arguably, the breakthrough in the field of microwave-assisted organic synthesis on its way from laboratory curiosity to standard practice started in the pharmaceutical industry around the year 2000.Medicinal chemists were among the first to fully realize the true power of this enabling technology. Microwave synthesis has since been shown to be an invaluable tool for medicinal chemistry and drug discovery applications since it often dramatically reduces reaction times, typically from days or hours to minutes or even seconds [71]. Many reaction parameters can therefore be evaluated in a few hours to optimize the desired chemistry. Compound libraries can then be rapidly synthesized in either a parallel or (automated) sequential format using microwave technology [71]. In addition, Nowadays the sintering of advanced materials such as core shell ceramics or nano size ceramics requires very fast sintering method in order to avoid both grain growth and inter diffusion. In this context, the microwave sintering is a very powerful method since it allows sintering in a very short time (several minutes).

Working Principle: The schematic representation of monomode microwave heating synthesis system is shown below in Figure 1.7. The microwave heating system comprises a microwave generator (SAIREM GMP 20 KSM, 2.45 GHz), which delivers a variable power up to 2kW and a standard R26 rectangular waveguide, section of 86.36 x 43.18 mm^2, which is equipped with two circulators and terminated by a rectangular microwave cavity. Two different resonance modes TE102 and TE103 (which permit an interaction with the magnetic field and electric field, respectively) can be generated depending of the length between the short circuit piston and the coupling iris [76,77]. Electromagnetic (EM) radiation is a form of energy radiated in the form of a wave traveling at the speed of light, comprising both electric and magnetic fields that oscillate at right angles to each other and in the direction of propagation shown in Figure 1.8. Generally, EM radiation is classified by the wavelength (in order of decreasing wavelength and increasing frequency) into radio waves, microwaves, infrared radiation, visible light, ultraviolet radiation, X-rays and gamma rays. Microwaves form part of the EM spectrum with frequencies ranging from 300 MHz to 300 GHz respectively.

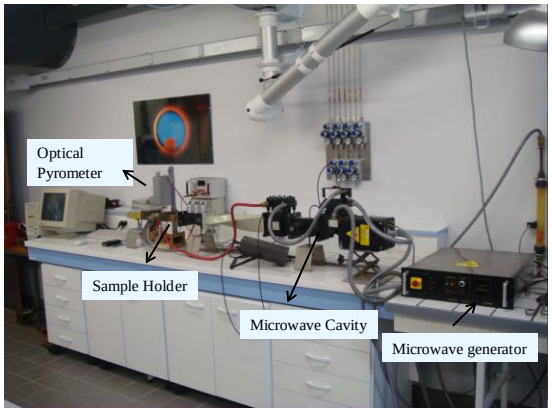

Figure 1.7. Schematic representation of monomode microwave heating synthesis system in laboratory.

A microwave oven uses microwaves to heat food. Microwaves are radio waves. In the case of microwave ovens, the commonly used radio wave frequency is roughly 2,500 megahertz (2.5 gigahertz). Radio waves in this frequency range have an interesting property: they are absorbed by water, fats and sugars. When they are absorbed they are converted directly into atomic motion and motion is converted into heat. Microwaves in this frequency range have another interesting property: they are not absorbed by most plastics, glass or ceramics. And metal reflects microwaves, which is why metals cause spark in a microwave oven. The

reason that metal reflects microwaves is that no electronic waves resident in inside of conductor because conductor's conductivity is infinity. Molecules of all compounds are consist of a dipole and have positive charge in one side and have negative charge in another side. If we put electromagnetic fields in this, all molecules are rearranged: +ve charge is to negative pole and –ve charge is to positive pole. In this process molecules heat is produced by friction.

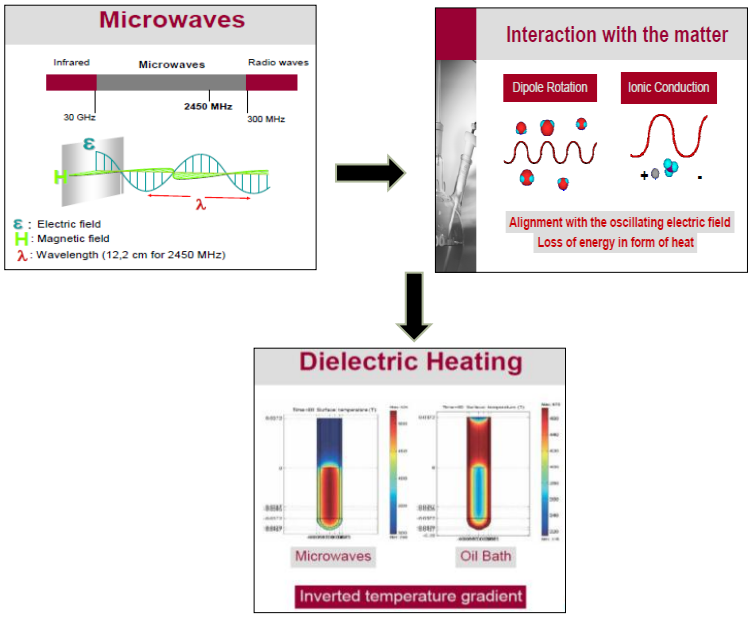

Figure 1.8. Working principle of microwave heating [78].

Modes of Microwave: Single and Multimode

Two types of microwave reactors can be used in the Laboratory. Multimode Microwave Reactors (figure 1.9) and Monomode Microwave Reactors (figure 1.10).
Multimode Reactor: This type of microwave reactor is used in household devices for cooking, heating and thawing of food. They have found use in organic laboratory for carrying out organic synthesis on the laboratory scale. These ovens (with limited power 800–1000 W) are characterized by a non-homogeneous distribution of electric field due to several reflections off the metallic walls of the oven. This is shown in figure 1.9. Since the field is heterogeneous, so their use in synthetic purposes requires mapping of the field, involving determination of hot spots of high energy using a filter paper sheet impregnated with a solution of cobalt chloride [79]. The use of multimode reactors has however, following limitations:

a) The distribution of electric field inside the cavity results from multiple reflections off the walls and reaction vessel and is consequently heterogeneous;

b) the temperature cannot be simply and accurately measured;

c) the power is not tunable.

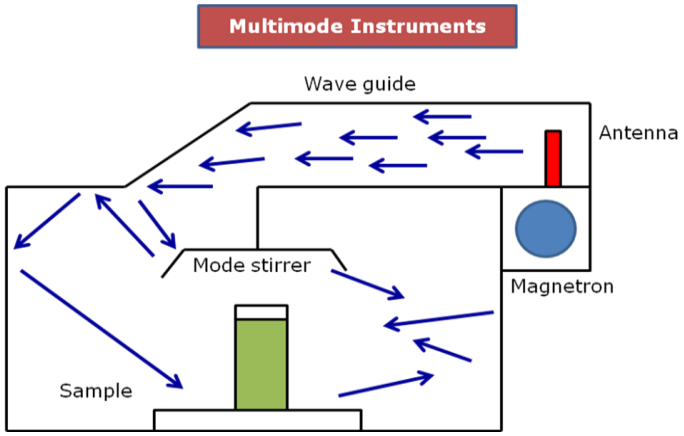

Figure 1.9. Multimode microwave reactor.

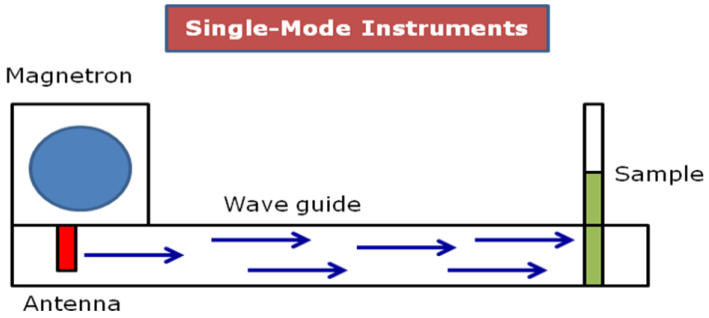

Figure 1.10. Single-Mode microwave reactor.

Single-Mode Reactor: In the monomode microwave oven the dimensions of wave belt (wave guide) and excitations are specially calculated so to allow only one mode of propagation or resonance. They are able to obtain a homogeneous distribution of the electric field in the wave belt (focalized fasciculus) and hence in the heated reaction mixtures. They are used with less power emitted with a high return of energy, and thus, the utilization of monomode reactor is energy efficient and leads to better yields in organic synthesis, while preserving the thermally unstable products.

Merit: It has been various advantages of microwave heating method such as rapid reactions, high purity of products, less side-products, improved yields, simplified and improved synthetic procedure, wider usable range of temperature, higher energy efficiency, sophisticated measurement and safety technology, modular systems enable changing from mg to kg scale.
De-merit: The synthesis method has disadvantages too such as it is difficult to control temperature during the synthesis of various organic and inorganic compounds.

1.3.3. Hydrothermal synthesis method

The first publications on hydrothermal synthesis of ceramics started appearing in the scientific literature in the middle of the 19th century [80]. In late 19th century, the hydrothermal research was conducted by geologists to understand and simulate the natural hydrothermal phenomena occurring in the earth's crust in the laboratory. Progress in synthesis was accelerated by significant developments in hydrothermal pressure vessel engineering. In 19th century, hydrothermal research mostly confined to Germany, France, Italy, and Switzerland but the 20th century was dominated by USA, the Soviet Union, and Japan as major centres for development of hydrothermal technology. Thus, 20th century is the period when hydrothermal synthesis was clearly identified as an important technology for materials synthesis, predominantly in the field of single crystal growth [81]. However, the severe (supercritical) reaction conditions required for growing single crystals have discouraged extensive commercialization for many materials. For example, hydrothermal epitaxy was very popular during the 1970's however, it did not achieve commercial success due to the high temperatures and pressures involved (T > 5OO °C, P > 1000 bars) [82]. In recent years, commercial interest in hydrothermal synthesis has been revived in part because a steadily increasingly large family of materials has emerged that can be prepared under mild conditions (T < 35O °C, P < 1000 bars) [83,84].

In broad terms, hydrothermal synthesis is a technology for crystallizing materials (chemical compounds) directly from aqueous solution by adept control of thermodynamic variables (temperature, pressure and composition). Some additives are used such as mineralising agent (organic/inorganic) to control pH and to promote solubility and other agents (organic/inorganic) to control the morphology or to promote the particle dispersion. Both physical and chemical parameters (temperature, pressure and time of reaction) play a vital role during hydrothermal processing in such a way that the direct correlation can be established between precursor and product. Temperature plays a crucial role in the kinetics of product formation as well as on the thermodynamic stability of the product phase. Pressure is essential for solubility, the supersaturation range directing to the crystallization process as well as for the thermodynamic stability of the product phase. Time is also an important parameter because the synthesis of kinetically stable phases are favoured in short term processes while thermodynamically stable phases are formed in long term experiments, corresponding to a suitable temperature and pressure. In earlier studies, the fundamental roles of temperature, pressure, precursors, and time on crystallization kinetics during the hydrothermal synthesis of various compounds are defined in detail [81]. In the hydrothermal synthesis, the solutions are prepared by using precursor materials in a Teflon liner for low temperature and low pressure synthesis (as shown in figure 1.11.a) and in stainless steel autoclave

for high temperature and high pressure synthesis (figure 1.11.b). The closed Teflon liners are placed into the sealed stainless steel autoclaves and put into the furnace whereas in case of high temperature synthesis set up, the stainless steel autoclave consists of precursor solution is placed in high temperature furnace.

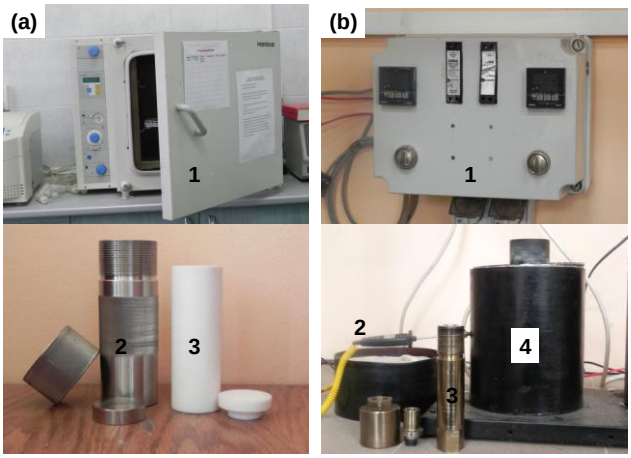

Figure 1.11. The hydrothermal synthesis set up for (a) low temperature (≤ 250 °C; 1:Furnace; 2: SS autoclave; 3:Teflon liner) and (b) high temperature (> 250 °C; 1: Temperature controller; 2: Thermocouple; 3: SS autoclave; 4: Furnace).

There are two kinds of hydrothermal process one is low temperature and low pressure hydrothermal process generally refers to soft hydrothermal method (T < 20O °C, P < 500 bars) and second type of process involve high pressure and high temperature in an aqueous solution refers as supercritical or hard process (T > 5OO °C, P > 1000 bars).These reactions involve reacting oxide precursors in an aqueous solution of HCl, water or NaOH. Typical reactions of this type are carried out in sealed, thin walled platinum or gold tubes called autoclave at temperatures ranging from 500 to 700 ^{0}C. An autoclave used for growing a quartz crystal is shown in figure 1.12. Crystal growth by using hydrothermal synthesis method depends on the solubility of minerals in hot water under high pressure. In this process, the powdered or crystalline nutrient is placed at one end of a pressure-resistant tube. A seed crystal is mounted on a wire frame near the other end and a water-based solution is added to the tube which is then sealed shut. The tube is placed in a furnace chamber with the nutrient-containing end of the tube resting on a heating element. As the floor of the furnace is heated, the bottom end of the tube becomes hotter than the top and dissolved nutrient material migrates toward the seed and crystallizes on its cooler surface [85]. Also, figure 1.11.b shows the autoclave (stainless steel) and furnace used for synthesis of various inorganic compounds under high pressure and high temperature (T < 45O °C, P < 1000 bars). On the ther hand soft hydrothermal process (low pressure and low temperature) has attracted various researchers to grow the various inorganic and organic compounds

at low temperature. A recently developed low temperature hydrothermal synthesis technique has proven successful technique in producing $CuAlO_2$ and $AgInO_2$ delafossite compounds at low temperature and pressure which generally are harder to produce by conventional synthesis method. This hydrothermal technique involves reacting oxide precursors in an aqueous NaOH solution sealed in a FEP (fluoro(ethylene-propylene)) Teflon pouch in an autoclave at a temperature of 175 °C [86].

Hydrothermal synthesis can be distinguished from solvothermal synthesis methods and soft solution processing [87]. Solvothermal synthesis utilizes non-aqueous solvents instead of an aqueous medium. Soft solution processing is a broad term that encompasses many well-established, processing routes that utilize mild reaction conditions, which include hydrothermal synthesis among other methods such as bio-mimetic processing, electro-deposition, self-assembly, etc. A variety of materials have been synthesized by hydrothermal methods, such as stabilized zirconia [88], $BaTiO_3$ [89], $Pb(Zr_xTi_{1-x})O_3$ [90], hydroxyapatite [91], quartz [92], zeolites [93], vanadates [94], and phosphates [81]. It appears that the hydrothermal technique is well suited not only for fabrication of simple and complex oxides, but also for non-oxide materials, such as fluorides, sulfides, and pure elements. For example, various forms of carbon, such as diamond [95] and multi-walled carbon nanotubes [96] can be fabricated under hydrothermal conditions. Figure 1.12a shows the low temperature and pressure set up for hydrothermal synthesis of various organic and inorganic compounds. Different types of delafossite compounds were synthesized by using the above mentioned low temperature set up by using a direct reaction between their respective precursors [84]. The low temperature process and experimental conditions employed during the hydrothermal synthesis of Ag and Cu based delafossite proved to be a significant synthesis method of various delafossite compounds.

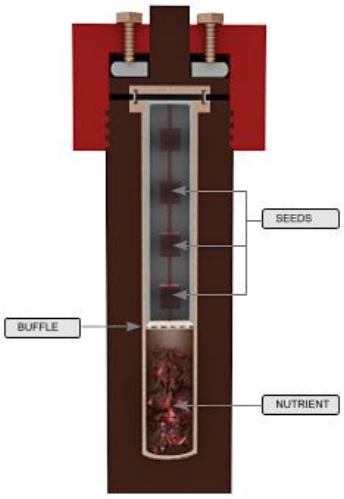

Figure 1.12. An Autoclave used for growth of Quartz Crystal

Thus, in conclusion, the unique pressure-temperature interaction of the hydrothermal solution allows the preparation of phases that are difficult to prepare with other synthetic methods. This has been particularly relevant to the manufacturing of single crystals. For example, no method other than hydrothermal synthesis can be used to grow large α-quartz single crystals [92].

Merit: Hydrothermal synthesis offers many advantages over conventional and non-conventional ceramic synthetic methods. All forms of ceramics can be prepared with hydrothermal synthesis, namely powders, fibers, and single crystals, monolithic ceramic bodies, and coatings on metals, polymers, and ceramics. Unlike many advanced methods that can prepare a large variety of forms, such as chemical vapor-based methods, the respective costs for instrumentation, energy and precursors are far less for hydrothermal methods. From the environmental perspective, hydrothermal methods are more environmentally benign than many other synthesis methods. This can be attributed in part to energy conservant low processing temperatures, ability to recycle waste, and safe and convenient disposal of waste that cannot be recycled. The low reaction temperatures also avoid other problems encountered with high temperature processes such as poor stoichiometry control due to volatilization of components (e.g., lead volatilization in lead-based ceramics) and stress-induced defects (e.g., micro-cracks) caused by phase transformations that occur as the ceramic is cooled to room temperature. From the standpoint of ceramic powder production, there are far fewer time- and energy-consuming processing steps since mixing and milling steps are not necessary. Moreover, the ability to precipitate the powders directly from solution regulates the rate and uniformity of nucleation, growth and aging, which affords size, morphology and aggregation control that is not possible with many synthesis processes [97,98].

In general, the formation of new compound from its components requires that the new composition have a lower free energy than the sum of the free energies of the individual components. So, high pressure can aid in the lowering of free energy in following ways.

a. Pressure delocalizes outer *d* electrons in transition metal compounds by increasing the magnitude of coupling between the *d* electrons on the neighboring cations, thereby lowering the free energy.
b. Pressure stabilizes the higher valence states of the transition metals, thus promoting the formation of a new phase.
c. Pressure can suppress the ferroelectric displacement of cations, thereby adding the new synthesis of new phase.
d. Pressure alters site-preference energies of cations, and facilitates the formation of new phase.

Possible advantages of the hydrothermal method over other types of crystal growth are following:

a. The ability to create crystalline phases which are not stable at the melting point.
b. Also, materials which have a high vapor pressure near their melting points can also be grown by the hydrothermal method.

c. The method is also particularly suitable for the growth of large good-quality crystals while maintaining good control over their composition.

Demerit: Disadvantages of the method include the need of expensive autoclaves, good quality seeds of a fair size and the impossibility of observing the crystal as it grows.

There are three different methods used in hydrothermal synthesis and crystal growing. These methods are mentioned below:

Temperature-Difference Method: The most extensively used method in hydrothermal synthesis and crystal growing. The supersaturation is achieved by reducing the temperature in the crystal growth zone. The nutrient is placed in the lower part of the autoclave filled with a specific amount of solvent. The autoclave is heated in order to create two temperature zones. The nutrient dissolves in the hotter zone and the saturated aqueous solution in the lower part is transported to the upper part by convective motion of the solution. The cooler and denser solution in the upper part of the autoclave descends while the counter flow of solution ascends. The solution becomes supersaturated in the upper part as the result of the reduction in temperature and crystallization sets in.

Temperature-Reduction Technique: In this technique crystallization takes place without a temperature gradient between the growth and dissolution zones. The super saturation is achieved by a gradual reduction in temperature of the solution in the autoclave. The disadvantage of this technique is the difficulty in controlling the growth process and introducing seed crystals. For these reasons, this technique is very seldom used.

Metastable-Phase Technique: This technique is based on the difference in solubility between the phase to be grown and that serving as the starting material. The nutrient consists of compounds which are thermodynamically unstable under the growth conditions. The solubility of the metastable phase exceeds that of the stable phase, and the latter crystallize due to the dissolution of the metastable phase. This technique is usually combined with one of the other two techniques above.

Challenges in hydrothermal synthesis of $ACrO_2$ (A=Cu,Ag) delafossite compounds: The delafossite-type oxides (ABO_2 compounds), owing to the large number of possible B-site cations, had been studied by various researchers mostly by William et.al under mild hydrothermal condition [84]. They explained the experimental process condition to obtain the various Cu and Ag based delafossite compounds. Also, it was reported that the minimum solubility ($\sim 10^{-4}$ mol/L) for the reactant oxides at the reaction temperature is a necessary condition for a hydrothermal reaction to occur. There are several key factors that enhance the product mass yield of delafossite type oxides. Some of them are mentioned as following:

a) Increasing the acidic character of the A-, B-site constituent metal oxide or both.

b) Elevating the NaOH mineralizer concentration in syntheses that involve B-site constituent metal oxides with more basic character.
c) Choosing the most soluble B-site metal oxide precursor (i.e., metal oxide, oxide hydroxide, or trihydroxide).

Despite of above mentioned key factors that enhances the final product yield of delafossite compounds there were certain delafossite-type oxides formed and a few others did not formed under mild hydrothermal process condition. The process condition illustrated in table 1.3 were unsuccessful attempts made to obtain the delafossite (Ag or Cu based mentioned in table 1.3) under mild hydrothermal condition [84]. Out of them, the $AgCrO_2$ delafossite is successfully synthesized by hydrothermal method in the following thesis work.

Table 1.3. Experimental process conditions used for hydrothermal synthesis of various Cu and Ag based delafossite [84].

Aim	reactants	NaOH (M)	temp (°C)	time (h)	products
$CuTiO_2$	$Cu_2O + Ti_2O_3$	1.0	210	60	Cu, TiO_2
$CuVO_2$	$Cu_2O + V_2O_3$	1.0	210	60	Cu, V_2O_5
$CuCoO_2$	$Cu_2O + 2CoOOH$	2.0	210	60	$CuCoO_2$ (3R), Co_3O_4
$CuNiO_2$	$Cu_2O + 2NiOOH$	2.0	210	60	CuO, NiO
$CuYO_2$	$Cu_2O + Y_2O_3$	2.5	210	60	Cu_2O, $Y(OH)_3$
$CuInO_2$	$Cu_2O + In_2O_3$	2.5	210	60	Cu_2O, $In(OH)_3$
$CuLaO_2$	$Cu_2O + La_2O_3$	2.5	210	60	Cu_2O, $La(OH)_3$
$CuEuO_2$	$Cu_2O + Eu_2O_3$	2.5	210	60	Cu_2O, $Eu(OH)_3$
$CuTlO_2$	$Cu_2O + Tl_2O_3$	2.5	210	60	Cu_2O, Tl_2O_3
$AgTiO_2$	$Ag_2O + Ti_2O_3$	1.0	210	60	Ag, TiO_2
$AgVO_2$	$Ag_2O + V_2O_3$	1.0	210	60	Ag, V_2O_5
$AgCrO_2$	$Ag_2O + 2Cr(OH)_3$	2.5	210	60	Ag, CrO_4^{2-}(aq)
$AgMnO_2$	$Ag_2O + Mn_2O_3$	1.5	210	60	Ag, $Na_xMnO_2.yH_2O$
$AgCoO_2$	$Ag_2O + 2CoOOH$	2.0	210	60	$AgCoO_2$ (3R), Co_3O_4
$AgYO_2$	$Ag_2O + Y_2O_3$	2.5	210	60	Ag_2O, $Y(OH)_3$
$AgLaO_2$	$Ag_2O + La_2O_3$	2.5	210	60	Ag_2O, $La(OH)_3$
$AgEuO_2$	$Ag_2O + Eu_2O_3$	2.5	210	60	Ag_2O, $Eu(OH)_3$
$AgTlO_2$	$Ag_2O + Tl_2O_3$	2.5	210	60	$AgTlO_2$ (3R), Ag, Tl_2O_3

Challenges: The solubility of monovalent copper and silver oxides plays a vital role in formation of all the delafossite-type oxides. The acidic character of the group 11 oxides increases as one descends the periodic table from copper to gold. Therefore, the acidic character of Ag_2O is higher as compared to Cu_2O that in turn increases the solubility in bases for Ag^+ ions compared to Cu^+ ions. Furthermore, hydrate species of Ag^+ ($Ag(OH)_2^-$) in an aqueous solution is stable at room temperature as compared to Cu^+ ions, which can disproportionate in an aqueous solution. This increased aqueous solubility of Ag^+ ions compared to Cu^+ ions not only plays an important role in reducing the maximum temperature and time required to form the silver delafossite-type oxide phases but also generates silver delafossite-type oxides

that did not form analogous copper delafossite-type oxides with the same B-site cation. It is well known that Cu^{+} ions disproportionate to Cu^{2+} ions and copper metal in aqueous solution at room temperature and ambient pressure [99,100]. However, the stability of aqueous Cu^{+} species increases with increase in temperature. This is due to the decreased dielectric constant of water that destabilizes the more highly charged Cu^{2+} ion, thereby reducing the driving force for disproportionation [101]. Cu^{+} ions, although stable, are limited in their solubility in alkaline aqueous media, with an estimated maximum of $[Cu^{+}] \approx 10^{-4}$ M at 200 °C. The monovalent oxidation state of Ag^{+} is stable in an aqueous solution at room temperature as compared to Cu+ ions. Also, Ag_2O showed the amphoteric character in an aqueous solution at room temperature [102]. In strong bases Ag^{+} ions exist primarily in the form of soluble hydrate $Ag(OH)_2^{-}$ species. The concentration and stability of soluble hydrate $Ag(OH)_2^{-}$ species increases with increase in temperature [103]. Ag^{+} ions have a significantly higher aqueous alkaline solubility as compared to Cu^{+} ions, with a maximum concentration of $[Ag^{+}] \approx 10^{-2.5}$ mol/L at 200 °C. At elevated temperature, the evolution of oxygen from Ag_2O to form silver metal becomes more favourable. It is well studied the unfeasibility of $AgCrO_2$ delafossite phase at low temperature (210 °C) and pressure (< 20 atm) under mild hydrothermal synthesis method. At low temperature, Ag_2O does not react with $Cr(OH)_3$ or CrOOH to form $AgCrO_2$ but rather generate excess amount of metallic silver and trivalent Cr^{3+} ions undergo oxidation to Cr^{6+} ions. A redox reaction occurs that speed up the decomposition of Ag_2O into metallic silver [84]. So, in conclusion, it is difficult to synthesize Ag based delafossite compounds by solid state in air because of low free energy of formation of Ag_2O (-2.6 kcal mol^{-1}) and its decomposition to metallic silver and oxygen at low temperatures [52]. Also, it is impossible to synthesize $AgCrO_2$ delafossite at low temperature and pressure under mild hydrothermal condition.

1.4. Magnetic and electrical properties of $ACrO_2$ compounds (A= Cu, Ag)

1.4.1. Electrical properties

Electrical conductivities of delafossite compound are anisotropic in nature. They can exhibit conductivities ranging from insulating to semi metallic depending upon the composition of the materials. Also, there exists a variation in the conductivity value with respect to the *z*-axis. The electrical conductivity comes from the hybridization of the linearly coordinated A cation d_z2-*s* orbital's, as well as d_z2-*s* and oxygen p_z state. Also we can increase the electrical conductivity of delafossite compounds by doping impurity in the compounds. In general doping in delafossites is not an effective means of increasing the conductivity of delafossite compound [64]. The electrical properties of all known delafossite compound are shown below in Table 1.4. Also, Table 1.4 includes the recently reported electrical conductivities [104] of various delafossite compounds which were not mentioned in earlier studies [64]. As we see clearly from the Table 1.4, the Pd and Pt delafossite compound exhibit metallic conductivity while Cu and Ag delafossite compound exhibit semi metallic conductivity. The possible explanation for metallic conductivity in Pd and Pt based delafossite compound is as follows. The d^9 electron configuration of the monovalent cations Pd and Pt creates an unfilled d_z2-*s* hybrid orbital which is mainly responsible for the metallic conductivity of these type compounds. As we said

earlier, there is variation in conductivity value with respect to *c*-axis. Table 1.5 consist the different values of conductivity with respect to c-axis. Typical values of conductivity for $PdCoO_2$ are 5×10^5 S/cm perpendicular to *c*-axis and 5×10^2 S/cm parallel to *c*-axis. It must be noted that B-cation p-states do not have a significant influence on the valence band properties.

Table 1.4. Electrical properties of all known ABO_2 delafossites [64].

Composition	form	σ (S/cm)	type	$cm^2/V.s$
$AgCoO_2$	Crystal	6.7×10^{-5}		
$AgCoO_2$	Film	0.2	*p*	
$AgCrO_2$	Bulk	1.4×10^{-6}		
$AgFeO_2$	Crystal	3.3×10^{-8}		
$AgInO_2$	Crystal	1×10^{-4}		
$AgInO_2$	Film	1×10^{-5}	*n*	
$AgNiO_2$	Bulk	100		
$CuAlO_2$	Crystal	6.3×10^{-4}	*p*	
$CuAlO_2$	Bulk	0.36	*p*	0.1-0.4
$CuAlO_2$	Film	0.015-2	*p*	0.13-0.1
$CuCoO_2$	Crystal	5×10^{-6}		
$CuCrO_2$	Crystal	3.36×10^{-5}	*p*[106]	
$CuCrO_2$	Bulk	3.5×10^{-5}	*p*	
$CuCrO_2$	film	1		0.1
$CuFeO_2$	Crystal	2	n	
$CuFeO_2$	Bulk	0.65	p	0.27
$CuFeO_2$	Bulk	1.9×10^{-5}	n	1×10^{-6}
$CuGaO_2$	Bulk	5.6×10^{-3}	p	0.1
$CuGaO_2$	Film	$5.6\text{-}6.3 \times 10^{-3}$	p	0.23
$CuScO_2$	Film	1.2×10^{-4}		
$CuSmO_2$	Bulk	0.18		
$CuYO_2$	Bulk	0.025		

Delafossite compounds with the monovalent A-cations having d^{10} electronic configurations, such as Cu and Ag, have a filled valance band and thus exhibit a semiconducting behavior. Furthermore, copper delafossite exhibit *p*-type conductivity in the absence of any internal doping. This comes from the combination of ionized copper vacancies and interstitial oxygen. Also, people demonstrated a significant improvement in conductivity by oxygen intercalation of $CuScO_2$, $CuYO_2$, and other rare earth delafossites. This phenomenon is not applicable to all delafossite because according to Ingram et al., the stability of an oxygen interstitial defect is dependent upon the lattice size [105]. The most likely location for an oxygen interstitial defect is in the basal plane (The plane which is perpendicular to the principal axis *c* axis in a tetragonal or hexagonal structure) within the layer of A-cations. Given the ionic radii for three-fold coordinated O^{2-} of 1.22 Å, the *a* lattice parameter fixes the size of the interstitial site and therefore determines the stability of the oxygen interstitial defect [64]. Large B-cation delafossites such as $CuScO_2$ (r_{Sc}^{3+} ~ 0.885 Å) and $CuYO_2$ (r_{Y}^{3+}~ 1.04 Å) have large *a*-axis lattice parameters with

large interstitial sites that can accommodate an oxygen interstitial. Delafossite compounds with smaller B cations such as $CuAlO_2$ (r_{Al}^{3+}~ 0.675 Å) cannot accommodate these oxygen interstitial defects. In $CuAlO_2$, it has been demonstrated that Cu/Al stoichiometry has a significant effect on conductivity. The $CuAlO_2$ delafossite synthesized by hydrothermal technique has a higher conductivity from the one synthesized by solid state reaction. Table 1.6 shows that a number of doped delafossite compounds exhibit very high conductivities, with Mg-doped $CuCrO_2$, Mg-doped $CuScO_2$, and Sn-doped $AgInO_2$ exhibiting the highest conductivity of all delafossite compounds. These are exceptional cases, and in general, doping in delafossites is not an effective means of increasing the conductivity.

Table 1.5. Room temperature resistivities (ρ) and activation energies (E_a) measured parallel and perpendicular along *c*-axis of various delafossite compounds [64].

Compound	ρ(parallel$_c$) ohm-cm	E_a(parallel$_c$) eV	ρ(perpend$_c$) ohm-cm	E_a(perpend$_c$) eV
$CuCoO_2$	5×10^7	0.7	2×10^5	0.2
$CuFeO_2$	3×10^3	0.23	5×10^{-1}	0.05
$AgFeO_2$	3×10^{10}	0.8	3×10^7	0.7
$AgCoO_2$			1.5×10^4	0.11
$AgInO_2$			1×10^4	0.15
$AgGaO_2$			5×10^7	0.5

Table 1.6. Electrical type and conductivity of various doped delafossite [64].

Compound	x	form	σ (S/cm)	type	$cm^2/V.s$
$CuCr_{1-x}Mg_xO_2$	0.05	Film	220	*p*	
$CuCr_{1-x}Mg_xO_2$	0.05	Bulk	0.01-0.077	*p*	<0.1
$CuAl_{1-x}Mn_xO_2$	0.03	Bulk	$<10^{-6}$	*p*	
$CuAl_{1-x}Mg_xO_2$	0.01	Film	4×10^{-4}	*p*	0.1
$CuY_{1-x}Ca_xO_2$	0.02	Film	1	*p*	
$CuIn_{1-x}Ca_xO_2$	0.07	Film	2.8×10^{-3}	*p*	
$CuIn_{1-x}Sn_xO_2$	0.05	Film	3.8×10^{-3}	*n*	
$CuGa_{1-x}Ca_xO_2$	0.05	Bulk	5.6×10^{-3}	*p*	0.1
$CuFe_{1-x}Mg_xO_2$	0.02	Bulk	8.9	*p*	0.1
$CuFe_{1-x}Sn_xO_2$	0.05	Bulk	2.4×10^{-4}	*n*	10^{-6}
$CuSc_{1-x}Mg_xO_2$	0.05	Film	30	*p*	
$AgIn_{1-x}Sn_xO_2$	0.05	Film	20-70	*n*	0.5-1.4

Table 1.7. Room temperature ρ (T) of Mn doped $CuCrO_2$ delafossite [107]

Compound	T (K)	ρ (ohm-cm)
$CuCrO_2$	300	3.4×10^3
$CuCr_{0.95}Mn_{0.05}O_2$	300	415×10^3
$CuCr_{0.9}Mn_{0.1}O_2$	300	245×10^3
$CuCr_{0.8}Mn_2O_2$	300	45×10^3

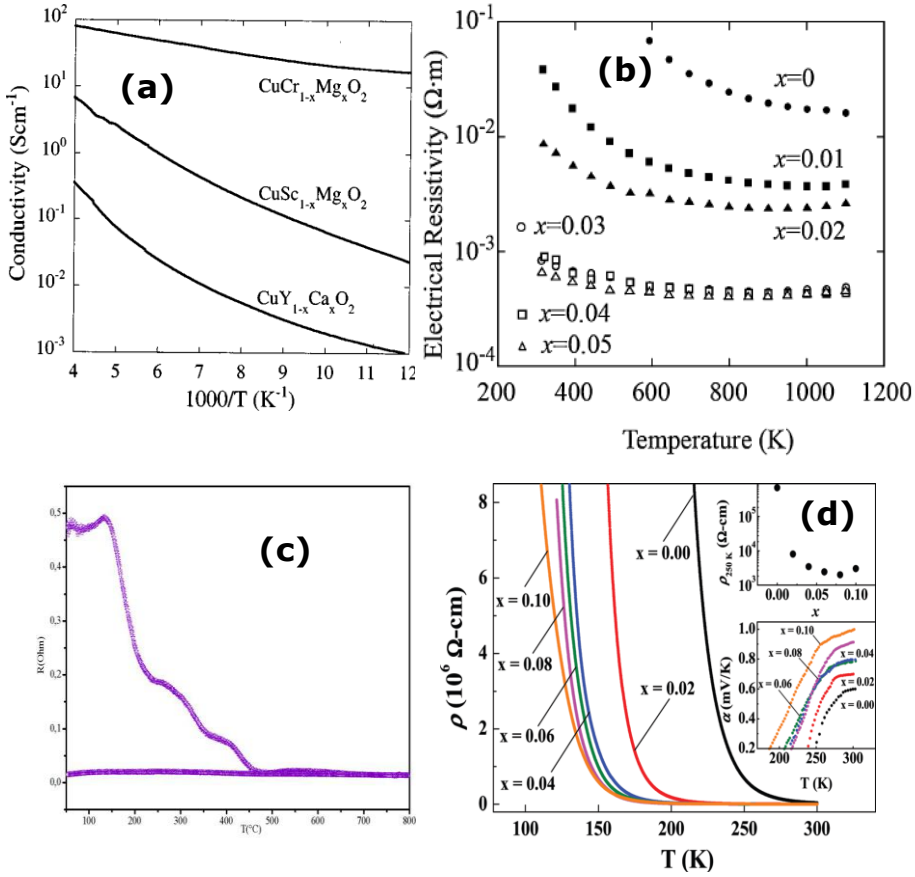

Figure 1.13. Temperature dependence of (a) conductivity of films of $CuCr_{1-x}Mg_xO_2$, $CuSc_{1-x}Mg_xO_2$, and $CuY_{1-x}Ca_xO_2$ [55] (b) Resistivity of $CuCrO_2$ with varying concentration of Mg. (c) Temperature depandance of the resistivity of the $Cu_{1-x}Ag_xCrO_2$ for x = 0.1[108]. (d) ρ (T) for $CuCr_{1-x}O_2$ with $0 \le x \le 0.10$. ρ_{250} K(x) and α(T) for the studied samples are plotted in the upper and lower right panels, respectively [109].

Continuous efforts are going on to improve the electrical conductivity of delafossite compounds by doping with different impurities to make them suitable candidate for transparent electronic devices. The dopant impurity must fulfill some basic requirement like must be having ionic radii approximately equivalent to the parental cationic site. We will discuss here electrical properties of $CuCrO_2$ doped with Mg [55] and doped with Mn [107].It is well known the effect of the Mg doping on electrical properties of $CuCrO_2$ [55]. Upon 5% Mg doping the conductivity increases by a factor of 1000. The previous conductivity data reported for thin film of $CuCrO_2$ without doping is 1 $S.cm^{-1}$ but Mg doped thin film of $CuCr_{0.95}Mg_{0.05}O_2$ exhibit conductivity of 200 $S.cm^{-1}$. Figure 1.13 above shows the conductivity and resistivity variation of $CuCrO_2$ delafossite compound doped with magnesium impurity. The resistivity decreases with temperature confirms the existence of semiconductor behavior in Mg doped copper delafossite compound. M.Amami et al. [108] reported in $Cu_{1-x}Ag_xCrO_2$ ($0 < x < 0.5$) that on heating, resistivity slightly increase around 200 °C, thenafter an abrupt decrease can be seen, followed by two losses of resistivity around 300 and 400 °C respectively. Above 450°C, the resistivity remains almost constant. These anomalies are not reversible in fact on cooling no significant changes of the resistivity can be seen on the whole range of temperature pointing out to metallic behaviour of the sample as shown in figure 1.13.c. Very recently, it is studied that chromium deficiency in $CuCr_{1-x}O_2$ ($0 \leq x \leq 0.10$.) has significant effect on electrical resistivity [109]. It is remarkable that resistivity significantly decreases with increasing x within a wide temperature range. This is shown in figure 1.13.d that Apparently, ρ_{250}(K) decreases by more than two orders of magnitude with increasing x up to 0.08 from 6.82 X 10^5 Ω-cm for $CuCrO_2$ to 1.98 X 10^3 Ω-cm for $CuCr_{0.92}O_2$ and then slightly increases to 3.03 X 10^3 Ω-cm for $CuCr_{0.90}O_2$.

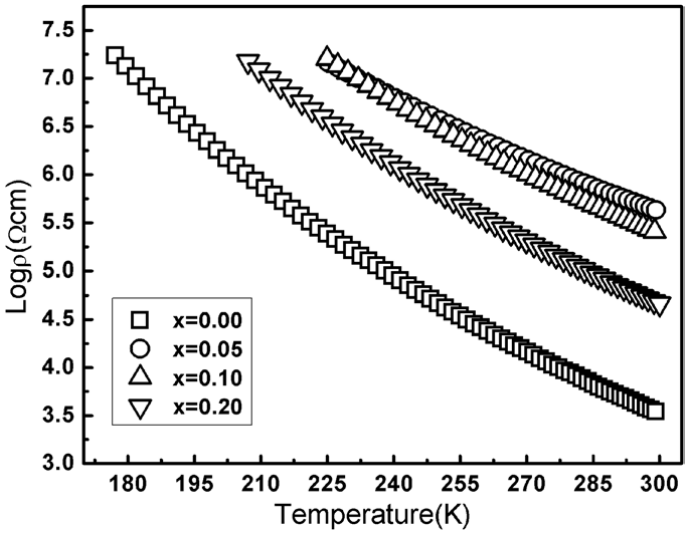

Figure 1.14. Temperature dependence of the resistivity of $CuCr_{1-x}Mn_xO_2$ semiconductors [107].

Also, Mn impurity doping in $CuCrO_2$ changes the electrical conductivity of parent compound. The temperature dependence of the resistivity of samples for $x < 0.30$ is shown in figure 1.14 [107]. The values of resistivity (ρ) at room temperature (300 K) for different concentration are shown in table 1.7, respectively. The resistivity of the Mn doped samples is larger than that of a pure $CuCrO_2$ semiconductor. And the resistivity of the samples increases as the Mn concentration increases for $x \leq 0.10$. Therefore, we can conclude that the valence state of Mn ions is 3+ in the $CuCr_{1-x}Mn_xO_2$ samples. Otherwise for $x > 0.10$ the resistivity decreases as the Mn concentration increases. Maybe some interactions, which enhanced the hole mobility, exist in the $CuCr_{1-x}Mn_xO_2$ semiconductors. A Double Exchange-like interaction could occur through Mn^{3+}–O–Cr^{3+} in terms of an identical electronic configuration ($t^3_{2g}e^0_g$) between Mn^{4+} and Cr^{3+} [110]. The Double Exchange (DE) mechanism was originally proposed by Zener for (La, A)MnO_3 (A = Ca, Sr or Ba) [111]. It is the replacement of A^{2+} for La^{3+} that results in the appearance of Mn^{4+} ions in these samples. As a result, an electron can jump from the Mn^{3+} site to the Mn^{4+} site leading to exchange coupling between the Mn^{3+} and Mn^{4+} ions. DE coupling between the Mn^{3+} and the Mn^{4+} ions is believed to be responsible for conductivity and ferromagnetism in the (La, A)MnO_3 system. The increase in the hole mobility could be due to this DE interaction between the Mn^{3+} and the Cr^{3+} ions. Thereby for $x \geq 0.10$ the resistivity of the samples decreased with the increase in Mn concentration. Otherwise, the DE interaction between the Mn^{3+} and the Cr^{3+} ions would be very weak because the resistivity of the doped samples is larger than the resistivity of the pure $CuCrO_2$ semiconductor. So, external impurity doping with Mg or Mn alters the electrical properties of $CuCrO_2$ delafossite compound.

1.4.2. Magnetic properties

Delafossite compounds (ABO_2) with magnetic ions on the B cation site have been found to possess interesting magnetic properties. Complex delafoosite compounds like $CuNi_{1/3}V_{2/3}O_2$ are antiferromagnetic in nature but the reciprocal magnetic susceptibility does not follow Curie–Wiess behavior. No long range ferro or ferrimagnetic ordering occurs in $CuNi_{1/3}V_{2/3}O_2$ and also there are no results as yet indicating antiferromagnetic ordering at low temperatures. Ag-based complex delafossites $AgCo_{0.5}Ti_{0.5}O_2$ and $AgCo_{0.5}Sn_{0.5}O_2$ possessed slightly different magnetic properties despite both compounds possessing Co^{2+} in the high spin configuration. $AgCo_{0.5}Ti_{0.5}O_2$ was found to possess ferromagnetic interaction while the magnetic interactions in $AgCo_{0.5}Sn_{0.5}O_2$ were found to be antiferromagnetic. In case of Mn-doped $CuAlO_2$, the Mn-doping causes an antiferromagnetic exchange coupling between Mn ions in the lattice, leading to paramagnetic behavior in the bulk sample. Oxygen intercalation in the rare earth delafossite causes the Cu ions to become magnetic, possessing a 2+ oxidation state and spin ½.

Magnetic properties in delafossite compounds have given rise to several theoretical and experimental investigations. These compounds are rhombohedrally stacked triangular-lattice antiferromagnetics, for which the spin Hamiltonian can be written as

$$\mathbf{H} = -2\mathbf{J}_1 \sum_{<i,j>} \mathbf{S}_i . \boldsymbol{S}_j - 2\mathbf{J}_1' \sum_{<i,j>} \mathbf{S}_i . \boldsymbol{S}_j + \mathbf{D} \sum_i \left(\boldsymbol{S}_i^z\right)^2 \qquad [112]$$

where J_1 (<0) and J_1' are the nearest neighbor interplane and interplane interactions, respectively, and D is the anisotropy constant as shown in the figure 1.15.

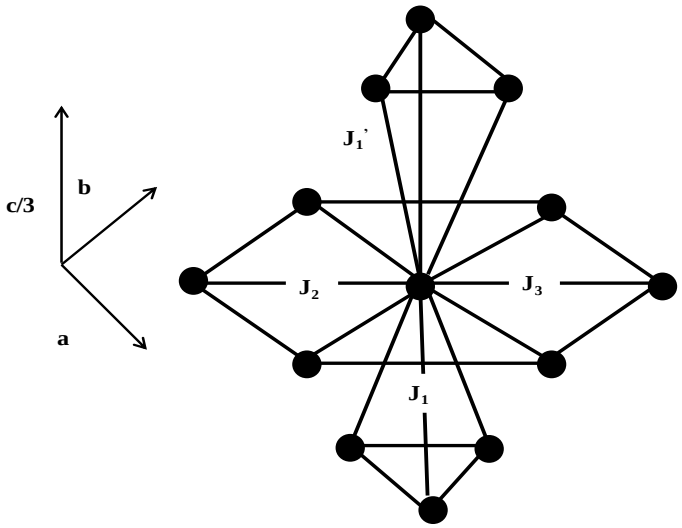

Figure 1.15. The Cr^{3+} ion lattice in $AgCrO_2$. J_1 and J_1' are the nearest neighbor interplane and interplane interactions, respectively. J_2 and J_3 are the second and third nearest neighbor interplane interactions. Three arrows, **a, b** and **c** indicate the unit lattice vector in the hexagonal units.

The magnitude of J_1 is much larger than the J_1' because the exchange path of the interplane interaction J_1', B-O-A-O-B, is much larger than the interplane interaction J_1, B-B and B-O-B. Thus, an ABO_2 compounds has been studied as a realization of a two dimensional triangular antiferromagnetic. In a Heisenberg two-dimensional triangular antiferromagnetic, the short range order of a 120° structure evolves as temperature decreases but no long-range order exists at finite temperature. Recent magnetic data of $CuCrO_2$ shows that in $CuCrO_2$, magnetic properties are dominated by Cr^{3+} ions ($3d^3$, S = 3/2) forming triangular lattice planes, and are well represented by a S = 3/2 Heisenberg triangular lattice antiferromagnetic (TLA). An early neutron powder diffraction study has indicated that $CuCrO_2$ undergoes magnetic ordering into the out-of-plane 120° structure characterized by the commensurate propagation vector (1/3,1/3,0) below $T_N \approx 24$ K [113]. Recently, magnetically-induced ferroelectricity has been reported for a polycrystalline sample below T_N [114]. More recently, Poienar et.al revisited the properties of $CuCrO_2$ single crystal grown by flux technique [106]. This study shows that the magnetization and specific heat data show of $CuCrO_2$ undergoes a unique antiferromagnetic transition at $T_N \sim 24.0$ K, in contrast to a recent report on $CuCrO_2$ single-crystals [115] showing the existence of two magnetic transitions, T_{N1}~24.2 K

and T_{N2}~23.6 K, depending on the orientation of the applied magnetic field along and perpendicular to *c*, respectively.

T. Okuda and group studied the magnetic, transport and thermoelectric properties of delafossite compounds i.e. $CuCr_{1-x}(Mg,Ca)_xO_2$ [116]. They investigated the effect of doping of magnesium ions in the $CuCrO_2$ delafossite. They investigated the structural, magnetic, transport and thermoelectric properties of polycrystalline delafossite oxides, $CuCr_{1-x}Mg_xO_2$ ($0 \le x \le 0.04$). They observed (shown in figure 1.16.a,b,c) that with the substitution of Mg^{2+} ions at the Cr site, the resistivity and Seebeck coefficient drastically decrease without a change of Neel temperature (T_N = 26K) [116]. Also, figure 1.16.d shows the magnetic and dielectric characterization curves reported in $AgCrO_2$ and $CuCrO_2$ prepared by conventional synthesis method [30]. In the temperature dependence of the resistivity of $CuCr_{1-x}Mg_xO_2$ ($x \ge 0.02$), an anomaly around T_N was observed by the same group and a negative magnetoresistance effect occurred around T_N [117]. Magnetic study of $Cu_{1-x}Ag_xCrO_2$ ($0<x<0.5$) samples [117] reveal the paramagnetic states at 300 K, and the magnetic susceptibility obeys a Curie-Weiss form ($\chi = C/(T+\Theta_{CW})$. Abrupt increases in magnetization appear at about 140 K implies a FM transition which should be due to the FM interaction through the Cr^{3+}-O-Cr^{3+} exchange. The magnetization of the samples decreases with increasing Ag concentration. Magnetic susceptibility for all the compounds deviates from the Curie–Weiss form below 150 K, around which the in-plane magnetic correlation develops as seen in some 2D antiferromagnetic magnetic systems.

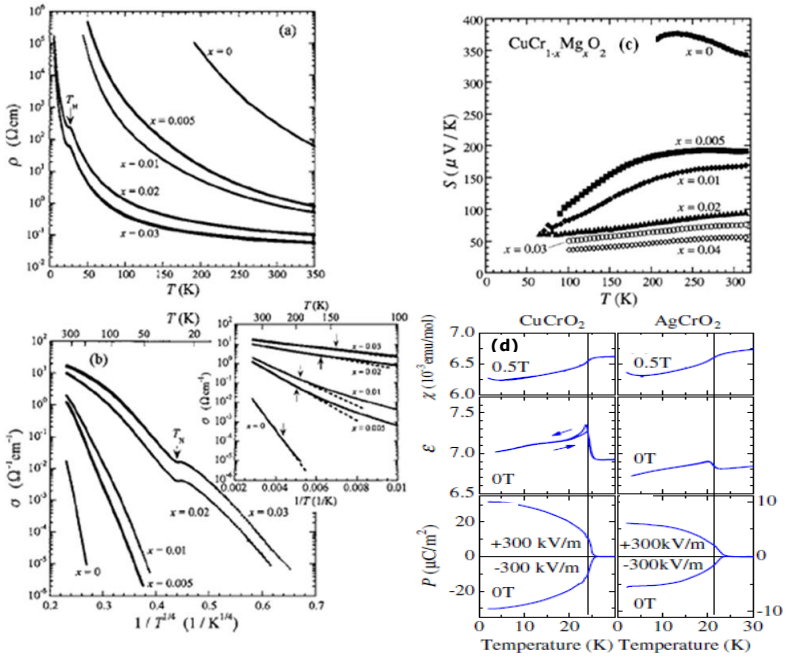

Figure 1.16. Temperature dependence of (a) the resistivity ρ (b) the electrical conductivity σ and (c) Seebeck coefficients S for $CuCr_{1-x}Mg_xO_2$ samples ($0 \le x \le 0.04$) [116]. (d) Magnetic and dielectric properties of $AgCrO_2$ and $CuCrO_2$ [30].

Recently, various researchers studied the multiferroic properties in Cu or Ag delafossite compound [118]. They reported inelastic neutron scattering measurements that provide a distinct dynamical "fingerprint" for the multiferroic ground state of 3.5% Ga-doped $CuFeO_2$. The complex ground state is stabilized by the displacement of the oxygen atoms, which contribute to the multiferroic coupling predicted in the "spin-driven" model. By comparing the observed and calculated spectrum of spin excitations, they concluded that the magnetic ground state is a distorted screw-type spin configuration with a distribution of turn angles [118]. M. Poienar et al. reported the spin dynamics of the geometrically frustrated triangular antiferromagnet multiferroic $CuCrO_2$ using inelastic neutron scattering. The relevant spin Hamiltonian parameters modelling the incommensurate modulated helicoid have been determined, and correspond to antiferromagnetic nearest and next nearest neighbor interactions in the *ab* plane with a strong planar anisotropy. The weakly dispersive excitation along *c* reflects the essentially two-dimensional character of the magnetic interactions. Classical energy calculations clearly point out the relevance of the balance between the adjacent planes coupling, the in-plane nearest-neighbor interactions anisotropy, and a weakly antiferromagnetic next-nearest-neighbor interaction, in stabilizing the three-dimensional magnetic order in $CuCrO_2$ [31].

1.4.3. Structural correlation with magnetic and electrical properties

Now we are at the stage where we can correlate the properties (magnetic and electrical) of delafossite compound with the structure. In table 1.8 below we have compared the values of the Neel temperature T_N, exchange integral J_{RW} and structural parameter of some delafossite oxides. As we see from the table 8, there exist a large variation in exchange integral of silver based delafossite and copper based delafossite compounds.

Table 1.8. Magnetic and structural data of delafossite compounds [119].

Phase	a (Å)	c (Å)	Cr Layer spacing (Å)	Cr-O-Cr (°)	d_{Cr-O} (Å)	J_{RW} (cm^{-1})	T_N (K)	J_{AF} (cm^{-1})
$CuCrO_2$	2.975	17.088	5.696	96.83	1.989	7.9	27	10.6
$AgCrO_2$	2.984	18.515	6.172	96.55	2.007	6.3	30	11.8

So, in conclusion (on the basis of experimental and theoretical data) we conclude following are the main factors which affect the crystal structure, magnetic, transport and electrical properties of delafossite compound (ABO_2). These factors are written below.

(a). **Cation A**: The characteristics of cation A and its interaction with oxygen ions are mainly responsible for the existence of the electrical properties in these delafossite compounds. This is to note that the electrical properties of these compounds are anisotropic in nature. This means if we have Pd and Pt at A cation site then it is metallic in nature and if Ag and Cu at A site then the compound are semi-metallic in nature. Also, in some delafossite compound the doping increases the conductivity drastically like as we have discussed in $CuCr_{0.5}Mg_{0.5}O_2$ (220 S/cm). Also, the conductivity varies with respect to *c*-axis. But these are exceptional cases, and in general the doping in delafossite is not an effective means of increasing the conductivity.
(b). **Cation B**: The ionic radii of cation B strongly influence the lattice parameter of the delafossite compound mainly *a*-axis. While *c*-axis is fixed by the O-A-O bond length. So, structure of these compounds is determined by the strongly ionic B^{3+} and O interaction. Also, replacement of B cation with the divalent cation (doping of external impurity) like Mn^{2+} and Mg^{2+} in delafossite compounds shows a significant magnetism in the compound with antiferromagnetic in the nature having Neel Temperature T_N = 26 K. So in conclude we can say that the magnetism in delafossite compounds comes mainly from the exchange interactions of B-B cations and B-O-B cations. But this is to note that doping of divalent cation (Mg^{2+}) in delafossite like $CuCrO_2$ there exist a drastic reduction in the resistivity and Seebeck coefficient of these material [120].

1.5. Physical and optical properties characterization methods

1.5.1. Physical properties characterization

The magnetic properties measurement system (MPMS-XL, Quantum Design) sample magnetometer is used for DC and AC magnetic characterization of all kind of samples (pellet form or powdered form), based on superconducting quantum interference device (SQUID) technology. The MPMS-XL provides solutions for a unique class of sensitive magnetic measurements in key areas such as high-temperature superconductivity, biochemistry, and magnetic recording media. The resistivity (ρ) measurements were made by the four-probe technique. The temperature dependent resistivity ρ(T) data is collected by using Quantum Design physical properties measurement system (PPMS) equipped with superconducting coils delivering maximum fields of 7 T or 9 T with temperatures up to 300 K. The dielectric and polarazation data is collected by using Quantum Design physical properties measurement system (PPMS) equipped with superconducting coils delivering maximum fields of 14 T.

In this work presented here in thesis, the temperature dependence magnetization M (T) data were recorded in a magnetic field of 0.1 T from 5 to 300 K, in zero field cooled (zfc) and field cooling (fc) modes. The ac magnetic susceptibility (χ', χ'') measurements were performed at different frequencies (10 Hz–10 kHz) using a physical properties measurement system (PPMS, Quantum Design). The dielectric measurement was made on a thin parallel plate capacitor. Contacts were made by using silver paste. The dielectric measurements were performed using an Agilent 4284A LCR meter at four different frequencies (5–100 kHz) during cooling and warming (2 K min^{-1}). The polarization was measured with a

Keithley 6517A electrometer. A static electric poling field of 135 kV m^{-1} was applied during cooling to align the electric dipoles and removed at 8 K. A waiting time of 5000 s was applied before measuring the polarization versus temperature upon warming (5 K min^{-1}).

1.5.2. Surface morphology characterization

Microscopy is an important tool utilized to understand many of the aspects of product and process development, including the role of experiments in granulation and agglomeration processes, optimizing milling and micronizing operations, and acquiring a basic knowledge of microstructure and morphology. The scanning electron microscope has many advantages over traditional microscopes. The SEM has a large depth of field, which allows more of a specimen to be in focus at one time. The SEM also has much higher resolution, so closely spaced specimens can be magnified at much higher levels. Because the SEM uses electromagnets rather than lenses, the researcher has much more control in the degree of magnification. All of these advantages, as well as the actual strikingly clear images, make the scanning electron microscope one of the most useful instruments in research today. The working principle diagram is shown in figure 1.17 [121].

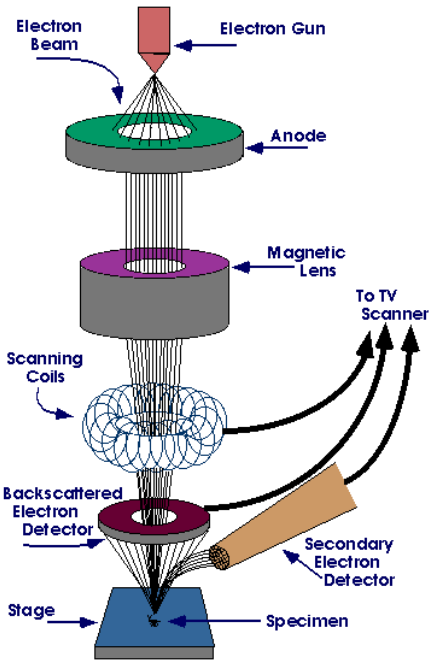

Figure 1.17. The schematic representation of working of SEM.

The SEM is an instrument that produces a largely magnified image by using electrons instead of light to form an image. A beam of electrons is produced at the top of the microscope by an electron gun (figure 1.17). The electron beam follows a vertical path through the microscope, which is held within a vacuum. The beam travels through electromagnetic fields and lenses, which focus the beam down toward the sample. Once the beam hits the sample, electrons and X-rays are ejected from the sample. Detectors collect these X-rays, backscattered electrons, and secondary electrons and convert them into a signal that is sent to a screen similar to a television screen (figure 1.18a). This produces the final image.

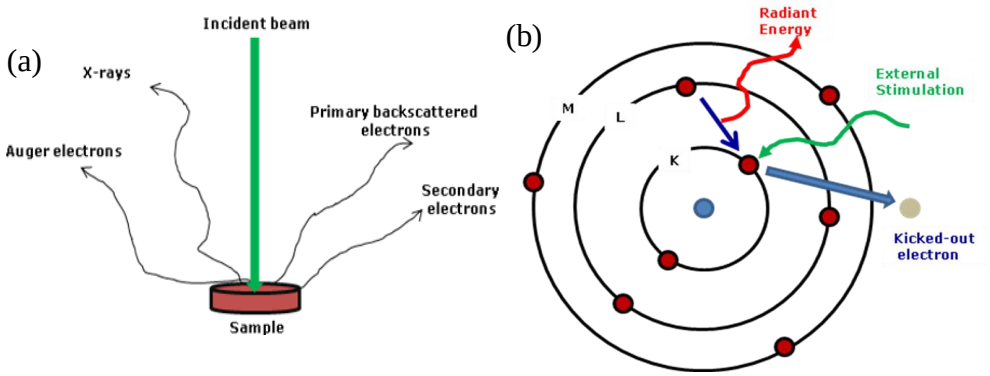

Figure 1.18. (a) The schematic presentation of interaction of incident beam with surface of the sample. (b) Principle of energy dispersive X-ray analysis.

Energy dispersive x-ray (EDX) analysis is used for determining the elemental composition of a specimen. It often works as an integrated feature of a SEM, and cannot operate on its own without the latter. During EDX analysis, the specimen is bombarded with an electron beam inside the scanning electron microscope. The bombarding electrons (primary electrons) collide with the specimen, knocking some of them off in the process (figure 1.18b). The vacancy in the specimen atoms created by the ejection of an inner shell electron is eventually occupied by a higher energy electron from an outer shell. During this transition, the transferring electron gives up its excess energy in the form of x-rays. The amount of energy released by the transferring electron depends on which shell it is transferring from, as well as which shell it is transferring to. Furthermore, the atom of every element releases x-rays, unique in energy during the transferring process, characteristic of that element. Thus, by measuring the energy of the x-rays emitted by a specimen during electron beam bombardment, the identity of the atom from which the x-ray was emitted can be established.

1.5.3. Optical properties characterizations

UV-Vis spectrophotometer: To measure the optical transmittance and reflectance of delafossite compounds and optical band gap measurement has been performed using UV-Visible spectrophotometer. A diagram of the components of a typical spectrometer is shown in the following figure 1.19 [122]. The UV-Visible spectrometer uses two light sources, a Deuterium (D2) lamp for ultraviolet light and tungsten (W) lamp for visible light. A beam of light from a visible and/or UV light source (colored red) is separated into its component wavelengths by a prism or diffraction grating. Each monochromatic (single wavelength) beam in turn is split into two equal intensity beams by a half-mirrored device. One beam, the sample beam (colored magenta), passes through a small transparent sample cuvette containing a solution of the compound being studied in a transparent solvent. The other beam, the reference (colored blue), passes through an identical cuvette containing only the solvent. The intensities of these light beams are then measured by electronic detectors and compared. The intensity of the reference beam, which should have suffered little or no light absorption, is defined as I_0. The intensity of the sample beam is defined as I. Over a short period of time, the spectrometer automatically scans all the component wavelengths in the manner described. The ultraviolet (UV) region scanned is normally from 200 to 400 nm, and the visible portion is from 400 to 800 nm. In our case the wavelength ranges from 300 nm to 1000 nm. The optical band gap of powdered sample was estimated by the equation $(\alpha h\nu)^2 = A(h\nu - E_g)$, where, α,ν, A and E_g are the absorption coefficient, the frequency of light, a constant and the band gap, respectively [123, 124]. The graph plotted between $(\alpha h\nu)^{1/2}$ *vs.* $h\nu$ gives the optical band gap. The extrapolation of the straight line to $(\alpha h\nu)^2 = 0$ axis gives the value of the optical band gap

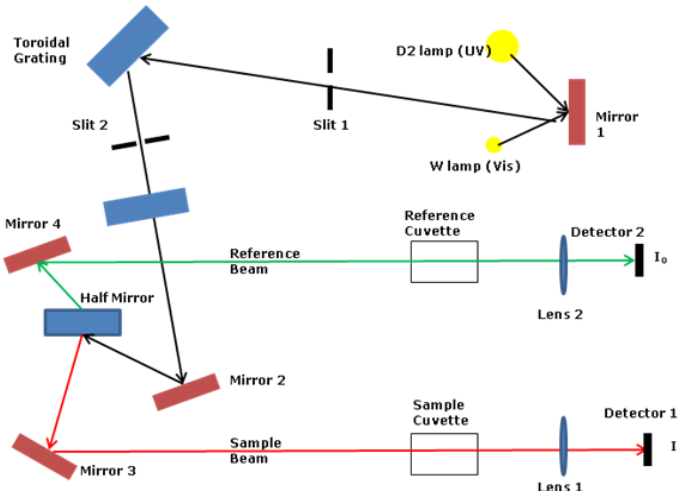

Figure 1.19. Working model of UV Visible spectrophotometer.

FT-IR: FT-IR stands for Fourier Transform Infrared, the preferred method of infrared spectroscopy. This is the analytical technique developed in 1970s to qualify and quantify compounds utilizing infrared absorption of molecules. In infrared spectroscopy, IR radiation is passed through a sample. Some of the infrared radiation is absorbed by the sample and some of it is passed through (transmitted). The resulting spectrum represents the molecular absorption and transmission, creating a molecular fingerprint of the sample. Like a fingerprint no two unique molecular structures produce the same infrared spectrum. This makes infrared spectroscopy useful for several types of analysis. FT-IR can identify unknown materials, determine the quality or consistency of a sample, and determine the amount of components in a mixture. Absorption occurs when the energy of the beam of light (photons) are transferred to the molecule. The molecule gets excited and moves to a higher energy state. The energy transfer takes place in the form of electron ring shifts, molecular bond vibrations, rotations, and translations. IR is mostly concerned with vibrations and stretching. A molecule is infra-red active if it possesses modes of vibration that cause a change in dipole moment. An infrared spectrum represents a fingerprint of a sample with absorption peaks which correspond to the frequencies of vibrations between the bonds of the atoms making up the material. Because each different material is a unique combination of atoms, no two compounds produce the exact same infrared spectrum. Therefore, infrared spectroscopy can result in a positive identification (qualitative analysis) of every different kind of material. In addition, the size of the peaks in the spectrum is a direct indication of the amount of material present. The signal can be measured very quickly, usually on the order of one second or so. Thus, the time element per sample is reduced to a matter of a few seconds rather than several minutes.

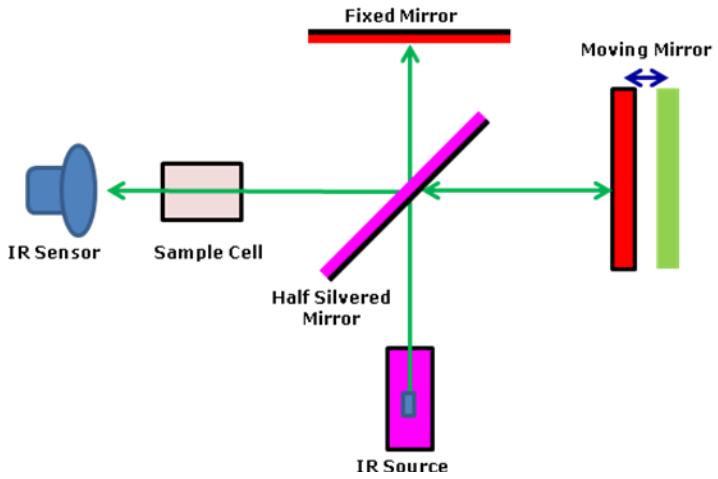

Figure 1.20. Working principle of FT-IR spectroscopy.

1.6. Interest and issues in $ACrO_2$ (A=Cu,Ag) delafossite compounds

In recent years, there has been a renewed interest in delafossite compounds of general formula $ACrO_2$ (A= Cu, Ag), mainly concerning either fundamental research such as frustrated magnetic interactions in triangular lattices , or the search for new materials such as transparent p-type conducting oxides and more recently thermoelectric materials. In this context, understanding the relationships between chemical composition and structural and physical properties is very interesting, and it can be helpful in order to design and optimize delafossite compounds for their integration in potential applications. In the search for new multiferroic materials, the symmetry of the structure is of prime importance and the possibility offered by magnetic structures to break the inversion symmetry has been used to discover numerous spin induced ferroelectrics and strong magnetoelectric (ME) coupling. In contrast, coupling between a spin glass and ferroelectricity has not been studied so extensively. Cationic disorder induced by substitution on one crystallographic site may generate magnetic and/or electric glassiness depending on the atoms involved. Disorder is in fact well known to be responsible for glassy properties, as shown in $(Sr,Mn)TiO_3$. Recently, polarization and magnetodielectric (MD) coupling in $CuFe_{0.5}V_{0.5}O_2$ spin glass were reported. The vanadium for iron substitution in the $CuFeO_2$ delafossite hinders the long range magnetic ordering at low temperature. $CuCrO_2$ that is an antiferromagnetic compound ($T_N \sim 24$ K) spin induced ferroelectric; the V^{3+} for Cr^{3+} substitution creates a disorder that favours short range magnetic order. It is still not clear whether V^{3+} or Cr^{3+} in $CuCr_{1-x}V_xO_2$, $0 \leq x \leq 0.5$ playing a vital role for the increased polarization value. In the following thesis work we have tried to solve out the above mentioned issue in $CuCr_{1-x}V_xO_2$ ($0 \leq x \leq 0.5$).

Nowadays, transparent electrical devices possess high demand in semiconductor technology. Transparent Conducting Oxides (TCOs) show high optical transparency (>80%) in the visible range as well as high electrical conductivity. TCO material with n-type conductivity exist many options but very few in p-type transparent conducting material. These TCO (n or p type) materials are potential candidate for transparent electronic device and solar cell application. Kawazoe *et al*. reported p-type conductivity in a highly transparent thin film of copper aluminium oxide ($CuAlO_{2+x}$) delafossite compound. This opened the gate for various researchers to develop improved p-type conductive TCO with delafossite structure. The main issue was synthesis of pure phase product of $ACrO_2$ (A= Cu, Ag) compound at low temperature and to design the low cost synthesis process to obtain pure phase of high quality product. Taking an example of hydrothermal synthesis method $AgCrO_2$ delafossite at low temperature (210 °C) and pressure (< 20 atm) was unsuccessful attempt. The reason was at low temperature, Ag_2O does not react with $Cr(OH)_3$ or CrOOH to form $AgCrO_2$ but rather generate excess amount of metallic silver and trivalent Cr^{3+} ions undergo oxidation to Cr^{6+} ions. Similarly, low free energy of formation of Ag_2O (-2.6 kcal mol^{-1}) doesn't allow the formation of Ag based delafossite compounds by solid state in air. In the work presented in this thesis, we tried to solve out the above mentioned issues and successfully presenting a facile, low cost synthesis of pure phase product of $AgCrO_2$ using mild hydrothermal process.

CHAPTER II
SYNTHESIS AND CHARACTERIZATION OF Cu BASED DELAFOSSITE

2.1. Fast synthesis of $CuCrO_2$ delafossite by monomode microwave heating

2.1.1. Microwave conditions of synthesis of $CuCrO_2$ delafossite

Numerous works have been devoted to the monomode microwave synthesis of rare earth iron garnets and rare earth iron binary oxides [125] and various pure and mixed oxide powders [126-128] under the microwave irradiation. The above mentioned study shows that these pure and mixed oxide powders are very sensitive to the electromagnetic beam of a low power (300 W) monomode microwave (MW) with frequency of 2.45 GHz. Microwave heating has potential application in solid state chemistry, especially when the precursor material is a microwave-absorbing material such as Cu_2O, Cr_2O_3, CuO, MnO_2 etc [128]. For example, if 5–6 g Cu_2O or Cr_2O_3 is exposed to 300 W of microwave radiation for 30 s, its temperature will rise to 900 K within a few minutes [128]. In the majority of studies of the synthesis of ceramics and metal oxides by microwave radiation, special sample holders with high microwave absorber, such as SiC, have been employed in order to efficiently absorb microwave radiation [129]. The basic requirement for microwave synthesis of inorganic and organic compounds is that the precursors used in the synthesis process should have good coupling with microwave irradiation.

As we discussed in chapter 1, $CuCrO_2$ delafossite compound is a special material of interest because of its remarkable structural, electrical and magnetic properties [55,56]. In previous papers [52,64], it has been shown that numerous methods (solid state reaction, sol-gel method, thin film processing) are available to synthesize the $CuCrO_2$ delafossite. Microwave heating is an alternative way for the synthesis and the processing of various inorganic and organic materials and has numerous advantages over conventional processes such as fast heating process, low energy consumption, volumetric heating processes etc [76,77,130]. Low temperature synthesis of $CuAlO_2$ using aluminium nitrate prepared by microwave irradiation proved to be a novel synthesis method to control over the surface morphology of delafossite compounds [131]. Microwave sintering allows to maintain the grain size at the nano-metric scale as compared to conventional sintering [130].

In search of a new structural phase and improved electrical and magnetic properties of $CuCrO_2$ delafossite, we made an attempt to prepare the $CuCrO_2$ by using microwave heating method. Here in this work, we report an original method for the synthesis of $CuCrO_2$ delafossite using a single mode microwave cavity as a source of heating, starting from a Cu_2O and Cr_2O_3 mixture. A single resonance mode

can be tuned in such a cavity that allows the materials to be subjected to a very high electromagnetic field, even at a relatively low amount of power. This leads to a very efficient process in comparison with multimode microwave process [130].

Figure 2.1.a shows the schematic representation of the whole microwave heating apparatus used for the synthesis of $CuCrO_2$ delafossite starting from a Cu_2O and Cr_2O_3 mixture. The microwaves are guided along a TE10 wave guide equipped with two circulators to absorb the reflected power so as to protect the generator. After the two circulators, a three-stub tuner is used to adapt the impedance of the wave guide with respect to the cavity. At the end of the line a TE10p rectangular microwave cavity is mounted in which the cavity length is tuned to excite the TE102 mode. For that, the length between the mobile iris and the mobile short-circuit (λ_g) is tuned at λ_g which is the guided wavelength (λ_g = 173.6mm) as shown in figure 2.1.b [77]. Powders (2 g) of Cu_2O (Sigma-Aldrich, > 99%) and Cr_2O_3 (Sigma-Aldrich, > 99%), weighted in the 1:1 stoichiometric ratio, were mixed by using a ball milling machine for 2 minutes and then, manually ground in an agate mortar for 15 minutes. The powders were then pressed in the shape of pellets (8 mm diameter, 5 mm thick) and placed into a cylindrical Al_2O_3 or SiC crucible, with an inner diameter of 10 mm, put in the centre of the rectangular cavity that was tuned for exciting the TE102 mode. The temperature was recorded by means of an infrared pyrometer (Raytek, Marathon series, 350-2000 °C) hanged vertically on the top of cavity and focused on the top surface of the samples [130]. The interface of the sample became incandescent red (shown in figure 2.2) with slight variation in microwave irradiation exposure. The measured temperature was about 600–700 °C. Then, the sample temperature (recorded with optical pyrometer) was adjusted to 1000–1100 °C by increasing microwave irradiation. About 2-5 min later the beam was switched off. After cooling, grey-geen colored pellet was observed.

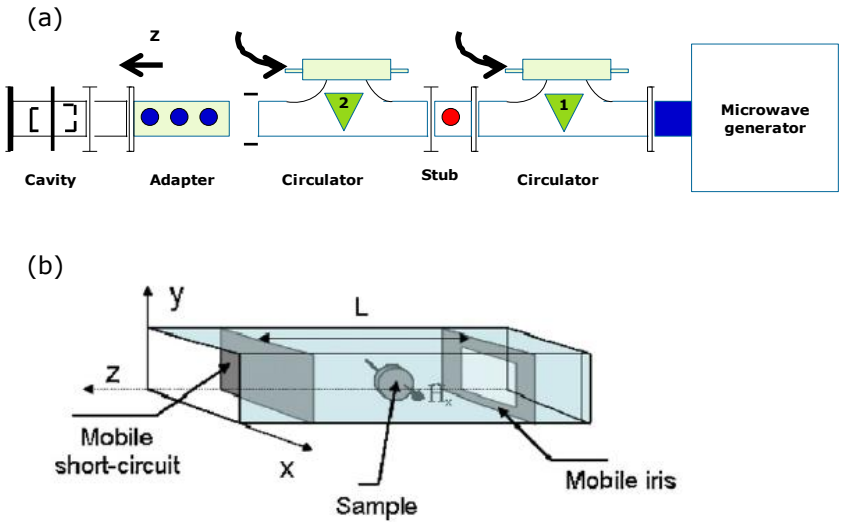

Figure 2.1. (a) Schematic representation of the whole microwave heating apparatus. (b) Schematic representation of the TE102 microwave cavity (single mode) [77].

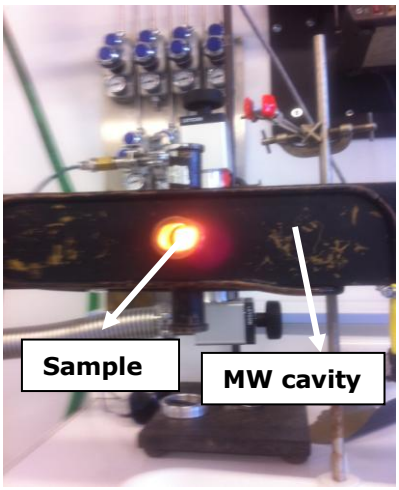

Figure 2.2. Photograph of the incandescent red sample of $CuCrO_2$ during heating cycle.

Several attempts were performed, varying the temperature, via the power, and the time. The optimized experimental process conditions are reported in table 2.1 for both kinds of crucibles. As mentioned in chapter 1, the disadvantage of microwave heating method is the uncontrollability of the process temperature during synthesis. To overcome this obstacle we tried to prepare samples in two different kinds of crucibles which are generally used for synthesis of various inorganic compounds. These crucibles are silicon carbide (SiC) and alumina crucible (Al_2O_3). A large bandgap, high breakdown electric field, high thermal conductivity, and outstanding chemical inertness makes silicon carbide (SiC) the semiconductor material of choice for fabricating high-temperature, high-power, and high-frequency devices [132]. In addition to this, the temperature controllability during the synthesis of $CuCrO_2$ is significantly higher in SiC crucible rather than in alumina crucible. Furthermore, in alumina crucible, the heating is provided by the direct coupling between the microwaves and the powder; this is so called direct microwave heating method (DMW labeled samples). When a silicon carbide crucible is used, the crucible itself heats and the powder is thus heated by both radiative (indirect) and microwave (direct) energy, called hybrid microwave heating (HMW labeled samples).

The quality of samples was systematically checked by powder X-ray diffraction (XRD) data collected by using a PANalytical X'pert Pro diffractometer (Cu K_α, $10^\circ \leq 2\theta \leq 110^\circ$). Also, D8 X-ray diffraction system was used to analyze the peak broadning of HMW, DMW, and SS sample. The data were analyzed by using FULLPROF program [66]. A Zeiss SUPRA 55 scanning electron microscope (SEM) was used to observe the microstructure of the samples (pallets). The volumetric particle size distribution of powder samples was measured by using laser particle size analyzer (Malvern Instruments, Inc. - Mastersizer 2000). The density of samples was also determined following the Archimedes method using ethanol as an immersion fluid. The temperature dependence of magnetic properties was measured

with a superconducting quantum interference device (SQUID-Quantum Design) magnetometer. The M(T) data were recorded in a magnetic field of 1 T from 5 to 300 K, in zero (zfc) and field cooling (fc) modes. The resistivity (ρ) measurements were made by the four-probe technique using a Quantum Design physical properties measurement system (PPMS) versus temperature.

Table 2.1. Experimental conditions

Code	Power (W)	Crucible	T (°C)	Time	XRD pattern
DMW	130	Al_2O_3	1100-1150	2 min	$CuCrO_2$ (R-3*m*)
HMW	320	SiC	1050	5 min	$CuCrO_2$ (R-3*m*)
SS	-	Pt	1200	12 hr	$CuCrO_2$ (R-3*m*)

2.1.2. Study of structural, electrical, magnetic and surface properties

2.1.2.1. Structure

Figure 2.3 shows the room temperature X-ray diffraction patterns of samples prepared by microwave heating (DMW and HMW) and conventional process (SS). The patterns are characteristic of the 3R delafossite and the structure is refined in the *R-3m* space group (n° 166), with cell parameters: *a* = 2.976(1) Å and *c* = 17.102(3) Å. No significant difference is observed between the three sets of parameters, within the accuracy of the technique. The broader shape of Bragg peaks in the DMW and HMW diffractograms suggests a smaller grain size for microwave heated samples compared to conventional method. This is illustrated with two series of peaks (00 12) and (110) shown in figure 2.4. The two series of peaks were normalized to the maxima of the broadened peaks. It can be clearly seen from figure 2.4, sample prepared by monomode microwave heating (HMW and DMW) indicates smaller grain size as compared to sample SS (conventional method). The fact that the processing time is very short with microwaves (a few minutes instead of a few hours for conventional process) accounts for this difference in grain size. It is also probably why a small extra peak of impurity is observed in the X-ray diffraction pattern of DMW, identified as Cr_2O_3. This result is in contrast to the one reported in [128]: for the same starting Cu_2O:Cr_2O_3 ratio and similar heating process but in quartz tube, Cu and Cu_2O are obtained in addition to the major $CuCrO_2$ phase. It confirms thus the importance of the sample holder for such experiments. DMW sample has been directly heated by microwaves, for a shorter time: the inverse thermal gradient develops within the sample i.e., the outer part is at a lower temperature compared to the inner part [77]. The synthesis conditions

are thus more difficult to control for DMW than HMW, leading thus to an inferior quality of samples.

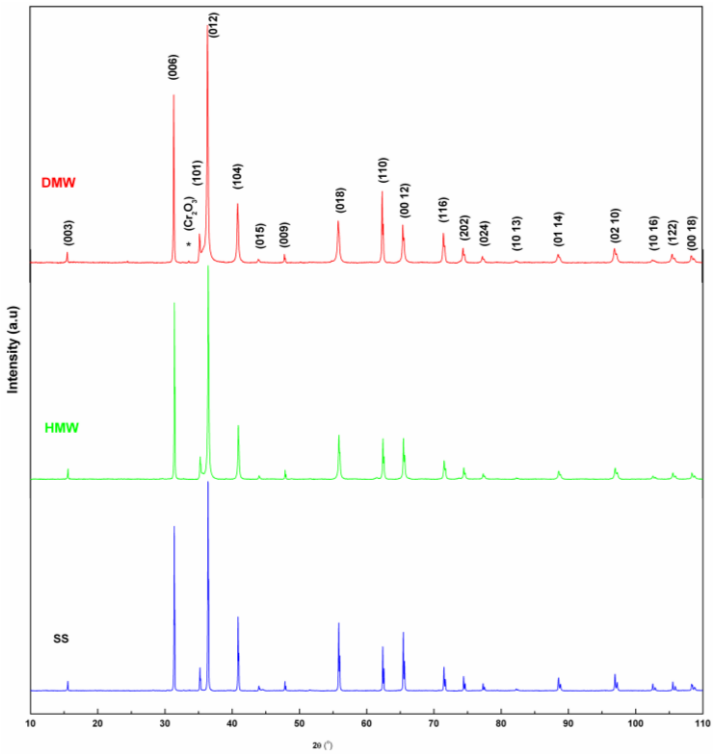

Figure 2.3. Room temperature X-ray diffraction patterns of samples prepared by monomode microwave heating (DMW and HMW) and conventional heating (SS).

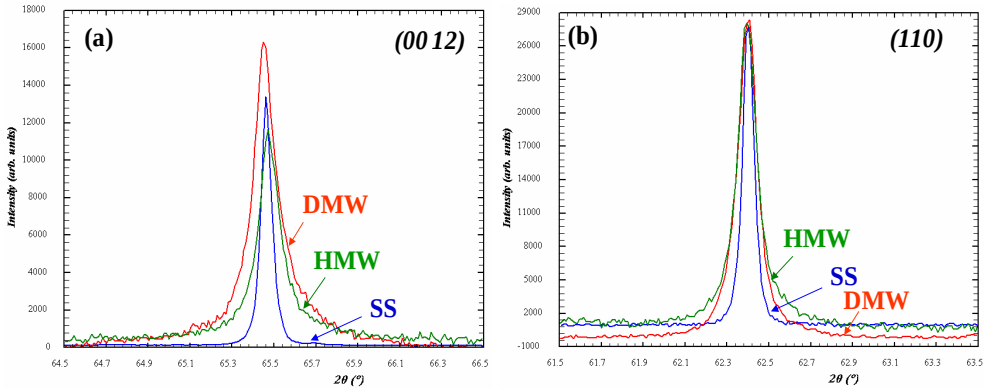

Figure 2.4. D8 X-ray diffraction pattern of the broadening of (00 12) and (110) normalized peaks with respect to the maxima of broadened peaks compared with SS.

2.1.2.2. Microstructure

The SEM images of samples HMW, DMW, and SS sample are shown in figure 2.5, 2.6, and 2.7 respectively. The HMW material is mainly composed of plate-like grains (figure 2.5), similar to the shape of the $CuCrO_2$ prepared by conventional method (figure. 2.7.c). It can be clearly seen from figure 2.5 and figure 2.7 that that the grain size is smaller in HMW sample compared to the conventionally synthesized sample (SS). This grain size is again smaller for sample DMW (figure 2.6) which also exhibits a small change in the morphology of the grains. The densities of DMW, HMW and SS samples are 4.80 $g.cm^{-3}$, 4.95 $g.cm^{-3}$, and 5.15 $g.cm^{-3}$, which correspond to 85%, 89% and 92% of the theoretical density, respectively.

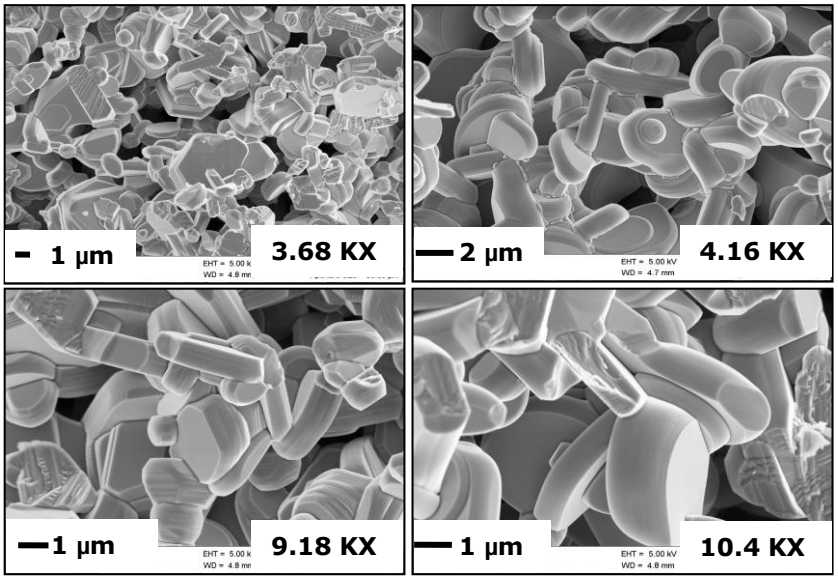

Figure 2.5. SEM images of HMW sample at different magnification shows the platelets shape micro crystals which correspond to the $CuCrO_2$ delafossite phase.

To go further, the volumetric particle size distribution was measured for the three samples which have been previously crushed for getting powder (figure 2.8). Also, we performed volumetric measurement on precursor mixed powder (Cu_2O and Cr_2O_3 mixture before synthesis) to get a clear view about the distribution of particle. The volumetric particle size distribution data of all samples are summarized in table 2.2. SS one shows a distribution maximum located at 10 µm, which is an usual value for a conventionally solid state synthesized ceramic and the DMW and HMW samples exhibit a distribution maximum located at roughly 500 nm, in agreement with the SEM observations. Nevertheless, these samples also contain a quite large

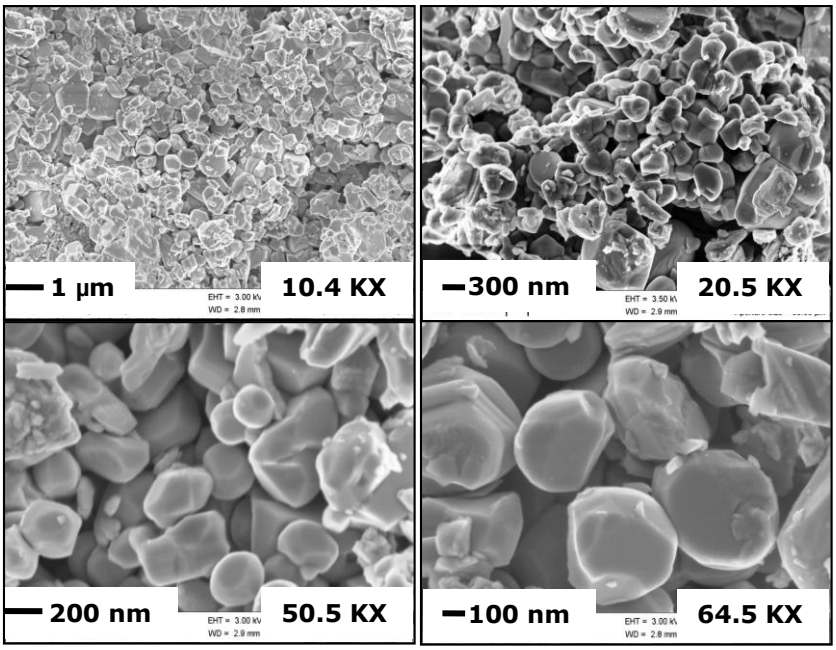

Figure 2.6. SEM images of DMW sample at different magnification show the spherical shape crystals which correspond to the $CuCrO_2$ delafossite phase.

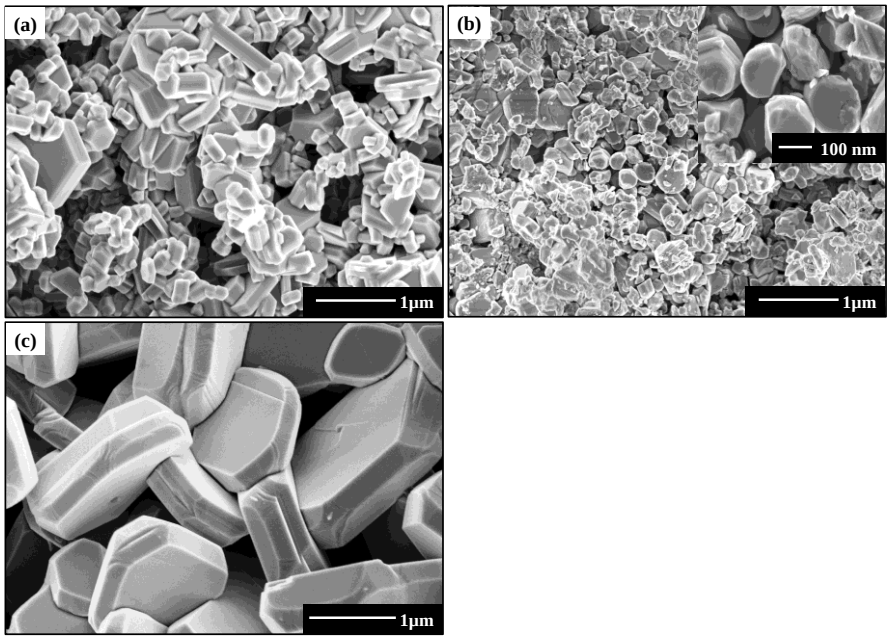

Figure 2.7. SEM images of (a) HMW (b) DMW and inset shows the morphology of DMW at higher magnification (c) SS sample.

volumetric fraction of micron-size particles as testified by their granulometric distribution (ranging from 1 to 30 μm for DMW and from 1 to 80 μm for HMW). It is obvious that the grain growth, at a given temperature, is mostly governed by the dwell duration of the high temperature stage. Consequently, owing to the very short processing time provided by microwaves, these samples have smaller particle sizes compared to conventional SS one.

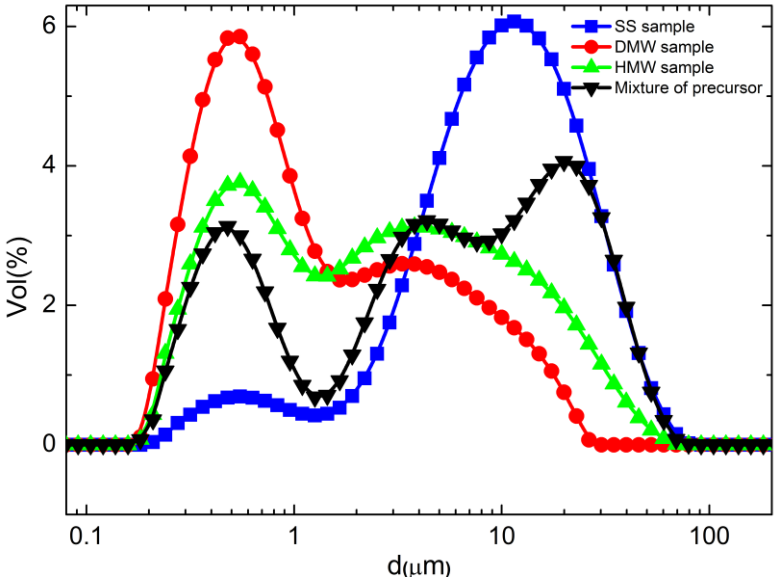

Figure 2.8. Volumetric particle size distribution curves of HMW, DMW and SS samples.

Table 2.2. Volumetric particle size distribution for different samples

Code	d(0.1)	d(0.5)	d(0.9)
Precursor Mixture (Cu_2O + Cr_2O_3)	0.3	5.3	26.6
SS	2.3	9.4	26.8
DMW	0.3	0.8	7.8
HMW	0.7	4.1	15.7

From the above characterizations, it appears thus that the HMW process is better than the DMW one, to prepare samples for electrical measurements, because the HMW sample is monophasic and its density is higher. Nevertheless, it could probably possible to increase the density of pellets by varying the pressure used for the compaction the pellets before heating, as previously done in [133].

2.1.2.3. Magnetic and electrical properties

DC magnetic characterization was performed on all three kinds of samples i.e. HMW, DMW, and SS using SQUID magnetometer. Figure 2.9.a illustrates the temperature dependence of magnetic susceptibility in the temperature range 5 K–300 K. It can be clearly seen that the samples prepared by monomode microwave heating (HMW, DMW, and SS) show an antiferromagnetic temperature dependence of the magnetic susceptibility with the Neel temperature T_N = 24 K. As expected these curves are characteristic of the $CuCrO_2$ delafossite i.e. an anomaly at T_N = 24 K corresponding to the antiferromagnetic transition in agreement with previous reports [30, 134]. Also, figure 2.9.b presents the inverse magnetic susceptibility in the temperature range 5 K–300 K. The temperature dependence of reciprocal magnetic susceptibility for HMW and DMW are linear in the paramagnetic region (> 150 K), and obeys the Curie- Weiss law with $\theta_{cw} < 0$. The χ^{-1} (T) curves for both samples are fitted by using Curie–Weiss law ($\chi = C/T-\theta_{cw}$). The effective magnetic moment is determined by using $\mu_{eff} = \sqrt{(3k_BC/N_A)}$.

Table 2.3. Parameters extracted from fitting of DC inverse magnetic susceptibility (χ^{-1}) data.

Code	T_N (K)	$\mu_{eff}^{experimental}$ (μ_B)	$\mu_{eff}^{Theoritical}$ (μ_B)	θ_{cw} (K)	$\lvert\theta_{cw}\rvert$ / T_N (K)
DMW	24	3.88	3.87	-197	8.2
HMW	24	3.87	3.87	-203	8.45
SS	24	3.8	3.87	-213	8.87

From the slopes in the linear regimes of reciprocal magnetic susceptibility (> 150 K), we have determined the Curie-Weiss constant θ_{cw} and the effective paramagnetic moment (μ_{eff}). The obtained values are given in table 2.3. A good agreement can be seen between the experimental and calculated values. The Curie-Weiss constant θ_{cw} for HMW and DMW is found to be -203 K and -197 K, indicates large antiferromagnetic fluctuations. These values were slightly larger than the value observed for SS sample i.e. -213. The degree of magnetic frustration is calculated by $|\theta_{CW}|/T_N$. The calculated value was ~ 8 in each sample showing a

strong antiferromagnetic coupling in both samples (HMW and DMW) prepared by monomode microwave. This value is close to the one reported for normal synthesis of $CuCrO_2$ by solid state. The effective paramagnetic moment per Cr^{3+} ions is μ_{eff} = 3.88 μ_B and μ_{eff} = 3.87 μ_B for DMW and HMW which is close to the one reported for conventional synthesized sample (SS, μ_{eff} = 3.8). The obtained values are close to the theoretical calculated magnetic moment for high spin Cr^{3+} (S = 3/2, $2[S(S+1)]^{1/2}$) μ_{eff} = 3.87 μ_B.

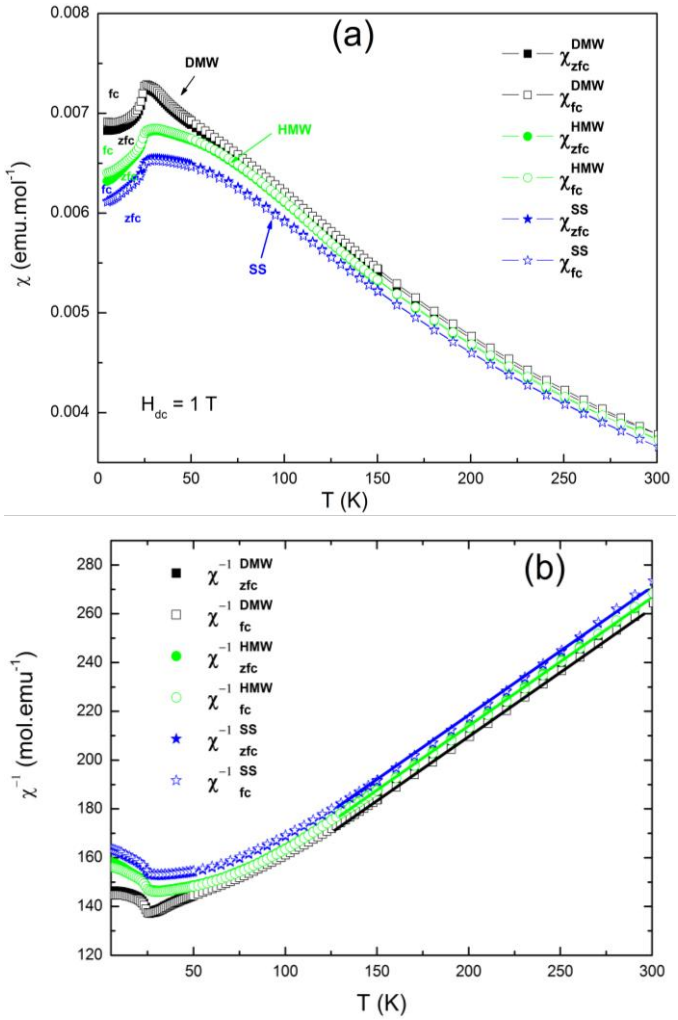

Figure 2.9. (a) Temperature dependence of dc molar magnetic susceptibility (χ) measured in zero field cooled (ZFC) and field cooled (FC) modes under magnetic field of 1 T for HMW, DMW, and SS sample. (b) Temperature dependence of the inverse molar magnetic susceptibility (χ^{-1}) of HMW, DMW, and SS sample. The solid line corresponds to the Curie-Weiss law fitting in the paramagnetic region (130 K-300 K).

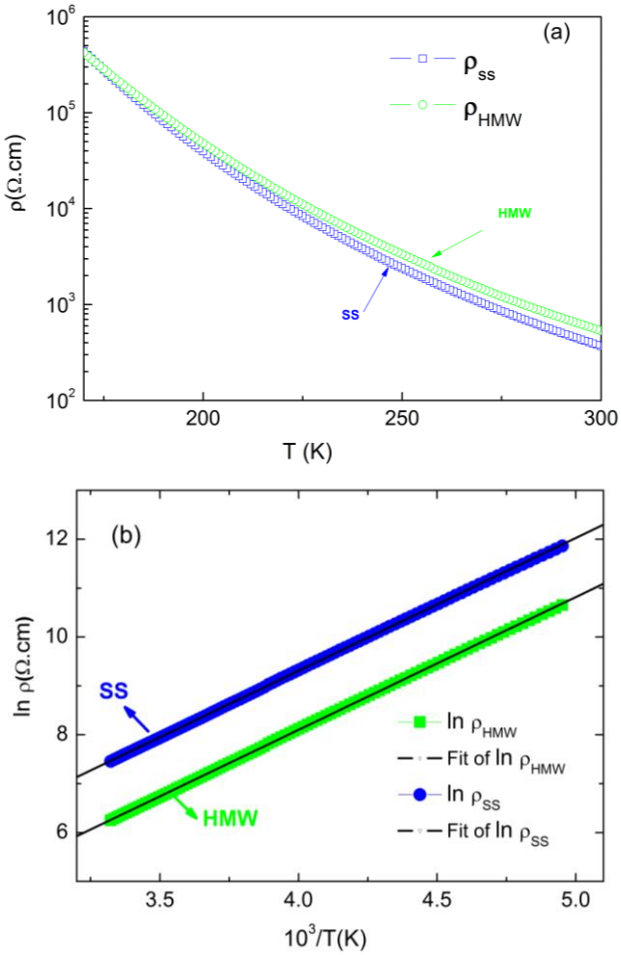

Figure 2.10. (a) Electrical resistivity $\rho(T)$ of SS and HMW samples. (b) Inverse temperature dependence of the high temperature resistivity values for HMW and SS sample. The solid line corresponds to the linear fitting of the inverse resistivity plot to calculate the activation energy (E_A).

Delafossites are also interesting for their electrical properties, and to characterize them it is necessary to obtain well sintered bars or pellets. By following the HMW process, we prepared a pellet (size 8 mm diameter and 5 mm thickness) to obtain the electrical properties. This method does not give the smaller grains but is clearly easier process to control as compared to DMW method. Also, HMW method avoids the cracks in the pellet during the synthesis which is important for electrical characterization. The temperature variation of the electrical resistivity was measured on the HMW sample and compared with SS sample (figure 2.10.a). Both ρ (T) curves are similar and account for a typical semiconducting behaviour. Inverse temperature dependence of the resistivity of HMW sample (figure 2.10.b) is

following an activated behaviour. The activation energy was calculated by using the activation energy formulae mentioned in equation 2.1. The final activation energy calculated for HMW sample was 235 meV, which is close to the reported value conventionally synthesized $CuCrO_2$ [134].

$$\rho\ (T) = \rho_0 * \exp\ (E_A/k_B * T) \qquad (2.1)$$

where E_A is the activation energy, k_B is Boltzman constant [135].

2.1.3. Conclusion

Single phase $CuCrO_2$ delafossite has been synthesized by using a single-mode microwave cavity working at 2.45 GHz within a few minutes. The rate of synthesis is significantly increased as compared to the solid state reaction method performed in a conventional furnace. In comparison to the DMW process, the HMW process leads to get a more homogeneous temperature distribution within the sample which is more suitable to synthesize single phases. SEM micrographs show that the grains size is smaller than in SS sample. The magnetization and resistivity curves show characteristics typical of the 3R delafossite. The hybrid microwave heating process is demonstrated to be a fast and efficient method for synthesizing delafossite compounds. This technique proved to be the fastest method to prepare $CuCrO_2$ compound with delafossite structure. After a successful attempt of synthesis of $CuCrO_2$ via monomode microwave, it open a wide gate for synthesis of other delafossite compound which are difficult to prepare via other method such as $CuVO_2$, $CuTiO_2$, and $CuNiO_2$.

2.2 Hydrothermal synthesis of $CuCrO_2$ with delafossite structure

2.2.1. Experimental set-up and precursor material

As we discussed in previous chapter, recent study reveals that hydrothermal synthesis method is one of the promising candidate to grow the single crystal of delafossite compound such as $AgCuO_2$ [136], $CuAlO_2$ [137], Ag_2CuMnO_4 [138]. The conventional synthesis method of $CuCrO_2$ compound requires the solid state reaction at high temperature (generally above 1000 $^{\circ}$C, and even 1200 $^{\circ}$C) and reaction time of several hours or in a few days. The advantage of the conventional method is wide collection of sources of raw materials, easy operation, easy to grasp. However, due to excessively high temperature causes increase in experimental set-up costs, and solid-state reaction required to do long-range atomic migration exercise, with the result that the reaction should not be thorough and often will produce multi-phase, mixed phase, and the repeated grinding that will increase the opportunities for the introduction of impurities, these will greatly affect the physical properties of the final products. In order to avoid these shortcomings, much more mild synthesis technology has been used, and hydrothermal method is one of excellent synthetic

methods used to prepare several organic and inorganic compounds. Hydrothermal method offers an alternative synthesis route for the multicomponent ceramic oxides.

Because the reactions are carried out in solution, the physicochemical properties of many reactions will change. Compared to high temperature solid state reactions, hydrothermal reactions need relatively low temperatures which favor the formation of low agglomeration, homogeneity and good sinterability ceramic powder. In addition, hydrothermal method is an open route to metastable phases. The present method is advantageous due to the use of relatively mild conditions, one-step synthesis procedure and easy handling.

In this work, we focused on the hydrothermal synthesis of $CuCrO_2$ with delafossite structure. In the system that has been prepared by traditional methods, a more soft synthesis route is explored and the results are compared with those obtained by other conventional synthesis method for the purpose to establish the relationship between the synthesis method and structure and properties of final products. A series of samples have also been prepared under different pressure, temperature, reaction time, also at varying molarity of molarizer (NaOH used here) by hydrothermal method in a finely controlled condition. Compared with the traditional solid state reaction methods, hydrothermal synthesis greatly reduced the reaction temperature, the samples of high purity, good crystallinity, grain uniformity, and some samples at surface electron microscope showing excellent morphology. Also with some samples prepared at high pressure revealed the coexistence of 2H structure as an impurity with 3R phase of $CuCrO_2$ with delafossite structure. No more data available in literature on the synthesis of 2H phase of $CuCrO_2$. The factors influencing the synthesis are also reported in detail, especially the pressure, reaction time and temperature of the reaction system. The Rietveld refinement of powder X-ray diffraction data showed that the crystal structures of final product shows the 3R phase of $CuCrO_2$ with delafossite structure with space group R-3m.

Series of samples were prepared by using hydrothermal experimental set-up for synthesis of $CuCrO_2$ at low and high pressure. Experiments were performed using high temperature stainless steel autoclave (12NiCr250, < 450 $^{\circ}$C, < 1000 bars) and low temperature stainless steel autoclave (comprises of Teflon liner, ≤ 250 $^{\circ}$C, < 100 bars) as shown in figure 2.11. The synthesis process consists of Teflon liners with varying volume capacity (30-110 ml capacity), stainless steel autoclave (High and low pressure) and the furnace assembly coupled with manometer as shown in figure 2.11 below. Temperature was recorded by means of temperature controller (E5CK-TAA1-500 100-240 AC Regulator Temperature OMRON) and the pressure was controlled by Kennedy's PVT diagram of water [81]. In case of samples prepared at high temperature (> 250 $^{\circ}$C) and pressure (> 100 bars), the as prepared solution was tight sealed in SS autoclave and placed in high temperature furnace (figure 2.11.b). For the low temperature synthesis (≤ 250 $^{\circ}$C), samples were prepared at different temperature (210 $^{\circ}$C, 220 $^{\circ}$C and 250 $^{\circ}$C) and reaction time (24 hrs, 60 hrs) in 1M and 2.5 M of NaOH molarity by using autoclave and Teflon liner shown in figure 2.11.a. After the given reaction time, autoclaves were taken out and allowed to cool at room temperature. Then after, the solution was taken out in a cylindrical beaker and the powder sample was allowed to settle down. The excess solution was removed from the beaker and the remaining powder was washed in ultrapure water and kept at room temperature for drying the powder.

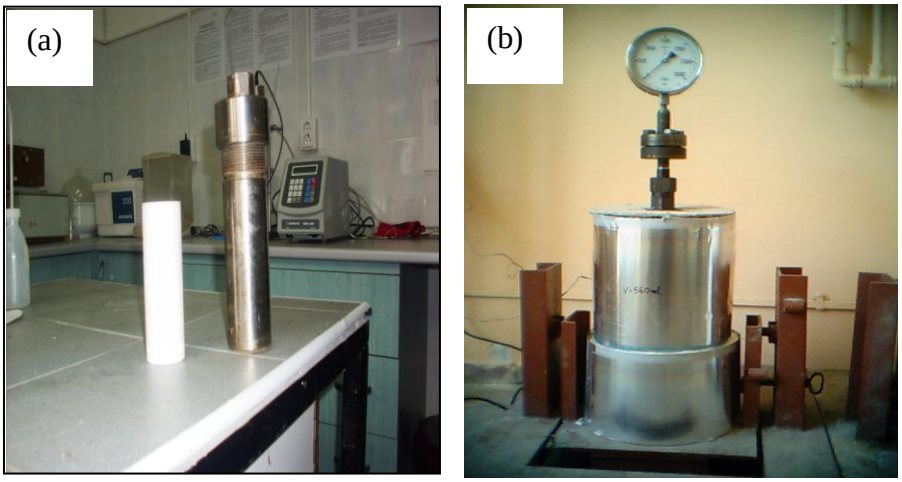

Figure 2.11. The experimental set up for the hydrothermal synthesis (a) Low pressure set up (b) High pressure set up

Table 2.4. The solubility product values of different precursors used during the synthesis.

	Precursor Material	Solubility Value in Water (K_{sp})
Cu precursor	Cu_2O	2×10^{-15}
	$Cu(OH)_2$	4.8×10^{-20}
Cr precursor	CrO_3	63 g/100 ml (25 °C)
	Cr_2O_3	Insoluble in water
	$Cr(OH)_3$	6.3×10^{-31}
	$Cr(NO)_3.9H_2O$	81 g/100 ml (20 °C)

Precursor Material: Selection of right kind of precursor material plays a vital role during the hydrothermal synthesis of final compound. To get the desired property of $CuCrO_2$ compound, we started with different set of precursor material listed in table 2.4 with their water solubility strength. We have chosen different precursors for the synthesis of $CuCrO_2$ compound based on their solubility product value and literature survey. In the beginning we tried different sets of precursors to

get $CuCrO_2$ with delafossite phase. We categorised each samples under different series and finally optimised the precursor material suitable for getting desired $CuCrO_2$ compound with delafossite structure.

2.2.2. Structural study of series I

2.2.2.1. Experimental condition

The precursor material used for this series were Cu_2O (1 mmol) for A site and $Cr(NO_3)_3.9H_2O$ (2 mmol) for B site to get $CuCrO_2$ (ABO_2) compound with delafossite structure. Table 2.5 below shows the different process condition used for the synthesis of delafossite compound with delafossite structure. The low temperature experimental set up generally known as soft hydrothermal synthesis method were used for synthesis of $CuCrO_2$ (ABO_2) compound as shown in above figure 2.11.a. The maximum temperature limit for the Teflon liner was 230 °C. But, for samples prepared at 250 °C and 280 °C, we have used different Teflon liner made up for high temperature synthesis.

Table 2.5. Experimental process condition used for series **I.**

Precursor		Process Condition				XRD Results
Cu	Cr	T (°C)	t (hr)	Fill (%)	M	
Cu_2O	$Cr(NO_3)_3.9H_2O$	220	60	70	0	**Cu_2O, CuO**, $CuCrO_2$*, $CuCr_2O_4$*
		220	60	70	2.5	**Cu_2O, CuO**, $CuCrO_2$*
		230	60	70	2.5	**Cu_2O, CuO**, $CuCrO_2$*
		250	60	70	2.5	**$CuCrO_2$**, Cu_2O*, CuO*
		280	60	70	2.5	**$CuCrO_2$**, CuO*

*minor phases, bold letters dominant phases

2.2.2.2. Results and discussion

Crystal structure of the final products was analyzed by powder X-ray diffractometry. We have prepared the samples with different molarity of NaOH to see the effect of varying molarity on the formation of the final product. It can be clearly seen from the figure 2.12 that varying molarity doesn't affect the crystal

structure of the final compound except reducing the spinel impurity from the final compound. This illustrates that with increase in molarity reduces the undesired impurity from the final compound. Figure 2.12 reveals the effect of varying NaOH molarity on the formation of final compound. It is clearly seen (figure 2.12.a) that the precursor impurity dominates the final form of the compound coexists with the CuO impurity and spinel impurity of $CuCr_2O_4$. It also gives an indication of formation of minor peaks of $CuCrO_2$ compound with delafossite phase. It clearly suggests that the temperature was not sufficient to dissolve the whole amount of precursor in solution containing chromium nitrate plus NaOH.

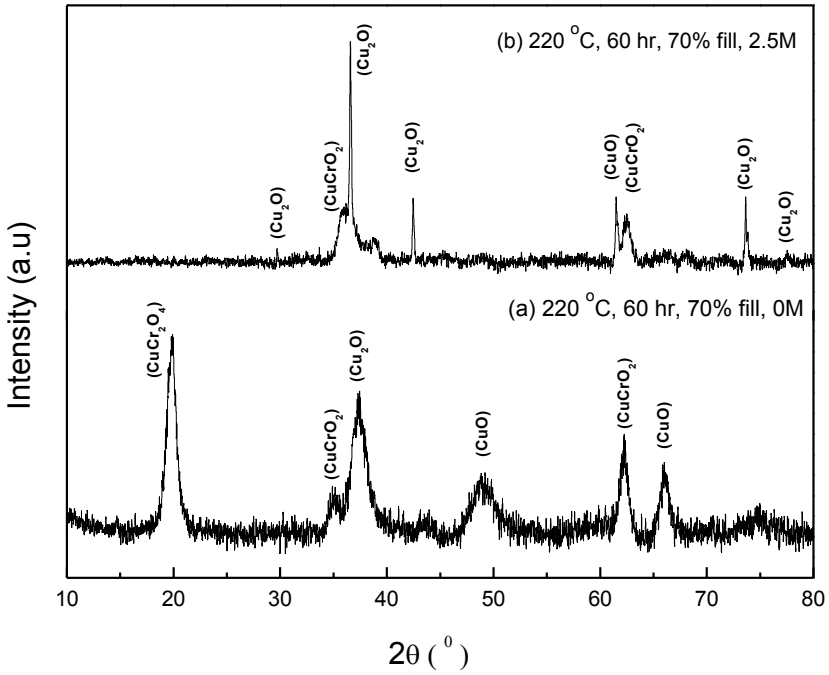

Figure 2.12. X-ray diffraction pattern of samples prepared at 220 °C for 60 hrs reaction time with varying molarities of NaOH under mild hydrothermal process condition.

Next, we have synthesized samples with increased temperature keeping molarity, reaction time and fill percent same under mild hydrothermal process condition as shown in table 2.5. Figure 2.13 shows the diffraction pattern of samples prepared at different reaction temperature 220 °C, 230 °C, 250 °C and 280 °C keeping process reaction time 60 hr in 2.5M of NaOH in 70 % fill of the volume of the Teflon liner. It suggests that at low temperature 220 C°, mixture of Cu^{2+} and Cu^{1+} impurity phases dominates the final form of product. It also indicates that at this temperature starts appearing very tiny peak of $CuCrO_2$ with delafossite

structure. This suggests that the temperature wasn't sufficient for the formation of final compound. This justifies the argument that at low temperature the precursor phase of Cu_2O doesn't dissolves to form the stable, aqueous soluble hydrate compound of copper responsible for formation of pure delafossite compound [136]. Also, increase in temperature increases the solubility of precursor phases of Cu_2O in an aqueous solution. It clears from the figure 2.13.b, c, d that with increase in temperature increases the possibility of formation of delafossite compound. This can also be seen XRD pattern column from table 2.5 (dominant phase's written in bold letters).

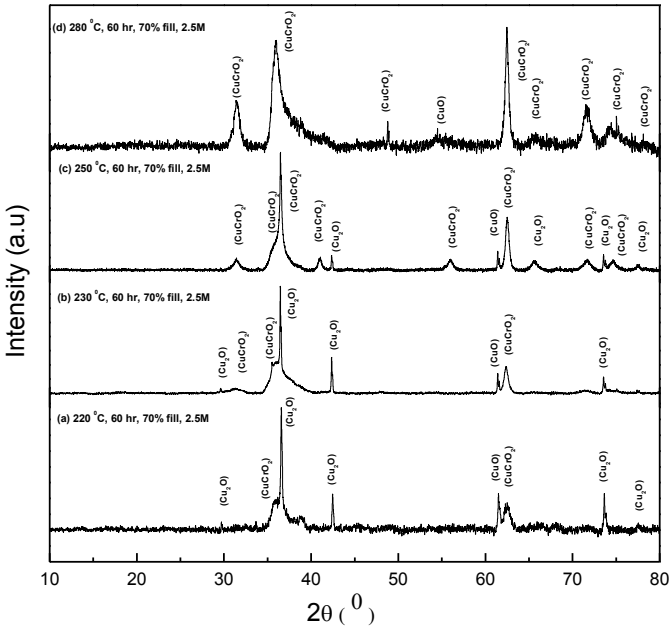

Figure 2.13. X-ray diffraction pattern shows the structural analysis of samples synthesized with increasing temperature at 2.5 M of NaOH for 60 hr of reaction time and 70 % fill percent under mild hydrothermal process condition.

Samples prepared at 230 °C showed the precursor impurity in final product but significant changes has been observed in XRD pattern of sample prepared at a bit higher temperature i.e. 250 °C coexists with minor phases of Cu_2O and CuO. Further increase in temperature suppresses the precursor impurity phases of Cu_2O but there exists a minor impurity phase of CuO. Figure 2.13 reveals the XRD pattern of sample prepared at 280 °C, shows the $CuCrO_2$ compound with delafossite structure with minute impurity of CuO.

2.2.2.3. Conclusion

We have tried to synthesize the $CuCrO_2$ by using copper (I) oxide and chromium nitrate as a precursor. The structural study of as prepared powder show the $CuCrO_2$ phase with delafossite structure in addition to minor impurity phases of CuO. The precursors used were Cu_2O and $Cr(NO_3)_3.9H_2O$ in 2.5M of NaOH with 70 % fill of volume of Teflon liner. The stability area of the Cu^{1+} ion increases with increasing temperature and NaOH concentration at the expense of the Cu^{2+} ion. The spinel impurity of $CuCr_2O_4$ was removed by the effect of NaOH in an aqueous solution. It is clearly seen that with increase in temperature increases the solubility of precursor materials increases which in turn gives rise to a stable hydrate compound of copper and chromium responsible for formation of delafossite compound.

2.2.3. Structural study of series II

2.2.3.1. Experimental condition

The precursor material used for this series was Cu_2O for A site and CrO_3 for B site to get $CuCrO_2$ (ABO_2) compound with delafossite structure. Table 2.6 below shows the different process condition used for the synthesis of delafossite compound with delafossite structure. We have used the same low temperature experimental set up which was used for synthesis of samples for **I** series as shown in figure 1.a. The maximum temperature limit for the Teflon liner was 230 °C. The sample at 250 °C was prepared in an autoclave with different Teflon liner.

Table 2.6. Experimental process condition used for series **II**

Precursors		Process Condition				XRD Results
Cu	Cr	T (°C)	t (hr)	Fill (%)	M	
Cu_2O	CrO_3	180	60	70	0	**$Cr(OH)_3$, CrOOH, Cu_2O**
		200	60	70	0	**$Cr(OH)_3$, CrOOH, Cu_2O,** CuO*
		220	60	70	0	**$Cr(OH)_3$, CrOOH, Cu_2O,** CuO*
		220	60	70	2.5	**Cu_2O, CuO**, $Cr^{3+,\&}$
		230	60	70	2.5	**Cu_2O, CuO**, $Cr^{3+,\&}$
		250	60	70	2.5	**Cu_2O, CuO,** $CuCrO_2$*

*minor phases, bold letters dominant phases, &in solution

2.2.3.2. Results and discussion

In this category we prepared the samples with varying process temperature by keeping same molarity. Figure 2.14 reveals the X-ray diffraction pattern of samples prepared without NaOH with increase in process temperature. It can be clearly seen from figure 2.14 the formation of hydrate compound of chromium like $Cr(OH)_3$ and orthorhombic phase CrOOH. This suggests that chromium which was having oxidation state +6 (CrO_3) before start of synthesis reduces to +3 in final compound. With all samples prepared without introducing sodium hydroxide in an aqueous solution showed the existence of hydrate compound of chromium which can be useful as one of the precursor for synthesis of $CuCrO_2$. In later section we will discuss in detail further about the possibility of using this mixture as a precursor to get desired compound with improved crystal and surface morphology.

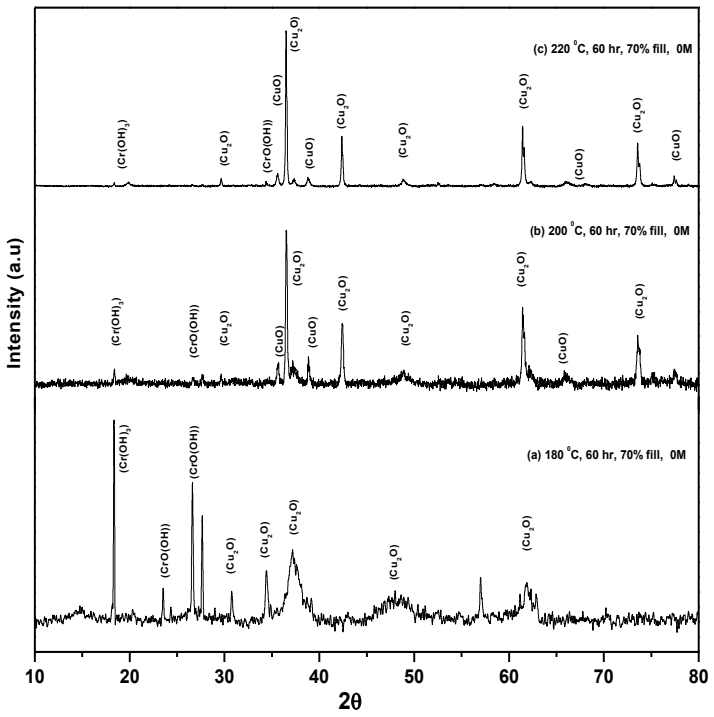

Figure 2.14. X-ray diffraction pattern of sample prepared in water with varying temperature for 60 hr of reaction time and 70 % fill percent under mild hydrothermal process condition.

Also, we prepared samples by introducing sodium hydroxide in an aqueous solution with varying process temperature keeping same reaction time and fill percent. Figure 2.15 shows the samples prepared in 2.5 M of NaOH with increase in temperature. It can be clearly seen from the XRD pattern that the precursor

impurity of Cu_2O leads to the final product in addition to CuO impurity phase. This indicates that the chromium as an impurity rests in solution. This suggests the oxidation of copper in a basic solution. Further increase in temperature reduces the impurity phases of Cu_2O and CuO and starts to appear delafossite phase of $CuCrO_2$ (3R). This suggests working further at high temperature may get the pure delafossite compound.

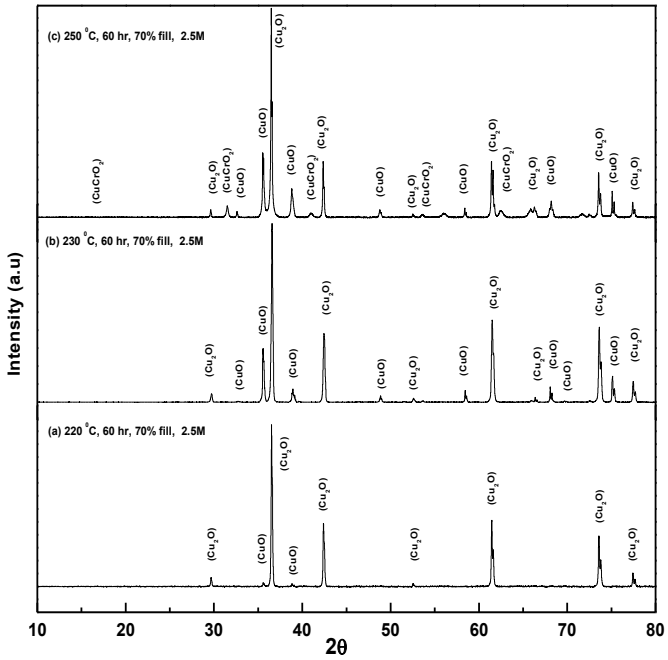

Figure 2.15. X-ray diffraction pattern shows the structural analysis of samples synthesized with increasing temperature at 2.5 M of NaOH for 60 hr of reaction time and 70 % fill percent under mild hydrothermal process condition.

2.2.3.3. Conclusion

To synthesize $CuCrO_2$ with delafossite structure we used precursor of Cu_2O (1mmol) and CrO_3 (2mmol) in water and 2.5M of NaOH with 70 % fill of volume of Teflon liner for 60 reaction time. In case of without NaOH in an aqueous solution, X-ray diffraction pattern shows the formation of mixed phases of chromium hydroxide and orthorhombic phases of CrOOH which can be used as a precursor powder. Introducing NaOH in an aqueous solution gives rise to oxidation of copper at low temperature, but destroys the CrOOH. CrOOH phases remains in the solution. Further increase in temperature reduces the precursor impurity of Cu_2O and also reduces the effect of oxidation. In next section of series we will focus on the mixed

phases of hydrate compound of chromium observed in X-ray diffraction pattern of samples prepared without introducing NaOH in an aqueous solution.

2.2.4. Structural study of series III

2.2.4.1. Experimental condition

In series III, we studied the effect of mixed compound as a precursor for the B site on the final product in ABO_2 compound. The precursor materials used for this series were $Cu(OH)_2$ and mixed powder of $Cr(OH)_3$ and CrO_3. To get the mixed phases of CrO_3 and $Cr(OH)_3$, 2.5 g of CrO_3 mixed properly using magnetic stirrer in an aqueous solution and as obtained solution then transferred to a Teflon liner. The stainless steel autoclave consists of Teflon liner treated at 200 °C for 60 hrs of reaction time. Then after the solution is taken out in a glass beaker and heated at 140 °C for 4 hrs using magnetic stirrer coupled with hot plate. For further drying the sample, the solution was placed into furnace at 100 °C for 2 hrs. The powder obtained after the furnace treatment is grinded well before analysing by X-ray diffraction. The powder sample showed mixed phases of CrO_3 and $Cr(OH)_3$. We have used this powder material and $Cu(OH)_2$ as a precursor to synthesize the samples in different molarity of NaOH at different temperature under mild hydrothermal condition mentioned in table 2.7. Table 2.7 below shows the different process condition used for the synthesis.

Table 2.7. Experimental process condition used for series **III**

Precursors		Process Condition				XRD Results
Cu	Cr	T (°C)	t (hr)	Fill (%)	M	
$Cu(OH)_2$	Mixture of $Cr(OH)_3$ and CrO_3	180	24	85	1	**CuO,** $CuCrO_2$* (3R),$CuCrO_2$ (2H) *
		220	24	85	1	**CuO,** Cu_2O*, $Cr^{3+,\&}$
		230	24	85	1	**CuO**, $Cr^{3+,\&}$
		180	24	85	2	**CuO,** $CuCr_2O_4$*
		220	24	85	2	**CuO**, $Cr^{3+,\&}$
		230	24	85	2	**CuO**, $Cr^{3+,\&}$
		230	24	85	2.5	**CuO**, $Cr^{3+,\&}$
		250	24	85	2.5	**CuO**, $Cr^{3+,\&}$

*minor phases, bold lettersdominant phases, &in solution

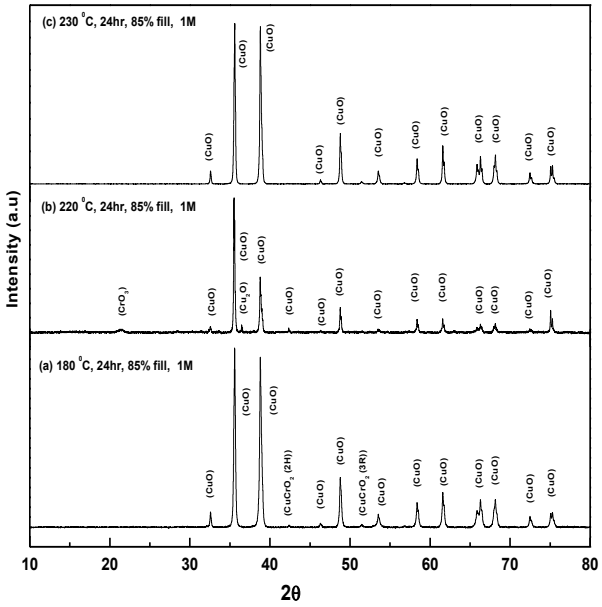

Figure 2.16. X-ray diffraction patterns show the structural analysis of samples synthesized with increasing temperature at 1 M of NaOH for 24 hr of reaction time and 85 % fill percent under mild hydrothermal process condition.

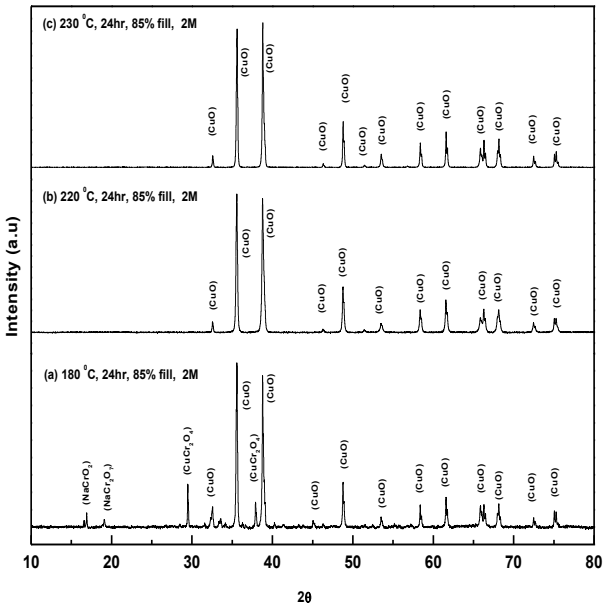

Figure 2.17. X-ray diffraction patterns show the structural analysis of samples synthesized with increasing temperature at 2 M of NaOH for 24 hr of reaction time and 85 % fill percent under mild hydrothermal process condition.

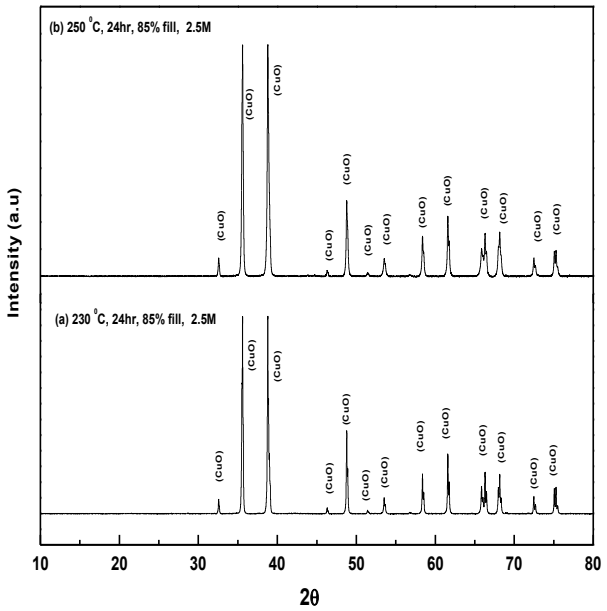

Figure 2.18. X-ray diffraction patterns show the structural analysis of samples synthesized with increasing temperature at 2.5 M of NaOH for 24 hr of reaction time and 85 % fill percent under mild hydrothermal process condition.

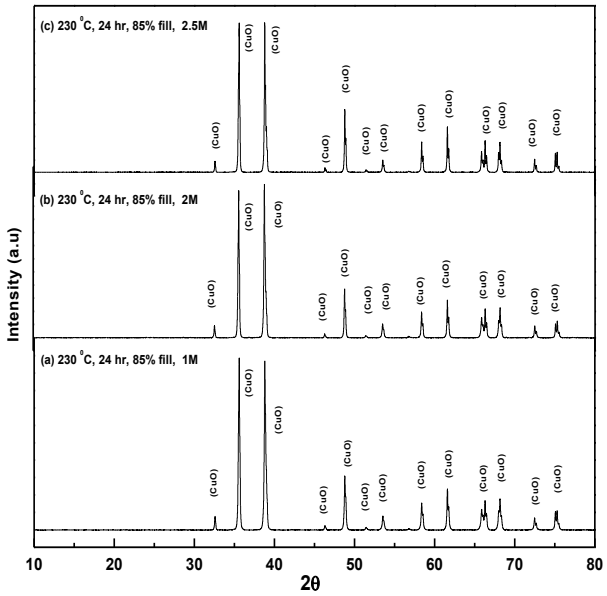

Figure 2.19. X-ray diffraction patterns show the comparative structural analysis of final products synthesized at 230 °C for 24 hr of reaction time in different NaOH molarities under mild hydrothermal process condition.

2.2.4.2. Results and discussion

Figure 2.16, figure 2.17 and figure 2.18 shows the X-ray diffraction pattern of samples prepared at different temperature by keeping the same molarity of NaOH. As it can be clearly seen, oxidation of Cu takes place without giving any signature of delafossite compound. Figure 2.19 shows the X-ray pattern of samples prepared at increasing the molarity by keeping the temperature same. The final product doesn't have any significant change in delafossite structure. It shows the impurity of CuO in the final product. We used $Cu(OH)_2$ precursor for A site and mixture of CrO_3 and $Cr(OH)_3$ for B site to synthesize $CuCrO_2$ with delafossite structure. Using this we prepared various samples in different molarity of NaOH with 85 % fill of volume of Teflon liner for 24h of reaction time. The samples prepared with increase in molarity keeping process temperature same showed the CuO dominated phase in X-ray diffraction pattern. Also, samples prepared at different process temperature by keeping the molarity same doesn't show any significant change in crystal structure of final product. This concludes that oxidation of copper takes place at temperature less than 250 °C temperatures. Instead of Cu^{+1} it oxides into Cu^{2+} which in turn forms CuO. It may possible to get delafossite compound if samples are prepared at high temperature at pressure. To keep this thing in mind we prepared some samples at high temperature and pressure to see the effect of pressure and temperature on final sample. In later series we discussed all results based on high temperature and pressure.

2.2.4.3. Conclusion

So, we can conclude that the evolution of Cu^{1+} ion in Cu^{2+} ion is favoured and emphasized by the $Cu(OH)_2$ precursors. Thus, in future experiments we will use the Cu_2O precursor for A site and hydrated CrO_3 precursor for B site.

2.2.5. Structural study of series IV

2.2.5.1. Experimental conditions

Experiments were performed using high temperature stainless steel autoclave (12NiCr250, < 450 °C, < 1000 bars) and low temperature stainless steel autoclave (comprises of Teflon liner, ≤ 250 °C, < 100 bars) as shown in figure 1.11 in chapter 1. Temperature was recorded by means of temperature controller (E5CK-TAA1-500 100-240 AC Regulator Temperature OMRON) and the pressure was controlled by Kennedy's PVT diagram of water [81]. Solutions were prepared by dissolving precise amounts of copper (I) oxide (0.141 g, purity > 97 %,), hydrated chromium trioxide CrO_3 (0.206 g, purity > 97 %,) and sodium hydroxide (NaOH, purity > 98 %) crystals in pure distilled water prepared by double distiller (2104, GFL, Germany). NaOH was used to control pH and the product solubility [120]. In case of samples prepared at high temperature (> 250 °C) and pressure (> 100 bars), the as prepared solution was tight sealed in SS autoclave and placed in high temperature furnace (figure 1.11.b). For the low temperature synthesis (≤ 250 °C), samples were prepared at different temperature (210 °C, 220 °C and 250 °C) and reaction time (24 hrs, 60 hrs) in 1M and 2.5 M of NaOH molarity. After the given reaction time, both autoclaves was taken out and allowed to cool at room temperature. Then after, the solution was taken out in a cylindrical beaker and the

powder sample was allowed to settle down. The excess solution was removed from the beaker and the remaining powder was washed in ultrapure water and kept at room temperature for drying the powder.

2.2.5.2. Results and discussion

Single phase $CuCrO_2$ polycrystals having sizes ranging from 0.7 μm to 3 μm and a rhombohedral R-*3m* structure has been successfully synthesized using 1 mmol Cu_2O (0.141 g), 2 mmol of hydrated CrO_3 (0.206 g) and 2.5 M of NaOH aqueous solution for reaction time of 48 hrs at 300 °C and 200 bars (Table 2.8: HT4; figure. 2.20.e). The XRD pattern of a powder sample is characteristic of the 3R delafossite and the structure is refined in the *R-3m* space group (n° 166), with cell parameters: *a* = 2.976(1) Å and *c* = 17.102(3) Å. No significant difference is observed between the three sets of parameters, within the accuracy of the technique. The stronger diffraction peaks are observed at 31.3°, 36.4°, 62.3° and 71.4° which corresponds to (006), (012), (112), and (116) planes of $CuCrO_2$ respectively (figure 2.20.e). The broad shape of Bragg peak observed in HT4 sample at 36.4° suggests a smaller grain size. Similar kind of peak broadening was observed in hydrothermal synthesis of $AgInO_2$ [86].

Table 2.8. Experimental conditions.

Code	Time (hr)	NaOH (M)	P (bars)	T (°C)	XRD Results
reaction temperature					
HT1	48	2.5	50	210	Cu_2O,CuO, Cr^{3+} (solution)
HT2	48	2.5	70	220	Cu_2O,CuO, Cr^{3+} (solution)
HT3	48	2.5	100	250	Cu_2O,CuO, **$CuCrO_2$ (3R)***
HT4	48	2.5	200	300	**$CuCrO_2$ (3R)**
reaction time					
HRT1	24	2.5	200	300	Cu_2O, $CuCrO_2$ (3R)*
HRT2	48	2.5	200	300	**$CuCrO_2$ (3R)**
molarity					
HM1	48	1	200	300	Cu_2O,CuO,$CuCrO_2$ (3R)*
HM2	48	2.5	200	300	**$CuCrO_2$ (3R)**

* Minor products, bold letters dominant phases

In the following section, the effect of reaction temperature, reaction time, NaOH molarities, and pressure on the crystal phase of the products is discussed. In case of hydrothermal synthesis, effects of reaction temperature and time on products cannot be overlooked. In previous papers [120, 139-142], effect of reaction time and temperature has been shown on hydrothermal synthesis of

various compounds and reveals that the crystallinity is improved with the elevation of reaction temperature. Table 2.8 summarizes the experimental process condition for samples prepared at increasing reaction temperature (HT labeled samples), reaction time (HRT labeled samples) and molarity (HM labeled samples).

2.2.5.2.1. Effect of temperature

To investigate the effect of reaction temperature on the final products, hydrothermal synthesis of $CuCrO_2$ using Cu_2O (0.141 g), hydrated CrO_3 (0.206 g) aqueous solution with 2.5 M of NaOH for reaction time of 48 hrs was performed at various temperatures (figure 2.20). As shown in figure 2.20.b-d samples prepared at 210 $^{\circ}$C, 220 $^{\circ}$C, and 250 $^{\circ}$C (HT1, HT2, HT3 labeled samples) show the majority of impurity phases of Cu_2O and CuO in diffraction patterns. Sample prepared at 250 $^{\circ}$C indicates the presence of minor phase of $CuCrO_2$ (R-3m) phase. Further increasing the reaction temperature gives rise to the formation of pure $CuCrO_2$ rhombohedral phase without presence of any impurity phase (figure 2.20.e). This justifies the argument that at low temperature Cu_2O does not dissolve in an aqueous solution to form stable species of Cu^+ [143]. With increase in temperature Cu_2O dissolves to form the stable, aqueous soluble hydrate compound of copper [119,85]. Also, for Cr^{3+}, in an aqueous solution, Cr^{3+} ions are stabilized by the formation of Cr $(OH)^-_4$ species and their concentration increases at elevated temperature [144]. Also, higher reaction temperature resulted in increasing the oxidation of the mixed solvent [139].

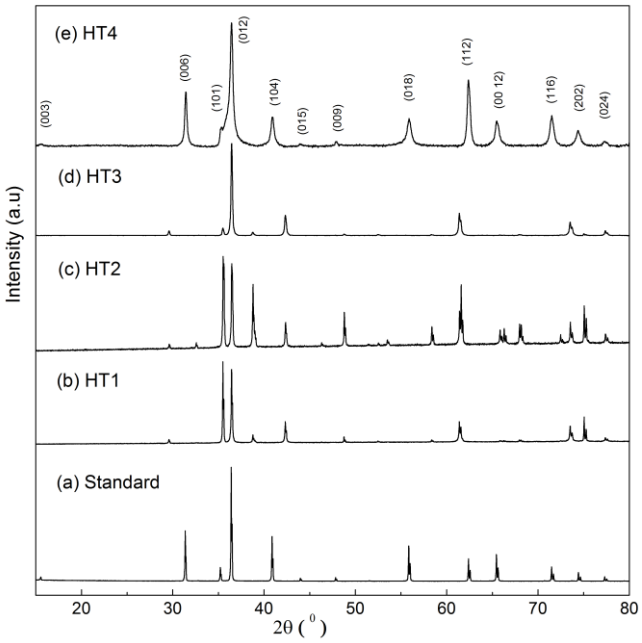

Figure 2.20. XRD patterns of samples prepared at (a) standard (b) 210 $^{\circ}$C (c) 220 $^{\circ}$C (d) 250 $^{\circ}$C (e) 300 $^{\circ}$C (delafossite phase) for 48 hrs reaction time in 2.5 M of NaOH.

2.2.5.2.2. Effect of reaction time and molarity

The effect of reaction time and molarity on the formation of $CuCrO_2$ from Cu_2O and hydrated CrO_3 is discussed. Figure 2.21.b and c shows the diffraction patterns of $CuCrO_2$ samples prepared at 300 $^{\circ}$C and 200 bars with 2.5 M of NaOH for reaction time of 24 hrs and 48 hrs (HRT1, HRT2 labeled samples). The fact that the processing time is short in case of HRT1 sample accounts the presence of precursor impurity phase of Cu_2O in addition to $CuCrO_2$ phase in XRD patterns. Also, this suggests the reaction time was not enough for the formation of hydrate species of Cu^{+} and Cr^{3+}. With further increase in reaction time (in case of HRT2 sample), the concentration of stable species of $Cu(OH)^{-}_2$ and $Cr(OH)^{-}_4$ increases that leads to the formation of pure phase of $CuCrO_2$.

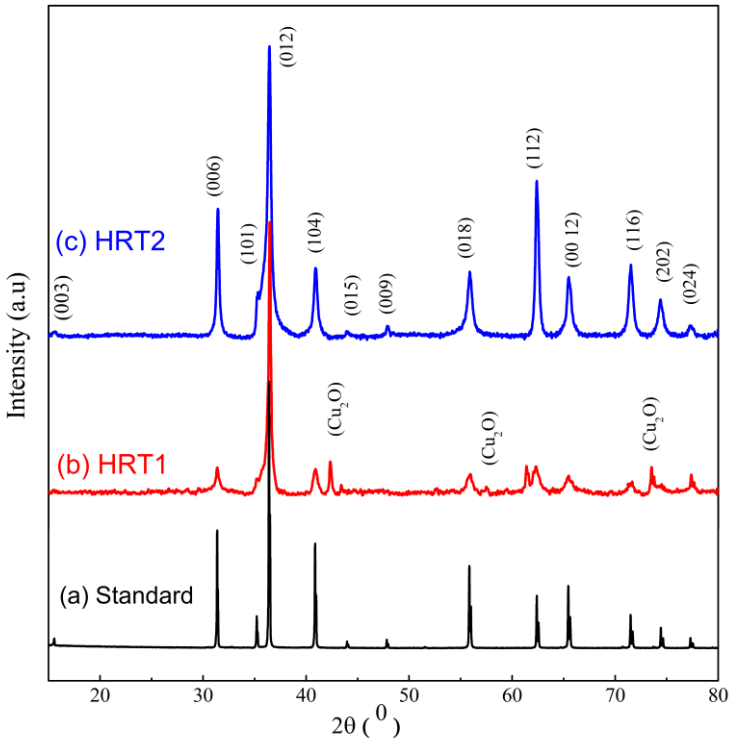

Figure 2.21. XRD patterns of samples prepared at (a) Reference Data (b) 24 hours (c) 48 hours (pure phase) at temperature 300 $^{\circ}$C and pressure of 200 bars in 2.5 M NaOH

It is well known that the conversion and reaction rate increases with NaOH concentration [84]. To investigate controllability of oxidation state of Cu with NaOH concentration, hydrothermal synthesis with Cu_2O (0.141 g) and hydrated CrO_3

aqueous solution with 1 M and 2.5 M of NaOH was performed at 300 °C for reaction time of 48 hrs. The effect of NaOH molarity on the crystal phase of the products was analyzed by X-ray diffraction (figure 2.22). As shown in figure 2.22, crystal phase of the products changed from Cu_2O and CuO (in case of HM1 labeled samples) to $CuCrO_2$ (HM2 labeled samples) with increase in NaOH molarity and also the product yield increased. It is clear that low molarity of NaOH favors mixed oxidation state of Cu (Cu^+ and Cu^{2+}) in an aqueous solution. Increase in molarity stabilizes the oxidation state of Cu into Cu^+ and for Cr into Cr^{3+} leads to the formation of pure phase of $CuCrO_2$ (figure 2.22.b). Thus, the high temperature (300 °C) and basicity of the solution (2.5 M) were allowed the fully replacement of Cu^{2+} ions.

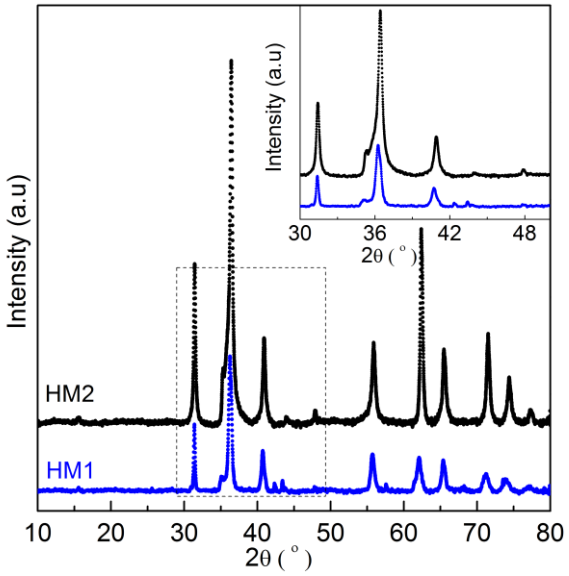

Figure 2.22. X-ray diffraction patterns of samples prepared at 300 °C for 48 hrs of reaction time in 1 M and 2.5 M of NaOH in an aqueous solution. The upper right inset is the region of dotted line.

Figure 2.23 shows the morphology of HT4 sample (single phase $CuCrO_2$, prepared at 300 °C for reaction time 48 hrs in 2.5 M NaOH). It is mainly composed of microspheres with diameter of about 2-4 μm. At higher magnification the microspheres appear a bunch of pure $CuCrO_2$ platelets of size ranges from 0.7 μm to 3 μm (figure 2.23.c-d). The EDX analysis leads to Cu/ Cr ratio close to 53/47 which is close to the one reported for conventionally synthesized $CuCrO_2$ [134].

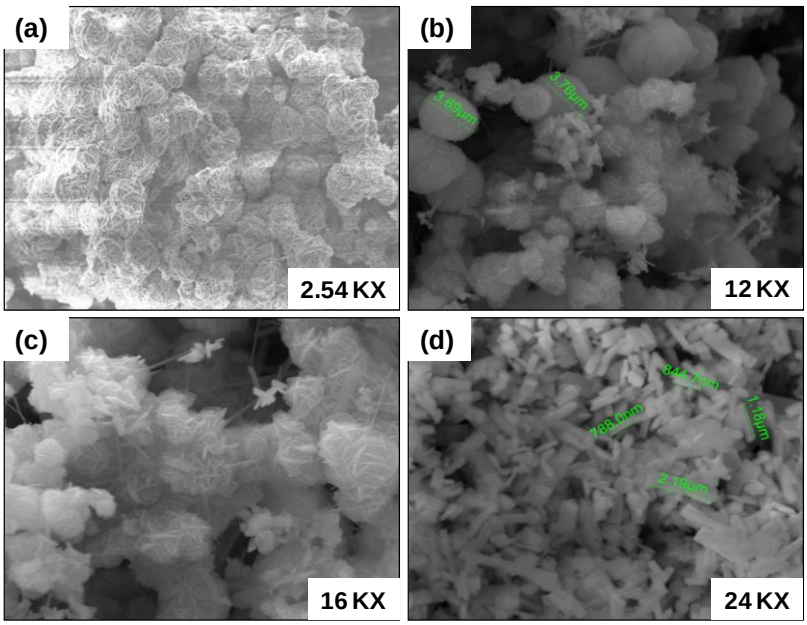

Figure 2.23. SEM images of sample HT4 (prepared at 300 °C for reaction time 48 hrs in 2.5 M NaOH) at different magnification.

2.2.5.2.3. Effect of the pressure

It is well known that high oxygen pressure during hydrothermal synthesis favors the desired oxidation state and single phase products [145-149]. In this section, the effect of varying pressure on the formation of $CuCrO_2$ phase from Cu_2O and hydrated CrO_3 is discussed. Experimental conditions and results are summarized in table 2.9. The effect of pressure on the crystal phase of the products was analyzed with X-ray diffraction pattern (figure. 2.24). As shown in figure. 2.24, samples prepared at 300 °C for reaction time of 48 hrs with 1 M NaOH (figure 2.24.a-c; HP1, HP2, HP3 labeled samples) leads to form a single phase of $CuCrO_2$ in addition to impurity phase of Cu_2O and CuO. SEM images show phase purity of $CuCrO_2$ increases with increase in pressure and grains exist in the form of pseudo-hexagonal platelets up to 0.5 μm thick and 3 μm in diameter. Also EDX analysis reveals decrease in Cu/Cr ratio with increase in pressure leads to the formation of $CuCrO_2$ phase.

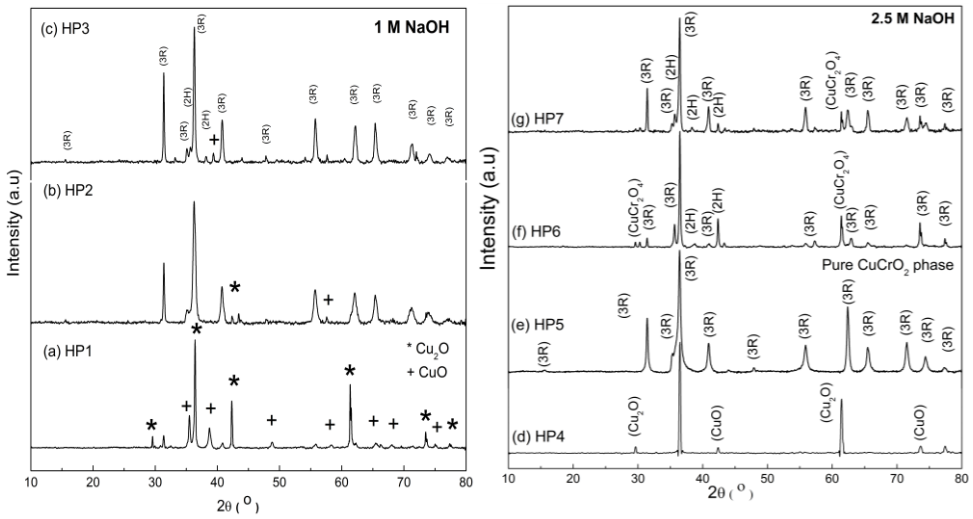

Figure 2.24. X-ray diffraction patterns of samples prepared at 300 °C for reaction time of 48 hrs with 1 M NaOH at pressure (a) 50 bars (b) 300 bars (c) 500 bars and with 2.5 M of NaOH at pressure (d) 50 bars (e) 200 bars (pure phase) (f) 500 bars (g) 700 bars.

Table 2.9. Experimental condition for samples prepared at different pressure.

Code	T (°C)	Time (hr)	NaOH (M)	P (bars)	XRD Results
HP1	300	48	1	50	Cu_2O, CuO, $CuCrO_2$ (3R)*
HP2	300	48	1	300	$CuCrO_2$ (3R), $CuCrO_2$(2H)*, Cu_2O *
HP3	300	48	1	500	$CuCrO_2$ (3R), $CuCrO_2$ (2H) *, CuO *
HP4	300	48	2.5	50	Cu_2O, CuO, $CuCrO_2$ (3R)*
HP5	300	48	2.5	200	**$CuCrO_2$ (3R)**
HP6	300	48	2.5	500	$CuCrO_2$ (3R), $CuCrO_2$ (2H) *, $CuCr_2O_4$*
HP7	300	48	2.5	700	$CuCrO_2$ (3R), $CuCrO_2$ (2H)*, $CuCr_2O_4$*

* Minor products, bold letters dominant phases

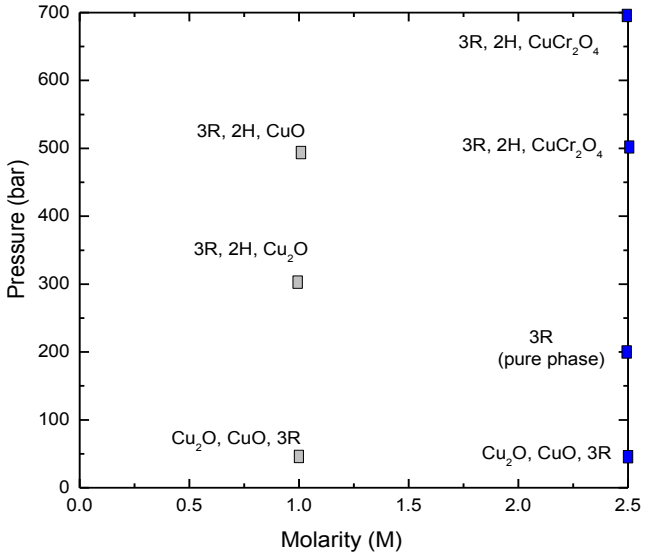

Figure 2.25. Phase diagram for pressure, molarity and reaction temperature system.

To increase the reactant solubility and controllability of oxidation state of Cu, samples were also prepared at 300 °C for reaction time of 48 hrs with 2.5 M of NaOH (figure 2.24.d-g; HP4, HP5, HP6, HP7 labeled samples) at different pressure. It is clear evidence of formation of pure single phase of $CuCrO_2$ at 200 bar of pressure without presence of any impurity phase. Investigating further at higher pressure (figure 2.24.g-h) the pure phase is formed in addition to the minor impurity phases of 2H phase of $CuCrO_2$ plus very minor peak of $CuCr_2O_4$. The impurity phases of 2H phase of $CuCrO_2$ becomes dominant with final product and and suppresses the impurity of $CuCr_2O_4$ with increase in pressure. There is a slight significance of phase transformation of $CuCrO_2$ with 3R phase into $CuCrO_2$ with 2H phase at elevated pressure (> 300 bars) as reported for other compounds [148]. Low pressure (200–300 bars) favors the pure phase stability compare to elevated pressure (> 500 bars) [147]. To analyze the pressure behavior, pressure-molarity phase diagram is plotted (figure 2.25) at 300 °C. Extreme low pressure region (< 200 bars) corresponds to the impurity phase zone. Colored region corresponds to the pressure region that leads to the formation of phase pure product. Further high pressure losses phase purity and gives rise to very minor impurity phase of $CuCr_2O_4$ keeping chromium into stable Cr^{+3} oxidation state.

2.2.5.3. Conclusion

In summary, we have first reported the synthesis of $CuCrO_2$ with delafossite structure (3R) by hydrothermal method. Powder XRD confirms the purification of $CuCrO_2$ phase with delafossite structure. SEM images shows microspheres with

diameter of about 2-4 μm. The micron size sphere appear a bunch of pure $CuCrO_2$ platelets of size ranges from 0.7 μm to 3 μm. Role of reaction temperature, reaction time, molarity and pressure is thoroughly discussed and reveal increase in reaction time, molarity and temperature increases the solubility of reactants and rate of conversion into their corresponding hydrate species. Effect of pressure study reveals that there was slight evidence of phase transformation ($CuCrO_2$ 3R phase into 2H phase) at elevated pressure. Samples prepared in the pressure regime between 200 to 300 bars leads to the formation of single crystal phase of $CuCrO_2$. The developing of the 2H phase could be correlated with the increase in pressure and future work will be focused on synthesis of pure $CuCrO_2$ with 2H phase (not achieved till date) under high pressure up to 2000 bars.

Finally, we conclude we prepared Cu based delafossite compounds by using 2 newly developed synthesis method: hydrothermal and monomode microwave. In order to improve electrical properties of Cu based delafossite compound, it is necessary to obtain a well sintered and high dense pellet. Thus, crystallite size and shape plays an important role in formation of high dense pellets. Therefore, hydrothermal method with crystallite size < 1 – 3 μm may enhance the electrical properties of Cu based delafossite compare to monomode microwave method. In comparision to hydrothermal method monomde synthesis method proved to be a fast method to obtain the Cu based delafossite compounds.

2.3. $CuCr_{1-x}V_xO_2$ ($0 \leq x \leq 0.5$): spin induced ferroelectricity to spin glass system

2.3.1. Introduction to ordered and disordered magnetism

Spin glasses (SG) are dilute magnetic alloys where the interactions between spins are randomly ferromagnetic or anti-ferromagnetic, and are considered as paradigmatic examples of frozen disorder. The presence of disorder (the random interactions between the spins) induces magnetic frustration and a greater difficulty for the system is to find optimal configurations. As a consequence, these systems exhibit non trivial thermodynamic and dynamic properties, different and richer than those observed in ordered system. The term "glass" refers to the fact that its magnetic disorder brings to mind the positional disorder of a conventional, chemical glass, e.g., a window glass. Figure 2.26 shows the schematic representation of randomly ordered spins (figure 2.26.a) and ordered antiferromagnetic spins (figure 2.26.b). Spin glasses can be modelled using Ising-like Hamiltonians where the bonds between spins can be positive or negative at random. Due to the heterogeneity of the couplings, there are many triples or loops of spin sequences which are frustrated, that is for which there is no way of choosing the orientations of the spins without frustrating at least one bond. As a consequence, even the best possible arrangement of the spins comprises for a large proportion of frustrated bonds. More importantly, since there are many configurations with similar degree of frustration one may expect the existence of many local minima of the free energy. In mean field models the effects of frustration are enhanced, and the thermodynamic scenario that emerges is novel and surprising. As compared to ordinary ferromagnets, where two pure states are present below the transition, mean field spin glasses exhibit at low temperature a

complex structure of infinitely many equilibrium states, organized in a hierarchical structure. At a formal level, the thermodynamics can be exactly solved using the Replica Theory, a mathematical approach that allows to appropriately dealing with the quenched disorder present in the Hamiltonian. The static order parameter is a function describing the structure in phase space of the (many) pure equilibrium states.

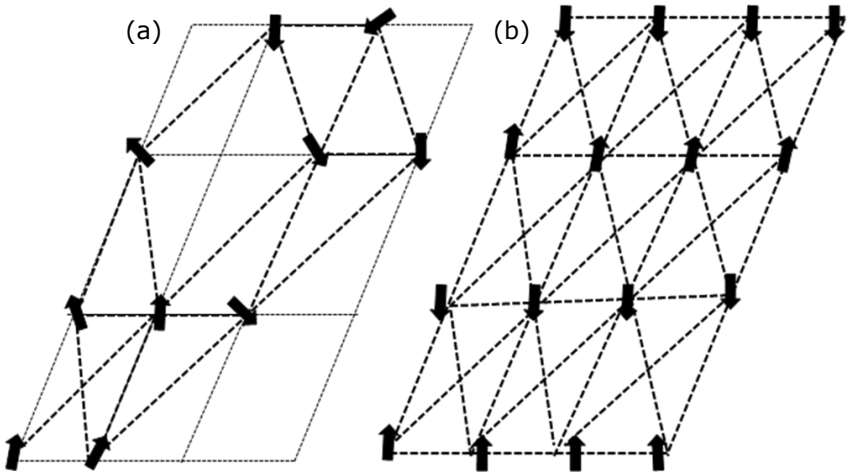

Figure 2.26. Schematic representation of (a) the random spin structure of a spin glass. (b) the ordered one of antiferromagnetic.

In spin glass system as we discussed above, the disorder is explicitly present in the Hamiltonian, typically under the form of random couplings J among the degrees of freedom σ,

$$H = H(\sigma; J) \tag{2.2}$$

The disorder J is completely specified by its probability distribution $p(J)dJ$ which is the same for each different coupling constant in the system. A famous example is the Edwards-Anderson model [150],

$$H = \sum_{<i,j>} J_{ij}\sigma_i\sigma_j \tag{2.3}$$

where the spins $\sigma_i = \pm 1$ are the degrees of freedom, and the couplings J_{ij} are Gaussian random variables. This is a finite dimensional model, since the sum is performed over nearest-neighbour spins. The disorder is quenched, meaning that the J is constant on the time scale over which the σ fluctuates. This will have a

crucial consequence on the way we will have to perform the averages over J, compared to σ. Also we discussed that spin-glasses are systems with quenched disorder that creates frustration i.e it becomes impossible to satisfy all the couplings at the same time, as it would be in a ferromagnetic system. Formally a system is frustrated if there exists a loop on which the product of the couplings is negative (for example figure 1.2 in chapter 1 describes magnetic frustration in triangular antiferromagnetic compound). In a frustrated loop, if we fix an initial spin, and starting from it we try to chain-fix the other spins one after the other according to the sign of the couplings, we are bound to return to the initial spin and flip it. The only way to avoid frustration is to consider a lattice where there are no loops. Frustration is the main reason for the proliferation of metastable states in disordered systems.

Ageing: At low temperature spin glasses also exhibit a non trivial dynamical behaviour, with off-equilibrium dynamics and ageing. At low temperature a unique situation arises when spins glasses are cooled and allowed to sit below its freezing temperature for a longer period of time. This phenomenon is called ageing in spin glasses. Aging is fully reinitialized by heating the sample above the glass transition temperature. It corresponds to the slow evolution of the system towards equilibrium, starting at the time of quench below glass transition temperature. Many aspects of aging are similar to the "physical ageing" phenomena that have been characterized in the mechanical properties of the glassy polymers [151]. The ageing of a spin glass, which obeys the same scaling laws as the ageing of glasses and polymers, thus consists of local rearrangements of spins that allow it to slowly approach equilibrium, but without ever actually reaching it. In this case magnetic susceptibility χ is being measured, i.e. the weak magnetisation that develops in response to the application of a weak alternating field. More precisely, it is the 'delayed' (or 'out of phase') component χ'' of χ that is presented here. It is zero in the paramagnetic phase (as all the spins respond in phase to the alternating field) but it is non-zero in the spin glass phase, which appears at low temperature and so is characterised by a delayed response.

In recent years, aging dynamics of SG systems has been extensively studied theoretically [152] and experimentally [153]. The low temperature SG phase below a SG freezing temperature T_g exhibits intriguing non-equilibrium dynamics which is characterized by the chaotic nature and ageing behaviour. The zero-field SG never reaches equilibrium. The non-equilibrium character can be experimentally observed from an age-dependence of the magnetic response. When the SG system is quenched from a high temperature above the SG transition temperature T_g to a low temperature T below T_g (this process is called the zero-field cooled (ZFC) aging protocol), the initial state is not thermodynamically stable and relaxes to more stable state. The aging behaviours depend strongly on their thermal history within the SG phase. The rejuvenation (chaos) and memory effects are also significant features of the aging dynamics. These effects are typically measured from the low frequency AC magnetic susceptibility. The SG phase is also susceptible to any perturbation in form of temperature or field changes, which consequently, if large enough, effectively reinitializes the ageing process (temperature chaos). Both aging behaviour and chaotic nature of the low temperature SG phase have been viewed first as additional difficulty in the understanding of SG's. However, it proved to be a key feature of the SG behaviour, offering the unique opportunity to explore the nature of the SG phase. Such an aging dynamics of SG phase is explained mainly in

terms of a real-space picture (the droplet model) [154]. In this picture, the SG coherence length for equilibrium SG order, grows up slowly in aging processes. The scaling properties of age-dependent macroscopic susceptibility can be described by a growing coherence length $L_T(t)$. The droplet model also predicts the following two key features.

(i) The equilibrium SG states at two temperatures with the difference DT are uncorrelated in length scales larger than the overlap length ΔT, i.e., so-called temperature (T)-chaos nature of the SG phase.
(ii) In the equilibrium and thermodynamic limits the SG phase is broken by a static magnetic field H of infinitesimal strength, thereby introduced is the crossover length L_H.

Also, when there is a majority of the ferromagnetic interactions and a minority of the antiferromagnetic interactions to create substantial spin frustration effect, the situation may drastically change. Such random spin systems are called a re-entrant ferromagnet. The time dependent magnetization study is also main area of research in spin glass system because of great application in sensor technology and memory devices.

Time-dependent magnetization: Slow spin dynamics is another characteristic feature of the glassy ground state. The effects of time dependence of the magnetization process in magnetic materials have attracted significant attention for its importance in theory and application. As we mentioned above, these time dependence magnetization study is highly relevant to sensor applications and magnetic-recording technology, in which fast writing and thermal stability of the written bits are important [155]. The thermally activated barrier hopping process originates the magnetization reversal at constant applied field, also known as magnetic after-effect (MAE). The thermally activated barrier hopping processes of a flat energy barrier distribution can be described by following equation 2.5 [156].

$$M(t) = M_0 - M_0 * S * \ln\left(1 + \frac{t}{t_0}\right) \tag{2.5}$$

where M_0 is the initial remanent magnetization, S is the magnetic viscosity that depends on the magnetic field, temperature and material, t_o is a reference time which depends on the sample and measurement procedure. S(T) is negative for measurements with increasing field and positive for measurements with decreasing field. Furthermore, the wait time dependence of the magnetic relaxation is illustrated by the relaxation rate $S(t)$ [156] defined by the following equation 2.6.

$$S(t) = \frac{1}{H}\frac{\partial M(t)}{\partial \ln(t)} \tag{2.6}$$

It is readily seen that the relaxation rate $S(t)$ attains a characteristic ageing maximum at an elapsed time very close to t_w, where there exists an inflection point in the $M(t)$ curves, and it shifts to longer observation times for longer values of t_w.

As we discussed in chapter 1, delafossite-type transition-metal oxides with general formulae ABO_2 crystallizes mainly in rhombohedral or hexagonal crystal

structure. The structure consists of a layered triangular lattice in which the B^{3+} magnetic cations form a triangular network which orders antiferromagnetically only at low temperature for example $CuCrO_2$ show an antiferromagnetic transition at ~ T_N = 24 K [113] and $CuFeO_2$ at ~ T_N = 14 K [157], respectively. This magnetic ordering is responsible for the origin of ferroelectricity at low temperature because of this these oxides belong to the family of the so-called spin induced ferroelectrics. It is also well known that substitution of trivalent diamagnetic cations for Fe^{3+} changes the antiferromagnetic state and induces ferroelectricity in $CuFeO_2$. This layered triangular lattice causes the magnetic spin frustration to trigger the spin-glass (SG) like magnetic behaviour. A continuous research is going on in the search for new multiferroic materials. The symmetry of the structure is of key source and the possibility offered by magnetic structures to break the inversion symmetry has been used to discover numerous spin induced ferroelectrics and strong magnetoelectric (ME) coupling [10]. In contrast to these results, coupling between a spin glass and ferroelectricity has not been studied so extensively [32]. Cationic disorder induced by substitution on one crystallographic site may generate magnetic and/or electric glassiness depending on the atoms involved. Disorder is in fact well known to be responsible for glassy properties [158], as shown in $(Sr,Mn)TiO_3$ [159].

Recent study of $CuFe_{0.5}V_{0.5}O_2$ spin glass show the polarization and magnetodielectric (MD) coupling in the system [32]. The vanadium for iron substitution in the $CuFeO_2$ delafossite destroys the long range magnetic ordering at low temperature. Similarly, vanadium for chromium substitution in the $CuCrO_2$ that is an antiferromagnetic compound (T_N ~ 24 K) and also exhibit spin induced ferroelectricity [30,113] reveals that the V^{3+} for Cr^{3+} substitution creates a disorder that favours short range magnetic order at low temperature, as reported by Nagarajan et al [42] and Ataoui et al [43], in agreement with pioneer works of Goodenough [160]. The Cr/V topological disordering at the B site favors random magnetic interactions of three types: strong antiferromagnetic ones (Fe–Fe), weaker antiferromagnetic ones (V–V) and ferromagnetic ones (V–Fe). This random exchange situation creates a disordered magnetic state at low temperature.

Here in this work, we have investigated an effect of V^{3+} substitution at the Cr^{3+} sites on structural, magnetic and dielectric properties in $CuCrO_2$, and reveal that V^{3+} substitution induces disordered magnetism (spin glass behavior) at the expense of ferroelectric nature. A $CuCr_{1-x}V_xO_2$ ($0 \leq x \leq 0.5$) series of polycrystalline samples is studied in order to determine the critical composition range exhibiting intermediate state of ferroelectricity and disordered magnetism i.e to find out the critical composition where the system becomes disordered (SG).

2.3.2. Experimental details

Polycrystalline series of samples of $CuCr_{1-x}V_xO_2$ ($0 \leq x \leq 0.5$) were prepared by solid-state reaction by mixing Cu(Sigma-Aldrich, > 99%), CuO(Sigma-Aldrich, > 99%), Cr_2O_3 (Sigma-Aldrich, > 99%) and V_2O_5 (Sigma-Aldrich, > 99%) within the stoichiometric ratios (1+2x): (1-2x):(1-x):(x). Powders (2 g) of Cu, CuO, Cr_2O_3 and V_2O_5, weighted in the above mentioned stoichiometric ratio. Equation 2.7 shows the balanced chemical reaction used for preparation of series of samples. The weighted precursors was carefully crushed, mixed together by using ball milling machine for 2 minutes and then, manually ground in an agate mortar for 30 minutes. 2 g of crushed powder were then pressed in the shape of the pellets (8 mm diameter and

4 mm thick) and placed in a platinum (Pt) crucible to avoid the intrusion of any impurity from the quartz tube used for vacuum sealing. The Pt crucible was then vacuum sealed in a silica quartz tube and fired at 1100 °C for 48 h following a slow cooling to room temperature. The pictorial representation of sample preparation is shown in figure 2.27. Also, we prepared pure parental $CuCrO_2$ compounds (which was prepared in air at 1200 °C for 12 hrs of reaction time) for comparative study.

$$(1+2x)\ Cu + (1-2x)\ CuO + (1-x)\ Cr_2O_3 + xV_2O_5 \rightarrow 2CuCr_{1-x}V_xO_2\ (0 \leq x \leq 0.5) \quad (2.7)$$

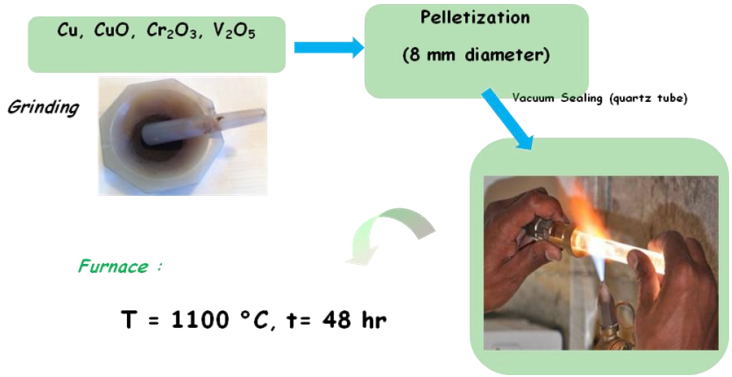

Figure 2.27. Schematic representation of sample preparation steps involved in preparing series of samples of the series $CuCr_{1-x}V_xO_2$ ($0 \leq x \leq 0.5$).

The quality of all samples were registered by powder X-ray diffraction (XRD) data collected by using a PANalytical X'pert Pro diffractometer (Cu K_α, $10^\circ \leq 2\theta \leq 110^\circ$) which confirmed that the samples are single phase, well crystallized, and demonstrate the expected delafossite structure with the 3R phase group. The structure was then refined by using the FullProf software [66]. The temperature dependence of magnetic properties was measured with a superconducting quantum interference device (SQUID-Quantum Design) magnetometer. The M (T) data were recorded in a magnetic field of 0.1 T from 5 to 300 K, in zero field cooled (zfc) and field cooling (fc) modes. The ac magnetic susceptibility (χ', χ'') measurements were performed at different frequencies (10 Hz–10 kHz) using a Quantum Design physical properties measurement system (PPMS). The dielectric measurement was made on a thin parallel plate capacitor. Contacts were made by using silver paste. The dielectric measurements were performed using an Agilent 4284A LCR meter at four different frequencies (5–100 kHz) during cooling and warming (2 K min^{-1}). The polarization was measured with a Keithley 6517A electrometer. A static electric poling field of 135 kV m^{-1} was applied during cooling to align the electric dipoles and removed at 8 K. A waiting time of 5000 s was applied before measuring the polarization versus temperature upon warming (5 K min^{-1}).

2.3.3. Structural and magnetic property analysis

2.3.3.1. Structural analysis

Structural and phase analysis has shown that all samples have characteristic of the 3R delafossite and the structure is refined in the *R-3m* space group (n° 166) and includes no impurity phases at higher content of vanadium (V) except for $CuCr_{1-x}V_xO_2$ ($0.04 \leq x \leq 0.18$) where minor peak of VO_2 (< 1% weight) coexists with the primary phase. Figure 2.28 shows the room temperature powder X-ray diffraction patterns of $CuCr_{1-x}V_xO_2$ ($0 \leq x \leq 0.5$). The powder diffraction patterns indicate the absence of any structural phase transition in the whole investigated range of the V^{3+} content. The lattice parameters changes linearly with increasing x: cell parameter *a* and *c* increases with increase in x. As a result the unit cell volume increase. Figure 2.29 show the variation in lattice parameters obtained by FullProf refinement. These results are consistent with the results of the earlier studies for a large V-doping range [43].

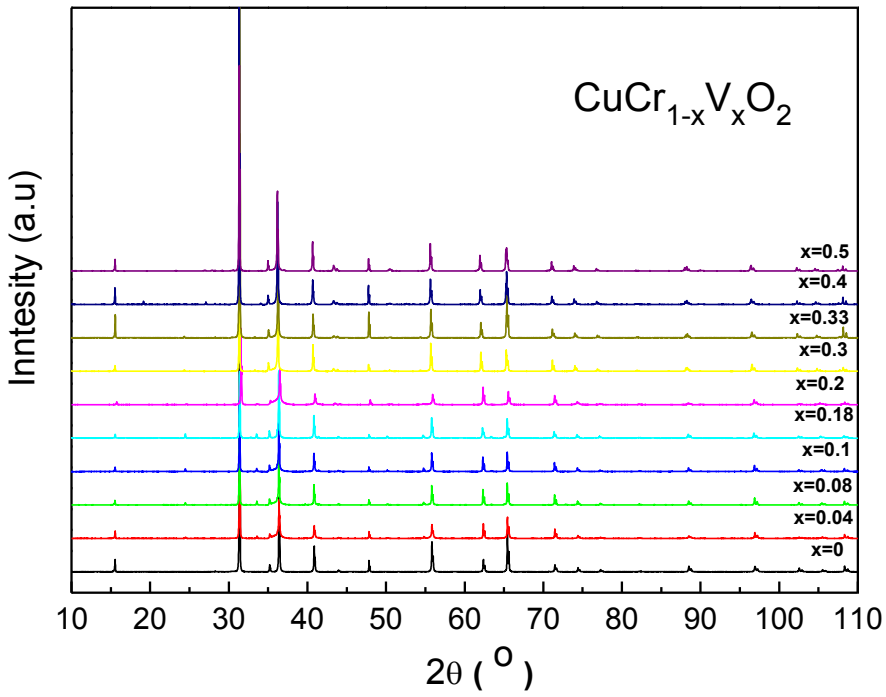

Figure 2.28. (Color online). Room temperature X-ray powder diffraction patterns of $CuCr_{1-x}V_xO_2$ ($0 \leq x \leq 0.5$).

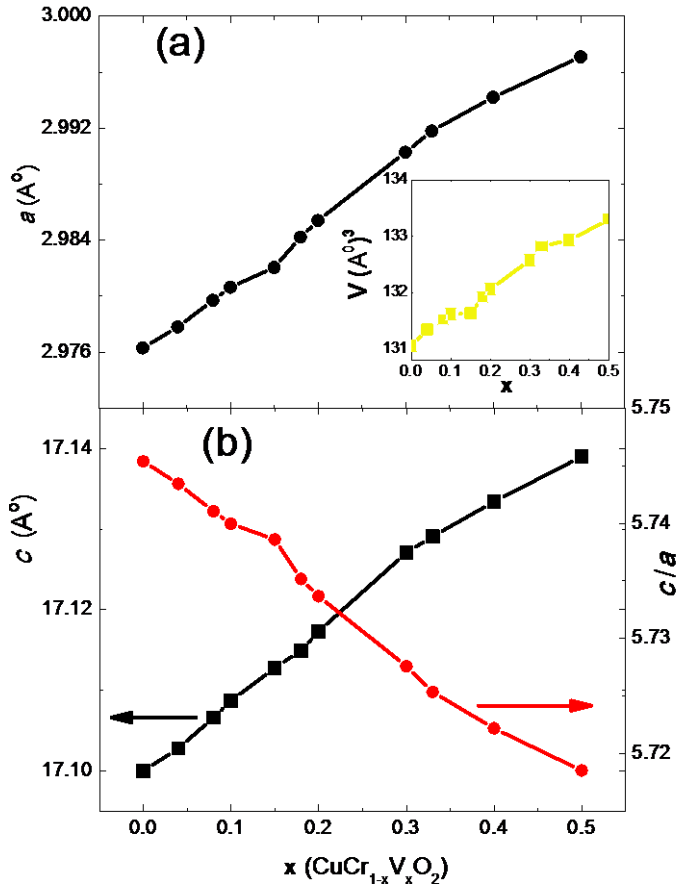

Figure 2.29. Refined unit cell parameters '*a*' and '*c*' as a function of V^{3+} content x is shown in (a) and (b), respectively. Inset (a) shows x dependence of the corresponding unit cell volume (closed squares, left y-axis). Right y-axis of (b) corresponds to x dependence of *c/a* (closed circles).

2.3.3.2. Magnetic property characterization

2.3.3.2.1. dc magnetization study

In order to probe the effect of the vanadium (V) substitution upon the magnetic transition of $CuCrO_2$, temperature dependent magnetic susceptibility (χ_{dc} = M/H) curves for the samples of the series $CuCr_{1-x}V_xO_2$ ($0 \le x \le 0.5$) were recorded in the zero field cooled (ZFC) and field cooled (FC) modes. A magnetic field of 0.1 T was applied during the measurements. The measurements were done in a temperature range of 5 K to 300 K. Figure 2.30 summarizes the temperature dependence magnetization curves M_{ZFC} (T) and M_{FC} (T) for ZFC and FC modes respectively. A broad anomaly (varies with x) is observed in the lower V^{3+}

substituted samples ($0 \leq x < 0.18$) where as in higher V^{3+} substituted samples ($0.18 \leq x \leq 0.5$), M_{ZFC} (T) exhibits a cusp at low temperature (< 15 K) and coalesces with M_{FC} (T) at a slightly higher temperature. M_{FC} (T) remains temperature independent below magnetic transition temperature. Inset of figure 2.30.a shows the enlargement in the magnetic transition temperature zone up to 30 K. This behavior is a reminiscent of spin glass [158].

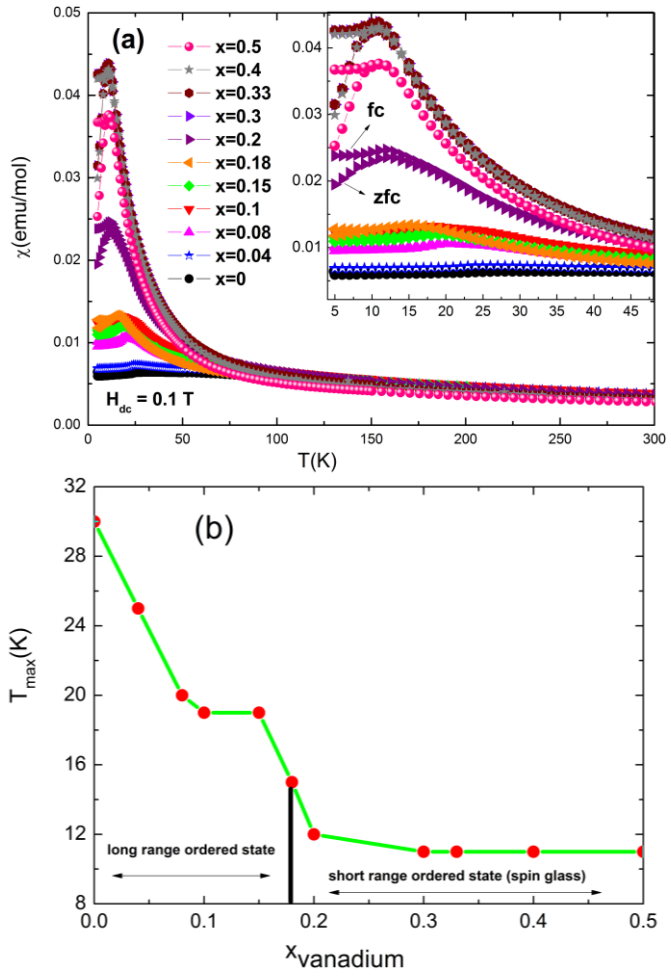

Figure 2.30. (Color online). Main panel (a) Temperature dependence of dc molar magnetic susceptibility (χ) measured in zero field cooled (ZFC) and field cooled (FC) modes under magnetic field of 0.1 T for samples of the series $CuCr_{1-x}V_xO_2$ (x values are labeled in the graph). Inset of (a) Enlargement in the transition temperature zone up to 30 K. (b) Variation of $T_{\chi(max)}$ (K) (the temperature at which maximum dc magnetic susceptibility is measured) with the composition of vanadium (x).

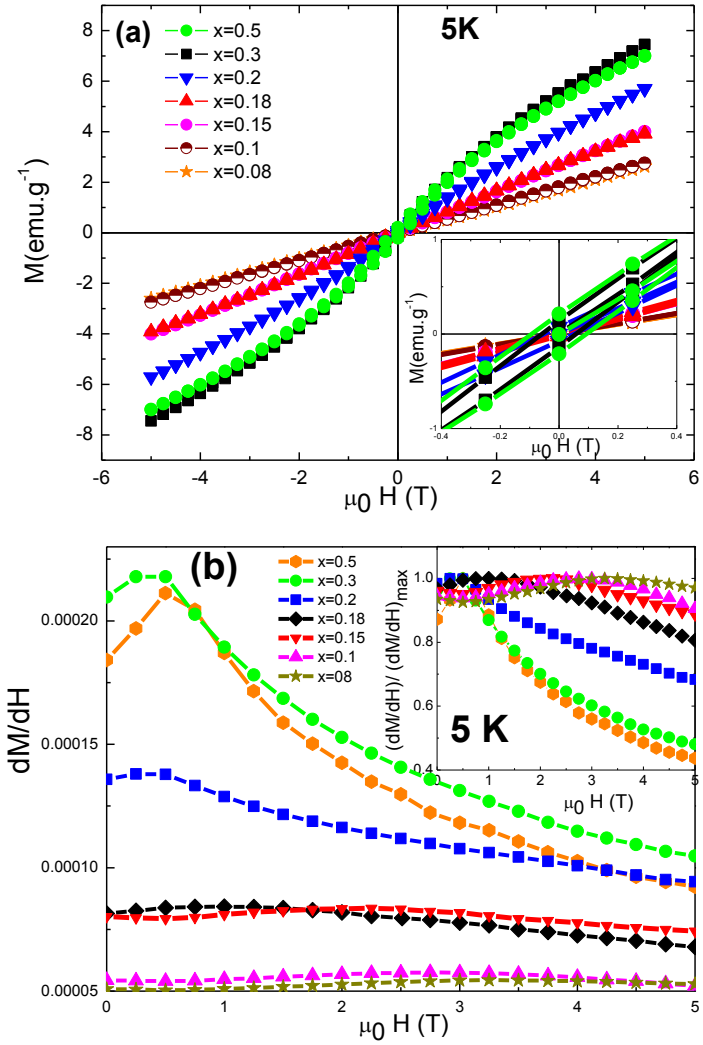

Figure 2.31. (Color online). (a) Isothermal magnetization as a function of magnetic field applied at constant temperature 5 K for the series of sample $CuCr_{1-x}V_xO_2$ (x=0.08, 0.1, 0.15, 0.18, 0.2, 0.3, 0.5). Inset (a) show the enlargement view of isothermal magnetization suggests the clear hysteresis for sample (S shape) with composition $x \ge 0.18$. (b) Derivative curve dM/dH for $CuCr_{1-x}V_xO_2$ (x=0.08, 0.1, 0.15, 0.18, 0.2, 0.3, 0.5). Inset (b) Normalized curves of dM/dH calculated by $(dM/dH)/(dM/dH)_{max}$.

The strong competing interaction between Cr^{3+} and V^{3+} cations gives rise to three types of magnetic interactions: strong antiferromagnetic interaction in Cr^{3+}-Cr^{3+}, weak antiferromagnetic interaction in V^{3+}-V^{3+}, and ferromagnetic interaction in Cr^{3+}-V^{3+}. These competing interactions are responsible for the origin of disordered magnetic behavior in $CuCr_{1-x}V_xO_2$ for $0.18 \le x \le 0.5$. The temperature ($T_{\chi(max)}$ (K)) at which maximum dc magnetic susceptibility is recorded was deduced from the dc

magnetization data on M_{ZFC} (T) curves. Figure 2.30.b shows the variation in $T_{\chi(max)}$ as a function of V^{3+} substitution in $CuCrO_2$. $T_{\chi(max)}$ decreases abruptly with increase in V^{3+} content for samples of series $CuCr_{1-x}V_xO_2$ ($0 \leq x < 0.18$) and remains almost constant (~ 11 K) for higher V^{3+} substitution in $CuCr_{1-x}V_xO_2$ ($0.18 \leq x \leq 0.5$). This illustrates that increase in V^{3+} content increases the randomness in the system. Figure 2.30 also illustrates that in low vanadium substituted samples ($0 \leq x < 0.18$) there exist a dominant long range ordering but in high vanadium substituted samples ($0.18 \leq x \leq 0.5$) short range ordering or random interactions of spins appears at the expense of long range ordering.

We also studied the isothermal magnetization (M) versus magnetic field (H) curves to get more insight of the magnetic properties for the samples of the series $CuCr_{1-x}V_xO_2$ ($0 \leq x \leq 0.5$). Figure 2.31.a demonstrates the isothermal magnetization (M) as a function of magnetic field (H). The data was recorded at a constant temperature of 5 K. For lower composition samples of $CuCr_{1-x}V_xO_2$ ($0 \leq x < 0.18$), M (H) almost remains linear (figure 2.31.a) like pristine $CuCrO_2$ suggesting the presence of long range ordering. The M-H curve of high vanadium content samples i.e. x=0.18, 0.2, 0.3, 0.5 are S shaped and different from the low vanadium content samples. This supports the argument that there exists different magnetic ground state at lower and higher V compositions. In order to get more insight of M-H curves, dM/dH is plotted for samples of x = 0.08, 0.1, 0.15, 0.18, 0.2, 0.3, 0.5 (figure 2.31.b). A clear bump is observed in dM/dH at a characteristic magnetic field which is known as H_{flop} and H_{flop} decreases with increasing V content. The S shape exists in M (H) curve (figure 2.31.a) and temperature independent magnetization (M_{FC} (T)) below 15 K (figure 2.30.a) for the samples of the series $CuCr_{1-x}V_xO_2$ ($0.18 \leq x \leq 0.5$) arrests characteristic of a spin glass and the lack of saturation reflects the randomness of the magnetic moments [161].

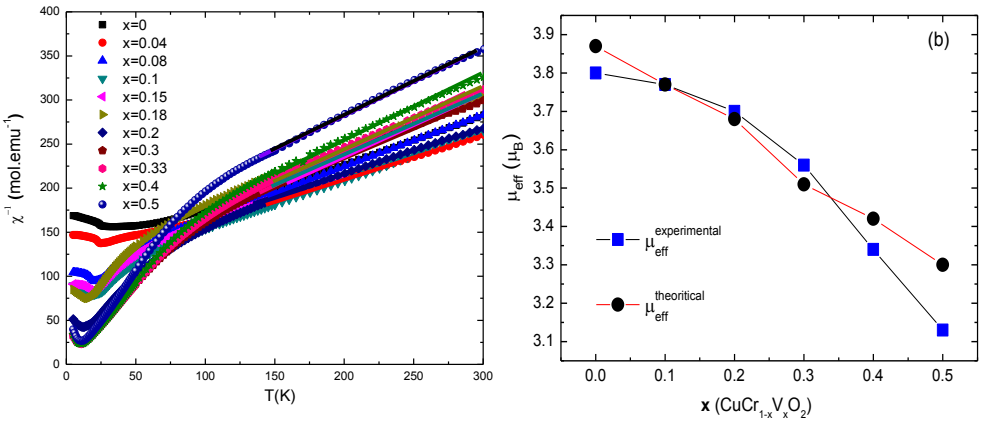

Figure 2.32. (Color online). (a) Temperature dependence of the inverse molar magnetic susceptibility (χ^{-1}) of $CuCr_{1-x}V_xO_2$ ($0 \leq x \leq 0.5$). The solid line corresponds to the Curie-Weiss law fitting in the paramagnetic region (150 K-300 K). (b) The theoretical values (closed circles; calculated from the formulae $\mu_{SO} = \{(1-x)\ \mu^2_{Cr3+} + x\ \mu^2_{V3+}\}^{1/2}$) and experimental values (closed squares; deduced from inverse magnetic susceptibility data (χ^{-1}) fitted in paramagnetic region) of the effective paramagnetic moment (μ_{eff}) for series of samples of $CuCr_{1-x}V_xO_2$ ($0 \leq x \leq 0.5$).

Figure 2.32.a shows the temperature dependence curves of the inverse magnetic susceptibility (χ^{-1}) for series of samples of $CuCr_{1-x}V_xO_2$ ($0 \le x \le 0.5$). All the compounds in high temperature region (> 150 K) obey Curie-Weiss behavior, $\chi = [C / (T-\theta_{cw})]$. The experimental effective magnetic moment for all samples is calculated from least squares fit in the linear region (>150 K). The linear fitting of inverse magnetic susceptibility in the paramagnetic region gives the slope and intercept value. The Curie Weiss constant (θ_{cw}) value was calculated by dividing the intercept value by slope value. Also, the experimental effective magnetic moment was calculated by $\mu_{eff}^{experimental}$ = 2.828 (slope value)$^{1/2}$.Assuming that the samples contain only Cr^{3+} (total spin, S=3/2) and V^{3+} (total spin, S =1), the spin only magnetic moment μ_{SO} which is also known as theoretical effective magnetic moment ($\mu_{eff}^{theoritical}$) for all the samples of the series of $CuCr_{1-x}V_xO_2$ ($0 \le x \le 0.5$) is calculated by using the formulae ($\mu_{eff}^{theoritical} = \{(1-x)\ \mu^2_{Cr3+}+x\ \mu^2_{V3+}\}^{1/2}$), where $\mu = [4S(S+1)]^{1/2}$. The experimental values of the magnetic moment of $CuCr_{1-x}V_xO_2$ ($0 \le x \le 0.5$) is comparable to the spin-only value (shown in figure 2.32.b) for the Cr^{3+}/V^{3+} combination indicating that Cr and V ions are present in their trivalent high-spin states. Table 2.10 shows the fitting parameters deduced from the DC inverse magnetic susceptibility data for $0 \le x \le 0.5$. The large negative values of θ_{cw} indicate the presence of large antiferromagnetic fluctuations for the lower V^{3+} substituted samples [134]. The decrease in θ_{cw} value with V^{3+} substitution in $CuCrO_2$ is an indicative of decrease in antiferromagnetic interactions.

Table 2.10. Parameters Extracted from Fitting of DC Inverse Magnetic Susceptibility (χ^{-1}) Data

x	$T_{\chi(inflection)}$ (K)	$\mu_{eff}^{experiemtnal}$ (μ_B)	$\mu_{eff}^{Theoritical}$ (μ_B)	θ_{cw} (K)	$\theta_{cw}/T_{\chi(inflection)}$
0	24	3.8	3.87	-213	-8.87
0.1	16.4	3.77	3.77	-210	-12.80
0.2	10.08	3.7	3.68	-207	-19.16
0.3	08.81	3.56	3.59	-180	-20.43
0.4	08.81	3.34	3.42	-161	-18.27
0.5	08.81	3.13	3.3	-149	-16.91

2.3.3.2.2. ac magnetization study

For further confirmation of spin glass (SG) like behavior in samples of $CuCr_{1-x}V_xO_2$ for $0.18 \le x \le 0.5$, the temperature dependent ac magnetic susceptibility measurement χ'_{ac} (T, f) were performed in zero dc magnetic field (H_{dc} = 0 Oe) at different frequencies ranging from 10 Hz up to 10 kHz, using a PPMS facility. The amplitude of the ac magnetic field H_{ac} was ~ 10 Oe. Figure 2.33, summarizes the χ'_{ac} (T) curves for higher V^{3+} substituted samples ($0.18 \le x \le 0.5$). As can be seen from the figure 2.33, a sharp cusp is visible in the in-phase

component, χ'_{ac} (T), for all samples. Its temperature, T_f (temperature of the maximum in χ'_{ac} (T)), is always slightly larger than the temperature of the maximum in the dc-χ_{dc} (T), $T_{\chi(max)}$. All samples for $0.18 \leq x \leq 0.5$ shows frequency dependent peaks in the ac susceptibility measurements, i.e., as the frequency is increased, T_f shifts to higher values associated with a decrease in the magnitude of χ_{ac} (T). The plot of the imaginary component of the ac magnetic susceptibility (inset of a-d in figure 2.33) show that the maximum of χ''_{ac} (T) appears at a lower temperature than the maximum of χ'_{ac} (T), and is also frequency dependent. This kind of frequency dependant ac magnetic susceptibility behavior strongly supports the argument of true spin glass in high vanadium substituted samples ($0.18 \leq x \leq 0.5$) [158, 161, 162].

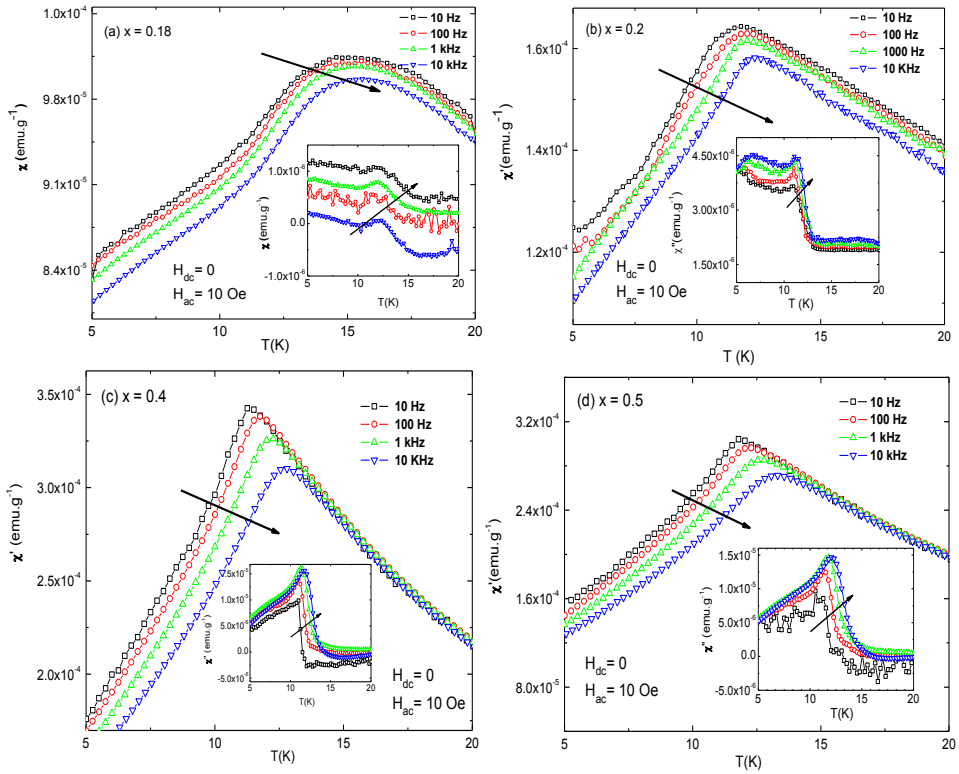

Figure 2.33. (Color online). The real χ'_{ac} and imaginary χ''_{ac} (main panel and inset of (a), (b), (c), and (d) respectively) components as a function of temperature in the vicinity of the transition to the spin glass phase of $CuCr_{1-x}V_xO_2$ ($0.18 \leq x \leq 0.5$) measured at different frequencies (10 Hz-10 kHz).

To further investigate the existence of a true spin glass behavior or of superparamagnetic behavior in series of $CuCr_{1-x}V_xO_2$ ($0.18 \leq x \leq 0.5$), we have analyzed the frequency dependence of the peak in χ'_{ac} (T, f) using the method

previously developed by Breard et al., [163] starting from the dynamic scaling theory, [164] which predicts a power law of the form $\tau = \tau_o \{(T_f - T_g)/T_g\}^{-z\nu}$ where τ_o is the shortest relaxation time available to the system, i.e., the microscopic flipping time of the fluctuating entities, T_g is the underlying spin glass transition temperature determined by the interactions in the system, z is the dynamic critical exponent, and ν is the critical exponent of the spin correlation length. The actual fittings were done using the equivalent logarithmic form of the power law i.e. in $\tau = \ln\tau_o - z\nu\ln\{(T_f - T_g)/T_g\}$. The value of T_g was adjusted in order to get the best linearity in a ln τ versus $\ln\{(T_f - T_g)/T_g\}$ plot. $z\nu$ and τ_o were derived from the parameters of the linear fitting. The remarkable linearity obtained for the plots of ln τ versus $\ln\{(T_f - T_g)/T_g\}$ using the fit parameters, shown in figure 2.34, indicates that these samples well obey the behavior expected for a spin glass like system [163,165,166]. Similar fittings were performed for all the other samples of the series, and the extracted parameters of this study have been listed in table 2.11.

Quantifying further the frequency dependence of χ'_{ac} (T, f) by the phenomenological parameter $p = (\Delta T_f/T_f)/(\Delta \log f)$, the calculated value of p for the series of $CuCr_{1-x}V_xO_2$ ($0.18 \le x \le 0.5$) lies in the range of ~ 0.04. In case of superparamagnetism, the value of p is higher (~ 0.1) [167]. This discards the possibility of superparamagnetic behavior in high vanadium substituted samples ($0.18 \le x \le 0.5$). For all samples of the series $CuCr_{1-x}V_xO_2$ ($0.18 \le x \le 0.5$) the spin relaxation time τ_o lies in the range of values typical of spin glass (10^{-10} s) [168], and the $z\nu$ values lies between 4 and 11. Thus, the power law model provides a satisfactory description of ac susceptibility data.

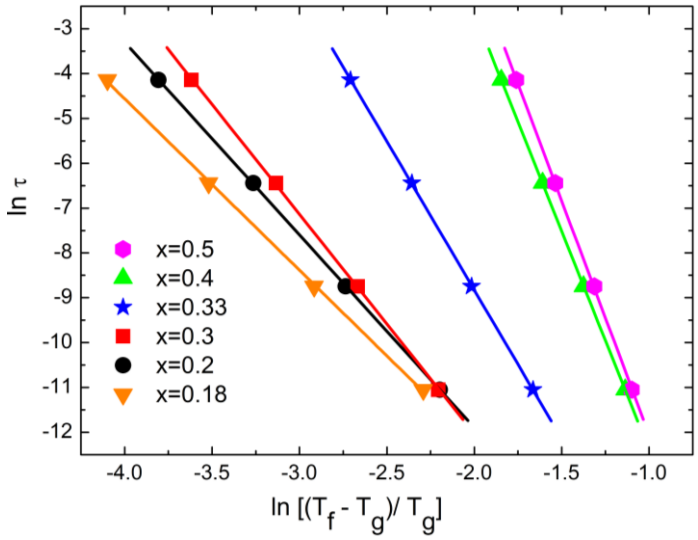

Figure 2.34. (Color online). ln(τ) as a function of $\ln\{(T_f - T_g)/T_g\}$ of (a) $CuCr_{0.7}V_{0.3}O_2$ (closed circles) (b) $CuCr_{0.6}V_{0.4}O_2$ (closed squares). The solid line is the best fit of the power law $\ln\tau = \ln\tau_o - z\nu\ln\{(T_f - T_g)/T_g\}$.

Table 2.11. Parameters Extracted from Fitting of AC Magnetic Susceptibility Data

Concentration (x)	T_f (K) from χ'_{ac} (T) at f = 10 Hz	Spin glass transition temperature T_g (K)	spin relaxation time τ_0 (s)	p	z ν
0.18	14.08	13.85	1.46×10^{-9}	0.018	4.01
0.2	11.5	11.25	1.38×10^{-9}	0.026	4.29
0.3	11.09	10.8	3.4×10^{-10}	0.034	4.89
0.33	11.04	10.35	2.57×10^{-10}	0.035	6.62
0.4	11	9.5	2.4×10^{-10}	0.04	9.74
0.5	10.9	9.3	1.7×10^{-10}	0.038	10.43

2.3.3.2.3. Ageing and memory effects

In order to go deeper into the understanding of the interacting and/or non-interacting behavior of the spins, time-dependent magnetization studies under ZFC protocols have been performed. It has been suggested [169-170] that the ZFC memory measurements could play a vital role in characterizing and distinguishing between frustrated and glassy magnetic states. In order to investigate the aging effect, we performed ZFC protocol on sample $CuCr_{0.7}V_{0.3}O_2$ to check single and double ageing effect. In single ageing ZFC protocol, the sample was cooled from a temperature T=100 K to a temperature T=5 K in zero field. Then the normal ZFC magnetization was recorded as a function of temperature in magnetic field H=100 Oe (reference curve). Again sample was cooled in ZFC mode from 100 K to 8 K with same rate as in reference curve and then let the system to wait for t_w=10 hrs (aging) at wait temperature, T_w=8 K and then again cool the sample down to 5 K. After reaching 5 K, the magnetization was measured in an applied field of 100 Oe while warming with same rate as in reference curve. Similar protocol was used for double ageing effect except the wait time and temperature. In double ageing protocol the system was allowed to wait at two different temperature T_{w1}=6 K and T_{w2}=9 K for same wait time t_w=6 hrs aging. Figure 2.35 shows the ZFC curves for the $CuCr_{0.7}V_{0.3}O_2$ sample, both after normal (without stops) and stop cooling procedures. It can be observed that the system remembers the stop temperature and show a broad dip at 8 K (for single aging) and at 6 K and 9 K for double aging. Also, it shows rejuvenation at higher temperature which proves the aging and memory effect in $CuCr_{0.7}V_{0.3}O_2$ sample. Inset of figure 2.35.a-b shows the numerical difference between the reference (normal) ZFC curve and the corresponding curves obtained after stop cooling protocol in both cases single and double aging. The memory and aging effects in ZFC experiments of $CuCr_{0.7}V_{0.3}O_2$ sample confirms the glassy magnetic state. Similar behavior was reported for other different types of compound [161,171,172].

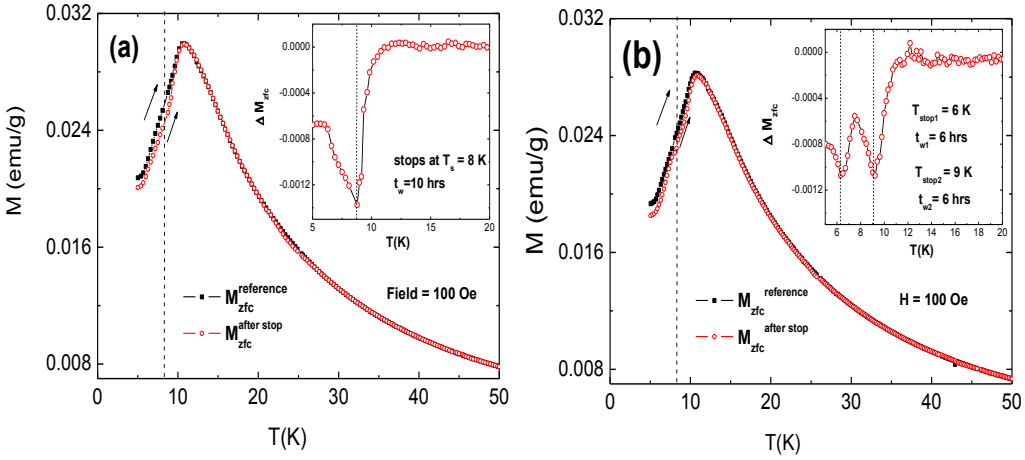

Figure 2.35. (a) (Color online). ZFC magnetization curve (magnetic field=100 Oe) after usual cooling (closed squares) and stop cooling protocols (open circles) recorded after a wait time t_w = 10 hrs at stop temperature T_s = 8 K for sample $CuCr_{0.7}V_{0.3}O_2$. Inset: The difference between the aged and normal ZFC magnetization ($M_{zfc}^{after\ stop} - M_{zfc}^{reference}$) as a function of temperature (see text for details). **(b)** ZFC magnetization curve (magnetic field=100 Oe) after usual cooling (closed squares) and stop cooling protocols (open circles) recorded after a wait time t_w = 6 hrs at stop temperature T_s = 6, 9 K for sample $CuCr_{0.7}V_{0.3}O_2$ (double aging phenomena).

2.3.3.2.4. Time dependent magnetization study of $CuCr_{0.7}V_{0.3}O_2$

As we know spin glass system is a frozen state of spin at low temperature. Thus, they react to the applied field slowly and also the magnetization curves obtained after the ZFC procedure do not give information about the thermal equilibrium of spin glass system but rather reflect a slow increase of magnetization (and thus susceptibility) with time [173]. The underlying physics is similar to the physics that governs the decay of the remanent magnetization with time. Since the discovery of aging effects in spin glasses, much effort has gone into determining the exact time dependence of the memory decay functions. In particular, memory effects show up in the thermoremanent magnetization (TRM) (or complementary zero-field cooled magnetization), where the sample is cooled through its spin glass transition temperature in a small magnetic field and held in that particular field and temperature configuration for a waiting time t_w. At time t_w, a change in the magnetic field produces very long time decay in the magnetization. The decay is dependent on the waiting time. Hence, the system has a memory of the time it spent in the magnetic field.

DC and AC magnetization data in above section already proves the spin glass behavior in $CuCr_{0.7}V_{0.3}O_2$ sample. In this section, we probe the time dependence of the low-temperature magnetization in sample $CuCr_{0.7}V_{0.3}O_2$. Therefore, we have recorded the time dependent magnetization data of the sample at selected temperature (T = 5, 7, 8, and 9 K; temperature less than the actual

transition temperature of $CuCr_{0.7}V_{0.3}O_2$ i.e. T_N = 11 K), both in the ZFC as well as the FC protocols for a wait time tw = 600 s, 1800 s, 3600 s, and 7200 s respectively. In the ZFC mode, the sample was cooled from T = 100 K to T = 8 K in zero field; then the sample was let it this temperature for a wait time t_w = 600 s and 1800 s, after which a magnetic field of H = 100 Oe was applied and the magnetization was recorded as a function of time. In the FC mode, the sample was cooled from the temperature T = 100 K in a constant magnetic field of 100 Oe to the selected temperature (T = 5, 7, 8, and 9 K). At these temperatures, the sample was given the wait of t_w = 600 s, 1800 s, 3600 s and 7200 before the field was switched off and the decay of remanent magnetization was recorded as a function of elapsed time longer than 5000 s. After the data collection, the sample was heated to T = 50 K to remove the history dependent effects. To demonstrate the ageing effects, t_w was varied over the range 600–7200 s. The results obtained following the above-mentioned protocols for the sample $CuCr_{0.7}V_{0.3}O_2$ are shown in figure 2.36. The magnetization values have been normalized with respect to the initial magnetization obtained at time t=0.

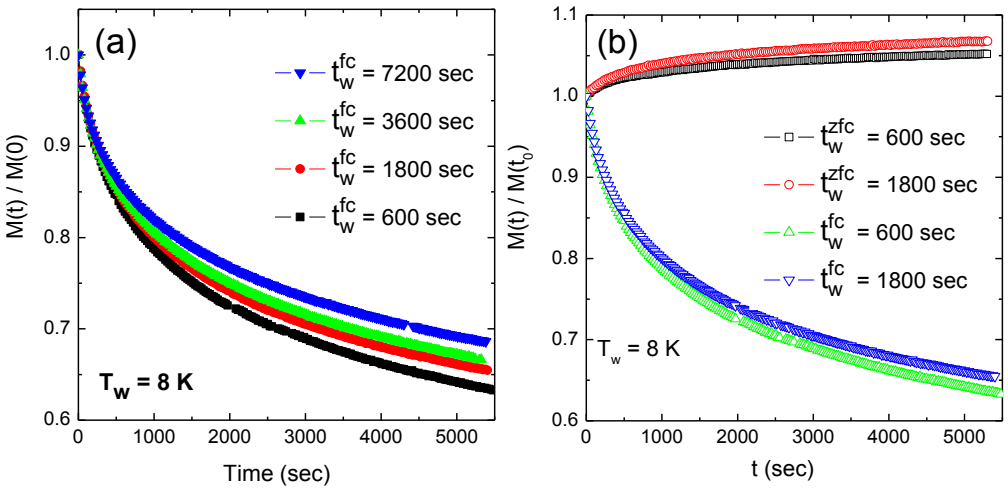

Figure 2.36. Magnetization Vs time at T = 8 K for $CuCr_{0.7}V_{0.3}O_2$ obtained under (a) ZFC protocol for wait time t_w = 600 s, 1800 s, 3600 s, and 7200 s and (b) ZFC and FC protocols for wait time t_w = 600 s and 1800 s.

Figure 2.36 clearly suggests a strong relaxation in magnetization in both the ZFC as well as the FC states. Also, from figure 2.36.b it can be clearly seen that neither the ZFC state nor the FC state are completely in equilibrium state. The existence of non-equilibrium state in ZFC and FC state can be due to the coexistence of different types of magnetic phase interactions: strong antiferromagnetic interaction in Cr^{3+}-Cr^{3+}, weak antiferromagnetic interaction in V^{3+}-V^{3+}, and ferromagnetic interaction in Cr^{3+}-V^{3+}. Similar reason was given for the other types of glassy system [174,175]. However, the FC state shows more

relaxation than the ZFC state, as is evident from figure 2.36.b. The change in magnetization after the ZFC process is only ~ 0.2 % whereas for the same time interval, the change in magnetization after the FC process is ~ 2 %.

Furthermore, in order to study the evolution of the arrested spin glass state of sample $CuCr_{0.7}V_{0.3}O_2$, we measured magnetization as a function of time at different temperatures. Figure 2.37 summarizes the time dependent magnetization data at different selected temperature. For measurement at each temperature, the sample was cooled in a magnetic field of H = 100 Oe from T = 100 K to T = 5 K. The magnetic field was then isothermally reduced to zero at T= 5 K, following which, the sample was warmed to the measurement temperature and magnetization was measured as a function of time for 3600 s. The time decay of remanent magnetization in the temperature range 5–9 K of the $CuCr_{0.7}V_{0.3}O_2$ compound is shown in figures 2.37. Figure 2.37 shows the evolution of thermo remanent magnetization after it is normalized to the respective values of magnetization at t = 0.

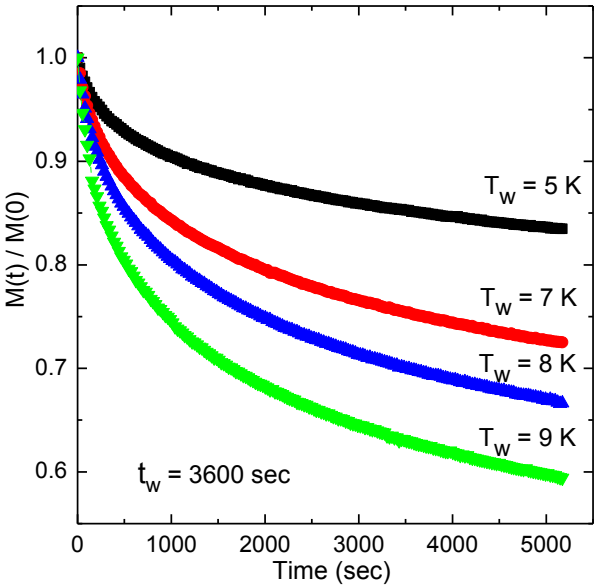

Figure 2.37. Thermo-remanent relaxation isotherms of the $CuCr_{0.7}V_{0.3}O_2$ compound recorded after cooling the sample from 100 K to different temperatures in a field of 100 Oe and switching off the field at t = 0 after a wait time (t_w) of 3600 s.

It is clearly seen from the figure 2.37 that the relaxation effect with no saturation in the entire time scales of measurement at all temperatures (T = 5 K, 7 K, 8K, 9K). Various functional forms are used to study the thermo-remanent magnetization as a function of time such as power law [176], stretched exponential

[177], logarithmic decay [178], etc for the analysis of compounds showing spin glass behavior. Here in our case, the decay of time dependent magnetization M (t) in the entire time window is well described by a logarithmic decay of the following functional form [156]. The detail information is already provided in above written equation 2.5.

$$M(t) = M_0 - M_0 * S * \ln\left(1 + \frac{t}{t_0}\right)$$

The logarithmic nature of the relaxation is associated with a distribution of energy barriers arising from the random and mixed interactions between the spin clusters or with time dependent activation energies. The temperature dependent magnetic viscosity S (T) estimated from the logarithmic relaxation measurements increases with decreasing temperature. The magnetic viscosity S(T) value was deduced from the thermo-remanent magnetic measurement at different selected temperature (T = 5 K, 7 K, 8K, 9K). The linear fitting of the plot between M(t) versus ln $(1+t/t_0)$ gives the magnetic viscosity values at different temperatures. Figure 2.38 shows the variation of magnetic viscosity parameter with increasing temperature. The plot between magnetic viscosity S (T) versus temperature shows a linear dependence on T.

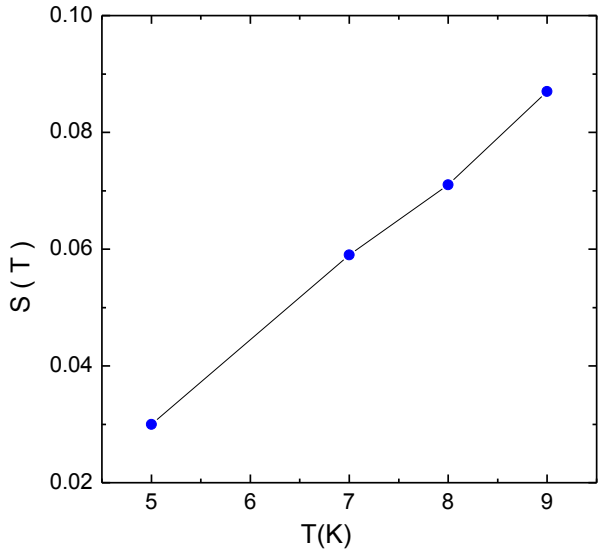

Figure 2.38. Temperature dependence of the magnetic viscosity *S(T)* obtained from the best fit of the experimental data as shown in figure 2.37 to magnetic viscosity equation ($M(t) = M_0[1-S(T)\ln(1+t/t_0)]$).

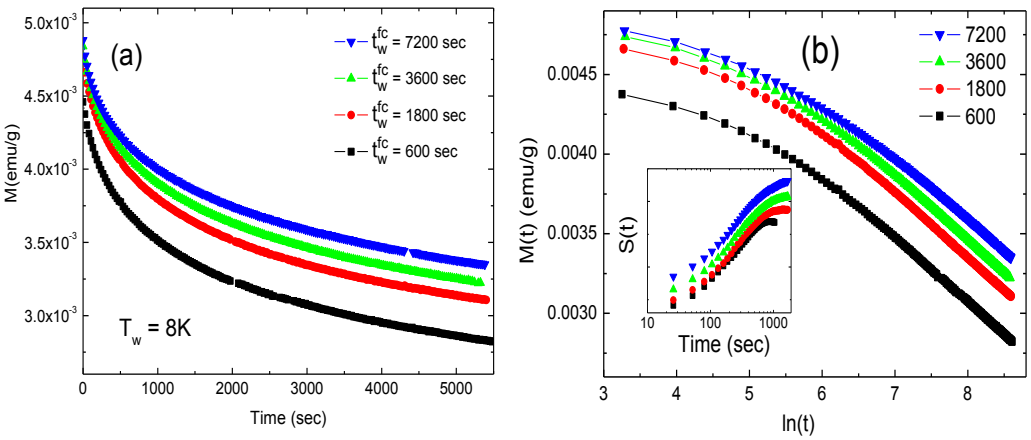

Figure 2.39. (a) The thermo-remanent relaxation isotherm at temperature 8 K (b) the corresponding relaxation rate curves for the $CuCr_{0.7}V_{0.3}O_2$ compound for different wait time (t_w). Inset of (b) shows the relaxation rate as function of time (calculated by $S(t) = 1/H[\partial M(t)/\partial \ln(t)]$). The sample is cooled from 300 to 8 K in a field of 100 Oe and the field is switched off at t = 0 after a t_w of 600, 1800, 3600 or 7200 s.

In addition to this, we have studied the thermo-remanent relaxation isotherm recorded at wait temperature T_w = 8 K for different wait time tw = 600 s, 1800 s, 3600 s, and 7200 s in FC protocol discussed above. Figure 2.39 (a) displays that the shape of M (t) curve changes with increasing wait time. This supports the age-dependent phenomena in the $CuCr_{0.7}V_{0.3}O_2$ compound. Also, the wait time dependence of the magnetic relaxation is illustrated by the relaxation rate S (t) deduced from the time dependent magnetization measurement at temperature 8 K. In figure 2.39 (b), the corresponding relaxation rates, $S(t)= 1/H(\partial M(t)/ \partial ln(t))$, are plotted versus ln (t) at different wait time. It is clearly seen from figure 2.39 (b) that the maximum in relaxation rate S(t) appears at the observation time where the inflection point is observed in the corresponding time-dependent magnetization M (t) curves. Similar curves were obtained for other wait time supporting the aging phenomena. This non-equilibrium behaviour in time-dependent magnetization M(t) and shape of relaxation rate S(t) is very similar to those reported in a variety of frustrated and disordered systems including some other SG perovskite compounds [179].

2.3.4. Dielectric properties of $CuCr_{1-x}V_xO_2$ ($0 \le x \le 0.5$)

The room temperature resistivity of all the samples of this series $CuCr_{1-x}V_xO_2$ ($0 \le x \le 0.5$) is the order of 10^6 Ω.cm and increases with decreasing temperature leads to insulator at low temperature. This is confirmed by the dielectric permittivity (ε′) and corresponding losses (tanδ) measured at 1 V ac bias field for different frequencies (5 kHz up to 100 kHz). Figure 2.40 shows the T-dependence of the dielectric permittivity (ε′) of $CuCr_{1-x}V_xO_2$ for vanadium content of x = 0, 0.04, 0.08, recorded upon warming, reveals a relationship between dielectric

anomaly strength and V^{3+} content in $CuCrO_2$ system. The presence of dielectric anomaly (figure 2.40) in T-dependent dielectric measurement confirms the long range ordering for x = 0, 0.04, 0.08. The strength of the dielectric anomaly (height) decreases with increase of vanadium content in $CuCrO_2$. This can be clearly seen in figure 2.41 which shows the relative dielectric permittivity calculated by $\varepsilon'_{ref} - \varepsilon'_{(T=7K)}/ \varepsilon'_{(T=7K)}$ as a function of temperature measured at frequency f = 100 kHz. As reported previously in $ACrO_2$ multiferroics [30], the weaker dielectric anomaly gives rise to the weaker electric polarization P according to the relation $\varepsilon-\varepsilon_\infty \propto <|\Delta P|^2>$ [41]. This is confirmed for the samples of $CuCr_{1-x}V_xO_2$ (x = 0.04, 0.08), as shown in figure 2.42. A static electric poling field of 135 kV/m was applied at a given temperature prior to field cooling in order to align the electric dipoles. The electric polarization decreases (~ 40 $\mu C/m^2$ for $CuCr_{0.96}V_{0.04}O_2$) with V^{3+} content (~ 2 $\mu C/m^2$ for $CuCr_{0.92}V_{0.08}O_2$) in $CuCrO_2$ at low level of substitution. Inset of figure 2.42 (b) shows the normalized electric polarization ($\Delta P/\Delta P_{max}$) as a function of temperature for the $CuCr_{1-x}V_xO_2$ samples with x=0.04, 0.08.

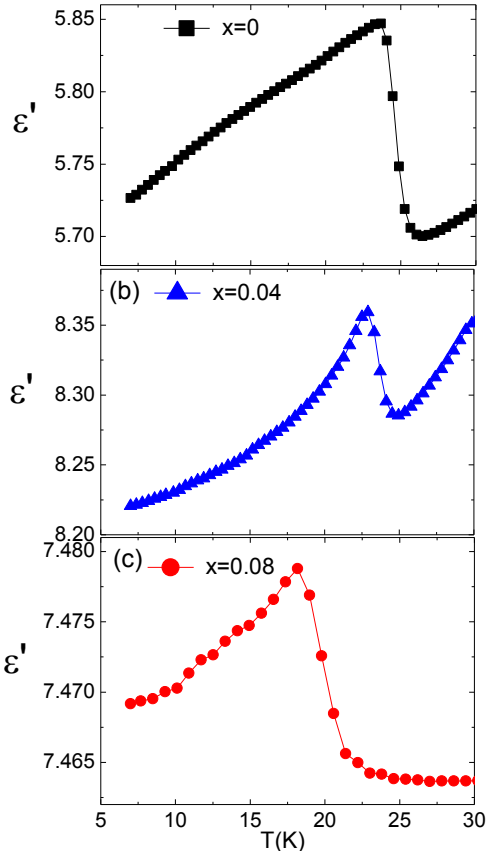

Figure 2.40. (Color online). Dielectric permittivity (f = 100 kHz) as a function of temperature of $CuCr_{1-x}V_xO_2$ with vanadium content (a) x=0; closed squares (b) x=0.04; closed triangles (c) x=0.08; closed circles.

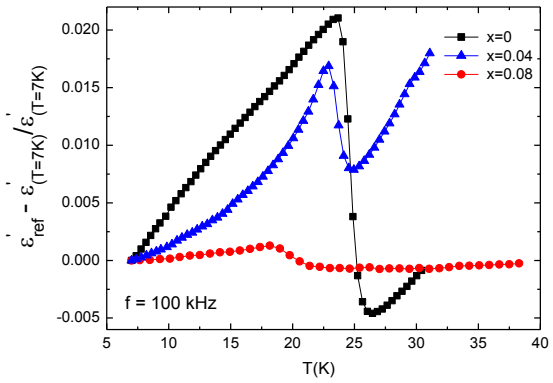

Figure 2.41. (Color online). Relative dielectric permittivity (ε'_{ref} - $\varepsilon'_{(T=7K)}$/ $\varepsilon'_{(T=7K)}$) as a function of temperature of $CuCr_{1-x}V_xO_2$ for x=0, 0.04, 0.08.

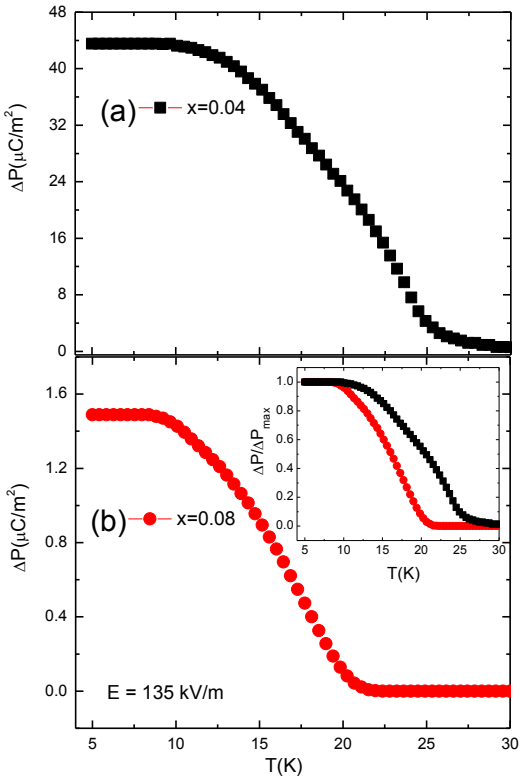

Figure 2.42. (Color online). Main panel (a) and (b) Temperature dependence of the electric polarization (poling electric field E= 135 kV/m) of $CuCr_{1-x}V_xO_2$ for x = 0.04 (open squares) and 0.08 (open circles). Inset of (b) shows relative electric polarization ($\Delta P/\Delta P_{max}$) as a function of temperature of $CuCr_{1-x}V_xO_2$ (x = 0.04, 0.08).

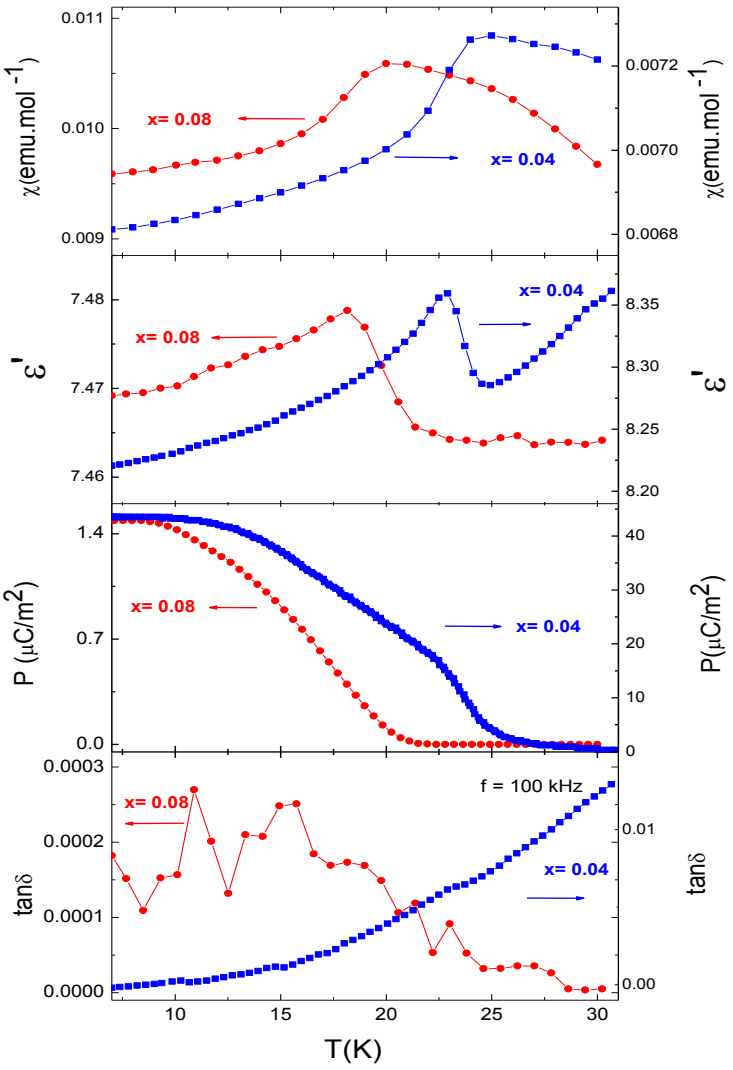

Figure 2.43. (Color online). Temperature profiles of magnetic susceptibility, dielectric permittivity (100 kHz), electric polarization and tanδ plots (from top to down panels) of $CuCr_{0.92}V_{0.08}O_2$ (left y-axis) and $CuCr_{0.96}V_{0.04}O_2$ (right y-axis) measured upon warming.

Figure 2.43 shows the temperature profiles of dc magnetic susceptibility, dielectric permittivity (recorded at frequency of 100 kHz), electric polarization and tanδ (imaginary part of dielectric permittivity data) of $CuCr_{1-x}V_xO_2$ (x = 0.04, 0.08) measured upon warming. The magnetic susceptibility shows a clear kink at $T_{\chi(inflection)}$ ~ 18 K and 21 K for x = 0.08 and x=0.04. At $T_{\chi(inflection)}$, the dielectric constant also shows a sharp anomaly, and the spontaneous electric polarization

begins to develop. All these features affirm the strong magnetoelectric coupling in different degree of freedoms. The direction of polarization can be reversed by reversing the poling electric field. These indicate the ferroelectric nature of the ground state of $CuCr_{1-x}V_xO_2$ (x = 0.04, 0.08). The polarization and dielectric anomaly confirms the presence of ferroelectric behaviour in $CuCr_{1-x}V_xO_2$ sample for (x=0.04, 0.08) as reported in previous studies for parent compound $CuCrO_2$ [30, 41, 56].

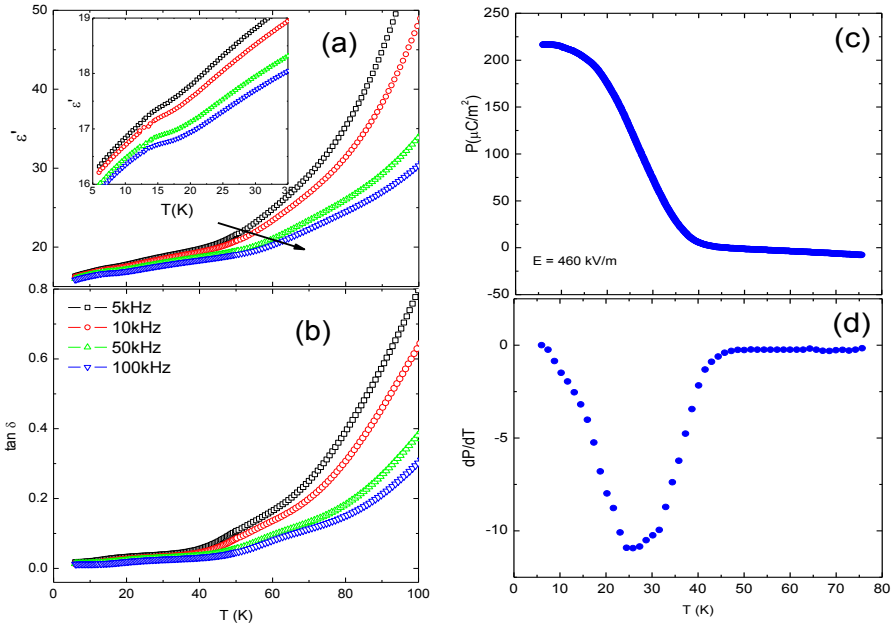

Figure 2.44. Main panel (a) and b) Temperature dependence of the real and imaginary part (tanδ) of an ac dielectric permittivity measured at different frequencies (5 kHz to 100 kHz) of $CuCr_{0.82}V_{0.18}O_2$. Inset (a) Enlargement view of dielectric permittivity at low temperature scale up to 35K. (c) Temperature dependence of electric polarization in positive poling electric field (E=460 kV/m) applied at T=35 K). (d) derivative of polarization (dP/dT) of $CuCr_{0.82}V_{0.18}O_2$.

To further support the argument of spin glass characteristic in high vanadium substituted samples such as x =0.18, 0.2, 0.5, we performed the dielectric permittivity and electrical polarization measurement. Figure 2.44, 2.45, and 2.47 summarizes the results of dielectric permittivity ε'(T), losses tanδ (T), electric polarization P (T) and derivative of electric polarization (dP/dT) of $CuCr_{1-x}V_xO_2$ (x = 0.18, 0.2, 0.5). The dielectric permittivity was measured at 1 V ac bias field for different frequencies (10 kHz up to 100 kHz). In real part of dielectric permittivity there is small dispersion in dielectric constant under different frequencies which can be clearly seen in the form of frequency dependent broad peak in tanδ. The tanδ value is very small which support the intrinsic origin of the

relaxor like behavior in these samples. Also, absence of any dielectric anomaly at transition temperature confirms the absence of ferroelectric state in these samples. High vanadium substitution in $CuCr_{1-x}V_xO_2$ ($x \geq 0.18$) brings the disorderness in the parent system $CuCrO_2$ at the expense of long range ordering i.e. ferroelectric nature. In each samples, at high temperature region > 100 K, the dielectric constant as well as the losses increases sharply at low frequency indicating the high electric conductivity in $CuCr_{1-x}V_xO_2$ (x = x=0.18, 0.2, 0.5) whereas at low temperature regime (< 100 K), the low losses in each case indicate that the samples are insulator (figure 2.44.b, 2.45.b, and 2.46.b). Inset of figure 2.44.a, 2.46.a and 2.47.a shows $\varepsilon'(T)$ up to lower temperature scale (< 50 K). Absence of any sharp anomaly around transition temperature (low temperature regime) indicates the existence of the spin glass behavior in high vanadium substituted samples $CuCr_{1-x}V_xO_2$ ($x \geq 0.18$). Dielectric results of $CuCr_{0.5}V_{0.5}O_2$ sample are consistent with the results of the earlier studies [180].

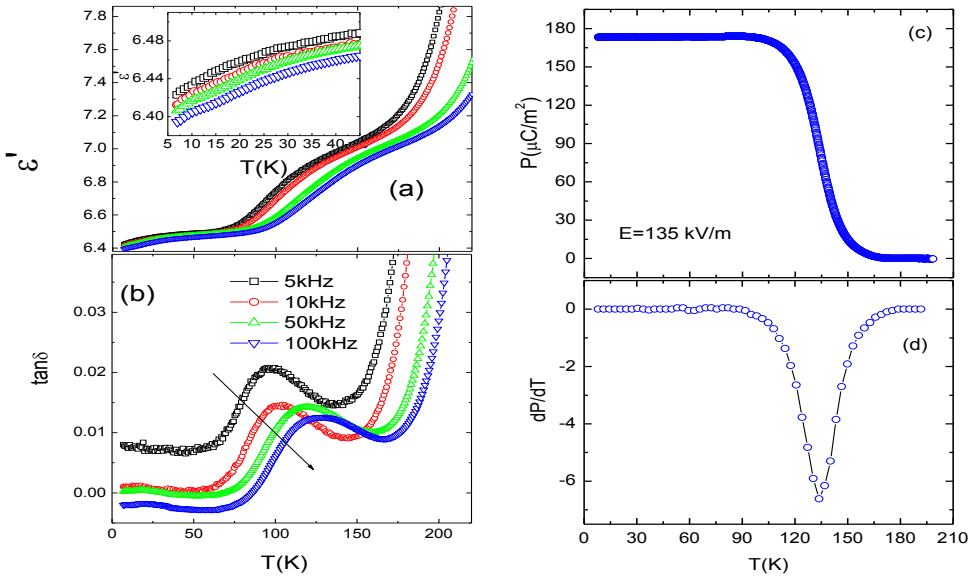

Figure 2.45. (Color online). Main panel (a) and b) Temperature dependence of the real and imaginary part (tanδ) of ac dielectric permittivity at different frequencies (5 kHz to 100 kHz) of $CuCr_{0.8}V_{0.2}O_2$. Inset (a) Enlargement of dielectric permittivity at low temperature scale up to 45K. (c) Temperature dependence of electric polarization in positive poling electric field (E=135 kV/m applied at T=150 K). (d) Derivative of polarization (dP/dT) of $CuCr_{0.8}V_{0.2}O_2$.

The electric polarization (P) was measured under a static electric poling field of 135 kV/m in case of sample with x = 0.2 and 0.5 whereas for sample x = 0.18 the applied electric field was 460 kV/m. The field was applied at given temperature T = 150 K for x = 0.2, T = 100 K for x = 0.5 and a slight lower temperature of T=35 K for x=0.18. Figure 2.44.c-d, 2.45.c-d and 2.46.c-d shows the electric

polarization and corresponding pyroelectric coefficient (dP/dT) as a function of temperature of $CuCr_{1-x}V_xO_2$ for x = 0.18, 0.2, 0.5 (high vanadium substituted samples). The maximum remnant polarization value recorded for $CuCr_{1-x}V_xO_2$ for x = 0.18, 0.2, 0.5 are ~220 $\mu C/m^2$, ~170 $\mu C/m^2$, and ~130 $\mu C/m^2$ and is greater than pristine $CuCrO_2$ because of different microscopic origin of polarization in x < 0.18 and 0.18 ≤ x ≤ 0.5 samples. High electric polarization observed in $CuCr_{0.82}V_{0.18}O_2$ could be due to existence of large disordered magnetic state in the sample. Figure 2.47 shows the comparative electric polarization for the high vanadium substituted samples. It can be clearly seen from the figure 2.47 that the magnitude of polarization decreases with increase in vanadium content (x=0.18, 0.2, 0.5). The maximum electric polarization was observed in sample with vanadium x = 0.18 ~ 220 $\mu C/m^2$.

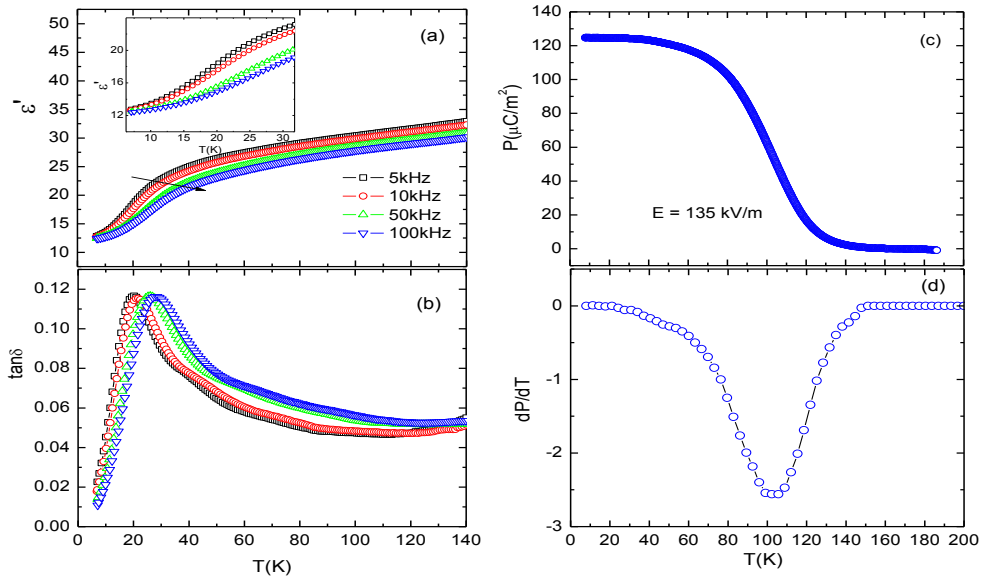

Figure 2.46. (Color online). Main panel (a) and (b) Temperature dependence of the real and imaginary part (tanδ) of ac dielectric permittivity at different frequencies (5 kHz to 100 kHz) of $CuCr_{0.5}V_{0.5}O_2$. Inset (a) Enlargement of dielectric permittivity at low temperature scale up to 35K. (c) Temperature dependence of electric polarization in positive poling electric field (E=135 kV/m applied at T=100 K). (d) Derivative of electric polarization (dP/dT) of $CuCr_{0.5}V_{0.5}O_2$.

As expected for a relaxor type material, its polarization has been found to depend on the poling T [181]. In figure 2.47, a polarization maximum is reached when the sample is poled at 35 K (x=0.18), 100 K (x=0.2), and 150 K (x=0.5) with a transition temperature at the midpoint of each corresponding temperature. In all cases, the observed polarization value is much larger than the measured in the pristine $CuCrO_2$ polycrystalline sample [29], and also is the transition temperature, 35 K, 100 K, and 150 K against 24 K (T_N) in $CuCrO_2$. These results demonstrate that

the mechanism responsible for the ferroelectric behavior in the $CuCr_{1-x}V_xO_2$ ($0.18 \leq x \leq 0.5$) delafossites is not induced by the magnetic ordering. In addition, the transition temperature in figure 2.47 for each sample (x=0.18, 0.2, 0.5) is much larger than the spin glass temperature T_{SG} (14.25 K for x=0.18, 11.25 K for x=0.2, 9.3 K for x =0.5), rules out a relation between the spin glass and the relaxor ferroelectric behaviors.

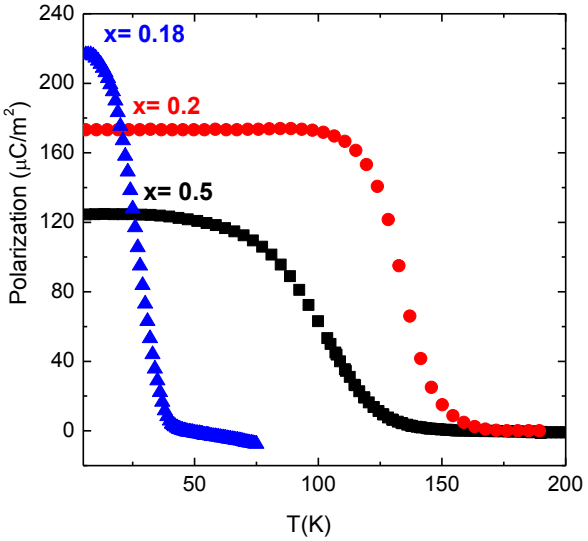

Figure 2.47. (Color online). Comparative electric polarization for sample of the series corresponds to high vanadium substitution of $CuCr_{1-x}V_xO_2$ (x= 0.18, 0.2, 0.5).

2.3.5. Conclusion

In conclusion, a detailed study has been performed on structural, magnetic, dielectric and polarization properties of series of sample $CuCr_{1-x}V_xO_2$ ($0 \leq x \leq 0.5$). Figure 2.48 show the phase diagram of electric polarization and dc magnetic transition temperature $T_{\chi(max)}$ (K) of sample of series $CuCr_{1-x}V_xO_2$ ($0 \leq x \leq 0.5$). It is clear that sample with composition x< 0.18 shows a long range ordering with ferroelectricity induced by spin ordering whereas in sample with $0.18 \leq x \leq 0.5$, there exist spin glass behaviour that precludes the existence of ferroelectricity induced by an antiferromagnetic state as observed in parent $CuCrO_2$. In that respect, $CuCr_{1-x}V_xO_2$ ($0.18 \leq x \leq 0.5$), cannot be regarded as a spin induced ferroelectric. In contrast, the existence of a spin glass state when the B site of the ABO_2 delafossite is occupied by two different cations shows that the Cr^{3+}/V^{3+} cations are randomly distributed. Random lattice disorder in oxides such as in the ABO_3 perovskites promotes the formation of dipolar impurities that can generate a ferroelectric state above the percolation threshold [182].

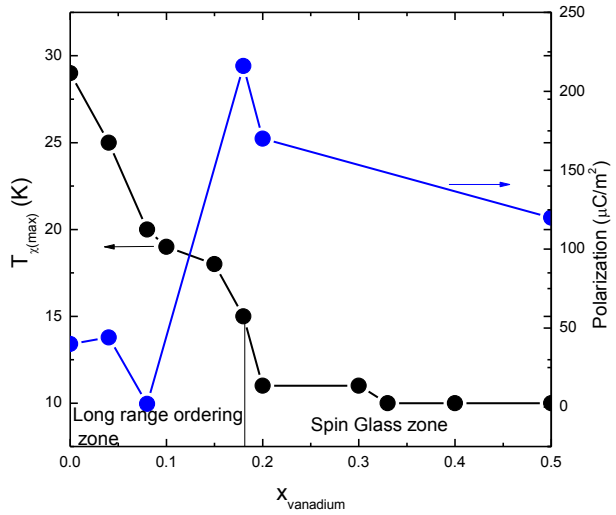

Figure 2.48. The dc magnetic transition temperature $T_{\chi(max)}$ (K) and polarization phase diagram of sample of series $CuCr_{1-x}V_xO_2$ ($0 \le x \le 0.5$).

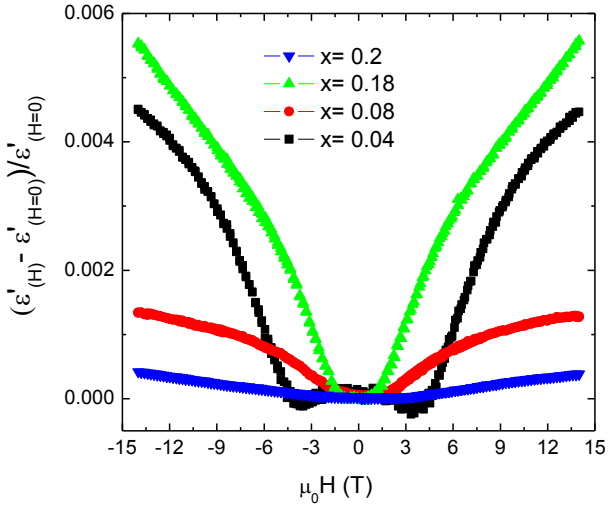

Figure 2.49. Compositional variation of the magnetodielectric effect MD = $[\varepsilon(H) - \varepsilon(H = 0)]/\varepsilon(H = 0)$ as a function of magnetic field at 100 kHz at temperature T = 5K.

There is no difference observed in the actual magnetic state of the $CuCrO_2$ for low content of vanadium in $CuCrO_2$ ($0 \le x < 0.18$) except the transition temperature shifts towards a lower temperature. The overall magnetic investigation allows us to conclude that the substitution of Cr^{3+} by V^{3+} in $CuCrO_2$ leads to the

formation of spin glass state for higher vanadium substituted samples ($0.18 \leq x \leq 0.5$). The occurrence of a spin glass state for higher vanadium substituted samples ($0.18 \leq x \leq 0.5$) is due to presence of competing interaction (antiferromagnetic interaction created by Cr^{3+}-Cr^{3+} and ferromagnetic interaction created by Cr^{3+}/V^{3+}). Higher content of vanadium create dominance in randomness of spins in the $CuCrO_2$ system which in turn destroys the long range ordering and leads to the formation of disordered magnetic state (spin glass). As mentioned by El Ataoui *et al* [43], the Cr^{3+}–O bonds are less covalent than the V^{3+}–O ones; in addition the V^{3+}–V^{3+} are able to dimerize and also the coexistence of different exchange strictions together provide several mechanisms that might be responsible for the creation of electric dipoles.

It is already reported the multiglass behaviour (dielectric glass and spin glass) in sample of $CuCr_{0.5}V_{0.5}O_2$ [181]. In continuation with this reported data, we have measured the magnetodielectric coupling effect (MD = $[\varepsilon(H) - \varepsilon(H = 0)]/\varepsilon(H = 0)$) as a function of magnetic field at frequency of 100 kHz at temperature T = 5K with varying vanadium content in $CuCrO_2$. Figure 2.49 show the magnetodielectric coupling of different samples with varying magnetic field. A large quadratic coupling is observed at for sample with x=0.18 (~ 0.6 %) and a smaller one at composition x = 0.5 (~ < 0.1 %) K. Similar value was reported in sample of $CuCr_{0.5}V_{0.5}O_2$ [181]. This nonlinearity curves are different from the situation reported by Shvartsman et al [159] who measured a linear effect with a change of sign in M when E changes its sign. This indicates the different reason for origin of large polarization in high vanadium substitution sample. In addition to the above measurement, the magnetic and ferroelectric properties of polycrystalline sample of series $CuCr_{1-x}V_xO_2$ ($0 \leq x \leq 0.5$) have been investigated. These properties differ from those of antiferromagnetic delafossites such as $CuFeO_2$ or $CuCrO_2$. For higher vanadium substituted samples ($0.18 \leq x \leq 0.5$), the existence of a spin glass state is evidenced by magnetization, ac susceptibility and dielectric property measurements. Large polarization values were observed in all high vanadium substituted samples ($0.18 \leq x \leq 0.5$). In that respect, the present study opens new routes to designing ferroelectric oxides beside the magnetically driven ferroelectrics. Thus, the delafossite structure, with its triangular layers of magnetic cations, offers an attractive framework for generating not only multiferroics but also glass-like relaxor ferroelectrics.

2.4. Hydrothermal Synthesis of $CuCr_{1-x}V_xO_2$ (x = 0.02, 0.04)

2.4.1. Experimental process condition

Samples of $CuCr_{1-x}V_xO_2$ (x = 0.02, 0.04) were also prepared by using hydrothermal method to compare their fundamental properties (structural and magnetic) with other conventionally synthesized samples as in discussed above section 2.3. Samples of $CuCr_{1-x}V_xO_2$ (x = 0.02, 0.04) were prepared at two different process condition i.e. at 2H condition and 3R condition. Under 2H condition samples were prepared at 200 °C for 60 h in 2.5 M of NaOH in an aqueous solution using Cu_2O and $Cr(OH)_3$ precursors. Similarly, under 3R condition samples of $CuCr_{1-x}V_xO_2$ (x = 0.02, 0.04) were prepared at 250 °C for 60 h in 2.5 M of NaOH in an aqueous solution using Cu_2O and $Cr(OH)_3$ precursors. Table 2.12 summarizes the experimental process condition used in both condition (2H and 3R condition).

Table 2.12. Experimental process condition used to prepare the samples of $CuCr_{1-x}V_xO_2$ (x = 0.02, 0.04)

Code	x	Reactant	Temp (°C)	t (hrs)	NaOH (M)	XRD
			3R Condition			
KS87	0.02	Cu_2O $Cr(OH)3$ V_2O_3	250	60	2.5	**$CuCrO_2$ (3R)** VO_2*
KS88	0.04		250	60	2.5	
			2H Condition			
KS90	0.02	Cu_2O $Cr(OH)3$ V_2O_3	200	60	2.5	**$CuCrO_2$ (2H)**
KS91	0.04		200	60	2.5	**$CuCrO_2$ (2H)**

*minor phases, bold letters dominant phases

2.4.2. Structural and magnetic characterization

Structural and phase analysis has shown that samples (KS87 and KS88) prepared in 3R condition have characteristic of the 3R delafossite in addition to minor impurity phase of VO_2 (< 1% weight) which coexists with the primary phase (figure 2.50). Also, figure 2.50 shows the room temperature powder X-ray diffraction patterns of $CuCr_{1-x}V_xO_2$ (x = 0.02, 0.04) prepared under 2H condition. Structural analysis has shown that samples (KS90 and KS91) have characteristic of the 2H delafossite without presence of any impurity phases as it appears in 3R condition. In both cases (2H and 3R condition), the powder diffraction patterns indicate the absence of any structural phase transition. Broad diffraction peaks in both kinds of samples (2H and 3R), clearly suggests the nano sized particles. Figure 2.51 shows the T-dependence of dc molar magnetic susceptibility (χ) and inverse magnetic susceptibility (χ^{-1}) measured in zero field cooled (ZFC) and field cooled (FC) modes under magnetic field of 0.1 T for sample of $CuCr_{0.96}V_{0.04}O_2$. The absence of any magnetic transition could be due to the nanoparticle size observed in sample $CuCr_{0.96}V_{0.04}O_2$. These results (structural and magnetic) observed in hydrothermally grown samples of $CuCr_{1-x}V_xO_2$ (x = 0.02, 0.04) are different with the one observed in samples prepared by solid state reaction method (section 2.3). Further work is required to study the magnetic behavior observed in vanadium doped sample prepared by hydrothermal.

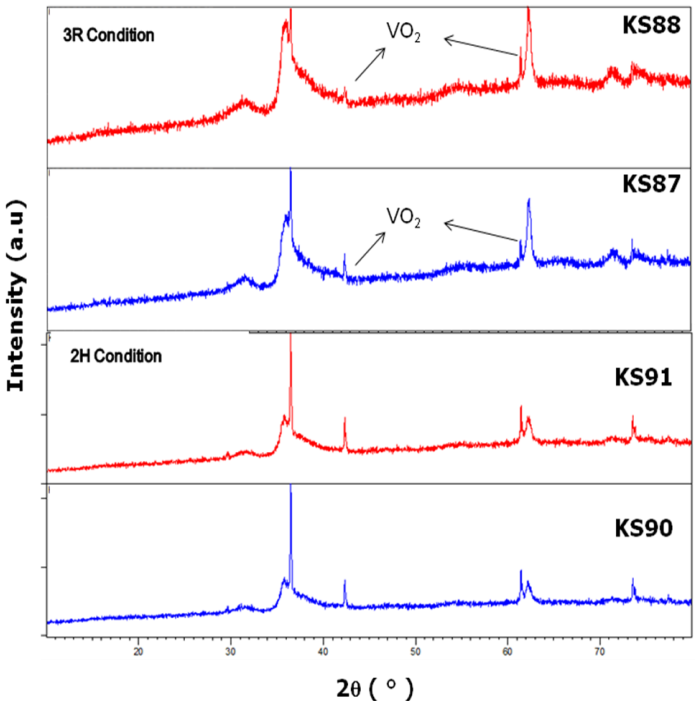

Figure 2.50. (Color online). Room temperature X-ray powder diffraction patterns of hydrothermaly prepared samples of $CuCr_{1-x}V_xO_2$ (x = 0.02, 0.04) under 2H and 3R condition.

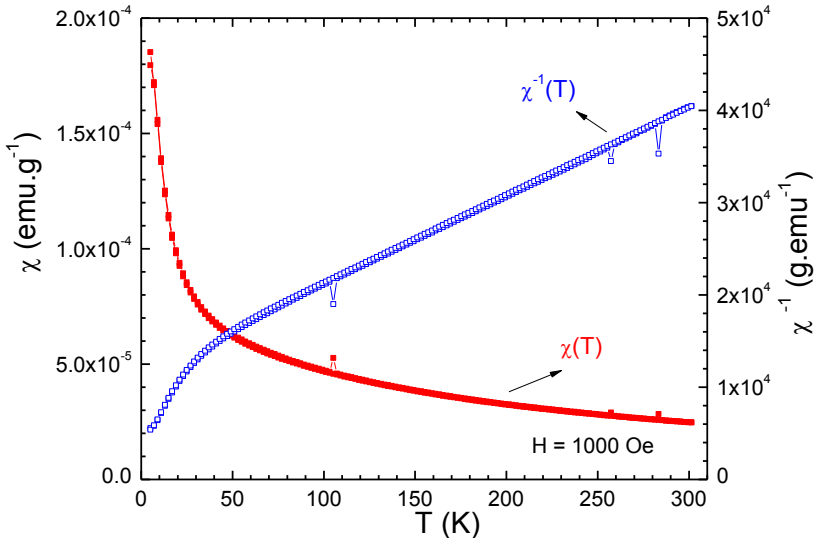

Figure 2.51. (Color online). T-dependence of dc molar magnetic susceptibility (χ) (left y-axis) and inverse magnetic susceptibility (χ^{-1}) (right y-axis) measured in zero field cooled (ZFC) and field cooled (FC) modes under magnetic field of 0.1 T for sample of $CuCr_{0.96}V_{0.04}O_2$.

CHAPTER III
HYDROTHERMAL METHOD: A NEW SINGLE STEP PROCESS TO SYNTHESIZE $AgCrO_2$

3.1. Introduction to $AgCrO_2$ delafossite

It is already been discussed in chapter 1 about the application and importance of $AgCrO_2$ delafossite compound in multifunctional devices and as a semiconductor photocatalysts for clean hydrogen energy production and environmental decontamination. In recent decades, oxides crystallizes in dealfossite-type structure are technologically promising materials due to their structural, optical and photo-catalytic properties [52,183-184,44]. $AgCrO_2$ delafossite compound crystallizes in the *R-3m* space group (with $a = b = 2.984$ Å, and $c = 18.515$ Å) [52] is very appealing because of its unique electronic, optical and photocatalytic properties [184-185, 64,42].

It is difficult to synthesize silver based delafossite compounds by solid state reaction method in air because of low free energy of formation of Ag_2O (-2.6 kcal mol^{-1}) and its decomposition to metallic silver and oxygen at low temperatures [52,186]. Consequently, silver based delafossite compounds are prepared by either direct reactions in a closed solid state systems [52,84,86] or by exchange reactions [52,186,187-189]. To the best of our knowledge, only few synthesis methods involving complex step reactions have been reported for $AgCrO_2$: via cation exchange method [184], solid state reaction method [30,190] and oxidizing flux reaction method [52]. Recently, hydrothermal synthesis method proved to be very valuable method for preparing various delafossite oxides in a facile single-step reaction [64,84]. William et al. [84], reported unfeasibility of $AgCrO_2$ delafossite phase at low temperature (210 °C) and pressure (< 20 atm) by hydrothermal method. It was reported, at low temperature, Ag_2O does not react with $Cr(OH)_3$ or CrOOH to form $AgCrO_2$ but rather generate excess amount of metallic silver and trivalent Cr^{3+} ions undergo oxidation to Cr^{6+} ions, redox reaction occurs that speed up the decomposition of Ag_2O into metallic silver and oxygen [84]. To overcome the above mentioned obstacle, we have revisited this compound at high temperature (>300 °C) and pressure (> 200 bars) by hydrothermal method.

In this work here for the first time the synthesis of a polycrystalline sample of $AgCrO_2$ by one-step hydrothermal process, starting from a mixture of Ag_2O and $Cr(OH)_3$ using $K_2Cr_2O_7$ as oxidizing agent in an aqueous solution. In this work, we present a possible detail explanation for the synthesis of $AgCrO_2$ in presence of $K_2Cr_2O_7$ in an aqueous solution. The obtained green color powdered material is single phase, well crystallized and exhibits grains whose size varies from 0.5 to 2 μm. We have studied the effect of, and optimizing, important experimental parameters including pressure, reaction time, and $K_2Cr_2O_7$. Also, we studied the effect of NaOH and KOH mineralizer on the synthesis of $AgCrO_2$ compound.

Furthermore, we have explored the FT-IR and optical properties in details for $AgCrO_2$ compound.

3.2. Study of the stability diagram for Ag-Cr-H_2O system

The hydrothermal synthesis of $AgCrO_2$ was done in a stainless steel (SS) autoclave (12NiCr250, < 450°C, < 1000 bars). The temperature was recorded by a temperature controller (E5CK-TAA1-500 100-240 AC regulator temperature OMRON) and the pressure was controlled by Kennedy's PVT diagram of water (experimental set-up is shown in figure 1.11 in chapter 1) [81]. Solutions were prepared by dissolving precise amounts of Ag_2O (Merck KGaA, purity > 99 %,) and $Cr(OH)_3$ ($Cr(OH)_3$ powder was prepared in laboratory, detail synthesis condition is discussed elsewhere [191]) using various different additives such as NaOH, KOH, H_2O_2, $K_2Cr_2O_7$ (Reactivil, purity > 99 %) in 28 ml SS autoclave in an aqueous solution. The stoichiometry of precursors in solution was kept at 1:2. The autoclave was then tightly sealed and placed in a high temperature furnace at the different reaction temperature (ranged from 200 °C to 400 °C) for different reaction time (ranged from 8 hr to 60 hr) and under a different pressure range (10 bar to 800 bar) (calculated from Kennedy's PVT diagram of water [81]). Table 3.1 summarizes the process conditions and structural results used to prepare $AgCrO_2$ compound via hydrothermal synthesis method using the precursor of Ag_2O and $Cr(OH)_3$ keeping same stochiometry 1:2 in an aqueous solution. After a fast cooling (50 °C/hr), the autoclave was opened and the green colored polycrystalline $AgCrO_2$ compound was recovered by filtration. Powder X-ray diffraction (XRD) patterns were collected by using a PANalytical X'pert Pro diffractometer (Cu K_α, $10^\circ \leq 2\theta \leq 110^\circ$). Rietveld refinement was performed by means of the FULLPROF program using a pseudo-Voigt profile function [66]. A scanning electron microscope (Inspect™ S, FEI) coupled with energy dispersive X-ray spectroscopy (EDX) was used to observe the microstructure and determine the cationic composition of the as-synthesized sample. UV-visible diffuse reflectance spectra of the powdered sample mixed with KBr were analyzed by using a UV-visible spectrophotometer (LAMBDA 950 UV/Vis/NIR Spectrophotometer, PerkinElmer, wavelength range up to 3300 nm). Powder of $AgCrO_2$ mixed with KBr was pressed in the shape of pellets (4 mm diameter, 1 mm thickness) to record vibrational spectra by means of a Fourier transforms infrared spectrophotometer (VERTEX 70 FT-IR spectrometer, Bruker). The temperature dependence of magnetic properties was measured with a superconducting quantum interference device (SQUID-Quantum Design) magnetometer. The M (T) data were recorded in a magnetic field of 0.1 T from 5 to 300 K, in zero (zfc) and field cooling (fc) modes.

Table 3.1 is divided into two different parts: part I belongs to the region of low temperature synthesis conditions (table 3.1.A subcritical condition) and part II belongs to the supercritical condition (table 3.1.B). Furthermore table 3.1.B divided into three parts. Part II belongs to the experimental conditions used to prepare the sample at temperature 380 °C in an aqueous solution, part II.a corresponds to the experimental conditions used for samples prepared at varying pressure (ranged from 200 bar to 800 bar), part II.b belongs to the experimental process condition used to prepare sample by using different additives in an aqueous solution to increase the solubility, and part II.c corresponds to the region of experimental

condition used to prepare samples at different paramtric conditions (temperature, reaction time, precursor amount) using 0.1 M of $K_2Cr_2O_7$ oxidizing agent in an aqueous solution.

Studying the table 3.1 thoroughly reveals that samples prepared at low temperature in subcritical condition ≥ 350 °C (table 3.1.A) shows the trace amount of metallic silver in the final product form. This suggests that at low temperature in aqueous solution silver decomposes in metallic silver and oxygen as reported in earlier studies [84]. Also, chromium (Cr^{6+}) rests in solution as an impurity. The important outcome of low temperature synthesis of samples was that by introducing NaOH or KOH in an aqueous solution, the final color of product powder turned out to be metallic silver without showing any sign of $AgCrO_2$ phase powder (green). This shows that in high basic solution, it is difficult to synthesize $AgCrO_2$ using Ag_2O and $Cr(OH)_3$ precursor at low temperature rather it gives a trace amount of metallic silver. In table 3.1.B, we modified the synthesis process by changing the working temperature range (high temperature ranged from 350 °C to 400 °C). The samples were prepared in water without using NOH/KOH in an aqueous solution. At elevated temperature silver with +1 oxidation state forms a soluble species of $Ag(OH)_2^-$ [84] and the concentration of soluble $Ag(OH)_2^-$ species increases with increase in temperature. Also, chromium with +1 oxidation state forms a soluble $Cr(OH)_4^-$ species in an aqueous solution [144,85]. This is the possible explanation of getting $AgCrO_2$ phase at 350 °C in addition to trace amount of metallic silver and CrOOH. In an aqueous solution at high temperature the silver remains in +1 oxidation state coexists with metallic silver. To remove the impurity of metallic silver from the final phase, we prepared the samples at different pressure range (200-800 bars (table 3.1.B part II.a), different additives in an aqueous solution (table3.1.B part II.b).

Table 3.1A. Experimental process conditions used to prepare $AgCrO_2$ with Ag_2O (A) + $Cr(OH)_3$ (B) precursors in subcritical condition

Code	Ratio (A+B) M	t (hr)	NaOH (M)	T (°C)	P (bars)	XRD results
Part I: subcritical condition						
KS29	0.05mmol + 0.1mmol	60	2.5	120	<10	**Ag**, Cr^{3+} &
KS13	1mmol + 2mmol	60	2.5	200	<20	**Ag**, Cr^{3+} &
KS16	1mmol + 2mmol	60	2.5	220	<20	**Ag**, Cr^{3+} &
KS7	1mmol + 2mmol	60	2.5	250	<20	**Ag**, Cr^{3+} &
KS15	1mmol + 2mmol	60	2.5	300	<50	**Ag**, Cr^{3+} &
KS52	0.25M + 0.5M	12	0	350	400	**$AgCrO_2$** , **Ag**, CrOOH*
KS59	0.25M + 0.5M	12	1	350	400	**CrOOH**, Ag *
KS60	0.25M + 0.5M	12	2.5	350	400	**Ag**, CrOOH*

* Minor products, bold letters dominant phases, & in solution

Table 3.1B. Experimental process conditions used to prepare $AgCrO_2$ with Ag_2O (A) + $Cr(OH)_3$ (B) precursors in supercritical condition

Code	Ratio (A+B) M	t (hr)	Additive	T (°C)	P (bars)	XRD results
Part II: supercritical condition						
KS89	0.125+0.25	8	0	380	200	**$AgCrO_2$**,Cr_2O_3,Ag_2O^*
KS86	0.125+0.25	12	0	380	200	**$AgCrO_2$**,Cr_2O_3,Ag_2O^*
KS70	0.125+0.25	12	0	380	800	**$AgCrO_2$**,**Ag**,$CrOOH^*$
Part IIa: pressure study						
KS72	0.125+0.25	12	0	400	800	**$AgCrO_2$**,**Ag**,$Cr_2O_3^*$,$CrOOH^*$
KS96	0.125+0.25	12	0	400	600	**$AgCrO_2$**,**Ag**,$CrOOH^*$,$Cr_2O_3^*$
KS73	0.125+0.25	12	0	400	400	**$AgCrO_2$**,**Ag**,$Cr_2O_3^*$
KS74	0.125+0.25	12	0	400	200	**$AgCrO_2$**,**Cr_2O_3**,Ag_2O^*
KS82	0.125+0.25	12	0	400	600 cooling rate 55 hr	**$AgCrO_2$**,Ag_2O/Ag^*
KS103	0.125+0.25	8	0	400	400	**$AgCrO_2$**,Ag^*
KS98	0.125+0.25	24	0	400	400	**$AgCrO_2$**,Ag,$CrOOH^*$
KS102	0.125+0.25	48	0	400	400	**$AgCrO_2$**,Ag,$CrOOH^*$
Part IIb: additives						
KS83	0.125+0.25	12	1M KOH	400	400	**Ag**,$CrOOH^*$
KS107	0.0625+ 0.125	12	0.1M NaOH	400	400	**Ag**, **$AgCrO_2$**,$CrOOH^*$
KS120	0.125+0.25	12	0.1M $K_2Cr_2O_7$	400	400	**$AgCrO_2$**
KS131	0.125+0.25	12	5% H_2O_2	400	400	**$AgCrO_2$**,Ag^{*-},$Ag_2CrO_4^{**}$
KS138	0.125+0.25	12	7% H_2O_2	400	400	**$AgCrO_2$**, Ag^{**},$Ag_2CrO_4^{**}$
KS139	0.125+0.25	12	15% H_2O_2	400	400	**$AgCrO_2$**,$Cr_2O_3^*$,Ag^{**}
KS140	0.125+0.25	12	20% H_2O_2	400	400	**$AgCrO_2$**, Ag^{**},Cr^{6+**}
Part IIc: parametric study for $K_2Cr_2O_7$						
reaction temperature						
KS133	0.125+0.25	12	0.1M $K_2Cr_2O_7$	200	400	**Ag_2CrO_4**,**Ag**,$AgCrO_2^*$
KS132	0.125+0.25	12	0.1M $K_2Cr_2O_7$	300	400	**$AgCrO_2$**,$Ag_2CrO_4^*$,Ag^*
KS135	0.125+0.25	12	0.1M $K_2Cr_2O_7$	350	400	**$AgCrO_2$** , $Ag_2CrO_4^*$,$CrOOH^*$
KS136	0.125+0.25	12	0.1M $K_2Cr_2O_7$	400	400	**$AgCrO_2$**
varying precursor						
KS108	0.0312+ 0.0625	12	0.1M $K_2Cr_2O_7$	400	400	**$AgCrO_2$**
KS136	0.125+ 0.25	12	0.1M $K_2Cr_2O_7$	400	400	**$AgCrO_2$**
reaction time						
KS136	0.125+0.25	12	0.1M $K_2Cr_2O_7$	400	400	**$AgCrO_2$**
KS120	0.125+0.25	60	0.1M $K_2Cr_2O_7$	400	400	**$AgCrO_2$**

* Minor products, bold letters dominant phases, ** high intensity, *- low intensity

But unfortunately in each case we observed the almost same X-ray diffraction pattern with additional impurities of chromium (Cr_2O_3) in final product except in condition KS120. The important point to note is that with increase in pressure increases the trace amount of metallic silver (pressure range of 400 bar to 800 bar) in final product whereas at low pressure (200 bar to 400 bar) results the Cr_2O_3 and CrOOH impurity phase in the final product. Thus in all cases, the metallic silver and Cr with 3+ oxidation state impurity coexists with $AgCrO_2$ phase in final product. Thus we studied the sample preparation using 0.1 M of $K_2Cr_2O_7$ as an oxidizing agent with varying process conditions mentioned in table 3.1.B.c. In table 3.1.B.c we studied the effect of reaction time, varying precursor amount and reaction time on the final product of $AgCrO_2$. The structural results reported in table 3.1.B.c shows the pure phase formation of $AgCrO_2$ in presence of $K_2Cr_2O_7$ oxidizing agent in an aqueous solution. Similarly, samples prepared by using other oxidizing agent such as H_2O_2 resulted pure phase of $AgCrO_2$ but in addition to metallic silver impurity.

Table 3.2. Experimental details of the samples prepared by using different mineralizer and oxidizing agents.

Additive in solution	T (°C)	P (bars)	Time (hr)	Concentration (M)	XRD Results
Water	400	400	12	0	$AgCrO_2^{\&}$, $Ag^{\&}$, $CrOOH^{*}$
NaOH	400	400	12	0.1	$Ag^{\&}$, $CrOOH^{*}$
KOH	400	400	12	1	$Ag^{\&}$, $CrOOH^{\&}$
H_2O_2	400	400	12	5 % - 20 %	$AgCrO_2^{\&}$, $Ag^{\&}$, $Ag_2CrO_4^{*}$
$K_2Cr_2O_7$	400	400	12	0.1	$AgCrO_2$

& = majority phase, * = minor phase

Table 3.2 summarizes the experimental conditions used to obtain the pure phase of $AgCrO_2$ by using different additives in an aqueous solution at temperature 400 and pressure 400 bars for 12 hr reaction time. We have been successfully prepared the pure phase of $AgCrO_2$ delafossite compound without any trace of metallic silver impurity in the final product. The possible explanation of synthesis of $AgCrO_2$ is discussed in detail in result and analysis section. All the experimental details and resulted structural results are formatted in the form of phase diagram between pressure and reaction temperature shown in figure 3.1. The N, K2, and H correspond to the samples prepared at low temperature, using oxidizing agent, and in water only.

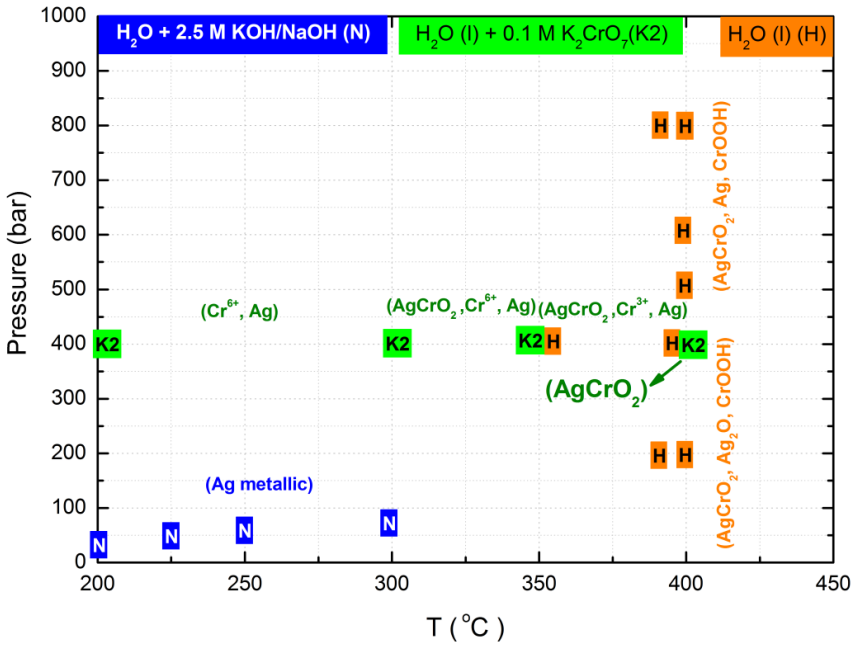

Figure 3.1. Temperature and pressure phase diagram of Ag_2O and $Cr(OH)_3$ precursors in an aqueous solution for 12 hr reaction time in 1:2 stoichiometry.

3.3. Results and discussion

3.3.1. Structural

The X-ray diffraction pattern of the sample prepared by hydrothermal synthesis (figure 3.2.a) is in agreement with the expected one for $AgCrO_2$ [52,184], no trace of metallic silver impurity is observed in addition as reported in earlier studies at low temperature synthesis [84]. The absence of trace amount of metallic silver impurity removes the additional post-synthesis leaching step with nitric acid reported in hydrothermal synthesis of other Ag based delafossite [52,84,86,192]. The sharpness of the diffraction peaks indicates that the product is well crystallized. Accordingly, the structure was refined using crystallographic parameters reported in [52], leading to cell parameters a = *b* = 2.9854(1) and *c* = 18.5091(3) Å, in the *R-3m* space group. Figure 3.2 shows the good agreement between the calculated and the observed profiles (figure 3.2.a) and the drawing of the structure (figure 3.2.b). As shown in the structure, each chromium atom surrounded by 6 neighboring oxygen atom forms an octahedra. Each octahedra linked to the next via sharing edges forming a chain of octahedra along ab plane (figure 3.2.b). Also, the structure contains an O-Ag-O layer that is sandwiched between the edge sharing CrO_6-octahedral layers. The structural results of the $AgCrO_2$ sample prepared by the hydrothermal method are in very good agreement with literature [184].

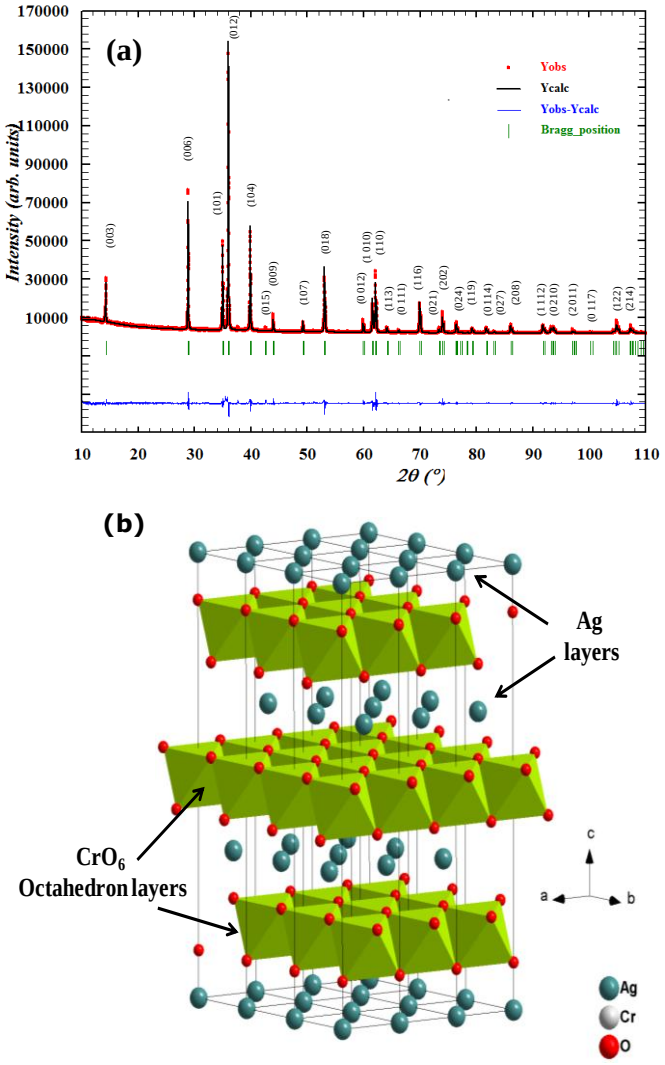

Figure 3.2. (a) Room temperature X-ray Rietveld refinement of the $AgCrO_2$ product (b) Resulting model of $AgCrO_2$ (rhombohedral).

Dealing with the possible formation mechanism for the synthesis of $AgCrO_2$, it is proposed that, at elevated temperature Ag^{+1} exists primarily in the form of soluble species of $Ag(OH)_2^-$ [84] and the concentration of soluble $Ag(OH)_2^-$ species increases with temperature. Also, Cr^{3+} ions in alkaline conditions are stabilized by the formation of the aqueous soluble $Cr(OH)_4^-$ species in an aqueous solution which increases at elevated temperatures [144,85]. At lower temperatures (200 °C, 300 °C, 350 °C) in strong alkaline solution (2.5 M NaOH solution) no $AgCrO_2$ was found, only silver metal and highly soluble CrO_4^{2-} species were established. The presence of

silver metal and CrO_4^{2-} in the mixtures prepared at subcritical temperature region is not surprising, spontaneous Ag_2O decomposition and in combination with Cr cations can undergo oxidation, that a redox reaction occurs [84].

An unexpected result was that at 350 °C and 400 bars, but in pure water, $AgCrO_2$ phase is found as part of a multiphase mixture which consists of Ag and CrOOH phases. It seems that the alkaline solution has also a main effect on the evolution of oxygen from Ag_2O to form silver metal, not only the temperature. In according with this observation, the following experiments were carried on only in the water, the temperature effect on Ag delafossite phase was studied. At 380°C and 400°C, $AgCrO_2$ phase continue to develop, but increasing of the temperature cannot remove in totally the present of silver metal phase. The evolution and competition between these phases have determined the study of another important hydrothermal parameter, the autogenous pressure. It seems that low pressure (up to 400 bars) has acted on the both Ag and Cr species, the dehydration of $Cr(OH)_3$ to Cr_2O_3 was revealed in our XRD measurement and in the same time with the limitation of the solubility of Ag_2O precursors. Increasing of the pressure (up to 800 bars) has established the same multiphase mixture which consists of $AgCrO_2$, Ag and CrOOH phases; CrOOH becomes more thermodynamically stable compared to Cr_2O_3 in high pressure domain.

In according with the above experimental results, the stability of $AgCrO_2$ pure phase requests the excess of the oxygen in the Ag-Cr-H_2O system which was provided by the oxidizing agent. Therefore, it is important to study how the formation of $AgCrO_2$ pure phase proceeds by oxidation and understanding of the mechanism which accelerates the stability of this phase. In this study, hydrogen peroxide and potassium dichromate were used as the oxidizing agent; the different decomposition temperature has been the main and requested its characteristics. Hydrogen peroxide decomposes exothermically into water and oxygen gas spontaneously at room temperature (equation 3.1):

$$2H_2O_2 \rightarrow 2H_2O + O_2 \quad (3.1)$$

A detailed study on $K_2Cr_2O_7$ with respect to temperature evaluation was already reported via analyzing DTA patterns [193]. It was studied that at elevated temperature below 400 °C, $K_2Cr_2O_7$ decomposes into K_2CrO_4 and CrO_3 (equation 3.2) whereas ≥ 780 °C the CrO_3 phase decomposes further into Cr_2O_3 and oxygen gas (equation 3.3)

$$K_2Cr_2O_7(l) \rightarrow K_2CrO_4(l) + CrO_3(l) \quad (3.2)$$
$$CrO_3(l) \rightarrow 0.5\,Cr_2O_3(s) + 0.75\,O_2(g) \quad (3.3)$$

In our case of the supercritical hydrothermal condition, the oxidation effect was observed at the lower temperature. Thus, we proposed that in supercritical hydrothermal solution, $K_2Cr_2O_7$ is decomposed into K_2CrO_4 and CrO_3 from 200 °C to 350°C (confirmed by the present of Cr^{6+} in Ag_2CrO_7 phase emphasized by XRD pattern; figure 3.3.a) and the second step was activated at 400 °C, when the metallic silver is fully oxidized and only $Ag(OH)_2^-$ species is established (figure 3.3.b). In according with these different temperatures of the present of oxygen gas in the

Ag-Cr-H_2O system, the effect of oxygen on the stability of $AgCrO_2$ phase was observed more or less thermodynamically favorable.

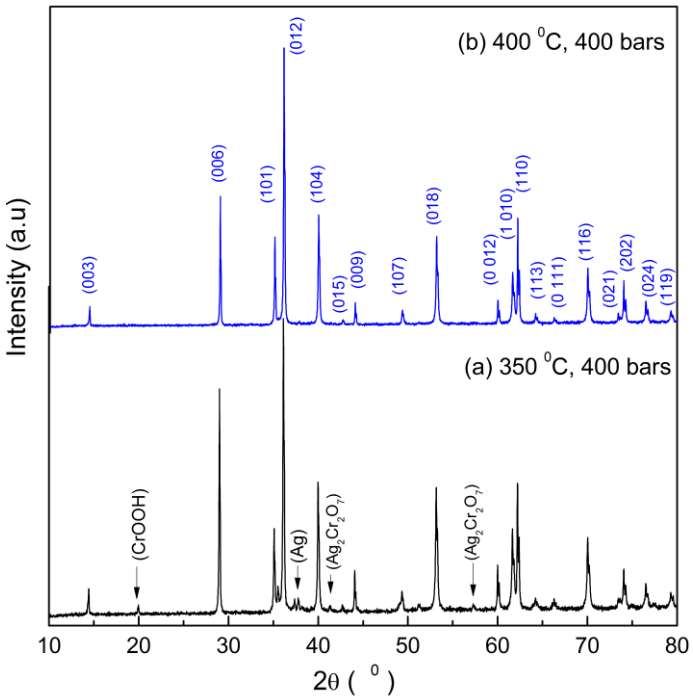

Figure 3.3. Room temperature X-ray diffraction pattern of (a) sample obtained at 350 °C, 400 bars and 12 h, (b) Sample obtained at 400 °C, 400 bars and 12 h.

Thus, in during of this study, the temperature (400 °C), pressure (400 bars) and time reaction (12 h) were kept constant. In the case of hydrogen peroxide, silver metal phase was observed whatever hydrogen peroxide concentration (up to 20 %), but in addition the minor impurity phases of Ag_2CrO_2 was establish. No oxidation effect on undesired silver metal phase and the occurrence of Cr^{6+} phase could be explained that the monovalent oxidation state of Ag^+ is stable in water at room temperature and the excess of oxygen brought by hydrogen peroxide will be used in oxidation of Cr^{3+} to Cr^{6+}. Consequently, chromate (CrO_4^{2-}) and $Ag(OH)_2^-$ species are present in aqueous solution and Ag_2CrO_2 phase was formed.

Contrary the hydrogen peroxide effect, the oxygen resulted by the decomposition of $K_2Cr_2O_7$ at 400 °C has inhibited the evolution of Ag_2O to silver metal exactly in the temperature range where is thermodynamically favorable. The possible formation mechanism for the synthesis of phase pure product of $AgCrO_2$ is suggested as the following. Thus for certain temperature, pressure, reaction time

and 0.1 M $K_2Cr_2O_7$ as oxidizing agent, the stability of $Ag(OH)_2^-$ and $Cr(OH)_4^-$ species is established, the suprasaturation is reached and $AgCrO_2$ is established. The Ag_2O (s) and $Cr(OH)_3$ (s) reactions involving these species are given in the follow equations:

$$Ag_2O(s) + 3H_2O(l) \rightarrow 2Ag(OH)_2^-(aq) + 3H^+(aq) \quad (3.4)$$

$$Cr(OH)_3(s) + H_2O(l) \rightarrow Cr(OH)_4^-(aq) + H^+(aq) \quad (3.5)$$

$$Ag(OH)_2^-(aq) + Cr(OH)_4^-(aq) + 2H^+(aq) \xrightarrow{K_2Cr_2O_7} AgCrO_2(s) + 4H_2O(l) \quad (3.6)$$

On the basis of above experimental results and results obtained from low temperature hydrothermal synthesis of various delafossite-type oxides (ABO_2) [84], table 3.3 summarizes the comparative analysis of A-site cation solubility. It is proposed that the solubility of Ag_2O ($10^{-2.5}$ M) is greater than Cu_2O (10^{-4} M) at low temperature (200 °C). A minimum solubility for both the reagent metal oxides at the reaction temperature is a necessary condition for the formation of delafossite oxides.

Table 3.3. Comparative analysis of A-site cation solubility Ag_2O ($10^{-2.5}$ M) **>** Cu_2O (10^{-4} M) at 200 °C.

amphoteric oxides ⟶ basic oxides

A^+	31 Ga 69.7	13 Al 26.9	25 Mn 54.9	24 Cr 52.0	26 Fe 55.8	21 Sc 44.9	45 Rh 102.9	27 Co 58.9	28 Ni 58.6	49 In 114.8	81 Tl 204.4	39 Y 88.9	63 Eu 152.0	57 La 138.9
29 Cu 63.5	√	√	√	√	√	√	√	√	X	X	X	X	X	X
47 Ag 107.9	√	√	X	√	√	√	√	√	√	√	√	X	X	X
[B] mol/L	1	10^{-1}	10^{-3}	10^{-4}	10^{-4}	10^{-4}	10^{-4}	10^{-5}	10^{-5}	10^{-5}	10^{-5}	10^{-6}	10^{-6}	10^{-6}

3.3.2. In-situ structural analysis

Phase structure and stability of $AgCrO_2$ powder sample was studied by in situ high temperature X-ray diffraction at temperatures from room temperature (RT; 25 °C) to 900 °C under vacuum. The crystal structures and lattice parameters of the $AgCrO_2$ powdered sample was characterized by in situ high-temperature X-ray diffraction (PANalytical X'pert Pro diffractometer) using Cu Ka radiation ($10^\circ \leq 2\theta \leq 110^\circ$). The sample was tested in a high temperature cell with a heated Pt sample holder up to 1000 °C under vacuum and a Pt–Rh thermocouple connected with heated Pt strip sample holder was used to measure the temperatures. The heating rates amounted to 10 °C /min. At each temperature step, the temperature was hold

for 60 min. Data was collected in continuous scan mode in the range of 10°–80°. In this in situ high temperature X-ray diffraction study we have analyzed the variation of lattice parameter and thermal expansion coefficient (TEC) with temperature. Also, the relationship between the thermal expansion coefficient and phase stability is proposed in this work. Figure 3.4 shows the X-ray diffraction patterns of $AgCrO_2$ powder under vacuum as the temperature was varied from room temperature to 900 °C. It is clearly seen from figure 3.4 that under vacuum, the X-ray diffraction patterns of $AgCrO_2$ oxide at different temperatures showed that this material remained in their delafossite structure during the temperature range up to 400 °C. After this temperature range the pure phase stability destroyed with increase in temperature (> 400 °C). At 900 °C temperature the pure phase is completely destroyed and decomposed in to metallic silver and Cr_2O_3.

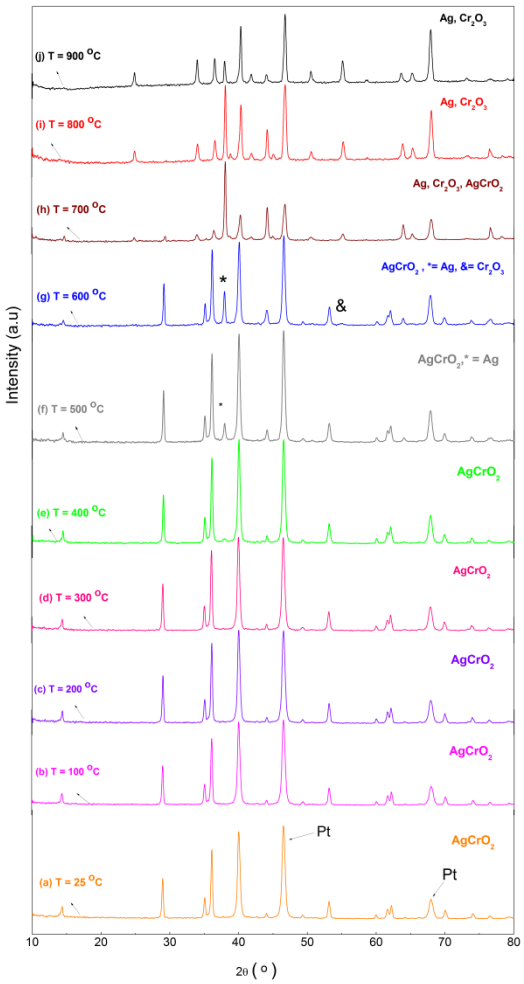

Figure 3.4. In-situ high temperature X-ray powder diffraction patterns of $AgCrO_2$ sample.

Figure 3.5.a shows the lattice parameters of $AgCrO_2$ delafossite at various temperatures calculated based on the X-ray diffraction data under vacuum. The lattice parameter *a* varies linearly with temperature. It increases with temperature till 400 $^{\circ}C$. After this temperature the pure phase product is not stable anymore. The $AgCrO_2$ phase after this temperature range decomposes into metallic silver and Cr_2O_3. Similarly, the lattice parameter *c* decreases with increase in temperature up to 400 $^{\circ}C$. Also, we have studied the thermal expansion coefficient (TEC) calculated by using the following definition $d(\Delta a/a_0)/dT$ (a: lattice constant, a_0: lattice constant at room temperature). By analyzing their lattice parameters as shown in figure 3.5.a, the TEC of $AgCrO_2$ is shown in figure 3.5.b with varying temperature. The TEC recorded at temperature 25 $^{\circ}C$, 100 $^{\circ}C$, 200 $^{\circ}C$, 300 $^{\circ}C$, 400 $^{\circ}C$ are 2.67 x 10^{-6} $^{\circ}C^{-1}$, 3.84 x 10^{-6} $^{\circ}C^{-1}$, 3.5 x 10^{-6} $^{\circ}C^{-1}$, 3.5 x 10^{-6} $^{\circ}C^{-1}$, and 8.3 x 10^{-7} $^{\circ}C^{-1}$. Thus it is clearly seen from figure 3.5.b that the thermal expansion coefficient at each temperature remains constant except at temperature 400 $^{\circ}C$. The less value of thermal expansion coefficient was observed at temperature 400 $^{\circ}C$ is due to the critical temperature range after which the pure phase of $AgCrO_2$ becomes unstable and destroys into Cr_2O_3 and metallic silver.

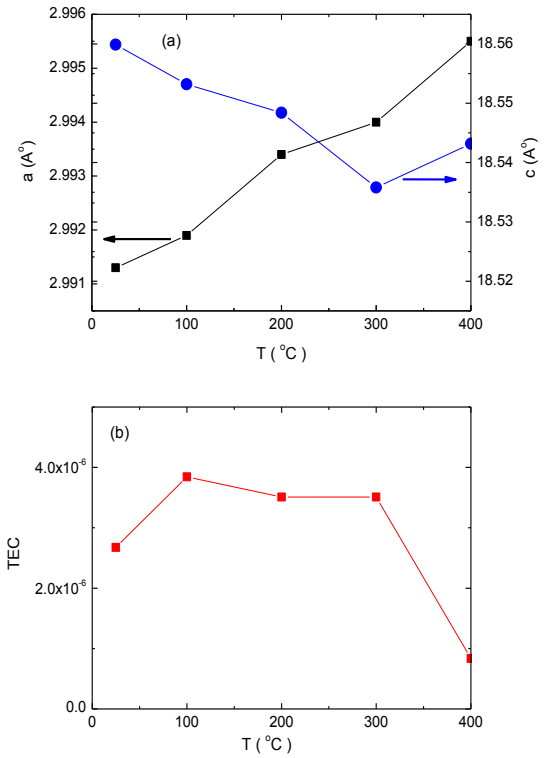

Figure 3.5. (a) Lattice parameter *a* (closed squares; left y-axis) and *c* (closed circle; right y-axis) varying with temperature. (b) Thermal expansion coefficient (TEC) varying with temperature.

3.3.3. Microstructure analysis

The morphology of the as prepared polycrystalline $AgCrO_2$ sample has been studied by SEM coupled with EDX (figure 3.6). SEM images show that the grains are in the shape of hexagonal platelets with average grain size between 0.5 to 2 μm that is slightly less than the size reported for the conventionally synthesized samples of $AgCrO_2$ [184]. The shape of the grains (hexagonal platelet) are similar to the one reported in case of $AgInO_2$ [86] or conventionally synthesized $AgCrO_2$ [184]. The cationic composition has been determined by EDX and the observed atomic Ag/Cr ratio ~ 51/49 confirms thus the expected stoichiometry (figure 3.6.b).

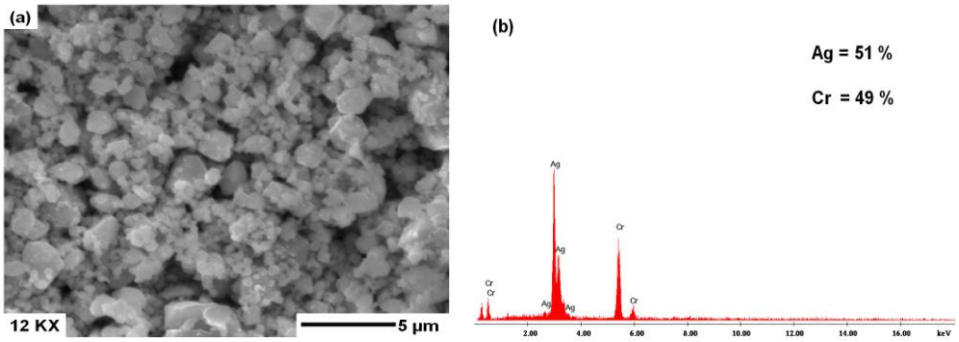

Figure 3.6. (a) SEM images of highly crystalline and uniform grains of $AgCrO_2$ at 12 KX magnification shows that the average grain size ranged from 0.5 to 2 μm. (d) EDX spectra shows the cationic composition of $AgCrO_2$.

3.3.4 dc magnetic study

Figure 3.7 shows the dc magnetic data of $AgCrO_2$ sample recorded in zero field cooled (ZFC) and field cooled modes (FC) under a magnetic field of 100 Oe in a temperature range 5–300 K. Figure 3.7.a shows the temperature dependence of the dc magnetic susceptibility data and inverse magnetic susceptibility data. Figure 3.7.b depicts the reciprocal magnetic susceptibility temperature derivative in the 5–120 K temperature range. The solid line in inverse magnetic susceptibility data (in paramagnetic temperature zone from 150-300 K) corresponds to the Curie-Weiss linear fitting. It is clear from the magnetization measurements that there exists a paramagnetic to antiferromagnetic phase transition, taken from the maximum of derivative of susceptibility temperature, around T_N = 21 K (figure 3.7.b). The temperature dependence of reciprocal magnetic susceptibility of $AgCrO_2$ is linear in the paramagnetic region (> 150 K), and obeys the Curie- Weiss law with $\theta_{cw} < 0$. The χ^{-1} (T) curve was fitted by using Curie–Weiss law ($\chi = C/T-\theta_{cw}$). The effective magnetic moment is determined by using $\mu_{eff} = \sqrt{(3k_BC/N_A)}$. The Curie-Weiss temperature was found to be $\theta_{cw} = -202$ K, which leads to $|\theta_{cw}|/T_N = 9.6$. The high value of $|\theta_{cw}|/T_N$ confirms the high degree of frustration in the $AgCrO_2$ system. The

effective paramagnetic moment per Cr^{3+} ions is μ_{eff} = 3.37 μ_B for $AgCrO_2$ sample which is close to the one reported for conventional synthesized sample [184]. The obtained values are close to the theoretical calculated magnetic moment for high spin Cr^{3+} (S = 3/2, $2[S(S+1)]^{1/2}$) μ_{eff} = 3.87 μ_B. Therefore, both X-ray diffraction and magnetic results are in agreement with literature [112,190].

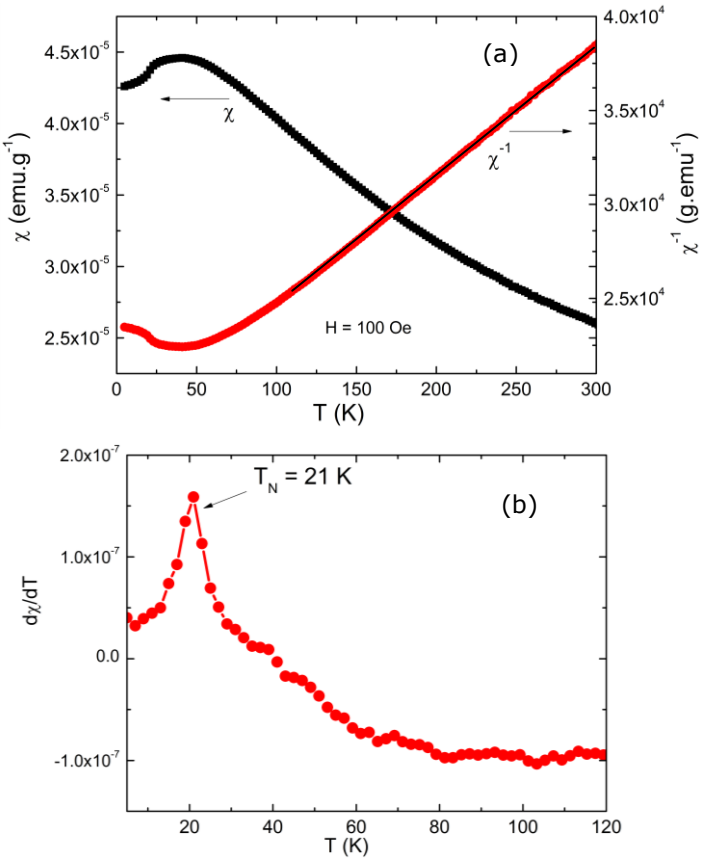

Figure 3.7. (a) dc magnetic susceptibility χ (closed squares; left y-axis) and χ^{-1} (closed circles;right y-axis) data as a function of temperature measured with H_{dc}= 100 Oe, from 5 to 300 K. The solid line in the paramagnetic region of χ^{-1} corresponds to Curie-Weiss fitting. (b) T-dependence of the reciprocal magnetic susceptibility temperature derivative in the 5–120 K temperature range.

3.3.5. Optical property study

To further investigate the optical properties of the hydrothermally grown sample of $AgCrO_2$, UV-Visible spectrum and FT-IR spectrum were recorded. The UV-visible diffuse reflectance spectrum (figure 3.8.a) shows a double absorption band in

the visible region with an absorption maxima at 400 nm and 600 nm. The optical band gap of $AgCrO_2$ was estimated by the equation $(\alpha h\nu)^2 = A(h\nu - E_g)$, where, α,ν, A, and E_g are the absorption coefficient, the frequency of light, a constant and the band gap, respectively [123-124]. The graph plotted between $(\alpha h\nu)^2$ *vs.* $h\nu$ gives the direct optical band gap. The extrapolation of the straight line to $(\alpha h\nu)^2 = 0$ axis gives the value of the optical band gap (figure 3.8.b), calculated to 1.69 eV which is slightly higher than the value reported in literature [184].

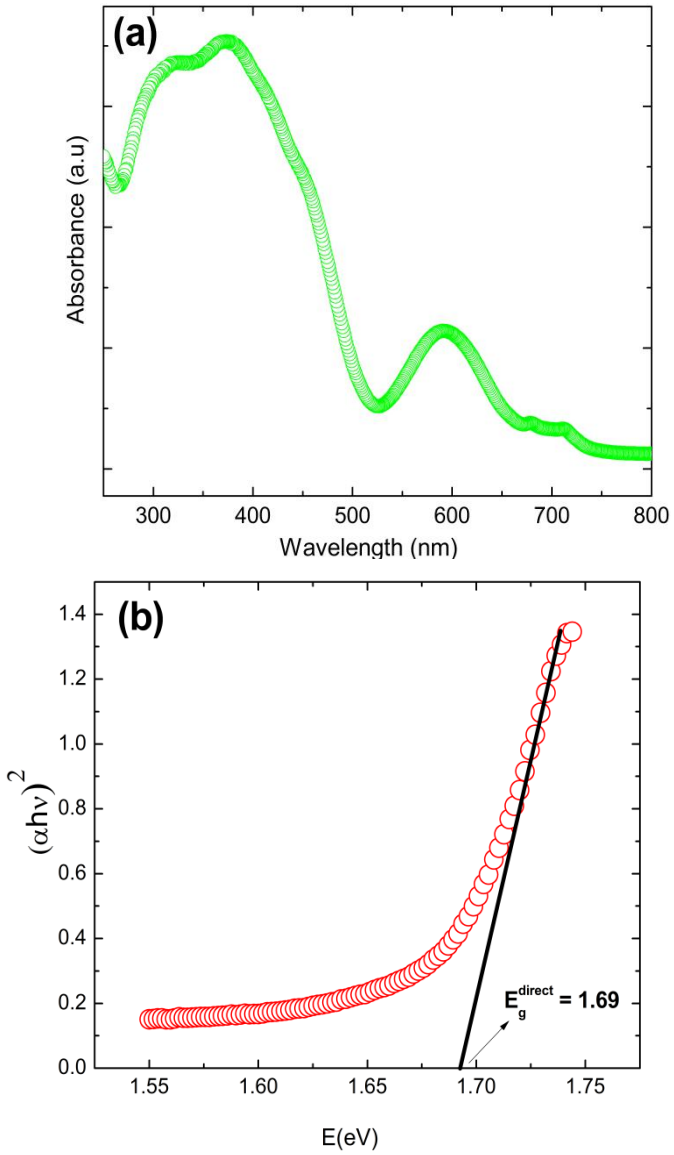

Figure 3.8. (a) UV-visible absorbance spectrum of $AgCrO_2$. (b) Band gap of $AgCrO_2$ calculated from the diffuse reflectance spectrum.

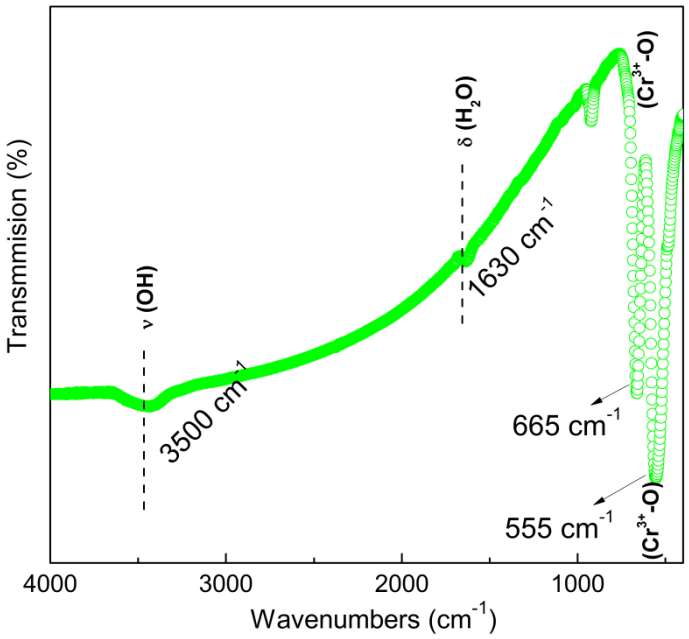

Figure 3.9. FT-IR spectrum of the $AgCrO_2$.

Furthermore, studying the FT-IR spectrum of $AgCrO_2$ shows the existence of several strong reflection peaks (figure 3.9). The strong and broad band at 3500 cm^{-1} can be attributed to the O-H vibrational mode and the absorption at 1630 cm^{-1} is assigned to the bending vibration of water, $\delta(H_2O)$ [194]. The band observed in the low-frequency 555 cm^{-1} and 665 cm^{-1} region is interpreted as vibration modes attributed to Cr^{3+}-O, close to the one reported in earlier studies [185,195,196]. Thus, the close frequency correlation of these bands in the spectra with those reported in the literature [185, 195,196] confirms the presence of silver (Ag^+) and chromium (Cr^{3+}) ions in $AgCrO_2$ compound.

3.4. Conclusion

In summary, for the first time, we have obtained a fast, high yield and controlled method for a one-step synthesis of $AgCrO_2$ polycrystalline sample using $K_2Cr_2O_7$ as oxidizing agent in an aqueous solution by new hydrothermal method. X-ray diffraction pattern attest of the quality of the material, crystallizing in *R-3m* with expected lattice parameters. Also, in situ high temperature X-ray diffraction method reveals the linear relationship between the lattice parameter with increasing temperature. The thermal expansion coefficient of $AgCrO_2$ is almost constant with increase in temperature until phase stability temperature i.e. 400 °C. At high temperature (>400 °C) the pure phase decomposes into metallic silver and Cr_2O_3

phase. SEM analysis reveals that the average particle size is in the 0.5-2 μm range. The UV-visible study and FT-IR measurement show double absorption band in the visible region with optical band gap of 1.69 eV and the absorptions due to vidrations of Cr^{3+}-O at 555 and 665 cm^{-1}, respectively. Dealing with the synthesis mechanism of $AgCrO_2$ pure phase using $K_2Cr_2O_7$ as oxidizing agent is formatted in phase diagram between temperature and pressure. Dealing with the synthesis mechanism of $AgCrO_2$ pure phase it is proposed that at temperature 400 $^{\circ}C$, the $K_2Cr_2O_7$ undergoes the following reaction:

$$4\ K_2Cr_2O_7(s) \rightarrow 4\ K_2CrO_4(s) + 2\ Cr_2O_3(s) + 3\ O_2(g) \quad [193]$$

At this temperature, the $K_2Cr_2O_7$ as an oxidizing agent gives excess oxygen in an aqueous solution that in turn oxidizes the metallic silver into Ag^+ oxidation state which reacts with the Cr^{3+} impurity in an aqueous solution. This leads to the formation of final $AgCrO_2$ compound with delafossite structure. The final compound is free of any impurity of metallic silver or CrOOH. The $K_2Cr_2O_7$ as an oxidizing agent improves the product quality and increases the product yield as compared to other oxidizing agent such as H_2O_2.

CHAPTER IV
HYDROTHERMAL SYNTHESIS OF Ag BASED SEMICONDUCTOR PHOTOCATALYST

4.1. Photo catalysis: An Introduction

Fossil fuels are non-renewable energy sources and cause the serious environmental problems accompanying their combustion. Thus, modern society has been searching for a new form of energy that is a clean, renewable, cheap, safe, and viable alternative to fossil fuels and nuclear energy. Recently, hydrogen has received considerable attention as a next-generation energy carrier and suitable energy source to replace the fossil fuel. It is well studied over the past years that photocatalytic overall water splitting using sunlight energy is a potential method of hydrogen production from renewable resources. Research interest grew in this field when photoelectrochemical (PEC) water splitting was demonstrated by using a single-crystal TiO_2 (rutile) photoanode and a Pt cathode with an external bias [197]. This effect is well-known as the Honda-Fujishima effect. In this effect, when an n-type semiconductor such as TiO_2 (anode) is illuminated by light with energy greater than the band gap of TiO_2, electrons and holes are generated in the conduction band and valence band, respectively. These electrons are collected by the Pt counter electrode when an anodic potential is applied through an external circuit. Thus, this reduces H^+ into H_2. The remaining holes behind on the surface of the TiO_2 oxidize water, forming O_2. The overall pictorial view of the reaction process is demonstrated in figure 4.1.a [198].

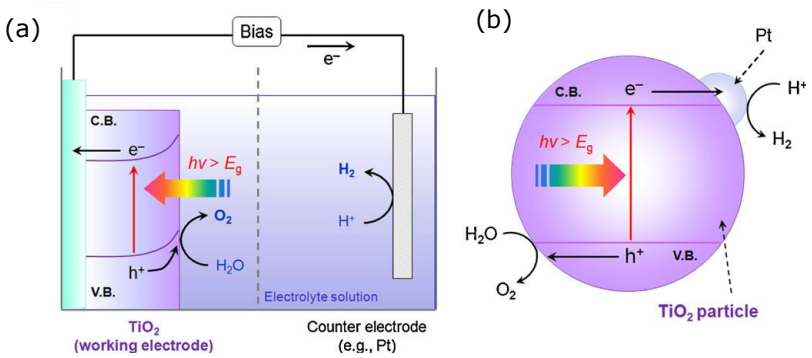

Figure 4.1. (a) Schematic representation of PEC water splitting using a TiO_2 photoanode, and (b) The corresponding short-circuit model of a PEC cell [198].

Recently, numerous PEC cells have been developed for the efficient utilization of solar energy. However, due to a lack of suitable photoelectrode materials with appropriate band-gap structures and stability, the hunt of efficient stable PEC is still on. Recently, a new proposed system such as integrated multi-layer and tandem systems is more complicated [199,200]. If the anode and cathode materials of a water-splitting PEC cell are directly coupled without an electric circuit, a metal–semiconductor composite is formed (e.g., Pt/TiO_2). Thus one can expect that water-splitting reaction is achievable on the material, as shown in figure 4.1.b. This composite (metal/semiconductor) structure has an advantage to macro-sized PEC cells. Therefore, the metal component (Pt) is generally called the "cocatalyst", and the semiconductor (TiO_2) is called the "photocatalyst".

The H_2 production via water splitting using a semiconductor particle is similar in many ways to the photosynthetic reaction. The reaction has been under investigation since last three decades, and has been widely studied by various researchers. For practical future applications, Domen et al. suggested that an area of 250,000 km^2, corresponding to 1% of the earth's desert area, would be required to provide one-third of the projected energy needs of human society in 2050 from solar energy, assuming a conversion efficiency of 10% and an integrated solar energy of AM1.5G (1 sun = 0.1 W cm^{-2}) irradiation for a day including a sunlight-angle correction [201].

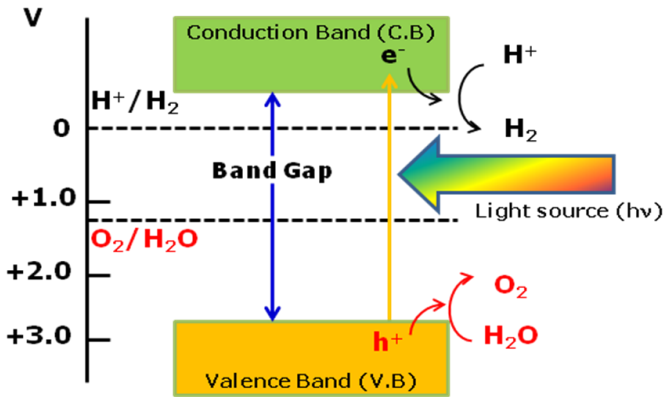

Figure 4.2. Working principle of overall water splitting on a semiconductor particle.

Figure 4.2 shows a schematic representation of the basic principles of overall water splitting on a semiconductor particle. Electron-hole pairs are generated when a semiconductor photocatalyst is illuminated by a light source with an energy equivalent to or greater than the band gap of the semiconductor photocatalyst. This excites the electrons in the valence band to the conduction band, leaving holes behind in the valence band. These photogenerated electrons and holes cause reduction of H^+ into H_2 and oxidation of water, respectively. To achieve overall

water splitting, the bottom of the conduction band must be more negative than the reduction potential of H^+ to H_2, while the top of the valence band must be more positive than the oxidation potential of H_2O to O_2. Therefore, the minimum photon energy thermodynamically required to drive the reaction is 1.23 eV, which corresponds to a wavelength of 1000 nm, in the near infrared region. Accordingly, it would appear possible to utilize the entire spectral range of visible light ($400 < \lambda < 800$ nm). However, there is an activation barrier in the charge transfer process between the photocatalyst and water molecules, requiring photon energy greater than the band gap of the photocatalyst to drive the overall water-splitting reaction at a reasonable rate. The reverse reaction that is water formation from H_2 and O_2 must be strictly inhibited, and the photocatalysts themselves must be stable in the reaction. Furthermore, although there are a large number of materials that possess suitable band-gap potentials, there is very few that function as a photocatalyst for overall water splitting, due to other factors that will be discussed below.

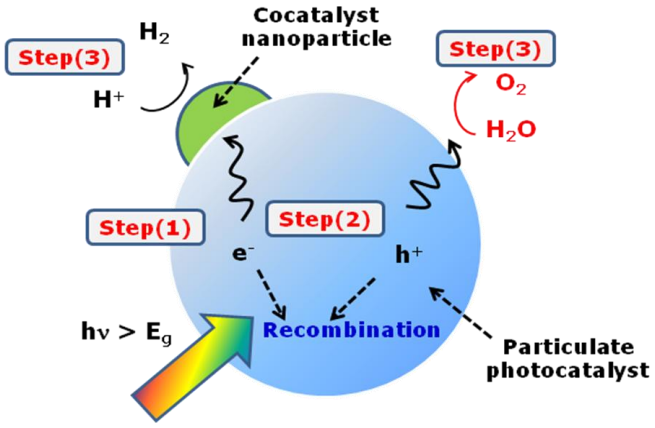

Figure 4.3. Overall steps involved in photocatalytic overall water splitting on a semiconductor particle.

Three main steps are involved in overall water splitting on a semiconductor photocatalyst as shown in figure 4.3. In step 1, the photocatalyst absorbs the photon energy that is greater than the band-gap energy of the semiconductor material and in turn generates photon excited electron–hole pairs in the bulk. In the step 2, the photon excited carriers gets separated and migrates to the surface without recombination. Finally in step 3, reduction and oxidation process takes place by the photon generated electrons and holes to produce H_2 and O_2, respectively. The first two steps are strongly dependent on the structural and electronic properties of the semiconductor photocatalyst.

In general, highly crystalline semiconductor photocatalyst has a positive effect on photoactivity. This is because the density of defects which act as

recombination centers between photogenerated carriers decreases with increasing crystallinity. Higher photocatalytic activity can also be obtained by reducing the particle size of a photocatalyst, because the diffusion length for photogenerated electron–hole pairs can be shortened. The third step, on the other hand, is promoted by the presence of a solid cocatalyst. The cocatalyst is typically a noble metal (e.g., Pt, Rh) or transition-metal oxide (e.g., NiO_x, RuO_2) and is loaded onto the photocatalyst surface as a dispersion of nanoparticles (typically < 50 nm in size) to produce active sites and reduce the activation energy for gas evolution. In most cases, cocatalysts are loaded for the promotion of H_2 evolution, presumably because most photocatalysts are unable to activate hydrogen on the surface. It is thus important to design both the bulk and surface properties of the material carefully so as to obtain a high activity for this photocatalytic reaction.

Thus, for the full utilization of solar energy spectrum or indoor artificial illuminations, broad research has been carried out to develop the more efficient visible-light sensitive photocatalysts. Recent studies of semiconductor photocatalysts for clean hydrogen energy production and environment decontamination have attracted much more attention because of demonstration of remarkable structural, optical and photocatalytic properties [197,183,202-205]. Transition-metal inorganic salts such as Ag_2CrO_4 and $Ag_2Cr_2O_7$ have been extensively studied for its application in lithium-ion batteries, photocatalysts and in the pigment industry [206-210]. Ag_2CrO_4 compound crystallizes in the orthorhombic crystal structure with a space group *Pnma* with a = 10.063 Å, b = 7.029 Å and c = 5.540 Å [211] whereas $Ag_2Cr_2O_7$ crystallizes in the triclinic space group P1 with a = 6.968 Å, b = 7.148 Å, c = 6.544 Å, α = 110.82, β = 96.11, γ = 91.05°, *and* z = 2 respectively [212]. Low-dimensional nanostructured Ag based photocatalysts are very appealing because of their unique electronic and optical properties [184,210, 212-214].

Numerous synthesis methods with complex synthesis steps have been used to synthesize Ag_2CrO_4 and very few for synthesis of $Ag_2Cr_2O_7$ compound. To the best of our knowledge, synthesis of Ag_2CrO_4 compound has been reported previously via slow diffusion process [215], cation exchange method [184], high-active acrylicamide template [214], metathetical method [215], electrosynthesis and direct precipitation method [216]; but there is no report of the synthesis of polycrystalline silver chromate and single crystal of silver dichromate by hydrothermal method at higher temperature and pressure (350 °C, 400 bars). The hydrothermal synthesis method has already been recognized as a very valuable method for processing of various complex oxides [84,64]. More recently, it is reported that the microstructure of Ag_2CrO_4 and $Ag_2Cr_2O_7$ compounds prepared via precipitation method can be controlled using sodium dodecyl sulphate (SDS) as a surfactant [212]. Also, importance of pH in an aqueous solution was reported in microwave hydrothermal synthesis of Ag_2CrO_4 compound [209].

Here, in this work we report for the first time a facile method for the synthesis of single phase Ag_2CrO_4 polycrystalline sample and single crystal of $Ag_2Cr_2O_7$ (size about ~ 3 mm x 2 mm) using a one-step hydrothermal process, starting from a mixture of Ag_2O and CrO_3 in an aqueous solution. The final products were characterized by X-ray diffraction (XRD), Scanning Electron Microscope (SEM) coupled with Energy dispersive X-ray spectroscopy (EDX), UV-visible diffuse reflectance spectroscopy (UV-visible DRS) and Fourier transform infrared

spectroscopy (FT-IR). The surface area analysis on Ag_2CrO_4 sample was performed via BET surface area analysis method. The final products are not only the single phase purity but also in line with the structural and optical properties reported in earlier studies [209-212,184,214].

4.2. Experimental details

We noticed Cr^{6+} impurity phase in addition to main phase of $AgCrO_2$ during the synthesis of $AgCrO_2$ compound at temperature less than 400 $^{\circ}$C. This is reported clearly in figure 3.1. Figure 3.1 (chapter 3) shows the temperature and pressure phase diagram of Ag_2O and $Cr(OH)_3$ precursors in an aqueous solution at temperature less than 400 $^{\circ}$C. The preliminary study of the phase diagram reported in chapter 3 allows us to further work on the synthesis of Ag_2CrO_4 or $Ag_2Cr_2O_7$ compounds by varying the process condition. To keep this goal in our mind, we prepared several samples via a direct reaction between Ag_2O and CrO_3 instead of $Cr(OH)_3$ (precursor used during the synthesis of $AgCrO_2$) using mild hydrothermal condition. We started with CrO_3 as a precursor because of high solubility at low temperature and it exhibit Cr^{6+} oxidation state in an aqueous solution in both acidic and basic medium. A stainless steel (SS) autoclave (12NiCr250, < 450 $^{\circ}$C, < 1000 bars) was used to prepare the polycrystalline sample of Ag_2CrO_4 and single crystal of $Ag_2Cr_2O_7$ compounds via hydrothermal. The temperature was recorded by a temperature controller (E5CK-TAA1-500 100-240 AC Regulator Temperature OMRON) and the pressure was controlled by Kennedy's PVT diagram of water [81]. Several synthesis conditions used to obtain the final pure compound of Ag_2CrO_4 and single crystal of $Ag_2Cr_2O_7$. Table 4.1 summarizes the experimental condition used during the synthesis of Ag based semiconductor photo catalysts. It is clear from the table 4.1 that the pH of the solution plays an important role in the formation of Ag_2CrO_4 and single crystal of $Ag_2Cr_2O_7$ as reported in earlier studies [209].

In case of synthesis of Ag_2CrO_4 polycrystalline compound, solutions were prepared by dissolving precise amounts of 2.263 g of Ag_2O (0.5 M, Merck KGaA, purity > 99 %,), 1.958 g of CrO_3 pellets (1 M, Merck KGaA, purity > 99 %,) and 1 M of NaOH pellets (Merck KGaA, purity > 99 %) in 28 ml SS autoclave filled with 19.6 ml of deionized water. NaOH was used to control the pH and the product solubility [120]. The room temperature pH value of a precipitated solution was calculated as 10.5. The precipitated solution was more basic in nature as revealed by the high pH value. The autoclave was then tightly sealed and placed in a high temperature furnace at the reaction temperature of 350 $^{\circ}$C for 12 hours and under a pressure of up to ~ 400 bars (calculated from Kennedy's PVT diagram of water [81]). After the given reaction time, the autoclave was allowed to cool at a rapid rate (50 $^{\circ}$C/hr). Then, the autoclave was opened and the brown powder of Ag_2CrO_4 was recovered by filtration. Whereas, single crystal of $Ag_2Cr_2O_7$ were grown by dissolving precise amounts of 2.263 g of Ag_2O (0.5 M) and 1.958 g of CrO_3 pellets (1 M) in 28 ml SS autoclave filled with 19.6 ml (70 % fill to the total volume of autoclave) of deionized water. Similarly as reported in case of Ag_2CrO_4, the room temperature pH value of a precipitated solution in this case was calculated as 2.5. The low value suggests the precipitated solution is more acidic in nature. The 70 fill percent volume of deionized water to the total volume of the autoclave will give the expected pressure range. In our case the calculated pressure (by Kennedy water phase diagram) was 400 bars.

The autoclave was then tightly sealed and placed in a high temperature furnace at the reaction temperature of 350 °C for 12 hours and under a pressure of up to ~ 400 bars (calculated from Kennedy's PVT diagram of water). After the given reaction time, the autoclave was allowed to cool at a rapid rate (50 °C/hr). Then, the autoclave was opened and black color crystal of $Ag_2Cr_2O_7$ was recovered by filtration. The crystal was grown two times under the same process condition mentioned in table 4.1 to check the repeatability of the synthesis process. Also, to check the effect of reaction time on the formation of final product of Ag2CrO4 compound has been studied.

Table 4.1. Experimental process condition used to synthesize Ag based photocatalysts.

Molar concentration	t (hr)	Mineralizer	T (°C)	P (bar)	XRD results
1mmol + 2mmol	12	2.5M NaOH	200	<10	**Ag_2O**,Cr^{6+}(solution)
1mmol + 2mmol	12	1M NaOH	200	<10	**Ag_2O**,Cr^{6+}(solution)
1mmol + 2mmol	60	2.5M NaOH	250	<20	**Ag_2O**,Ag* Cr^{6+}(solution)
1mmol + 2mmol	24	2.5M NaOH	250	<20	**Ag_2O**,Ag* Cr^{6+}(solution)
1mmol + 2mmol	24	1M NaOH	250	<20	**Ag_2O**,Ag* Cr^{6+}(solution)
1mmol + 2mmol	12	1M NaOH	300	<50	**Ag**,Ag_2O* Cr^{6+}(solution)
0.25M + 0.5M	24	0.2M of oxylic acid	250	<20	CrOOH,$Ag_2Cr_2O_7$*
0.25M + 0.5M	24	0.1M of oxylic acid	250	<20	**Ag_2CrO_4***,Ag*, $AgCrO_2$*,Ag_2O*
0.5M + 1M	1	1M NaOH	350	400	**Ag**,Cr^{6+}(solution)
0.5M + 1M	6	1M NaOH	350	400	Ag_2CrO_4'
0.5M + 1M	12	1M NaOH	350	400	**Ag_2CrO_4**
0.5M + 1M	12	0	350	400	$Ag_2Cr_2O_7$ crystals

bold = majority phase, * = minor phase, '= less intense

Powder X-ray diffraction (PXRD) patterns were collected on powdered samples of Ag_2CrO_4 and Ag_2Cr2O_7 (crystals crushed into powder) by using a PANalytical X'pert Pro diffractometer (Cu K_α, $10^\circ \leq 2\theta \leq 80^\circ$). Rietveld refinement was performed using the FULLPROF program using Pseudo-Voigt profile function

[66]. A Scanning Electron Microscope (Inspect^{TM} S, FEI) coupled with Energy dispersive X-ray spectroscopy (EDX) was used to observe the microstructure and determine the cationic compositions of the as synthesized Ag_2CrO_4 (powder sample) and $Ag_2Cr_2O_7$ (single crystal). The topographical images of $Ag_2Cr_2O_7$ crystal was studied by atomic force microscopy (AFM Model Nanosurf® EasyScan 2 Advanced Research). The UV-visible diffuse reflectance spectra of the powdered samples of Ag_2CrO_4 and Ag_2Cr2O_7 (crystal crushed into powder) mixed with $MgCO_3$ were analyzed by UV-visible spectrophotometer (LAMBDA 950 UV/Vis/NIR Spectrophotometer, PerkinElmer, wavelength range up to 3300 nm). The vibrational spectrum of the powdered samples of Ag_2CrO_4 and Ag_2Cr2O_7 mixed with KBr were then pressed in the shape of pellets (4 mm diameter, 1 mm thickness) was recorded by means of Fourier transforms infrared spectrophotometer (VERTEX 70 FT-IR spectrometer, Bruker). The Brunauer–Emmett–Teller (BET) surface area was determined on powder of Ag_2CrO_4 sample by nitrogen adsorption–desorption isotherm measurements at 77 K on a Quantachrome NOVA200E system.

4.3. Results and discussion

4.3.1. Structural Analysis

The X-ray diffraction pattern of the polycrystalline sample of Ag_2CrO_4 prepared by hydrothermal synthesis (figure 4.4.a) is in agreement with the expected one for Ag_2CrO_4 [208], no impurity is observed in addition. The sharpness of the diffraction peaks indicates that the product is well crystallized. Accordingly, the structure was refined using crystallographic parameters reported in [208], leading to cell parameters a = 10.0423(6) Å, *b* = 7.0247(4) Å and *c* = 5.5358(3) Å, in the *Pnma* space group. The X-ray diffraction pattern was refined by using FullProf software. Figure 4.4 shows the good agreement between the calculated and the observed profiles (figure 4.4.a) and the corresponding drawing of the structure (figure 4.4.b). As shown in the structure, the two crystallographically independent silver atoms form different polyhedra. The Ag1 atom creates octahedra with surrounding 6 oxygen atoms whereas second Ag2 atom creates badly distorted tetrahedra with surrounding 4 oxygen atoms. While Cr atom makes tetrahedra with 4 oxygen atoms. The CrO_4 tetrahedra and AgO_4 distorted tetrahedral are connected via vertexes whereas the AgO_6 octahedra are connected via edges. The two kinds of tetrahedra (CrO_4 tetrahedra and AgO_4 distorted tetrahedra) lie between AgO_6 octahedral layers connected via their corresponding vertexes with AgO_6 octahedra. The chains of AgO_6 octahedra and layers of CrO_4 and AgO_4 construct a three-dimensional network. The structural results of the sample prepared by the hydrothermal method are consistent with the ones reported for conventionally synthesized sample of Ag_2CrO_4 [208-211,184,213-214].

Similarly, the powder X-ray diffraction pattern of the $Ag_2Cr_2O_7$ powder sample (piece of the crystal powdered) prepared by hydrothermal synthesis is found to be characteristic of a triclinic crystal structure with the space group *P*-1 (figure 4.5.a). The measured cell parameters are *a* = 6.9512(5) Å, *b* = 7.1268(5) Å, *c* = 6.5288 (4) Å, α = 110.86(3), β = 96.10(4), and γ = 91.03(5) which are consistent with previous reports [212]. The powder X-ray diffraction pattern was recorded on single crystal of $Ag_2Cr_2O_7$ as shown in figure 4.5.b. A small piece of crystal was

crushed into powder and X-ray diffraction was collected (photo of crystal is shown in inset of figure 4.5.b. Accordingly, Rietveld refinement was performed for the $Ag_2Cr_2O_7$ sample choosing the initial parameters from reported values [212]. The deduced crystal structure of $Ag_2Cr_2O_7$ is shown in figure 4.6 by both polyhedral (figure 4.6.a) and ball-stick model (figure 4.6.b). As shown in the crystal structure, the two crystallographically independent silver atoms form different polyhedra. The Ag1 atom creates a distorted octahedra with surrounding 6 oxygen atoms whereas

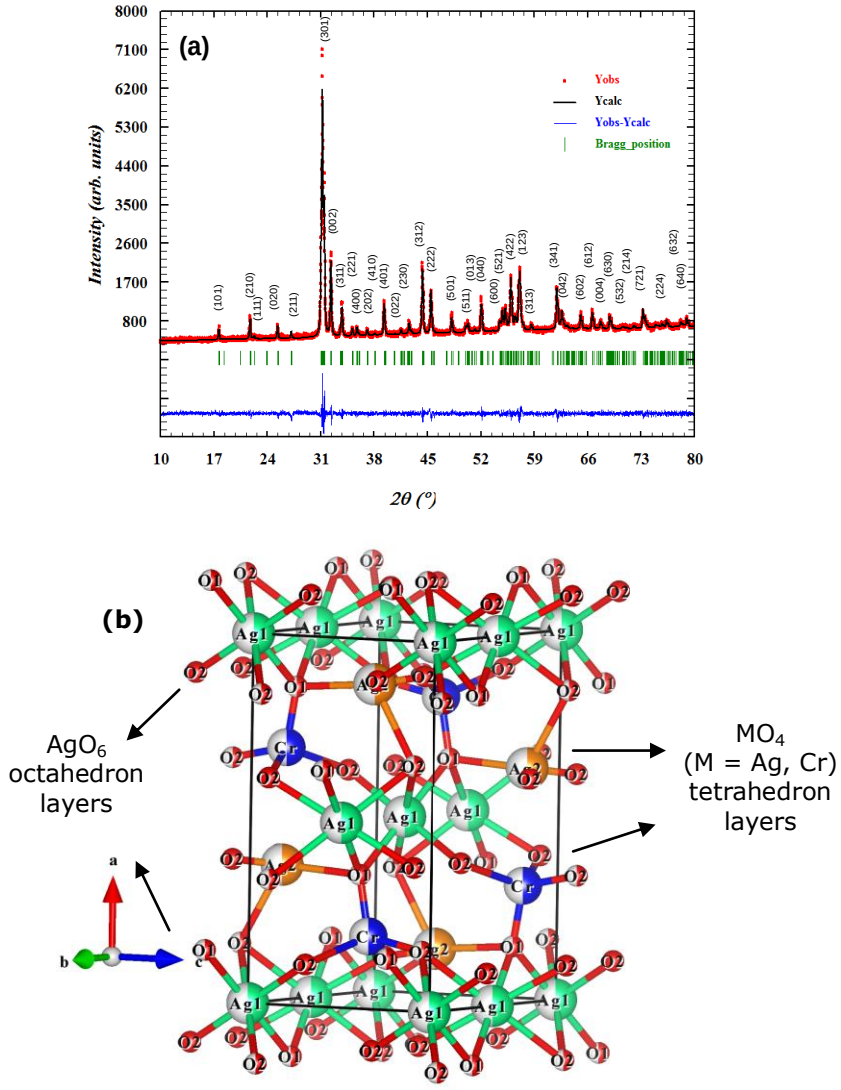

Figure 4.4. (a) Room temperature X-ray Rietveld refinement of the Ag_2CrO_4 product (b) Resulting ball and stick model of Ag_2CrO_4 (orthorhombic structure).

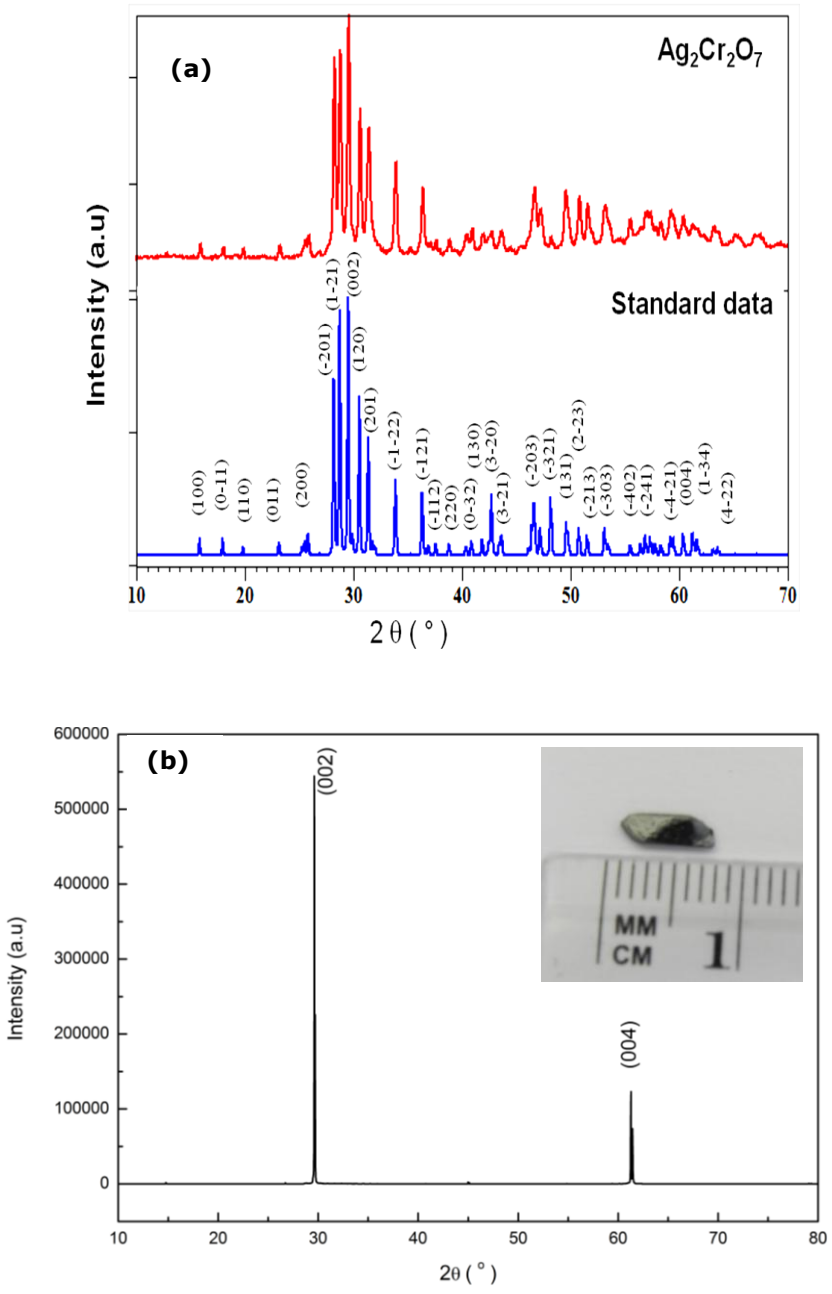

Figure 4.5. (a) Room temperature X-ray diffraction pattern of the powdered sample of $Ag_2Cr_2O_7$ and (b) Room temperature X-ray diffraction pattern of $Ag_2Cr_2O_7$ single crystal (inset shows the photo of the crystal used for XRD).

second Ag2 atom creates badly distorted tetrahedra with surrounding 4 oxygen atoms. Similarly Cr atom creates two types of tetrahedral. Cr1 atom forms a normal tetrahedral surrounded by four oxygen atoms whereas the Cr2 atom forms a slightly distorted tetrahedra that also surrounds 4 oxygen atoms. The slightly distorted CrO_4 (formed by Cr1 and Cr2 atom) tetrahedral shares the vertexes with distorted octahedra (formed by Ag1 atom) and badly distorted tetrahedra (formed by Ag2 atom). The two kinds of polyhedra, AgO_6 distorted octahedra and badly distorted AgO4 tetrahedra are connected via edges. The corresponding chains of the different types of polyhedra construct a three-dimensional network.

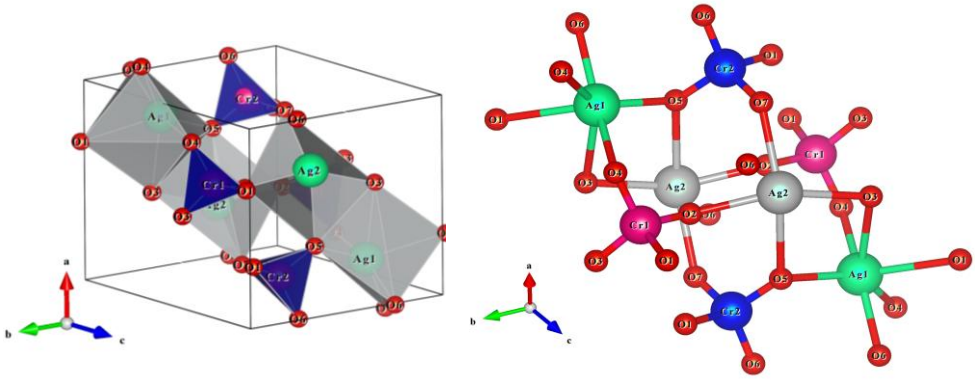

Figure 4.6. Resulting triclinic structure (P-1 space group) shown by (a) polyhedra and (b) ball-stick model deduced from the FullProf refinement.

Dealing with the synthesis mechanism involved in the formation of polycrystalline sample of Ag_2CrO_4 and single crystal of $Ag_2Cr_2O_7$ we propose the following mechanism. It is well studied that Ag^{+1} exists primarily in the form of soluble $Ag(OH)_2^-$ and the concentration of soluble $Ag(OH)_2^-$ species increases with temperature [84]. The Cr^{6+} ions in aqueous solution exist in the following form of reversible equation (4.1).

$$Cr_2O_7^{2-}(aq) + H_2O\ (l) \Longleftrightarrow 2\ CrO_4^{2-}(aq) + 2\ H^+\ (aq) \quad \log k_1 = 14.85 \quad (4.1)$$

Also, it was reported in earlier studies [217] that, chromium (VI) is present in aqueous solution as chromate (CrO_4^{2-}) and dichromate ($Cr_2O_7^{2-}$) species. In acidic condition (pH < 6), dichromate ions ($Cr_2O_7^{2-}$) predominates over chromate ions (CrO_4^{2-}). Thus, adding Ag_2O and CrO_3 in an aqueous solution gives $Ag(OH)_2^-$ and chromate ($Cr_2O_7^{2-}$) species in acidic solution (pH value of the precipitated solution recorded at room temperature was 2.5), which in turn leads to the formation of the $Ag_2Cr_2O_7$ single crystal at elevated temperature (350 °C) and pressure (400 bars). Similarly, adding NaOH in an aqueous solution as in case of synthesis of Ag_2CrO_4

sample turn the solution more basic. The pH value of the precipitated solution (basic medium) recorded at room temperature was 10.5. Thus in this case under the basic medium the reverse condition takes place that is chromate ions (CrO_4^{2-}) predominates over dichromate ions ($Cr_2O_7^{2-}$). This suggests that direct reaction between Ag_2O and CrO_3 in the presence of NaOH (1 M) at 350 °C temperature and pressure of 400 bars leads to the formation of Ag_2CrO_4 polycrystalline sample.

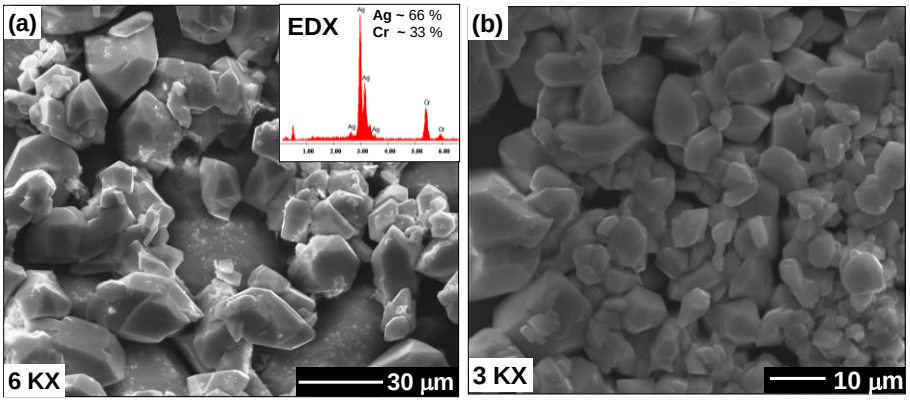

Figure 4.7. (a) and (b) SEM images of highly crystalline and uniform grains of Ag_2CrO_4 at different magnification. Inset of (a) shows EDX spectra shows the cationic composition of Ag_2CrO_4.

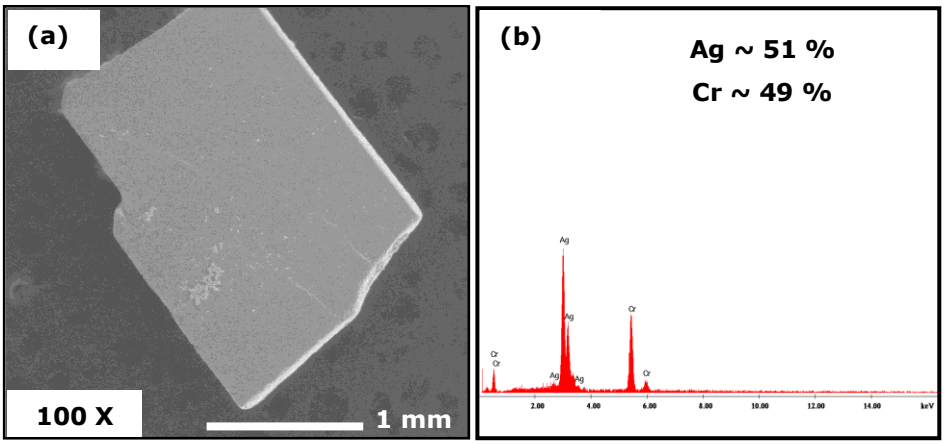

Figure 4.8. (a) SEM images $Ag_2Cr_2O_7$ at 100 X magnification (b) EDX spectra shows the cationic composition of $Ag_2Cr_2O_7$.

4.3.2. Surface Analysis

The surface morphology of the as prepared powdered sample of Ag_2CrO_4 and crystal of $Ag_2Cr_2O_7$ has been studied by SEM coupled with EDX (figure 4.7 and 4.8). Figure 4.7 shows the SEM images of Ag_2CrO_4 sample at different magnification. SEM images show the non uniformity in grain size. The grain size of Ag_2CrO_4 samples varies from 1 μm to 10 μm. The average grain size of the hydrothermally synthesized Ag_2CrO_4 sample is larger than the one reported for the conventionally synthesized samples of Ag_2CrO_4 [211, 184, 214-216]. The silver and chromium cationic composition has been determined by EDX and the observed Ag/Cr ratio ~ 66/33 confirms the desired stoichiometry of Ag_2CrO_4 (inset of figure 4.7.a). Similarly, figure 4.8 shows the SEM images of the single crystal of $Ag_2Cr_2O_7$. The silver and chromium cationic composition has been determined by EDX and the observed Ag/Cr ratio ~ 1 confirms the desired stoichiometry of $Ag_2Cr_2O_7$. To study the topographical images of the crystal, the atomic force microscopy was performed on the crystal of $Ag_2Cr_2O_7$. Figure 4.9 shows the AFM planner view of the 3 mm by 2 mm size crystal of $Ag_2Cr_2O_7$. Atomic force microscopy images (figure 4.9.a-b) disclose AFM 3D images of crystal. The defects can be clearly seen from the figure 4.9a-b 3D images.

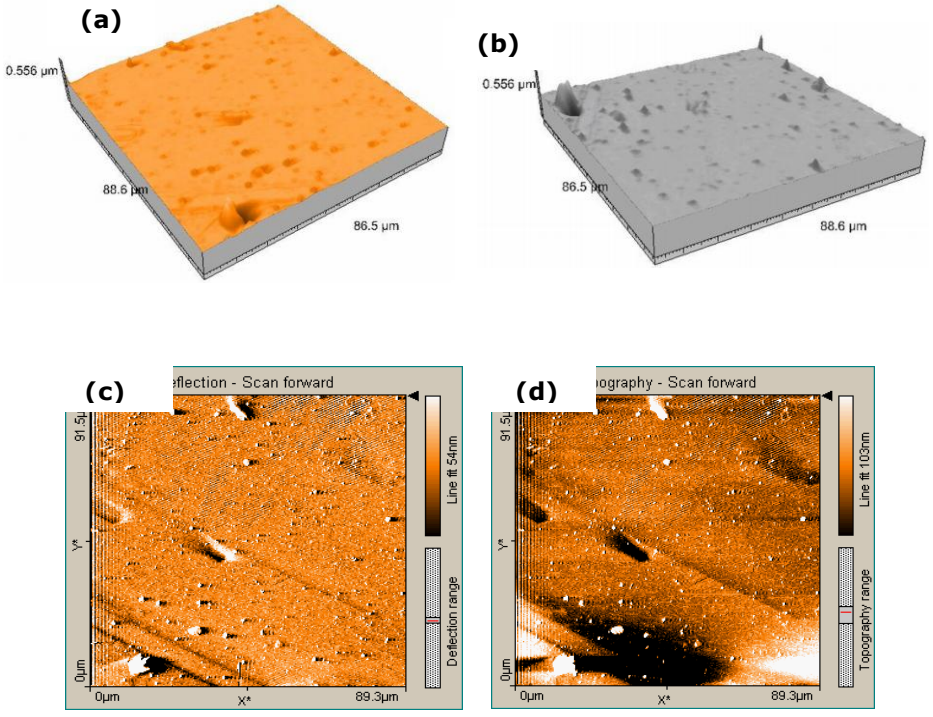

Figure 4.9. (a), (b) AFM 3D images of $Ag_2Cr_2O_7$ single crystal at 88.6 X 88.6 µmm^2. (c), (d) The dark dig in deflection and topography scan shows the dislocation.

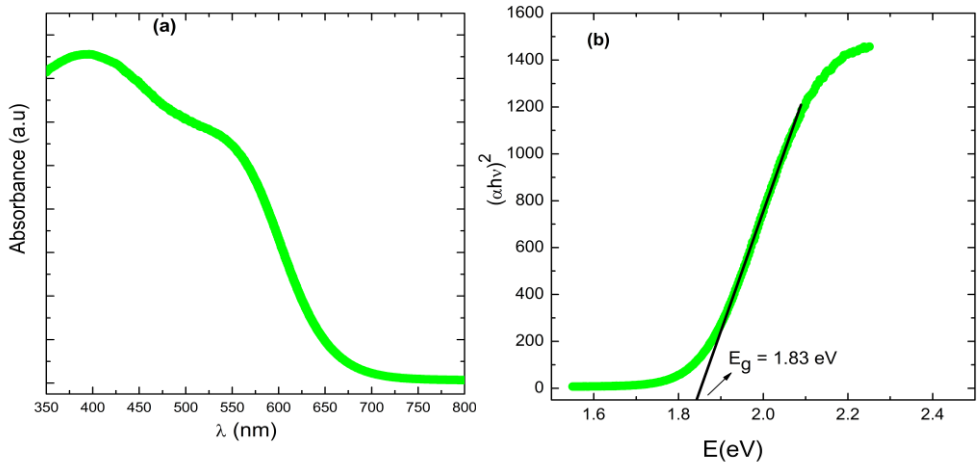

Figure 4.10. (a) UV-visible absorbance spectra of Ag_2CrO_4. (b) Band gap of Ag_2CrO_4 calculated from absorbance spectra.

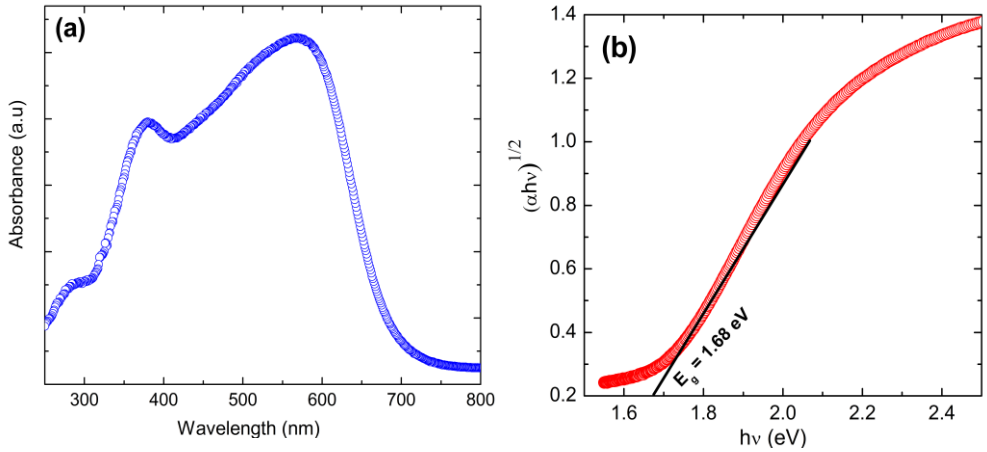

Figure 4.11. (a) UV-visible absorbance spectra of $Ag_2Cr_2O_7$. (b) Band gap of $Ag_2Cr_2O_7$ calculated from absorbance spectra.

4.3.3. Optical property characterization

To further investigate the optical properties of the hydrothermally grown powdered sample of Ag_2CrO_4 and $Ag_2Cr_2O_7$, UV-Visible spectrum and FT-IR spectrum were recorded. Figure 4.10, 4.11, 4.12, and 4.13 shows the UV-visible

diffuse reflectance spectrum and FT-IR spectrum of the Ag_2CrO_4 and $Ag_2Cr_2O_7$ powdered sample. It is clear from figure 4.10.a that the hydrothermally grown Ag_2CrO_4 sample shows the sharp absorption band in the visible region maxima at 520 nm. The shape of absorption spectrum for Ag_2CrO_4 compound differs from the one reported in Ag_2CrO_4 sample prepared by the cation exchange method [184]. The indirect optical band gap of the Ag_2CrO_4 sample was estimated by the equation $(\alpha h\nu)^{1/2} = A(h\nu - E_g)$, where, $\alpha, \nu,$ A and E_g are the absorption coefficient, the frequency of light, a proportionality constant and the band gap respectively [123-124]. The slope of the graph between $(\alpha h\nu)^{1/2}$ and $h\nu$ gives the value of the optical band gap. In this case, the calculated indirect optical band gap of Ag_2CrO_4 (figure 4.10.b) is 1.62 eV which is slightly less than the one reported in earlier studies [184]. This slight difference in band gap could be due to non uniform average grain size in hydrothermally grown sample of Ag_2CrO_4 compared to conventional methods [211, 184, 214-216, 218,219]. We have studied the optical properties of single crystal of $Ag_2Cr_2O_7$ not reported in earlier studies [208,211]. Figure 4.11 shows the absorbance spectrum of $Ag_2Cr_2O_7$ powder sample (piece of crystal crushed into powder). The UV-visible diffuse reflectance spectrum (figure 4.11.a) shows a double absorption band in the visible region with absorption maxima at 380 nm and 570 nm. The indirect optical band gap was estimated by the equation $(\alpha h\nu)^2 = A(h\nu - E_g)$. The indirect band gap of $Ag_2Cr_2O_7$ sample was calculated to 1.68 eV as shown in figure 4.11.b.

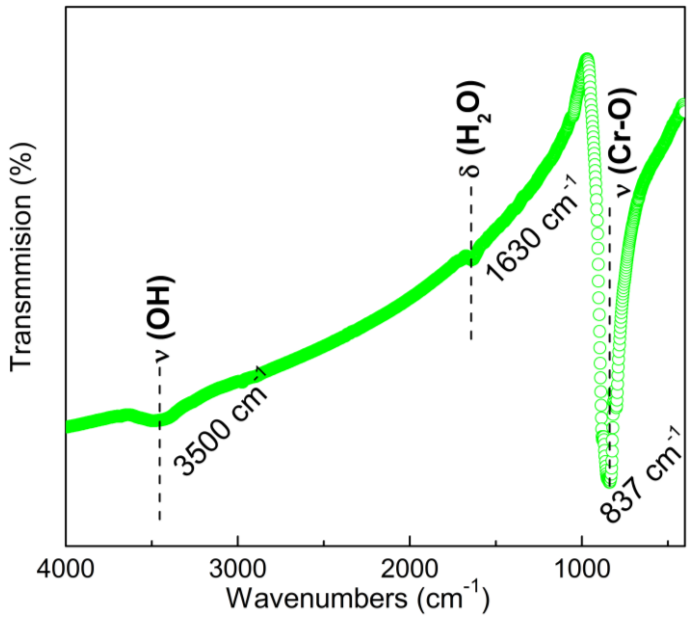

Figure 4.12. The FT-IR spectra of Ag_2CrO_4 product.

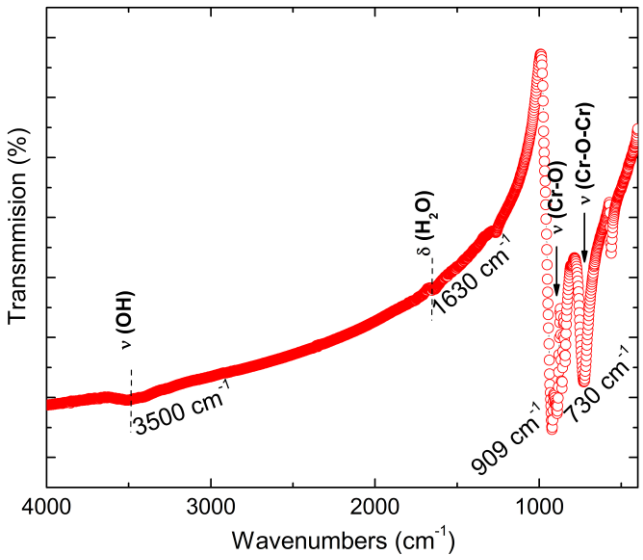

Figure 4.13. The FT-IR spectra of $Ag_2Cr_2O_7$ product.

Furthermore, studying the FT-IR spectrum of Ag_2CrO_4 and $Ag_2Cr_2O_7$ product shows the existence of reflection peaks (figure 4.12 and 4.13). FT-IR spectrum of polycrystalline sample of Ag_2CrO_4 is shown in figure 4.12. It is clear from the figure 4.12 that the strong and broad band appearing at 3500 cm^{-1} can be attributed to the O-H vibrational mode. The absorption at 1630 cm^{-1} is assigned to the bending vibration of water, $\delta(H_2O)$ [198]. The other band observed in the low-frequency 837 cm^{-1} region of the IR spectrum is interpreted as the vibrational modes attributed to the Cr-O vibration which is close to the one reported in earlier studies [214, 220].

Similarly, FT-IR study on the powder sample of $Ag_2Cr_2O_7$ is shown in figure 4.13. As observed in Ag_2CrO_4 sample above, the O-H vibrational mode and bending vibration of water, $\delta(H_2O)$ was observed at the same frequency in $Ag_2Cr_2O_7$ sample. The other bands are observed in the low-frequency region at 910 cm^{-1} and 730 cm^{-1}. These bands corresponds to the vibration modes (particularly ν_{as}) of Cr(VI)-O and Cr(VI)-O-Cr(VI) vibrational bands. These vibrational band values are close enough to the one reported in earlier studies [202, 221]. Thus, FT-IR study reveals that both compounds i.e. Ag_2CrO_4 and $Ag_2Cr_2O_7$ shows the existence of Cr(VI)-O and Cr(VI)-O-Cr(VI) vibrational bands at their perspective frequencies.

4.3.4. Surface area study (BET analysis)

The BET method is the most widely used procedure for the determination of the surface area of solid materials and involves the use of the BET equation shown below in equation 4.2 [222].

$$\frac{1}{W\left(\left(\frac{P}{P_o}\right)-1\right)} = \frac{1}{W_m C} + \frac{C-1}{W_m C}\left(\frac{P}{P_o}\right) \qquad (4.2)$$

where W is the weight of gas adsorbed at a relative pressure, P/P_0, and W_m is the weight of adsorbate constituting a monolayer of surface coverage. The term C, the BET C constant, is related to the energy of adsorption in the first adsorbed layer and consequently its value is an indication of the magnitude of the adsorbent/adsorbate interactions. The BET equation requires a linear plot of $1/[W(P/P_0)-1]$ vs. P/P_0 which for most solids, using nitrogen as the adsorbate, is restricted to a limited region of the adsorption isotherm, usually in the P/P_0 range of 0.05 to 0.35. This linear region is shifted to lower relative pressures for microporous materials.

The performance of a battery can be characterized according to the amount of energy that it can store or the amount of power that it can produce. For a particular cell chemistry and battery size, the performance can be optimized for high energy capacity or high power. The power of a battery or its current handling capacity is dependent on the rate of the reaction between the electrodes and electrolyte. This is affected by the particle size distribution of the electrode material, as this defines the available surface area. Thus, particle size of the electrode material used in the Li-ion batteries plays an important role in the device performance [223-224].

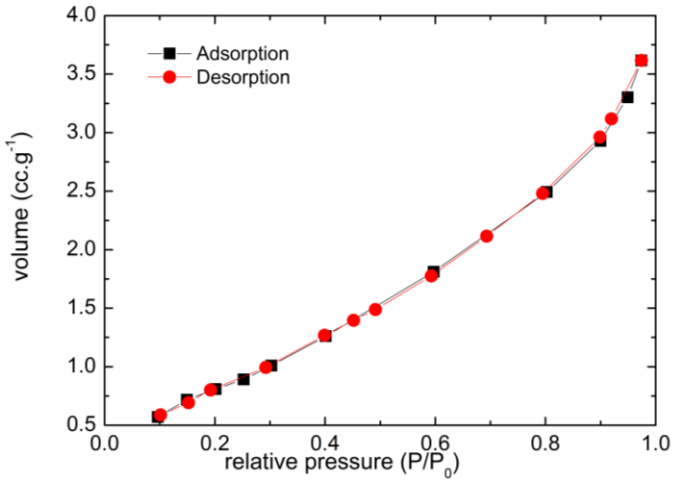

Figure 4.14. BET isotherm of Ag_2CrO_4 sample (relative pressure versus volume plot).

Herein, the surface area of Ag_2CrO_4 sample was recorded by BET (Brunauer, Emmett, and Teller) surface area measurement system. For each analysis ~ 0.2 g of sample was used. The accuracy of measurements performed by this equipment was

± 5 %. Figure 4.14 shows the type II N_2 adsorption-desorption isotherm cycle for Ag_2CrO_4 sample. In this type of surface isotherm measurement the adsorption occurs on nonporous powders or powders with diameters exceeding micropores. Inflection point occurs near the completion of the first adsorbed monolayer. The specific surface area of hydrothermally grown Ag_2CrO_4 sample is 3.42 $m^2.g^{-1}$. This value is larger than the values reported in recent study of Ag_2CrO_4 sample prepared via microwave hydrothermal and direct precipitation method [209-210]. The non uniform particle size distribution in Ag_2CrO_4 sample could be the possible reason for enhancement in surface area value. From the pore volume distribution curve (figure 4.15), the pore volume and average pore diameter of Ag_2CrO_4 sample was found to be 0.01 $cm^3.g^{-1}$ and 3.42 nm. Thus the large value of surface area reported in hydrothermally grown Ag_2CrO_4 sample may also enhance the performance of Li-ion batteries. Therefore further work is required to check the photocatalytic and battery performance by using the Ag_2CrO_4 sample grown by hydrothermal under mild condition described above.

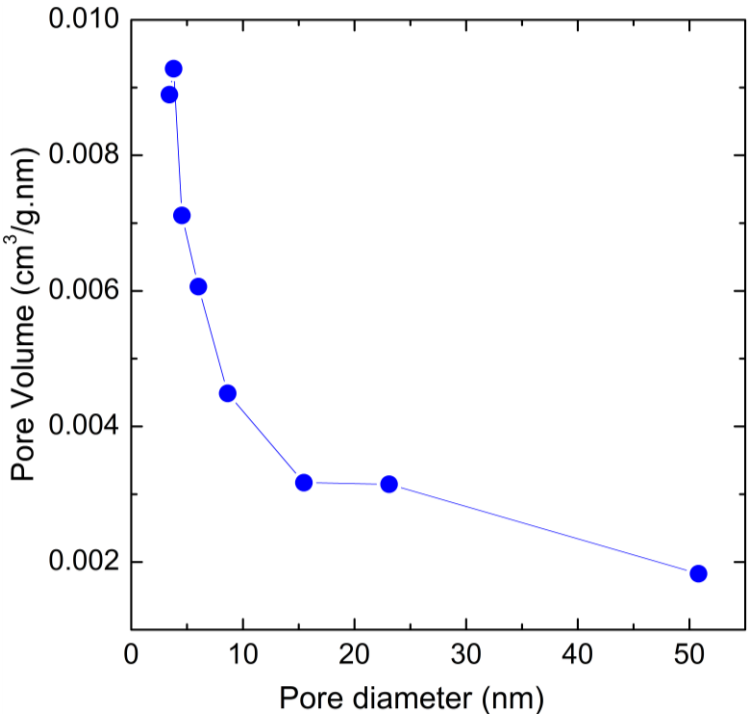

Figure 4.15. Pore size distribution of Ag_2CrO_4 sample.

4.4. Conclusion

In summary, for the first time we have explored a simple, fast and easily controlled method for the synthesis of single phase of polycrystalline sample Ag_2CrO_4 and single crystal of $Ag_2Cr_2O_7$ via direct reaction between Ag_2O and CrO_3 precursors under mild hydrothermal condition. pH value of the solution played an important role during the final phase formation. It is concluded that sample prepared in acidic medium gives rise to the formation of single crystal of $Ag_2Cr_2O_7$ whereas addition of the NaOH in the solution turns the solution more basic that leads to the formation of Ag_2CrO_4 compound (polycrystalline sample). X-ray diffraction pattern of the Ag_2CrO_4 sample is typical characteristic of an orthorhombic crystal structure with the space group *Pnma.* Similarly, the powder X-ray diffraction pattern of the $Ag_2Cr_2O_7$ powder sample (piece of the crystal crushed into powder) prepared by hydrothermal synthesis is found to be characteristic of a triclinic crystal structure with the space group *P*-1*.* SEM analysis of Ag_2CrO_4 sample revealed that the average particle size varied from 1 to 10 μm with Ag/Cr ratio ~ 2 confirms the desired stoichiometry of Ag_2CrO_4. While in case of $Ag_2Cr_2O_7$ sample the SEM-EDX confirms the desired stoichiometry of Ag/Cr ratio ~ 1. The UV-visible study and FT-IR measurement of Ag_2CrO_4 sample show a sharp absorption band in the visible region with absorption maxima located at 500 nm with indirect optical band gap of 1.62 eV and the vibrational peak of Cr-O at 837 cm^{-1}, respectively. The FT-IR study of $Ag_2Cr_2O_7$ sample reveals the vibrational band at frequency 910 cm^{-1} and 730 cm^{-1}. These bands correspond to the vibration of Cr(VI)-O and Cr(VI)-O-Cr(VI). The UV-visible diffuse reflectance spectrum shows a double absorption band in the visible region with an absorption maxima located at 380 nm and 570 nm. The indirect optical band gap of $Ag_2Cr_2O_7$ sample was estimated to 1.68 eV. The surface area of Ag_2CrO_4 sample is found to be 3.42 m^2/g larger than the one reported in Ag_2CrO_4 sample prepared by conventional method. The pore volume and average pore diameter of Ag_2CrO_4 sample was found to be 0.01 $cm^3.g^{-1}$ and 3.42 nm. Thus the large value of surface area reported in hydrothermally grown Ag_2CrO_4 sample may also enhance the performance of Li-ion batteries. Therefore further work is required to check the photocatalytic and battery performance by using the Ag_2CrO_4 sample grown by hydrothermal under mild condition described above

CHAPTER V
CONCLUSIONS AND FUTURE WORK

5.1. Conclusions

Delafossite compounds of general formula ABO_2 (A= Cu, Ag; B= Cr, Al, Fe etc) have been received extensive interest because of their remarkable structural, magnetic and dielectric properties for the application of magnetoelectric and transparent electronic devices. The main research is concerned either fundamental research such as frustrated magnetic interactions in triangular lattices in sight of a new multiferroic material, or the search of a new synthesis method to improve the fundamental properties of delafossite compounds. In context to this, basic understanding of the relationships between structural and physical properties of $ACrO_2$ (A= Cu, Ag) compounds with delafossite structure are very interesting in technological point of view. In the present thesis work, $ACrO_2$ (A= Cu, Ag) compound with delafossite structure have been synthesized by using different synthesis techniques. The techniques used to synthesize these compounds were hydrothermal method (subcritical and supercritical method), monomode microwave solid state reaction and conventional solid state reaction method. This work reports the synthesis and characterization of $(Ag,Cu)CrO_2$ prepared via hydrothermal method and the basic fundamental properties was compared with the samples prepared by using conventional solid state method or a newly developed method in this thesis i.e. monomode microwave solid state heating method. Furthermore, samples of $CuCr_{1-x}V_xO_2$ ($0 \leq x \leq 0.5$) have been prepared by using both hydrothermal and solid state reaction method to study and compare the structural and magnetic properties. Also within this work, the synthesis and characterization of silver-based photocatalysts prepared via hydrothermal method have been studied. The main results of this thesis work are as following:

i. In this work, a new synthesis method was developed to enhance the structural, magnetic, and electrical properties of $CuCrO_2$ compound with delafossite structure (See publication in Material Letters **70**, 2012, 40-43). Herein, $CuCrO_2$ compound with delafossite structure has been synthesized via a direct reaction between Cu_2O and Cr_2O_3 using monomode microwave heating method. The single phase $CuCrO_2$ delafossite was obtained by using a single-mode microwave cavity working at 2.45 GHz within a few minutes (2-5 minutes) at temperature ranged from 1000 $^{\circ}$C-1100 $^{\circ}$C. The samples were prepared in two different kinds of crucible using alumina crucible and silica crucible. In alumina crucible, the heating is provided by the direct coupling between the microwaves and the powder; this is so called direct microwave heating method (DMW). When a silicon carbide crucible is used, the crucible itself heats and the powder is thus heated by both radiative (indirect) and microwave (direct) energy, called hybrid microwave heating (HMW). The rate of synthesis is significantly increased as compared to the solid state reaction method performed in a conventional furnace. In

comparison to the DMW process, the HMW process leads to get a more homogeneous temperature distribution within the sample which is more suitable to synthesize single phases. SEM micrographs show that the grains size is smaller than in sample prepared by solid state (SS) method. The magnetization and resistivity curves show characteristics typical of the 3R delafossite. This technique was proved to be the fastest method to prepare $CuCrO_2$ compound with delafossite structure.

ii. To study the effect on structural and magnetic properties of $CuCrO_2$ compound, hydrothermal process was developed to synthesize $CuCrO_2$ micron size particles. In the first part of work, the precursor materials were optimized. Different precursors were used such as Cu_2O and $Cr(NO_3)_3.9H_2O$ (series A), Cu_2O and CrO_3 (series B), $Cu(OH)_2$ and mixture of $Cr(OH)_3$ and CrO_3(series D), and Cu_2O and mixture of $Cr(OH)_3$ and CrO_3(series C) respectively. Finally, using series C process condition, the single phase of $CuCrO_2$ was obtained at 300 $^{\circ}$C for 48 h of reaction time in presence of 2.5 M of NaOH in an aqueous solution at pressure of 200 bars. Powder X-ray diffraction pattern confirms the purification of $CuCrO_2$ phase with delafossite structure. SEM images shows microspheres with diameter of about 2-4 μm. The micron size sphere appear a bunch of pure $CuCrO_2$ platelets of size ranges from 0.7 μm to 3 μm. In the second part of this work, role of reaction temperature, reaction time, molarity and pressure is thoroughly discussed and the results revealed that increase in reaction time, molarity and temperature increases the solubility of reactants and rate of conversion into their corresponding hydrate species. Samples were also prepared at different pressure ranged from 50 bars to 700 bars in 1 M/2.5M of NaOH at 300 $^{\circ}$C for 48 h in an aqueous solution. Effect of pressure study reveals that there was slight evidence of phase transformation ($CuCrO_2$ 3R phase into 2H phase) at elevated pressure. Samples prepared in the pressure regime between 200 to 300 bars leads to the formation of single crystal phase of $CuCrO_2$. The developing of the 2H phase could be correlated with the increase in pressure and future work will be focused on synthesis of pure $CuCrO_2$ with 2H phase (no detail properties are reported yet) under high pressure up to 2000 bars. (Corresponding publication is ready to submit).

iii. In this work, the effects of vanadium substitution at Cr site in $CuCrO_2$ compound with delafossite crystal structure have been studied. This work demonstrates the detailed study of structural, magnetic, and dielectric properties of series of sample $CuCr_{1-x}V_xO_2$ ($0 \leq x \leq 0.5$). Polycrystalline series of samples of $CuCr_{1-x}V_xO_2$ ($0 \leq x \leq 0.5$) were prepared by solid-state reaction method by mixing Cu, CuO, Cr_2O_3 and V_2O_5. The powder pressed in the shape of the pellets placed in a platinum (Pt) crucible which was then vacuum sealed in a silica quartz tube and fired at 1100 °C for 48 h. Structural analysis showed that series of sample $CuCr_{1-x}V_xO_2$ ($0 \leq x \leq 0.5$) have characteristic of the 3R delafossite. X-ray powder diffraction patterns indicate the absence of any structural phase transition in the whole investigated range of the V^{3+} content in series of sample $CuCr_{1-x}V_xO_2$ ($0 \leq x \leq 0.5$). DC Magnetic susceptibility (χ_{dc} = M/H) study showed that M_{ZFC} (T) exhibits a broad anomaly (varies with vanadium content in $CuCrO_2$) for the lower V^{3+} substituted samples ($0 \leq x < 0.18$) whereas in higher V^{3+} substituted samples ($0.18 \leq x \leq 0.5$), M_{ZFC} (T) exhibits a cusp at low

temperature (< 15 K) and merge with M_{FC} (T) at a slightly higher temperature. M-H curves recorded at 5 K revealed the linear curve in lower vanadium substituted samples of $CuCr_{1-x}V_xO_2$ ($0 \leq x < 0.18$) and S shaped curve for high vanadium content samples i.e. x=0.18, 0.2, 0.3, 0.5. The ac magnetic susceptibility measurement for higher vanadium substituted samples ($0.18 \leq x \leq 0.5$) shows frequency dependent peaks, i.e., as the frequency is increased, T_f (temperature of the maximum in χ'_{ac} (T)) shifts to higher values associated with a decrease in the magnitude of χ_{ac} (T). DC, AC and M-H magnetic measurement revealed the long range AFM behavior in lower V^{3+} substituted samples ($0 \leq x < 0.15$) and spin glass behavior in higher V^{3+} substituted samples ($0.2 \leq x < 0.5$). The unclear frequency dependence (ac magnetic measurements) in samples of x = 0.18 and 0.15 suggests that there exists an intermediate boundary where ($0.15 < x < 0.20$) long range magnetic ordering (AFM) starts to disappears and short range ordering (spin glass) starts to appear. The strong competing interaction between Cr^{3+} and V^{3+} cations gives rise to the origin of disordered magnetic behavior in $CuCr_{1-x}V_xO_2$ for $0.18 \leq x \leq 0.5$. In order to understand the low temperature aging and memory phenomenon, the time dependant and aging (single and double) protocol have been studied on sample $CuCr_{0.7}V_{0.3}O_2$. It can be observed that the system remembers the stop temperature and show a broad dip at stop temperature 8 K (for single aging) and at stop temperature 6 K and 9 K for double aging. Also, it shows rejuvenation at higher temperature which proves the aging and memory effect in $CuCr_{0.7}V_{0.3}O_2$ sample. The memory and aging effects in ZFC experiments of $CuCr_{0.7}V_{0.3}O_2$ sample confirms the glassy magnetic state. Dielectric property characterization of sample with x=0.04, 0.08 showed a long range ordering with ferroelectricity induced by spin ordering (long range ordering) whereas in sample with $0.18 \leq x \leq 0.5$, there exist spin glass behaviour that precludes the existence of ferroelectricity induced by an antiferromagnetic state as observed in parent $CuCrO_2$. Thus, finally it is concluded that the magnetic and ferroelectric properties of polycrystalline sample of series $CuCr_{1-x}V_xO_2$ ($0 \leq x \leq 0.5$) proved that higher vanadium substituted samples ($0.2 \leq x \leq 0.5$) showed the existence of a spin glass state is evidenced by dc and ac magnetization and dielectric property measurements. (Corresponding publication is in progress). To study the effect of synthesis process on the structural and magnetic properties, $CuCr_{1-x}V_xO_2$ (x = 0.02, 0.04) samples were developed by hydrothermal method. The structural result showed the R-3m (rhombohedral) phase in both samples without presence of any impurity of VO_2. Magnetic characterization of both the samples didn't show any magnetic transition i.e. AFM transition as observed in samples prepared by solid state reaction method.

iv. In this work, for the first time the hydrothermal method was developed to obtain $AgCrO_2$ polycrystalline sample. The single phase $AgCrO_2$ sample was prepared by using a direct one step reaction between Ag_2O and $Cr(OH)_3$ at supercritical condition i.e. temperature of 400 $^{\circ}C$, pressure of 400 bar in an aqueous solution using $K_2Cr_2O_7$ as oxidizing agent. In this thesis work, for the first time a detail synthesis mechanism is proposed. Dealing with the synthesis mechanism at temperature 400 $^{\circ}C$, the $K_2Cr_2O_7$ as an oxidizing agent gives excess oxygen in an aqueous solution that in turn oxidizes the metallic silver into Ag^+ oxidation state which reacts with the Cr^{3+} impurity in

an aqueous solution. This leads to the formation of final $AgCrO_2$ compound with delafossite structure. The $K_2Cr_2O_7$ as an oxidizing agent improves the product quality and increases the product yield as compared to other oxidizing agent such as H_2O_2. X-ray diffraction pattern attested the quality of the material, crystallizing in *R-3m* with expected lattice parameters. SEM analysis reveals that the average particle size is in the 0.5-2 μm range. The dc magnetic data of $AgCrO_2$ sample showed a clear AFM transition temperature anomaly at T_N = 21 K.The UV-visible study and FT-IR measurement showed the properties in line with literature. The optical band gap was calculated to be 1.69 eV, respectively. Also, in situ high temperature X-ray diffraction method reveals the linear relationship between the lattice parameter with increasing temperature. (Corresponding publication is in progress).

v. Also, this thesis work focused on synthesis and structural, surface, and optical property characterization of Ag based photocatalysts. Herein, for the first time, it has been proposed a simple, fast and easily controlled method for the synthesis of single phase of polycrystalline sample Ag_2CrO_4 (T= 350 $^{\circ}$C, 1 M of NaOH, 12 h) and single crystal of $Ag_2Cr_2O_7$ (T= 350 $^{\circ}$C, 0 M of NaOH, 12 h) via direct reaction between Ag_2O and CrO_3 precursors under mild hydrothermal condition. X-ray diffraction pattern of the Ag_2CrO_4 sample is typical characteristic of an orthorhombic crystal structure with the space group *Pnma* and for $Ag_2Cr_2O_7$ powder sample is found to be characteristic of a triclinic crystal structure with the space group *P*-1. SEM analysis of Ag_2CrO_4 sample revealed that the average particle size varied from 1 to 10 μm with Ag/Cr ratio ~ 2 confirms the desired stoichiometry of Ag_2CrO_4. While in case of $Ag_2Cr_2O_7$ sample the SEM-EDX confirms the desired stoichiometry of Ag/Cr ratio ~ 1. The optical measurement of Ag_2CrO_4 and $Ag_2Cr_2O_7$ sample revealed indirect optical band gap of 1.62 eV and 1.68 eV. The surface area of Ag_2CrO_4 sample is found to be 3.42 m^2/g which is larger than the one reported in Ag_2CrO_4 sample prepared by conventional method. Thus the large value of surface area reported in hydrothermally grown Ag_2CrO_4 sample may also enhance the performance of Li-ion batteries. (Corresponding publication is ready to submit).

5.2. Future work

As a final remarks, it is concluded that for the first time, hydrothermal process was developed to prepare the complex $ACrO_2$ (A= Cu, Ag) compounds with delafossite structure. These compounds generally require high process temperature and exhibit impurity phases prepared via other conventional methods. After a successful growth of $CuCrO_2$ and $AgCrO_2$ compounds via hydrothermal method, future work will be focused on to grow the single crystal of these compounds which is a basic block of fabrication of highly efficient transparent optoelectronic devices, microelectronics, spintronics, and sensors. Future work will be emphasized to develop the hydrothermal process to obtain the single crystal of $AgCrO_2$. In addition to this, further work is required to study the dielectric and magnetic property of the single crystal of $AgCrO_2$ in search of a new and efficient multiferroic material for magnetoelectric devices. Also, for the first time, within this thesis work single

crystal of $Ag_2Cr_2O_7$ and polycrystalline sample of Ag_2CrO_4 compounds were successfully grown by hydrothermal method applicable for semiconductor photocatalyst. Further work is required to study the phtocatalytic properties of these compounds in detail in sight of an improvement in the performance of semiconductor photocatalyst and Li-Ion batteries. Also, further work is required to develop the process to control the particle size of Ag_2CrO_4 compound. This thesis work reported the large particle size in polycrystalline sample of Ag_2CrO_4. Further work requires to modify the synthesis process and to introduce external additive to obtain nanostructured material to improve the performance of a semiconductor photocatalysts and also more suitable for energy device application.

Publication

1) Miclau M, Ursu D, **Sanjay K**, Grozescu I, *J. Nanoparticle Research,* **14**, 1110, 2012.
2) Kiran Singh, Antoine Maignan, Charles Simon, **Sanjay Kumar**, Christine Martin, Oleg Lebedev, Stuart Turner and Gustaaf Van Tendeloo, *J. Phys. Condens. Matter,* **24**, 226002, 2012.
3) **Sanjay Kumar**, Marinel S, Miclau M, Martin C, *Material Letters*, **70**, 40, 2012.

In Progress

4) **Sanjay Kumar**, M. Miclau, D. Ursu, I. Grozescu and C. Martin" Direct hydrothermal synthesis of $AgCrO_2$ with delafossite structure in supercritical water: a new single-step process (to be submitted).
5) **Sanjay Kumar**, K. Singh, M. Miclau and C. Martin, C. Simon, A. Maignan" $CuCr_{1-x}V_xO_2$ ($0 \leq x \leq 0.5$): Spin Induced Ferroelectricity to Disordered Magnetism" (to be submitted).
6) **Sanjay Kumar**, M. Miclau, D. Ursu, and I. Grozescu"Parametric study of the synthesis conditions of $CuCrO_2$ synthesized by hydrothermal method" (to be submitted).
7) **Sanjay Kumar**, M. Miclau, D. Ursu, I. Grozescu and C. Martin "Facile single-step hydrothermal synthesis of Ag_2CrO_4 microstructure with enhanced surface area" (to be submitted).
8) **Sanjay Kumar**, M. Miclau, D. Ursu, I. Grozescu, and C. Martin "Preparation and characterization of $Ag_2Cr_2O_7$ single crystal by hydrothermal method" (to be submitted).

Conferences

1) 6th International Conference on Material Science and Condensed Matter Physics, September 11-14, **2012**, Chisinau, Moldova (poster)
2) 4th International Symposium on Structure-Property Relationships in Solid State Materials, Bordeaux, France, 24th -29th June, **2012** (poster).
3) SOPRANO annual meeting in Stuttgart, Germany, 2nd - 6th April **2012** (Oral).
4) Physics Conference TIM-11, 24th - 27th November **2011**, Timisoara, Romania (Oral).
5) Workshop on Neutron Scattering, 19th – 21st September **2011**, University of Rennes 1, France.
6) "European School on Magnetism", Targoviste, Romania, 22nd August – 02nd September **2011**.
7) Complementary skills workshop, IPDIA, Caen, France, 22nd -23rd June **2011**.
8) SOPRANO annual meeting in Timisoara, Romania, 6th - 8th April **2011** (Oral).
9) Mid-term review meeting of SOPRANO, Bordeaux, France, 15th-17th of September **2010**.
10) Seventh International Conference on Inorganic Materials, Biarritz, France, 12th -14th September **2010** (poster).

References

[1] P. A. Cox, "Transition Metal Oxides: An Introduction to their electronic structure and properties", Oxford University Press, 1992.
[2] N. A. Spaldin, M. Fiebig, *Science*, **309**, 391, 2005.
[3] E. Dagotto, *Science*, **309**, 257, 2005.
[4] C. W. Nan, M. I. Bichurin, S.X. Dong, D. Viehland, G. Srinivasan, *J. Appl. Phys.*, **103**, 031101, 2008.
[5] W. Eerenstein, N. D. Mathur, J. F. Scott, *Nature*, **422**, 759, 2006.
[6] N. A. Hill, *J. Phys. Chem. B*, **104**, 6694, 2000.
[7] M. Fiebig, N. A. Spaldin, *Eur. Phys. J. B*, **71**, 293, 2009.
[8] M. Liu, O. Obi, J. Lou, Y. Chen, Z. Cai, S. Stoute, M. Espanol, M. Lew, X. Situ, K. S. Ziemer, V. G. Harris, N. X. Sun, *Adv. Funct. Mater.*, **19**, 1826, 2009.
[9] C. W. Baek, N. K. Oh, G. Han, W. H. Yoon, J. W. Kim, J. J. Choi, B. D. Han, D. S. Park, K. D. Sung, J. H. Jung, D. Y. Jeong, J. J. Kim, J. Ryu, *Mater. Sc. Engg. B*, **177**, 451, 2012.
[10] T. Kimura, T. Goto, H. Shintani, K. Ishizaka, T. Arima, Y. Tokura, *Nature*, **426**, 55, 2003.
[11] J. Wang, J. B. Neaton, H. Zheng, V. Nagarajan, S. B. Ogale, B. Liu, D. Viehland, V. Vaithyanathan, D. G. Schlom, U. V. Waghmare, N. A. Spaldin, K. M. Rabe, M. Wuttig, R. Ramesh, *Science*, **299**, 1719, 2003.
[12] D. I. Khomskii, *J. Phys. Condens. Matter*, **20**, 434201, 2008.
[13] Z. M. Tian, Y. S. Zhang, S. L. Yuan, M. S. Wu, C. H. Wang, Z. Z. Ma, S. X. Huo, H. N. Duan, *Mater. Sci. Engg. B*, **177**, 74, 2012.
[14] N. Hur, S. Park, P. A. Sharma, J. S. Ahn, S. Guha, S. W. Cheong, *Nature*, **429**, 392, 2004.
[15] L. Q. Yan, F. Wang, Y. Zhao, T. Zou, J. Shen, Y. Sun, *J. Magn. Magn. Mater.*, **324**, 2579, 2012.
[16] L. Jeuvrey, O. Pena, A. Moure, C. Moure, *J. Magn. Magn. Mater.*, **324**, 717, 2012.
[17] K. F. Wang, J. M. Liu, Z. F. Ren, *Adv. Phys*, **58**, 321, 2009.
[18] J. V. D. Brink, D. I. Khomskii, *J. Phys. Condens. Matter*, **20**, 434217, 2008.
[19] M. Bibes, A. Barthélémy, *Nature Mater.*, **7**, 425, 2008.
[20] D. Khomskii, *Physics*, **2**, 20, 2009.
[21] H. Schmid, "Multiferroic Magnetoelectrics", Ferroelectrics, **162**, 317, 1994.
[22] G. A. Smolenskii, I. E. Chupis, *Sov. Phys. Usp.*, **25**, 475, 1982.
[23] S. W. Cheong, M. Mostovoy, *Nature mater.*, **6**, 17, 2007.
[24] Y. Tokura, S. Seki, *Adv. Mater.*, **22**, 1554, 2010.
[25] K.F.Wang, J. M. Liu, Z. F. Ren, *Adv. Phys.*, **58**, 321, 2009.
[26] D. I. Khomskii, *J. Magn. Magn. Mater.*, **306**, 1, 2006.
[27] H. Katsura, N. Nagaosa, A. V. Balatsky, *Phys. Rev. Lett.*, **95**, 057205, 2005.
[28] M. Mostovoy, *Phys. Rev. Lett.*, **96**, 067601, 2006.
[29] K. Singh, B. Kundys, M. Poienar, C. Simon, *J. Phys.Condens.Matter*, **22**, 445901, 2010.
[30] S. Seki, Y. Onose, Y. Tokura, *Phys. Rev. Lett.*, **101**, 067204, 2008.
[31] M. Poienar, F. Damay, C. Martin, J. Robert, and S. Petit, *Phys. Rev. B* **81**, 104411, 2010.

[32] K. Singh, A. Maignan, C. Martin, and Ch. Simon, *Chem. Mater*., **21**, 5007, 2009.
[33] Y. J. Choi, H. T. Yi, S. Lee, Q. Huang, V. Kiryukhin, S. W. Cheong, *Phys. Rev. Lett*., **100**, 047601, 2008.
[34] G. Giovannetti, A. Stroppa, S. Picozzi, D. Baldomir, V. Pardo, S. Blanco-Canosa, F. Rivadulla, S. Jodlauk, D. Niermann, J. Rohrkamp, T. Lorenz, J. Hemberger, S. Streltsov, D. I. Khomskii, *Phys. Rev. B*, **83**, 060402, 2011.
[35] N. Terada, S. Mitsuda, T. Fujii, K. Soejma, I. Doi, H. A. Katori, Y. Noda, *J. Phys. Soc. Jpn*., **74**, 2604, 2005.
[36] S. Kanetsuki, S. Mitsuda, T. Nakajima, D. Anazawa, H. A. Katori, K. Prokes, *J. Phys. Condens. Matter*, **19**, 145244, 2007.
[37] T. Nakajima, S. Mitsuda, S. Kanetsuki, K. Tanaka, K. Fujii, N. Terada, M. Soda, M. Matsuura, K. Hirota, *Phys. Rev. B*, **77**, 052401, 2008.
[38] N. Terada, S. Mitsuda, Y. Tanaka, Y. Tabata, K. Katsumata, A. Kikkawa, *J. Phys. Soc. Jpn*., **77**, 054701, 2008.
[39] N. Terada, T. Nakajima, S. Mitsuda, H. Kitazawa, K. Kaneko, N. Metoki, *Phys. Rev. B*, **78**, 014101, 2008.
[40] B. Kundys, A. Maignan, D. Pelloquin, C. Simon, *Solid State Sci*., **11**, 1035, 2009.
[41] E. Pachoud, C. Martin, B. Kundys, C. Simon, A. Maignan, *J. Solid State Chem*., **183**, 344, 2010.
[42] R. Nagarajan, N. Duan, M. K. Jayaraj, J. Li, K. A. Vanaja, A. Yokochi, A. Draeseke, J. Tate, A. W. Sleight, *Int. J. Inorg. Mater*., **3**, 265, 2001.
[43] K. E. Ataoui, J. P. Doumerc, A. Ammar, P. Gravereau, L.Fournes, A. Wattiaux, M. Pouchard, Solid State Sci., **5**, 1239, 2003; K. E. taoui, J. P. Doumerc, A. Ammar, J. C. Grenier, L. Fournes, A. Wattiaux, M. Pouchard, *Solid State Sci*., **7**, 710, 2005.
[44] H. Kawazoe, M. Yasukawa, H. Hyodo, M. Kurita, H. Yanagi, H. Hosono, *Nature*, **389**, 939, 1997.
[45] J. Cui, A. Wang, N. L. Edleman, J. Ni, P. Lee, N. R. Armstrong, T. J. Marks, *Adv. Mater*., **31**, 1476, 2001.
[46] J. Park, J. Song, Y. W. Heo, J. H. Lee, J. J. Kim, W. T. Lim, L. Stafford, D. P. Norton, S. J. Pearton, *J. Vac. Sci. Technol. B*, **24**, 2737, 2006.
[47] Y. Kwon, Y. Li, Y. W. Heo, M. Jones, P. H. Holloway, D. P. Norton, Z. V. Park, S. Li, *Appl. Phys. Lett*., **84**, 2685, 2004.
[48] H. H. Hsieh, C. C. Wu, *Appl. Phys. Lett*., **89**, 041109, 2006.
[49] C. H. Seager, D. C. McIntyre, W. L. Warren, B. A. Tuttle, *Appl. Phys. Lett*., **68**, 2660, 1996.
[50] M. W. J. Prince, K. O. Gross-Holtz, G. Muller, J. B. Cillessen, J. B. Giesbers, R. P. Weening, R. M. Wolf, *Appl. Phys. Lett*., **68**, 3650, 1996.
[51] G. Thomas, *Nature*, **389**, 907, 1997.
[52] C. T. Prewitt, R. D. Shannon, D. B. Rogers, *Inorg. Chem*., **10**, 719, 1971.
[53] D. B. Rogers, R. D. Shannon, C. T. Prewitt, J. L. Gillson, *Inorg. Chem*., **10**, 723, 1971.
[54] F. A. Benko, F. P. Koffyberg, *J. Phys. Chem. Solids*, **45**, 57, 1984.
[55] R. Nagarajan, A. Draeseke, A. W. Sleight, J. Tate*, J. Appl. Phys*., **89**, 8022, 2001.
[56] K. Singh, A. Maignan, C. Martin, C. Simon, *Chem. Mater*., **21**, 5007, 2009.
[57] **K. Sanjay**, S. Marinel, M. Miclau, C. Martin, *Mater. Lett*., **70**, 40, 2012.
[58] J. R. Monnier, M.J. Hanrahan, G. Apai, *J. Catal*., **92**, 119, 1985.

[59] T. Nagaura, *Prog. Batteries Solar Cells*, **4**, 105, 1982.
[60] H. Yanagi, T. Hase, S. Ibuki, K. Ueda, H. Hosono, *Appl. Phys. Lett*., **78**, 1583, 2001.
[61] P. W. Sadik, M. Ivill, V. Craciun, D. P. Norton, *Thin solid Films*, **517**, 3211, 2008.
[62] H. Sato, T. Minami, S. Takata, T. Yamada, *Thin Solid Films*, **236**, 27, 1993.
[63] K. Tonooka, N. Kikuchi, *Thin Solid Films*, **515**, 2415, 2006.
[64] M. A. Marquardt, N. A. Ashmore, D. P. Cann, *Thin Solid Films*, **496**, 146, 2006.
[65] B. V. Beznosikov, K. S. Aleksandrov, *J. Struc. Chem*., **50**, 102, 2009.
[66] J. Rodriguez-Carvajal, *Physica B*, **192**, 55, 1993.
[67] R. Gedye, F. Smith, K. Westaway, H. Ali, L. Baldisera, L. Laberge, J. Rousell, *Tetrahedron Lett*., **27**, 279, 1986.
[68] V. C. H. Wiley, H. B. L Weinheim, Microwave Synthesis: Chemistry at the Speed of Light, CEM Publishing, 2002.
[69] R. A. Abramovitch, *Organic Preparations and Procedures International*, **23**, 685, 1991.
[70] I. R. Baxendale, S. V. Ley, M. Nessi, C. Piutti, *Tetrahedron*, **58**, 6285, 2002.
[71] J. L. Krstenansky, I. Cotterill, *Current Opinion in Drug Discovery & Development*, **4**, 454, 2000.
[72] D. Bogdal, P. Penczek, J. Pielichowski, A. Prociak, *Advances in Polymer Science*, **163**, 193, 2003.
[73] S. Barlow, S. R. Marder, *Adv. Func. Mater*., **13**, 517, 2003.
[74] M. Tsuji, M. Hashimoto, Y. Nishizawa, M. Kubokawa, T. Tsuji, *Chem. A Euro. J*., **11**, 440, 2005.
[75] J. M. Collins, N. E. Leadbeater, *Organic and Biomolecular Chem*., **5**, 1141, 2007.
[76] J. Cheng, D. Agrawal, Y. Zhang, R. Roy, A. K. Santra, *J. Alloys Compd*., **491**, 517, 2010.
[77] S. Marinel, E. Savary, *J. Mater. Process. Techn*., **209**, 4784, 2009.
[78] J. S. Schanche, *Mol. Diversity*, **7**, 293, 2003.
[79] A. Loupy, A. Petit, P. Sud, Special Researches, Universite Paris-Sud, **84**, 1997.
[80] K. F. E. Schafthaul, G. A. Bayer, *Akad*., **20**, 557, 1845.
[81] K. Byrappa, M. Yoshimura, "Handbook of Hydrothermal Techn.", Noyes Publications/William Andrew Publishing LLC, Norwich, NY, U.S.A., 2001.
[82] M. J. G. V. Hout, J. C. Verplanke, J. M. Robertson, *Mater. Res. Bull*., **10**, 125, 1975.
[83] M. Yoshimura, W. L. Suchanek, K. Byrappa, *Mater. Res. Bull*., **25**, 17, 2000.
[84] W. C. Sheets, E. Mugnier, A. Barnabe, T. J. Marks, K. R. Poeppelmeier, *Chem. Mater*. **18**, 7, 2006.
[85] J. L. Allen, K. R. Poeppelmeier, *Polyhedron*, **13**, 1301, 1994.
[86] D. Y. Shahriari, N. Erdman, T. M. H. Ulrika, M. C. Zarzyczny, L. D. Marks, K. R. Poeppelmeier, *J. Phys. Chem. Solids*, **64**, 1437, 2003.
[87] M. Yoshimura, W. L. Suchanek, K. Byrappa, *Mater. Res. Bull*., **25**, 17, 2000.
[88] S. Somiya, "Hydrothermal Reactions for Materials Science and Engineering. An Overview of Research in Japan", Elsevier Science Publishers Ltd., London, 1989.
[89] J. O. Eckert, C. C. Hung-Houston, B. L. Gersten, M. M. Lencka, R. E. Riman, *J. Am. Ceram. Soc*., **79**, 2929, 1996.
[90] M. M. Lencka, R. E. Riman, *Chem. Mater*., **7**, 18, 1995.

[91] W. Suchanek, H. Suda, M. Yashima, M. Kakihana, M. Yoshimura, *J. Mater. Res*., **10**, 521, 1995.
[92] R. A. Laudise, *Chem. Eng. News*, Sept., **28**, 30, 1987.
[93] T. Bein, "In Supramolecular Architecture. Synthetic Control in Thin Films and Solids", ACS Symp. Series, **499**, 274, 1992.
[94] M. S. Whittingham, *Opinion Solid State Mater. Sci.*, **1**, 227, 1996.
[95] A. Szymanski, E. Abgarowicz, A. Bakon, A. Niedbalska, R. Salacinski, J. Sentek, *Diamond and Related Mater*., **4**, 234, 1995.
[96] W. L. Suchanek, J. Libera, Y. Gogotsi, M. Yoshimura, *J. Solid State Chem*., **160**, 184, 2001.
[97] T. Sugimoto, "Fine Particles, Synthesis, Characterization, and Mechanisms of Growth, Marcel-Dekker", Inc., New York, 2000.
[98] R. E. Riman, "High Performance Ceramics: Surface Chemistry in Processing Technology", edited by R. Pugh and L. Bergstrom, Marcel-Dekker, NY, 29, 1993.
[99] W. M. Latimer, "The Oxidation States of the Elements and Their Potentials in Aqueous Solutions", 2nd ed., Prentice Hall, New York, 1964.
[100] I. M. Kolthoff, J. F. Coetzee, *J. Am. Chem. Soc*., **79**, 1852, 1957.
[101] P. Kamau, R. B. Jordan, *Inorg. Chem*., **40**, 3879, 2001.
[102] N. M. Nikolaeva, L. P. Pogodina, V. I. Malkova, *Zh. Neorg. Khim*., **30**, 1059, 1985.
[103] B. G. Pound, D. D. Macdonald, J. W. Tomlinson, *Electrochim. Acta*, **24**, 929, 1979.
[104] J. E. Clayton, D. P. Cann, N. Ashmore. *Thin Solid Films*, **411**, 140, 2002.
[105] B. J. Ingram, G. B. Gonzalez, T. O. Mason, D. Shahriari, A. Barnabe, D. Ko, K. R. Poppelmeier, *Chem. Mater*., **16**, 5616, 2004.
[106] M. Poienar, V. Hardy, B. Kundys, K. Singh, A. Maignan, F. Damay, C. Martin. *J. Solid State Chem*., **185**, 56, 2012.
[107] D. Li, X. Fang, W. Dong, Z. Deng, R. Tao, S. Zhou, J. Wang, T. Wang, Y. Zhao, X. Zhu, *J. Phys. D: Appl. Phys*., **42**, 055009, 2009.
[108] M. Amami, F. Jlaiel, P. Strobel, A. B. Salah, *IOP Conf. Series: Mater. Sci. Engg*., **13**, 012001, 2010.
[109] D. C. Ling, C. W. Chiang, Y. F. Wang, Y. J. Lee, P. H. Yeh. *J. Appl.Phys*., **109**, 07D908, 2011.
[110] Y. Sun, T. Wei, X. J. Xu, Y. H. Zhang, *Appl. Phys. Lett*., **78**, 643, 2001.
[111] Zener, *Phys. Rev*., **82**, 403, 1951.
[112] Y. Oohara, S. Mitsuda, H. Yoshizawa, N. Yaguchi, H. Kuriyama, T. Asano, M. Mekata, *J. Phys. Soc. Jpn.*, **63**, 847, 1994.
[113] M. Poienar, F. Damay, C. Martin, V. Hardy, A. Maignan, G. André, *Phys. Rev. B*, **79**, 014412, 2009.
[114] T. Nakajima S. Mitsuda, S. Kanetsuki, K. Prokes, A. Podlesnyak, H. Kimura, Y. Noda, *J. Phys. Soc. Jpn*., **76**, 043709, 2007.
[115] K. Kimura, H. Nakamura, K. Ohgushi, T. Kimura, *Phys. Rev. B*, **78**, 140401, 2008.
[116] T. Okuda, N. Jufuku, S. Hidaka, N. Terada, *Phys. Rev. B*, **72**, 144403, 2005.
[117] T. Okudaa, T. Onoea, Y. Beppua, N. Teradaa, T. Doia, S. Miyasakab, Y. Tokurac, *J. Magn. Magn. Mater*., **310**, 890, 2007.
[118] J.T.Haraldsen, F. Ye, R. S. Fishman, J. A. Fernandez-Baca, Y. Yamaguchi, K. Kimura, T. Kimura, *Phys. Rev. B*, **82**, 020404, 2010.

[119] B. Beverskog, I. Puigdomenech, *J. Electrochem. Soc*., **144**, 3476, 1997.
[120] T. Sato, K. Sue, H. Tsumatori, M. Suzuki, S. Tanaka, A. Kawai-Nakamura, K. Saitoh, K. Aida, T. Hiaki, *J. Supercritical Fluids*, **46**, 173, 2008.
[121] http://www.purdue.edu/rem/rs/sem.htm.
[122] http://bouman.chem.georgetown.edu/S00/handout/spectrometer.htm
[123] M. A. Butler, *J. Appl. Phys*., **48**, 1914, 1977.
[124] J. Tauc, R. Grigorovici, A. Vancu. *Phys. Status Solidi*, **15**, 627, 1966.
[125] M. Gasgnier, J. Ostore´ro, A. Petit, *J. Alloys Comp*., **41**, 275, 1998.
[126] M. Gasgnier, A. Petit, H. Jullien, A. Loupy, *Mater.Res. Bull*., **31**, 1101, 1996.
[127] E. Reguera, C. Diaz-Aguila, H. Yee-Madeira, *J. of Mater. Sc*., **40**, 5331,2005.
[128] M. Gasgnier, A. Petit, *J. Alloys Comp*. **358**, 302, 2003.
[129] M. A. Janney, C. L. Calhoun, H. D. Kimrey, *J. Am. Ceram. Soc*., **75**, 341, 1992.
[130] Savary E, Marinel S, Gascoin F, Kinemuchi Y, Pansiot J, Retoux R, *J. Alloys Compd*., **509**, 6163, 2011.
[131] L. Torkian, M. M. Amini, Materials Letters, **63**, 587, 2009.
[132] C. E. Weitzel, J. W. Palmour, A. H. Carter, K. Moore, K. K. Nordquist, S. Allen, C. Thero, M. Bhatnagar, *IEEE Trans. Electron. Dev*. **43**, 1732, 1996.
[133] T. Subramanian, P. Venkatesh, K. Nagarajan, P. R. Vasudeva Rao, *Mater. Lett.*, **46**, 120, 2000.
[134] A. Maignan, C. Martin, R. Frésard, V. Eyert, E. Guilmeau, S. Hébert, M. Poienar, D. Pelloquin, *J. Solid State Commun*., **149**, 962, 2009.
[135] A. A. Sattar, *Egypt. J. Sol*., **26**, 113, 2003.
[136] D. Munoz-Rojas, R. Cordoba, A. Fernandez-Pacheco, J. M. D. Teresa, G. Sauthier, J. Fraxedas, R. I. Walton, N. Casan-Pastor, *Inorg. Chem*. **49**, 10977, 2010.
[137] D. Y. Shahriari, A. Barnabe, Thomas O. Mason, K. R. Poeppelmeier, *Inorg. Chem*. **40**, 5734, 2001.
[138] D. Munoz-Rojas, G. Subıas, J. Oro-Sole, J. Fraxedas, B. Martınez, M. Casas- Cabanas, J. Canales-Vazquez, J. Gonzalez-Calbet, E. Garca-Gonzlezd, R. I. Walton, N. Casan-Pastor, *J. Solid State Chem*. **179**,3883, 2006.
[139] D. Chen, R. Xu, *J. Solid State Chem*., **137**, 185, 1998.
[140] S. Wang, X. Jiang, D. Guodong, Z. Guo, J. Jang, S. J. Kim, *Mater. Lett.*, **21-22**, 3265, 2011.
[141] G. C. Collazzo, S. L. Jahn, N. L. V. Carreno, E. L. Foletto, *Brazilian J. Chemical Engg*. **28**, 265, 2011.
[142] N. Zhang, R. Yi, Z. Wang, R. Shi, H. Wang, G. Qiu, X. Liu, *Materials Chemistry and Physics*, **111**, 13, 2008.
[143] S. Zhou, X. Fang, Z. Deng, D. Li, W. Dong, R. Tao, G. Meng, T. Wang, X. Zhu, *J. Crystal Growth*, **310**, 5375, 2008.
[144] B. Beverskog, I. Puigdomenech, *Corros. Sci*., **39**, 43, 1997.
[145] B. U. Kohler, M. Jansen, *J. Solid State Chem*., **71**, 566, 1987.
[146] L. Yan, Y. Li, Z. X. Deng, J. Zhuang, X. Sun, *International J. Inorg. Mater*., **3**, 633, 2001.
[147] Y. Yang, L. Xiao, Y. Zhao, F. Wang, *International J. Electrochemical Science*, **3**, 67, 2008.
[148] Y. Peng, Z. Meng, C. Zhong, J. Lu, W. Yu, Z. Yang, Y. Qian, *J. Solid State Chem*., **159**, 170, 2001.
[149] M. N. Viswanathiah, J. A. K Tareen, K. V. Krishnamurthy, *J. Crystal Growth*, **49**, 189, 1980.

[150] S. F. Edwards, P. W. Anderson, *J. Phys. F5*, 965, 1975.
[151] L. C. E. Struik, "Physical Aging in Amorphous Polymers and Other Materials", Elsevier, Amsterdam, 1978.
[152] L. Berthier, J. P. Bouchaud, *Phys. Rev. Lett*., **90**, 059701, 2003.
[153] L. Lundgren, P. Svedlindh, O. Beckman, *Phys. Rev. B* **26**,3990, 1982.
[154] D.S. Fisher, D.A. Huse, *Phys. Rev. Lett*., **56**, 1601, 1986.
[155] M. P. Sharrock, *J. App. Phys*., **76**, 6413, 1994.
[156] K. H. Muller, "Magnetic viscosity Encyclopedia of Materials: Science and Technology", **5**, 2001.
[157] T. Kimura, J. C. Lashley, A. P. Ramirez, *Phys. Rev. B*., **73**, 220401, 2006.
[158] J. A. Mydosh, "Spin Glass an Experimental Introduction", Taylar & Francis, London, 1993.
[159] V. V. Shvartsmann, S. Bedanta, P. Borisov, W. Kleemann, A. Tkach, P. M. Vilarinho, *Phys. Rev. Lett*. **101**, 165704, 2008.
[160] J. B. Goodenough, "Magnetism and the Chemical Bond", Huntington, New York, **174**, 1976.
[161] S. Karmakar, B. K. Chaudhuri, C. L. Chan, D. Yang, *J. Appl. Phys*., **108**, 113916, 2010.
[162] S. Korner, A. Weber, J. Hemberger, E.W. Scheidt, G. R. Stewart, *J. Low Temp. Phys*., **121**, 105, 2000.
[163] Y. Bréard, V. Hardy, B. Raveau, A. Maignan, H.J. Lin, L.Y. Jang, H. H. Hsieh, C. T. Chen, *J. Phys.Condens. Matter*, **19**, 216212, 2007.
[164] P.C. Hohenberg, B.I. Halperin, *Rev. Mod. Phys*., **49**, 435, 1977.
[165] L. S. Lakshmi, A. K. Nigam, *J. Phys.Condens. Matter*, **23**, 086006, 2011.
[166] A. Malinowski, V. L. Bezusyy, R. Minikayev, P. Dziawa, Y. Syryanyy, M. Sawicki, *Phys. Rev. B*, **84**, 024409, 2011.
[167] T. Sarkar, V. Pralong, V. Caignaert, B. Raveau, *Chem. Mater*. **22**, 2885, 2010.
[168] K. Gunnarsson, P. Svedlindh, P. Nordblad, L. Lundgren, H. Aruga, A. Ito, *Phys. Rev. Lett*. **61**, 754, 1988.
[169] M. Sasaki, P. E. Jonsson, H. Takayama, P. Nordblad, *Phys. Rev. Lett*., **93**, 139701, 2004.
[170] P. E. Jonsson, R. Mathieu, P. Nordblad, H. Yoshino, H. A. Katori, A. Ito, *Phys. Rev. B*, **70**, 174402, 2004.
[171] C. R. Sankar, P. A. Joy, *Phys. Rev. B*, **72**, 132407, 2005.
[172] K. Jonason, E. Vincent, J. Hammann, J. P. Bouchaud, P. Nordblad, *Phys. Rev. Lett*., **81**, 3243, 1998.
[173] K. Binder, A. P. Young, *Rev. Mod. Phys*., **58**, 801, 1986.
[174] G. Aurelio, J. Curiale, R. D. Sanchez, G. J. Cuello, *Phys. Rev. B*, **76**, 214417, 2007.
[175] Md. Motin Seikh, V. Caignaert, V. Pralong, Ch. Simon, B. Raveau, *J. Phys.: Condens. Matter*, **20**, 015212, 2008.
[176] N. Bontemps, R. Orbach, *Phys. Rev. B*, **37**, 4708, 1988.
[177] R. S. Freitas, L. Ghivelder, F. Damay, F. Dias, L. F. Cohen, *Phys. Rev. B*, **64**, 144404, 2001.
[178] I. G. Deac, S. V. Diaz, B. G. Kim, S.W. Cheong, P. Schiffer, *Phys. Rev. B*, **65**, 174426, 2002.
[179] D. N. H. Nam, K. Jonason, P. Nordblad, N. V. Kheim, N. X. Phuc, *Phys. Rev. B*, **59**, 4189, 1999.

[180] K. Singh, A. Maignan, C. Simon, **S. Kumar**, C. Martin, O. Lebedev, S. Turner, G. V. Tendeloo, *J. Phys.Condens. Matter,* **24**, 226002, 2012.
[181] A. Maignan, C.Martin, K.Singh, Ch.Simon, O.I.Lebedev, S.Turner, *J. Solid State Chem*., 2012, (http://dx.doi.org/10.1016/j.jssc.2012.01.063)
[182] L. E. Cross, *Ferroelectrics*, **76**, 241, 1987.
[183] S. Ouyang, H. Zhang, D. Li, T. Yu, J. Ye, Z. Zou, *J. Phys. Chem. B*, **110**, 11677, 2006.
[184] S. Ouyang, Z. Li, Z. Ouyang, T. Yu, J. Ye, Z. Zou, *J. Phys. Chem. C*, **112**, 3134, 2008.
[185] B. M. Abu-Zied, *Appl. Catal. A*, **198**, 139, 2000.
[186] K. Ramesha, A. S. Prakash, M. Sathiya, G. Madras, A. K. Shukla, *Mater. Sci. Eng. B*, **176**, 141, 2011.
[187] T. Otabe, K. Ueda, A. Kudoh, H. Hosono, H. Kawazoe, *Appl. Phys. Lett*., **72**, 1036, 1998.
[188] A. Wichainchai, P. Dordor, J. P. Doumerc, E. Marquestaut, M. Pouchard, P. Hagenmuller, *J. Solid State Chem*., **74**, 126, 1988.
[189] Y. J. Shin, J.P. Doumerc, P. Dordor, M. Pouchard, P. Hagenmuller, *J. Solid State Chem*., **107**, 194, 1993.
[190] A. M. L. Lopes, G. N. P. Oliveira, T. M. Mendonca, J. A. Moreira, A. Almeida, J. P. Araujo, V. S. Amaral, J. G. Correia, *Phys. Rev. B*, **84**, 014434, 2011.
[191] M. Miclau, D. Ursu, **K. Sanjay**, I. Grozescu, *J. Nanopart. Res*., **14**, 1110, 2012.
[192] W. J. Croft, N. C. Tombs, R. E. England, *Acta. Crystallogr*., **17**, 313, 1964.
[193] S. Sekiya, H.Okuda, *J. Crystal Growth*, **46**, 410, 1979.
[194] H. Wang, X. Xiang, F. Li, D. G. Evans, X. Duan, *Appl. Surf. Sci*., **255**, 6945, 2009.
[195] A. A. Athawale, P. A. Desai, *Ceramics International*, **37**, 3037, 2011.
[196] M. Stefanescu, M. Barbu, T. Vlase, P. Barvinschi, L. Barbu-Tudoran, M. Stoia, *Thermochimica Acta*., **526**, 130, 2011.
[197] A. Fujishima, K. Honda, *Nature*, **238**, 37, 1972.
[198] K. Maeda, *J. Photochemistry Photobiology C: Photochemistry Reviews* **12**, 237, 2011.
[199] Y. Sakai, S. Sugahara, M. Matsumura, Y. Nakato, H. Tsubomura, *Can. J. Chem.*, **66**, 1853, 1988.
[200] O. Khaselev, J. A. Turner, *Science*, **280**, 425, 1998.
[201] K. Maeda, K. Domen, *J. Phys. Chem. Lett*., **1**, 2655, 2010.
[202] M. I. Zaki, N. E. Fouad, J. Leyrer, H. Knozinger, *Appl. Catalysis*, **21**, 359, 1986.
[203] A. Kudo, K. Domen, K. Maruya, T. Onishi, *Chem. Phys. Lett*., **133**, 517, 1987.
[204] R. Asahi, T. Morikawa, T. Ohwaki, K. Aoki, T. Taga, *Science*, **293**, 269, 2001.
[205] Y. Maruyama, H. Irie, K. Hashimoto, *J. Phys. Chem. B*, **110**, 23274, 2006.
[206] J. H. Xiang, S. H. Yu, Z. L. Xu, *Cryst. Growth Des*., **4**, 1311, 2004.
[207] J. Sinko, Prog. Org. Coat., **42**, 2001, 267-282.
[208] V. Brunetti, H. M. Villullas, T. M. Lopez, *Electrochim. Acta*., **44**, 4693, 1999.
[209] L. Yu, Y. Hongbing, C. Mei, S. Jingwen, *Catalysis Communications*, **26**, 63, 2012.
[210] F. Soofivand, F. Mohandes, M. Salavati-Niasari, *Micro Nano Letters*, **7**, 283, 2012.
[211] M. L. Hackert, R.A. Jacobson, *J. Solid State Chem*., **3**, 364, 1971.

[212] A. Durif, M. T. Averbuch-Pouchot, *Acta Cryst*. B, **34**, 3335, 1978.
[213] P. Cignini, M. Icovi, S. Panero, G. Pistoia, *J. Power Sources*, **3**, 347, 1978.
[214] J. K. Liu, C. X. Luo, N. J. Quan, *J. Nanopart. Res*., **10**, 531, 2008,.
[215] C. G. Maria, A. Bartecki, M. Raczko, *Polyhedron*, **7**, 601, 1988.
[216] R. F. Alamdari, S. S. Hajimirsadeghi, I. Kohsari, *Inorg.Mater*., **46**, 60, 2010.
[217] V. G. Poulopoulou, E. Vrachnou, S. Koinis, D. Katakis, *Polyhedron*, **16**, 521, 1997.
[218] M. M. Mikhailov, A. C. Verevkin, *Rousian Phys. J.*, **47**, 600, 2004.
[219] T. P. Sharma, D. Patidar, N. S. Saxena, K. Sharma, Indian *J. Pure Appl. Phys*., **44**, 125, 2006.
[220] N. Weinstock, H. Schulze, A. Muller, *J. Chem. Phys*., **59**, 5063, 1973.
[221] J. A. Campbell, *Spectrochimic Aacta*, **21**, 1333, 1965.
[222] S. Brunauer, P. H. Emmett, E. Teller, *J. Am. Chem. Soc*., **60**, 309, 1938.
[223] Y. Sato, T. Nakano, K. Kobayakawa, T. Kawai, A. Yokoyama, *J. Power Sources*, **75**, 271, 1998.
[224] S. H. Choi, J.W. Son, Y. S. Yoon, J. Kim, *J. Power Sources*, **158**, 1419, 2006.